# Lessons learned from device modeling of organic & perovskite solar cells

Le Corre, Vincent

**IMPORTANT NOTE: You are advised to consult the publisher's version (publisher's PDF) if you wish to cite from it. Please check the document version below.**

*Document Version*
Publisher's PDF, also known as Version of record

*Publication date:*
2021

[Link to publication in University of Groningen/UMCG research database](#)

# LESSONS LEARNED FROM DEVICE MODELING OF ORGANIC & PEROVSKITE SOLAR CELLS

Vincent M. LE CORRE

Lessons learned from device modeling of organic & perovskite solar cells
Vincent M. Le Corre
PhD thesis
University of Groningen, The Netherlands

NWO
Nederlandse Organisatie voor Wetenschappelijk Onderzoek

# university of groningen

# LESSONS LEARNED FROM DEVICE MODELING OF ORGANIC & PEROVSKITE SOLAR CELLS

## PhD thesis

to obtain the degree of PhD at the
University of Groningen
on the authority of the
Rector Magnificus Prof. C. Wijmenga
and in accordance with
the decision by the College of Deans.

This thesis will be defended in public on

26 March 2021 at 11.00 hours

by

## Vincent M. LE CORRE

born on 13 October 1992
in Villiers-le-bel, France

**Supervisors:**

Prof. L.J.A. Koster
Prof. M. A. Loi

**Assessment committee:**

Prof. C.J. Brabec
Prof. E. Garnett
Prof. M.S. Pchenitchnikov

*That's what I do,*
*I drink and I know things.*

Tyrion Lannister

# CONTENTS

# LIST OF SYMBOLS, ACRONYMS AND MATERIALS

## FUNDAMENTAL CONSTANTS

| | | |
|---|---|---|
| $c$ ............... | Speed of light in vacuum ................... | $299792458 \, \text{m s}^{-1}$ |
| $\epsilon_0$ ............... | Dielectric permittivity of free space ........ | $8.854 \times 10^{-12} \, \text{F m}^{-1}$ |
| $h$ ............... | Planck's constant ........................... | $6.626 \times 10^{-34} \, \text{J s}$ |
| $k_B$ .............. | Boltzmann's constant ...................... | $1.381 \times 10^{-23} \, \text{J K}^{-1}$ |
| $q$ ............... | Charge of the electron...................... | $1.602 \times 10^{-19} \, \text{C}$ |

## SYMBOLS

| | |
|---|---|
| $C_{n(p)}$ ............ | Electron (hole) capture coefficient |
| $D_{n(p)}$ ............ | Electron (hole) diffusion coefficient |
| $E_C$ ............... | Conduction band energy |
| $E_g$ ............... | Band gap |
| $\epsilon$ ................ | Dielectric constant |
| $\epsilon_r$ ............... | Relative dielectric constant |
| $E_{\text{trap}}$ ............ | Trap state energy |
| $\Sigma_T$ ............... | Trap density |
| $E_V$ ............... | Valence band energy |
| $\gamma$ ................ | Bimolecular/Band-to-band recombination rate constant |
| $J_{n(p)}$ ............ | Electron (hole) current density |
| $J_{SC}$ .............. | Short-circuit current density |
| $L_D$ ............... | Exciton diffusion length |
| $\mu_{n(p)}$ ............ | Electron (hole) mobility |
| $n$ ................ | Electron density |
| $N_{c(v)}$ ............ | Effective density of states of the conduction (valence) band |
| $N_D^+$ ............... | P-type doping density (donor-type) |
| $N_A^-$ ............... | N-type doping density (acceptor-type) |
| $n_i$ ............... | Intrinsic carrier concentration |
| $p$ ................ | Hole density |
| $\phi_{n(p)}$ ............ | Electron (hole) injection barrier at the cathode (anode) |
| $\Sigma_T^+$ ............... | Hole trap density |
| $\Sigma_T^-$ ............... | Electron trap density |
| $T$ ................ | Temperature |
| $V_{app}$ ............ | Applied voltage |
| $V_{bi}$ .............. | Built-in voltage |

$V_{OC}$ ............ Open-circuit voltage
$V_T$ ............. Thermal voltage
$X_a$ ............. Anion density
$X_c$ ............. Cation density

## ACRONYMS

BHJ ............ Bulk heterojunction
BW ............. Backward
CT ............. Charge transfer
D/A ............ Donor/Acceptor
DoS ............ Density of states
ETL ............ Electron transport layer
EQE ............ External quantum efficiency
FA ............. Fullerene acceptor
FF ............. Fill factor
FW ............. Forward
GB ............. Grain Boundary
HOMO ......... Highest occupied molecular orbital
HTL ............ Hole transport layer
JV ............. Current-voltage
LUMO ......... Lowest unoccupied molecular orbital
MC ............. Monte Carlo
NFA ............ Non-fullerene acceptor
OPV ............ Organic photovoltaic
OSC ............ Organic solar cell
PCE ............ Power conversion efficiency
PL ............. Photoluminescence
PSC ............ Perovskite solar cell
SCLC ........... Space-charge limited current
TA ............. Transient absorption
TDCF .......... Time-delayed collection field
TL ............. Transport layer
TOF ............ Time-of-flight
TPC ............ Transient photocurrent

## MOLECULES, POLYMERS AND MATERIALS

CuSCN ........ Copper (I) thiocyanate
EH-IDTBR ...... 2-ethylhexyl rhodanine-benzothiadiazole-coupled indacenodithiophene
DPO ............ 2-(1,10-phenanthrolin-3-yl)naphth-6-yl)diphenylphosphine oxide
F4TCNQ ........ (2,3,5,6-tetrafluoro-2,5cyclohexadiene-1,4-diylidene)dimalononitrile

F6-TCNNQ ...... 2,2'-(perfluoronaphthalene2,6- diylidene) dimalononitrile

IDIC ............ Indacenodithiophene end capped with 1,1-dicyanomethylene-3-indanone

IT-2Cl .......... 3,9-bis(2-methylene-((3-(1,1-dicyanomethylene)-chloro)-indanone))-5,5,11,11-tetrakis(4-hexylphenyl)-dithieno[2,3-d:2',3'-d']-s-indaceno[1,2-b:5,6-b']dithiophene

IT-4F ........... 3,9-bis(2-methylene-((3-(1,1-dicyanomethylene)-6,7-difluoro)-indanone))-5,5,11,11-tetrakis(4-hexylphenyl)-dithieno[2,3-d:2',3'-d']-s-indaceno[1,2-b:5,6-b']dithiophene

ITIC ............ 3,9-bis(2-methylene-(3-(1,1-dicyanomethylene)-indanone)-5,5,11,11-tetrakis(4-hexylphenyl)-dithieno[2,3-d:2',3'-d']-s-indaceno[1,2-b:5,6-b']-dithiophene)

IT-M ............ 3,9-bis(2-methylene-((3-(1,1-dicyanomethylene)-6/7-methyl)-indanone))-5,5,11,11-tetrakis(4-hexylphenyl)-dithieno[2,3-d:2',3'-d']-s-indaceno[1,2-b:5,6-b']dithiophene

ITO ............. Indium tin oxide

MEH-PPV ....... Poly[2-methoxy-5-(2-ethylhexyloxy)-1,4-phenylenevinylene]

P3HT ............ Poly(3-hexylthiophen-2,5-diyl)

PBDTT-FTTE ... Poly[4,8-bis(5-(2-ethylhexyl)thiophen-2-yl)benzo[1,2-b;4,5-b']dithiophene-2,6-diyl-alt-(4-(2-ethylhexyl)-3-fluorothieno[3,4-b]thiophene-)-2-carboxylate-2-6-diyl)]

PBDTTT-C ...... Poly[(4,8-bis-(2-ethylhexyloxy)-benzo(1,2-b:4,5-b')dithiophene)-2,6-diyl-alt-(4-(2-ethylhexanoyl)-thieno[3,4-b]thiophene-)-2-6-diyl)]

PC$_{61}$BM ......... [6,6]-phenyl-C61-butyric acid methyl ester

PC$_{71}$BM ......... [6,6]-phenyl-C71-butyric acid methyl ester

PhIm ............ N1,N4-bis(tri-p-tolylphosphoranylidene) benzene-1,4-diamine

PTAA ............ poly[bis(4phenyl)(2,4,6-trimethylphenyl)amine]

PTB7 ........... Polythieno[3,4-b]-thiophene-co-benzodithiophene

Spiro-OMeTAD . 2,2',7,7'-Tetrakis-(N,N-di-p-methoxyphenylamine)9,9'-spirobifluorene

SF-PDI$_2$ ......... Spirobifluorene perylenediimide

TaTm ............ N4,N4,N4",N4" -tetra([1,1'-biphenyl]4-yl)-[1,1':4',1" -terphenyl]-4,4" -diamine

Y6 .............. (2,20 -((2Z,20 Z)-((12,13-bis(2- ethylhexyl)-3,9-diundecyl-12,13-dihydro-[1,2,5] thiadiazolo[3,4-e] thieno[2,"30 ':4',50 ] thieno[20 ,30 :4,5]pyrrolo[3,2-g] thieno[20 ,30 :4,5] thieno[3,2-b]indole-2,10-diyl)bis(methanylylidene))bis(5,6-difluoro-3-oxo-2,3-dihydro-1H-indene-2,1-diylidene))dimalononitrile)

# 1

# INTRODUCTION

E NERGY, ever since the dawn of the industrial revolution our world has been striving for more and more of it. As we develop new technologies we also create new needs, some useful some not. In either case, these ever-growing needs push us to produce at an exponentially growing rate. To sustain this production our world mostly has relied on fossil energy. As a consequence in under a century, we used more fossil energy than the previous millennia of human history.

As our need for energy increased, humans turned from biomass fuels (namely wood, plants...) to more energy-dense materials such as coal, oil. In fact, the main limitation of the use of biomass fuels is that they do not produce a lot of energy, with an energy density around $10^5$ MJ m$^{-3}$ [1,2] and take time and space to renew. [1] To sustain our way of life we would have probably ended up cutting trees at a rate too intense to allow for the regeneration of the forests. [3]

In contrast, fossil energy is a lot more energy-dense, however, its use appears to be almost as shortsighted as the use of biomass energy as it takes millions of years to renew. [1,2] While being convenient at the present time we are draining the Earth of its natural resources, created over millennia, such as the future generations will most likely not be able to rely on them as our reserves will eventually fade.

In a cruel turn of fate, this may not even be the main issue. In fact, the use of fossil energy leads to the production of greenhouse gases which ultimately affect the climate and lead to global warming. [4] While variations in the global temperature are not unprecedented in Earth history it is the first time that the change happens this fast. Even optimistic predictions estimate that if we keep going the temperature will increase by 2 to 4°C within the next 50–100 years. [5] It appears obvious that while the ecosystems were able to adapt to temperature variations over centuries such a fast change can only lead to a natural disaster.

The use of nuclear power could be a solution as it produces a massive amount of energy and remains to date the most energy-dense production method. However, the risk of such energy production may not fully outweigh the benefits. Historical disasters such as Chernobyl and Fukushima have already shown the dramatic consequence of an accident involving radioactive materials on human activity and ecosystems. Besides, the

storage of nuclear waste and the dismantling of aging nuclear power plants also remains a major issue.

Renewable energies then appear as the only viable long term solution to cut greenhouse gas emissions and have acceptable risks. However, it is not all sunshine and rainbows as there are three major obstacles to reach clean energy production: efficient and cheap production, transport and storage.

In fact, most of the renewable energy sources, such as wind and solar, all suffer from one main issue: they are intermittent. Because they are intermittent, they cannot provide energy 24/7 as we would need, hence, we cannot solely rely on them. They need to be combined with other methods of production to compensate for the downtime or efficient and cheap storage.

While the transport and storage of the energy remain major issues to a 100% clean energy production there is still a lot of room for improvement in our current situation. As of 2017, the proportion of the global energy production is still dominated mostly by fossil energies with 85% of our yearly consumption and only 4% from renewable sources 20% out of which are generated by solar energy, the rest being produced by nuclear and other energies. [6,7]

Solar energy is one of the most abundant and promising renewable energy sources and can be converted in various ways from photoelectrochemical cells for hydrogen production via water splitting to photovoltaic applications. The focus of this thesis will be on the latter.

Photovoltaic solar cells, as implied by the name coming from the Greek "phōs" meaning light and "volt" for the unit of the electromotive force, directly convert sunlight into electricity. The current solar cell market is dominated by crystalline silicon solar cells that represent over 90% of the production. [8,9] While the cost of solar cells has dropped consequently over the past decade [8], it is yet to become an important part of our power grid and further investments are still necessary to reach a greener energy production. [8,10]

One of the best ways to reduce the cost and payback time of solar cells is to improve the efficiency of the module. The best silicon cells efficiency now reach 26.7% in the labs [8,11] and 17-21% for commercial modules. [8] These numbers represent ≈80% and ≈64% of the maximum theoretical efficiency [12] (≈32%) for an ideal material with the same bandgap. While there is still some room for improvement from the lab to the production line, we are getting close to the best of what silicon can do on its own.

One of the most promising ways to further improve the efficiency of silicon solar cells is to combine it with another cheap material in a tandem or multi-junction configuration by stacking two or more solar cells on top of each other. Perovskite materials appeared as the front runner for this application.

While improving the efficiency of current modules is important, the emergence of new applications will be critical to increase the portion of our energy production that comes from solar. The use of semitransparent and/or flexible modules could also help opening-up new ways of producing our energy and reducing our fossil energy consumption. For this kind of application, silicon may not be the best option. In fact, even if it has been demonstrated that silicon-based semitransparent solar cells are possible [13] as well as flexible ones [14] it requires extra steps which may increase the production price.

For this kind of application organic and perovskite materials could be the solution as

both can be used to make semitransparent and/or flexible modules. [15–23] Besides, both technologies can be solution-processed and printed over large area.

This thesis explores the device physics of organic and perovskite-based solar cells to bring more understanding on the processes limiting their performance. It starts with an introduction of some fundamental background on organic and perovskite semiconductors and what makes them special materials. Then the device model used throughout this thesis is introduced as well as the relevant physical processes that are included in the model to simulate both organic and perovskite materials. This work is divided into two parts corresponding to the two studied technologies, the first part on organic solar cells (OSCs) and the second part on perovskite solar cells (PSCs).

Starting with organic solar cells, **chapter 2** discusses the exciton diffusion length in new high performing non-fullerene acceptors (NFA). The exciton diffusion length is a crucial property to ensure charge separation in low dielectric constant organic semiconductor blends. The exciton diffusion length was measured on 9 acceptors using both electrical and optical measurements and showed that NFAs exhibit largely improved exciton diffusion length up to 45 nm compared to the 10 nm reported for fullerene acceptors (FA). This chapter also provides some insight on the influence of the chemical structure of the non-fullerene acceptors on the exciton diffusion length and especially the influence of end-groups.

After discussing the exciton dynamic and its importance for the generation of free charges, the extraction dynamics of the said charges in OSCs are investigated in **chapter 3**. More specifically the influence of dispersion on the extraction time under steady-state operating conditions. In fact, the accuracy and relevance of the values obtained when characterizing the transport of organic semiconductors using classical methods were called into question as they usually underestimate the influence of non-thermalized charges. Here, we combine experiments and simulations to show that non-thermalized carriers only have a small influence on the extraction under operating conditions.

In the second part of this thesis, the properties of perovskite materials and their application to solar cells are discussed. In a typical perovskite solar cell, the perovskite layer is usually multi-crystalline, while the understanding of the properties of the multi-crystalline film is of utmost importance, the understanding of the intrinsic properties of perovskite semiconductor is also a key to improve the device efficiency. One of the most common techniques used to investigate the intrinsic properties of perovskite materials is the measurement of single-carrier devices made of perovskite single crystal, the so-called space-charge-limited measurements. **Chapter 4** presents a perspective on the pitfalls of using such a technique on perovskite materials and especially how the ionic movement can drastically influence the outputs and lead to ill-based conclusions on the defect density extracted from these measurements. An alternative method to get reliable measurements that are less affected by ionic motion is also proposed.

To build an efficient solar cell the perovskite layer is usually stacked between two charge transport layers (TLs). In **chapter 5** the effect of the transport properties of the TLs on the device efficiency is examined. Two new figures of merits are introduced to help the optimization of the TLs in terms of thickness and/or conductivity. The results

**1**

are supported by both experimental results on solution and vacuum processed PSCs as well as extensive simulations.

Finally, in **chapter 6** the use of simulation trained machine learning as a tool for the identification of the dominant recombination process in PSCs is presented. The machine learning toolbox provides a good platform to quickly identify the dominant loss without having to perform any kind of fitting procedure of the experimental data and could be used in combination with high-throughput experimentation. This chapter also provides an in-depth analysis of the light intensity dependence of the open-circuit voltage ($V_{OC}$) and how it relates to the dominant recombination process. It also shows that the analysis of such a measurement needs to be made with care as transport and doping properties of the different layers also influence the results.

## **1.1.** ORGANIC SEMICONDUCTORS FOR SOLAR CELL APPLICATIONS

Organic compounds are defined as carbon-based materials, while they were originally derived from living organisms they are now also produced in the lab. While most organic compounds are insulating a class of these materials shows semiconducting properties. This change in conducting properties arises from a different bonding between the atoms. For organic insulators, the main bonding between the carbon atoms is the results of $\sigma$-bonds. However, if the carbon is only surrounded by three atoms an out of plane $\pi$-bond will be formed as a result of the overlap of two $2p_z$ orbitals forming a double-bond. If three or more of these orbitals overlap the electrons in the $\pi$-bonds are delocalized over the length of the so-called conjugation. The conjugation is defined by a system with overlapping p-orbitals with delocalized electrons in a molecule. This conjugation usually stabilizes the systems which end up in a reduction of the bandgap ($E_g$) and also allows for carrier transport of the delocalized electrons in the $\pi$-bonds which gives rise to semiconducting properties in conjugated organic molecules and polymers. The filled $\pi$-bonds and the empty $\pi^*$-bonds will form the highest occupied molecular orbital (HOMO) and lowest unoccupied molecular orbital (LUMO) respectively. The energy difference between the HOMO and LUMO will define the bandgap of the semiconductor and are usually treated as the valence ($E_V$) and conduction ($E_C$) band in a traditional semiconductor. [24,25]

Traditional inorganic semiconductors are usually made of giant covalent ordered structures where the electrons are delocalized over the whole system. However, organic semiconductor molecules are linked by weak Van-der-Waals forces and tend to be a lot more disordered hence the carriers are not delocalized over the whole systems. Because of these properties, the charges tend to be a lot more localized in organic than in traditional inorganic semiconductors. [25]

This spatial localization of the charges and the energetic and spatial disorder inherent to organic systems give rise to two unfortunate properties. First, a low dielectric constant which leads to the formation of Frenkel exciton, a coulombically bound electron-hole pair, upon light absorption and not directly free charges as in inorganic semiconductors that tend to have larger dielectric constants. Secondly, the charge transport is usually not

described as band-like transport where the charge can move freely. Instead, the charge carriers are mostly localized on one molecule or one segment of a molecule or polymer and need to "hop" from one site to the other. The following sections describe these two processes: (1) exciton and free charge generation and (2) charge transport. [25]
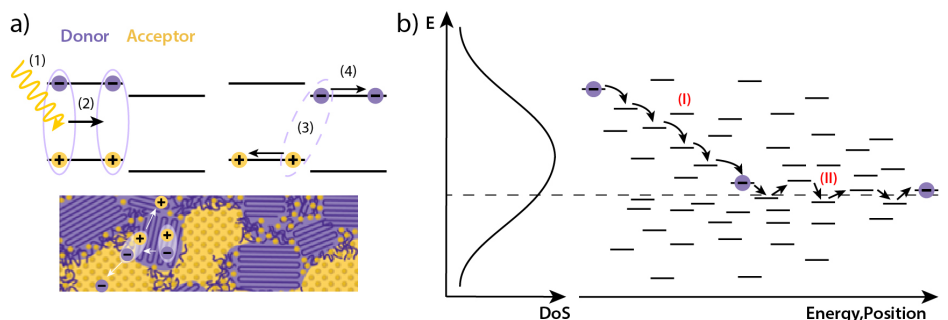


Figure 1.1: Schematic (a) of the processes leading to the charge separation in OSCs with (1) photon absorption, (2) exciton diffusion, (3) exciton dissociation and (4) free charge transport. Charge relaxation and transport (b) through a gaussian density of states (DoS) with first (I) a fast relaxation toward the bottom of the DoS and then (II) an isoenergetic transport (hopping) around the transport energy (dashed line).

### 1.1.1. EXCITON AND FREE CHARGE GENERATION IN ORGANIC SEMICON-DUCTORS

As discussed previously, the low dielectric of organic semiconductors leads to the formation of strongly bound electron-hole pairs called excitons upon light absorption. [26–29] To overcome the Coulomb interaction and split the exciton into free charges two or more materials are usually blended to form a so-called bulk heterojunction (BHJ). Historically, the BHJ were composed of two materials, [30] one electron donor and one electron acceptor, the idea being that the offset between the energy level of the donor and acceptor would promote the exciton dissociation at the D/A interface.

A schematic picture of the process leading to the exciton dissociation is presented in figure 1.1.a. First, upon the absorption of a photon an exciton is created (1), here represented in the donor but the same process can happen if the exciton is created in the acceptor. Then the exciton can migrate (2) through the material and either dissociate into free charges or recombine. The average distance traveled by an exciton before it recombines defines the exciton diffusion length $L_D$. The $L_D$ will be discussed in **chapter 2** for several acceptors including FA and NFA.

Step (3) represents the exciton dissociation at the D/A interface, this separation can be driven by different factors. The driving force governing the exciton dissociation is not yet clear in OSCs and is likely to be system dependent. The formation of a so-called charge transfer (CT) state at the D/A interface has often been invoked to explain the exciton dissociation, especially in fullerene-based OSCs. [31–34] However, the formation of CT-states with a lower energy than the singlet is not always necessary for efficient charge generation. In fact, recently reported NFA-based OSCs have shown that efficient charge

generation can be achieved without the presence of an energetic offset between the singlet and CT-states. [35–37]

In either case, a complete understanding of the exciton dissociation mechanism is yet to be achieved while several processes have been proposed [31–41] there is no consensus and general theory to explain that phenomenon for all systems.

Finally, step (4) refers to the free charge transport through the material that will be discussed in the next section.

### 1.1.2. CHARGE TRANSPORT

The charge transport mechanism in organic semiconductors is different from that of typical inorganic semiconductors. As mentioned previously the weak bonding between the molecules or polymers component of the materials combined with the "large" degree of disorder (compared to inorganic semiconductors) both spatial and energetic does not allow for band-like transport of charges. Instead, charges are localized to discrete energy sites with a Gaussian energy distribution, as pictured in figure 1.1.b. In order to move in the material charge carriers need to "hop" from one site to the other. Several models have been introduced to describe this phenomenon including Miller-Abrahams [42] and Marcus [43] formalisms. Both models estimate the transfer rate between two sites depending on their energy difference, distance or overlap and reorganization energy.

In general, two regimes can be distinguished (I) a fast relaxation to the bottom of the density of states (DoS) until thermal equilibrium with the lattice is reached, this phenomenon is called thermalization of the charges. [44] Followed by an isoenergetic hopping transport around the transport energy.

While the regime (I) is energetically favorable and leads to fast charge transport, i.e. high mobilities, the regime (II) is not and leads to significantly reduced mobilities. This phenomenon is one of the bottlenecks of OSCs as low mobilities, obviously, have a detrimental effect of the device efficiency and limit the thickness of the organic layer to a few tens to hundreds of nm.

**Chapter 3** will discuss the influence of those two regimes on the charge carrier extraction in OSCs under operating conditions.

### 1.1.3. STATE-OF-THE-ART ORGANIC SOLAR CELLS

In the early days of OSCs, the active layer was made of a bilayer with the donor and acceptor stacked on each other. However, because of the limited diffusion length of the excitons and the low surface of contact area between the donor and the acceptor, the efficiency of those devices were limited to values around 1%. [45] To overcome this issue BHJ were introduced [46] and nowadays standard configuration for state-of-the-art OSCs consist of a BHJ stacked between two TLs, ideally selective for one type of carrier, and two electrodes, as shown in figure 1.2.a. After a short stagnation period between 2011-2016 in terms of single-junction OSC efficiency to around 11%, see figure 1.2.b, the performance of OSCs is on the rise again with the accession of new highly efficient acceptors. With the highest efficiency to date over 18% [47] OSCs are well on their way to reach the 20% milestone. [48]

While there have been numerous studies on the stability of OSCs it remains a critical challenge. The wide variety of materials that can be used OSCs as well as the diversity of solvent, additive and processing conditions makes the analysis of the driving force for the degradation a very complex problem. Several suggestions have been made to explain the degradation in OSCs but no general rules can be made and the degradation mechanism is highly system-dependent. [49–59]
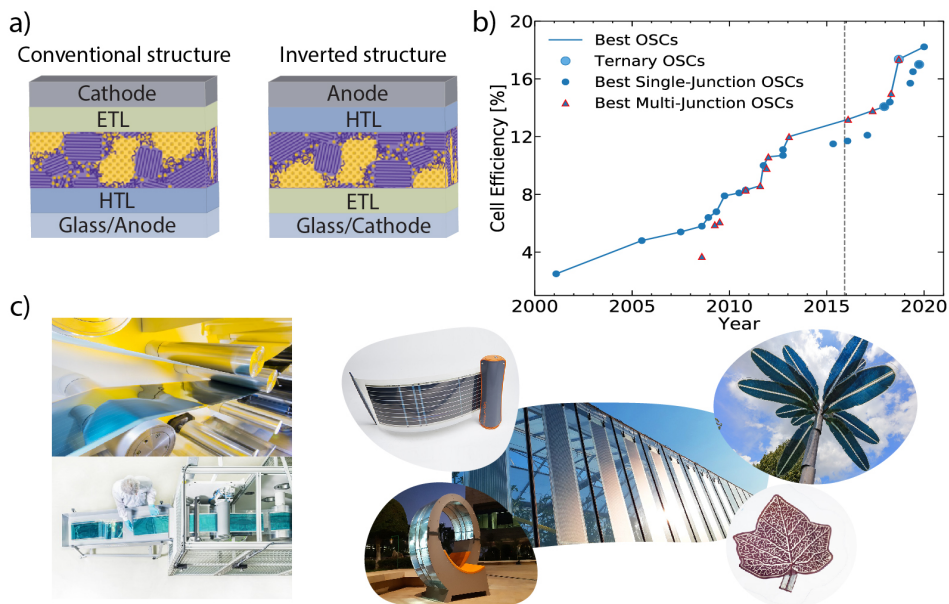


Figure 1.2: (a) Schematic of conventional and inverted device architecture of typical OSCs. (b) Evolution of the OSCs best efficiency overtime for single and multi-junction, taken from Ref. 11,30,47,60–73. The dashed grey line correspond to the beginning of this PhD project. (c) Commercial applications for OSCs by Heliatek®,[72] ASCA®-Armor[71] and OPVIUS®[73] (from left to right).

The upscaling to larger area[69,74–76] and industrially compatible deposition techniques[75,77–81] also represents major challenges. Nonetheless, companies such as ASCA®-Armor[71], OPVIUS®[73] and Heliatek®[72] have already demonstrated that it is possible to produce large area and customizable products with OSCs as seen in figure 1.2.c. These examples show us well how versatile OSC technology could be, it can be made transparent, light-weight flexible, with tunable shape and colors which allows it to be used for building integration, urban design applications as well as for special products such as a solar charger for small batteries and even for more artistic products. In addition, for some of these applications a 15-20 years lifetime would most likely not even be required placing OSCs as a competitive option.

Organic semiconductors are also often used as TLs in perovskite solar cells but this will be discussed in the next section.

## 1.2. PEROVSKITE SEMICONDUCTORS FOR SOLAR CELL APPLICATIONS

### 1.2.1. PEROVSKITE STRUCTURE AND PROPERTIES

The designation 'perovskite' corresponds to a class of material with a crystal structure $ABX_3$, in which A and B are cations and X represents an anion, see figure 1.3.a. Each unit cell of $ABX_3$ crystal comprises of corner-sharing $BX_6$ octahedra, with the A cation occupying the cuboctahedral cavity. It owes its name to the crystal structure of the $CaTiO_3$ that was named after Lev Perovski.
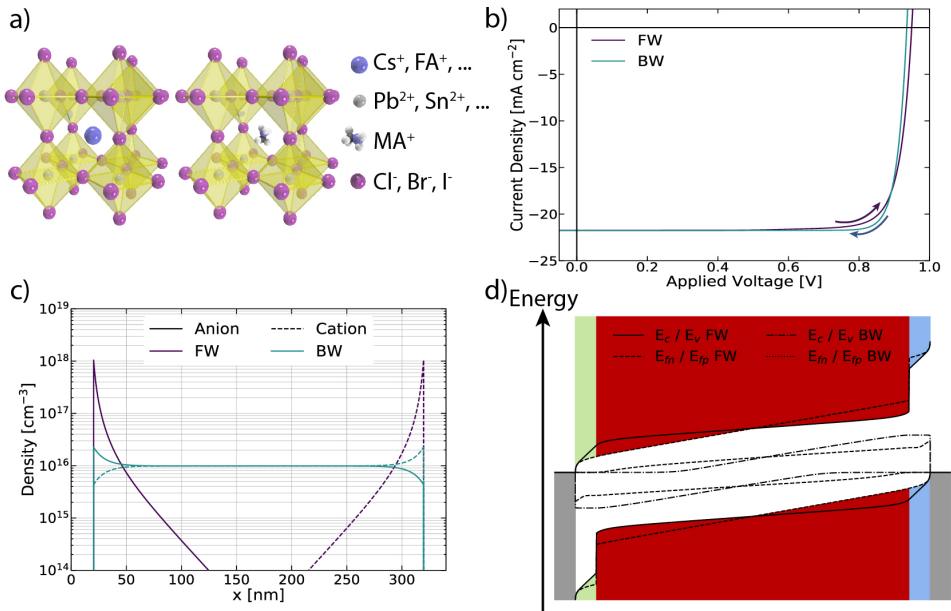


Figure 1.3: (a) General crystal structure of inorganic and hybrid organic-inorganic perovskite. (b) Example of the hysteresis effect between the forward (FW) and backward (BW) direction JV-scan in presence of moving ions. Accumulation of ions at the perovskite/TL interface (c) during FW scan compared to the BW scan creates a reduction of the field leading to almost flat band conditions under short-circuit conditions (d). This effect is responsible for the hysteresis observed in (b).

The A-site cation, in the most common perovskites used for solar cell application, is typically a monovalent organic (such as $CH_3NH_3^+$ (MA) or $(NH_2)_2CH^+$ (FA)) or inorganic (such as $Cs^+$ or $K^+$) cations. The B- site cation usually consists of a divalent cation such as $Pb^{2+}$ and $Sn^{2+}$ and the X-site is occupied by a halide anion (such as $Cl^-$, $Br^-$, $I^-$). Perovskites used as absorber materials in solar cells are based on metal halide perovskite and can be purely inorganic, such as $CsPbI_3$, or 'hybrid' with both organic and inorganic components such as $MAPbI_3$.
The first report of metal halide perovskite dates back to the late 70s[82] and nearly

30 years after its discovery it was used for the first time as an absorber for solar cell application. [83] While it was first developed to be used as a sensitizer in dye-sensitized solar cells, [83] the real breakthrough of perovskite started in 2012 with the first reports of all-solid-state PSCs [84,85] which quickly broke the record of dye-sensitized solar cells.

Metal halide perovskites are particularly suited for solar cell applications. They benefit from outstanding optoelectronic properties with high absorption coefficient [86] thanks to there direct or only slightly indirect bandgap [87–90] which can also be tuned using mixed composition [86] and high carrier mobilities. [88,91] In addition, the low exciton binding energy and high dielectric constant [87,92–95] allows for the generation of free charges upon the absorption of a photon.

However, PSCs are still limited by non-radiative recombination especially at grain boundaries and at the interface with the TLs, [96–98] as will be discussed in chapter 5 & 6. In addition to the recombination losses, perovskite materials are prone to ionic motion which in term can also limit the performance and stability of PSCs. [99–104]

## 1.2.2. Ion migration

The ionic conduction in perovskite-type halides was reported already in the 80s. [105] However, the influence of ion migration and its influence on current-voltage (JV) characteristics was only noted in PSCs in 2014 when the hysteresis—different JVs depending on the scan direction and voltage scan rate —in the JV curves was first reported. [99] Figure 1.3.b shows an example of hysteresis for two JVs with different scan directions and moving ions. Since the first report of hysteresis in PSCs this process has been thoroughly studied and it is now widely admitted that moving ions are the main responsible for this effect. [99–104,106–110]

While there are numerous simulation studies either based on first-principles [111–114] or DD [102,106,115–117] that aimed to access the nature of these moving ions and their properties (diffusion coefficient, activation energy and density) [107] it appears to be very challenging to confirm those numbers experimentally as it is difficult to decorrelate the influence of each moving charge. [107–110]

The hysteresis is due to the change in the ionic distribution throughout the perovskite layer. When the JV-curve is measured rapidly from 0 V to open-circuit the ions do not have enough time to move and keep their original position or only move a little and accumulate at the perovskite/TL interfaces because of the built-in field, see figure 1.3.c. This creates a reduced the field leading to almost flat band conditions and can even a small energetic barrier, see figure 1.3.d, forcing the charges to move by diffusion. However, when the device is pre-bias at $V > V_{OC}$ the ions are mostly in the bulk of the perovskite and therefore the charges can now drift toward the right electrode. This results in the different JV-characteristics observed between the FW and BW scan. Thus when reporting JV-curves of PCSs the two scan directions need to be shown to ensure a faithful report of the actual device efficiency. [118]

In the next chapters, the simulated JV-curves will always refer to stabilized JVs unless stated otherwise.
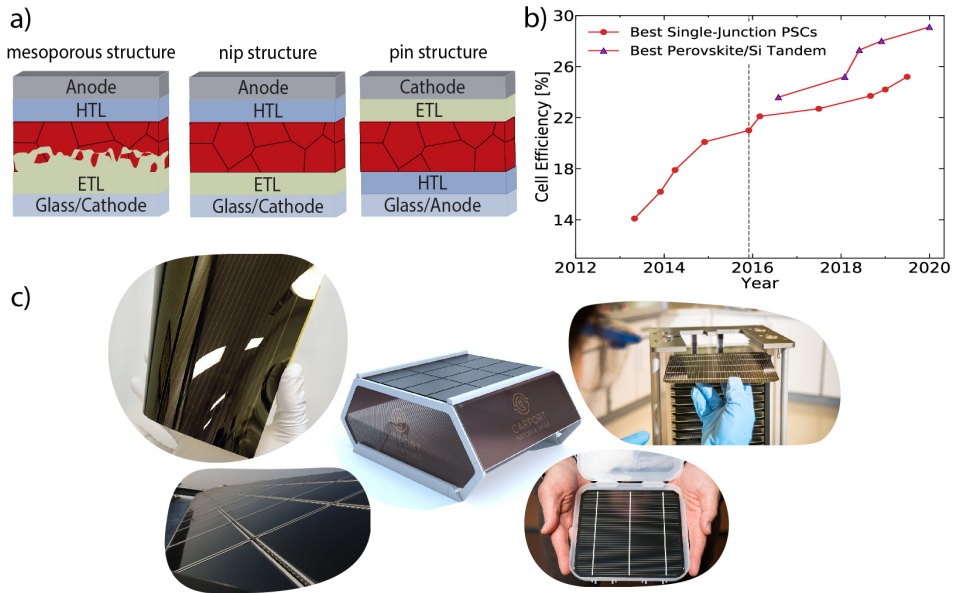
Figure 1.4: (a) Schematic of typical PSCs device architectures. (b) Evolution of the PSCs best efficiency over-time for single and multi-junction, taken from Ref. 11,60,119–121. The dashed grey line corresponds to the beginning of this PhD project. (c) Commercial applications for PSCs by Solliance[®][122], Wonder Solar[®][123], Saule technology[®][124] and OxfordPV[®][121] (from top to bottom and left to right).

## 1.2.3. STATE-OF-THE-ART PEROVSKITE SOLAR CELLS

Historically, perovskites were used as sensitizers in dye-sensitized solar cells,[83] but then evolved in all-solid-state PSCs. The first structures reported mainly consisted of mesoporous structure, see figure 1.4.a, using $TiO_2$ as ETL and Spiro-OMeTAD as HTL.[84,85] Later on planar nip and pin structure, see figure 1.4.a, were also introduced. The mesoporous structure still holds the record for the highest efficiency in single-cell configuration with 25.2%[60], see figure 1.4.b, but the planar structure has been catching up quickly in recent years and are now only a couple of percent behind.[125,126]

In just about 10 years of development, organic-inorganic perovskite solar cells have already caught up with the classical inorganic technologies overpassing the best thin-film (CIGS, CdTe) and multi-crystalline silicon solar cells while getting close to the best monocrystalline silicon cells at 26.7%.[11,60] However, this is not the end of the road as recent models predict a practical efficiency limit of above 30% even for single-junction perovskite cells.[127,128] To reach such efficiencies further optimization of the charge transport layers (TLs) and reduction of nonradiative defect recombination at the inter-faces and/or grain boundaries are still necessary.

PSCs present several advantages compared to typical inorganic solar cells. Just like OSCs they can be solution-processed, made semi-transparent and process on flexible substrates. Moreover, perovskites are highly relevant for a range of tandem applications, promising even higher performances, for example, all-perovskite tandem cells reached

24.8%, [129] tandem cells with CIGS 23.3% [130] and even more promising in combination with silicon up 29.1% [11,121] has been reported even 30.2% [131] in bifacial configuration. Nonetheless, reaching high efficiency is not the only challenge that perovskite materials will have to face before being commercial products. First in terms of stability, if perovskites are meant to be used in combination with silicon they will need to reach a similar stability regime, i.e. around 20 years. While tremendous progress has been made in term of stability with devices being stable over 1000 hours the mechanisms driving the degradation are yet to be fully revealed and ways to properly characterize and report stability of PSCs is still under heavy discussions. [118,132] Secondly, the highest efficiency PCSs are unfortunately all lead-based and the toxicity of the lead compounds could be a major obstacle toward the commercialization of perovskite-based solar cells. [133] In Europe, for example, the Restriction of Hazardous Substances (RoHS) legislation [134] restricts the amount of lead that can be used in commercial products to < 1000 ppm. And while companies like Saule technologies have already reported modules that satisfy this requirement [135] the question of the impact of lead in perovskite-based materials remains. A recent study [133] has shown that "lead from halide perovskite is more dangerous than other sources of the lead contamination already present in the ground as it is ten times more bioavailable". Which really questions whether the use of lead-based perovskite would be a good approach. The development of tin-based perovskites, which are less-bioavailable according to the same study [133] could be a viable alternative but still have a long way to go to catch up in terms of efficiency. Another alternative could be the use of clever encapsulation that can capture the lead potentially leaking from damage solar cells as demonstrated recently. [136]

Nevertheless, the issue of the lead toxicity will need to be addressed whether by smart engineering of the PSCs panels or/and by stronger governmental policies on the amount of lead and on how to dispose of damaged or aging modules.

## 1.3. Charge carrier recombination processes

The main recombination processes in both organic and perovskite semiconductors are mainly related to two distinct mechanisms: (1) band-to-band/bimolecular recombination and (2) trap-assisted recombination. In this thesis, we will neglect Auger recombination as it unlikely to influence organic and perovskite solar cell performances under 1 sun illumination intensity. [137–139]

### 1.3.1. Band-to-band/Bimolecular recombination

Band-to-band/bimolecular recombination corresponds to the direct recombination of a free electron from the conduction band (LUMO) with a free hole from the valence band (HOMO), see figure 1.5.a. The band-to-band denomination will be used when referring to perovskite and bimolecular when referring to organic semiconductors. This type of recombination is usually accompanied by the emission of a photon with the same energy as the bandgap and is, hence, also called radiative recombination. However, this is not always the case, especially, in organic semiconductors, as that energy can be dispersed by other pathways that are nonradiative. [140–142]

11

The band-to-band/bimolecular recombination rate ($R_B$) is given by

$$R_B = \gamma \left(np - n_i^2\right), \tag{1.1}$$

where $n$ and $p$ are electron and hole densities respectively, $\gamma$ is the bimolecular recombination rate constant and $n_i$ is the intrinsic carrier concentration.
In OCSs, $\gamma$ is often written according to the reduced Langevin formula:

$$\gamma = \gamma_{pre} \times \gamma_L = \gamma_{pre} \times \frac{q}{\epsilon} \left(\mu_n + \mu_p\right) \tag{1.2}$$

with $\gamma_{pre}$ the reduction factor for the Langevin law [143] that was introduced for the recombination of ions in a gas. $\gamma_{pre}$ typically varies between $10^{-4}$ - 1 and $\gamma$ between $10^{-11}$ - $10^{-10}$ cm³ s⁻¹. [144,145] Owing to the low mobility and dielectric constant of organic semiconductors, bimolecular recombination is often found to be the dominant recombination process in OSCs, [140,144] even though in new systems with NFAs this may not always be true.
Perovskites, however, with their larger mobility and dielectric constant, do not suffer as much from band-to-band recombination, see figure 1.5.b. $\gamma$ values typically range between $10^{-11}$ - $10^{-9}$ cm³ s⁻¹. [146–150] The low band-to-band recombination rate in PSCs may be explained by lattice distortion leading to a spatial separation of electrons and holes decreasing the probability of charge carriers to recombine. [147] Instead, the recombination is mostly dominated by nonradiative recombination. [96–98,106]

### 1.3.2. TRAP-ASSISTED RECOMBINATION

Trap-assisted recombination consists of the recombination of an electron and a hole via a localized state within the bandgap, see figure 1.5.c. Under steady-state conditions, the trap-assisted recombination rate is usually described by the Shockley-Read-Hall (SRH) equation [151,152] such as:

$$R_{SRH} = \frac{C_n C_p \Sigma_T}{C_n(n + n_1) + C_p(p + p_1)} \left(np - n_i^2\right), \tag{1.3}$$

where $\Sigma_T$ is the trap density, $n_1$ and $p_1$ are constants which depend on the trap energy level ($E_{trap}$), and $C_n$ and $C_p$ are the capture coefficients for electrons and holes respectively. $n_1$ and $p_1$ are defined as followed:

$$n_1 = N_c \exp\left(-\frac{E_C - E_{\text{trap}}}{k_B T}\right) \quad \text{and} \quad p_1 = N_v \exp\left(-\frac{E_{\text{trap}} - E_V}{k_B T}\right) \tag{1.4}$$

with $k_B$ the Boltzmann's constant, T the absolute temperature, $N_c$ and $N_v$ the effective density of states for the conduction and valence band respectively. In the remainder of this thesis we will consider in the simulations that $N_c = N_v$ and only use the notation $N_c$. The nature and origin of the trap in OSCs remain obscure. Several potential sources for the trap states have been suggested such as impurities either from remaining from synthesis or due to the processing condition (atmosphere, solvent, additives...), structural defects of the polymer or molecules, self-trapping and presence of water but there
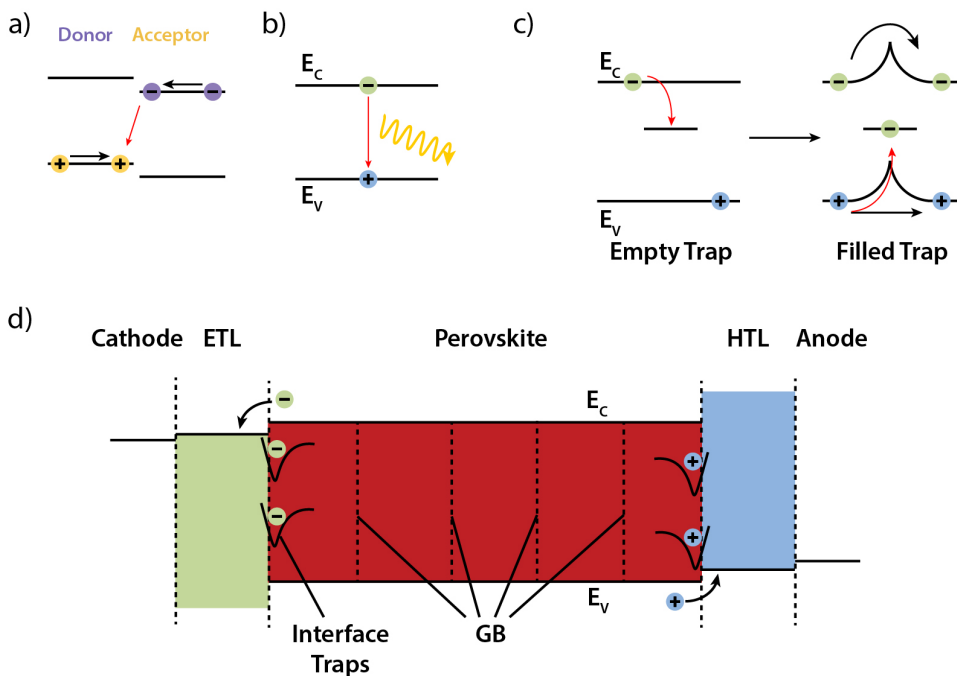
Figure 1.5: (a) Bimolecular recombination process in a donor-acceptor blend as in OSC with charges being confined to their own domains. (b) Radiative band-to-band recombination as in classical semiconductor with the emission of a photon. (c) Trap-assisted recombination at an electron trapping center and the creation of an energetic barrier upon filling of the trap state. (b) The localization of typical recombination centers in PSCs with traps states mainly localized at grain boundaries (GB) or at the interfaces with the TLs.

is no consensus in the literature as of their real nature.[141,142,153,154]

In PSCs the traps usually originate from either vacancies in the crystal lattice, break in the crystal such as grain boundaries or at the interface with the TLs, see figure 1.5.d.[111,113,114,155] First-principle calculation studies have also shown that defect tend to migrate out of the bulk and toward the grain boundaries (GB) and interfaces leaving low trap densities within the bulk.[111,113,114,155] Which was confirmed by photoluminescence (PL) measurements, where grains typically show bright emission and grain boundaries are comparatively dark, i.e. more trap-assisted nonradiative recombination.[156,157] Similar results were found at the interface between the perovskite and the TLs where the PL is significantly quenched at the interface.[96,97,158]

## 1.4. DRIFT-DIFFUSION EQUATIONS AS A DEVICE MODEL FOR ORGANIC AND PEROVSKITE SOLAR CELLS

The device model used throughout this thesis (in chapter 3-6) is based on 1D drift-diffusion equations. The so-called drift-diffusion simulations consist of three main sets

of equations. The Poisson equation:

$$\frac{\partial}{\partial x}\left(\epsilon(x)\frac{\partial V(x)}{\partial x}\right) = -q\left(p(x) - n(x) + C_i(x)\right), \tag{1.5}$$

with $x$ is the position in the device,* $V$ the electrostatic potential, $n$ and $p$ the electron and hole concentrations, and $\epsilon$ the permittivity. $C_i$ can represent any other type of charges in the systems such as: (i) doping with $N_A^-$ and $N_D^+$ being the ionized p-type and n-type doping respectively, (ii) ions with $X_c$ and $X_a$ the cation and anion densities and (iii) the charged traps $\Sigma_T^+$ and $\Sigma_T^-$ for hole and electron traps. Such as the Poisson equation may be written as:

$$\frac{\partial}{\partial x}\left(\epsilon\frac{\partial V}{\partial x}\right) = -q\left(p - n + N_D^+ - N_A^- + X_c - X_a + \Sigma_T^+ - \Sigma_T^-\right) \tag{1.6}$$

The current continuity equations:

$$\begin{aligned}\frac{\partial J_n}{\partial x} &= -q\left(G - R\right) \\ \frac{\partial J_p}{\partial x} &= q\left(G - R\right)\end{aligned} \tag{1.7}$$

with $J_{n,p}$ the electron and hole currents, $G$ and $R$ the generation and recombination rate respectively. The movement of these free charges is governed either by diffusion due to a gradient in carrier density or by drift following the electric field such as the electron and hole currents can be written as: [159]

$$\begin{aligned}J_n &= -qn\mu_n\frac{\partial V}{\partial x} + qD_n\frac{\partial n}{\partial x} \\ J_p &= -qp\mu_p\frac{\partial V}{\partial x} - qD_p\frac{\partial p}{\partial x}\end{aligned} \tag{1.8}$$

with $\mu_{n,p}$ the charge carrier mobilities and $D_{n,p}$ carrier diffusion coefficients. The carrier diffusion coefficients can be written following Einstein equation such as: [159]

$$D_{n,p} = \mu_{n,p}V_T \tag{1.9}$$

with $V_T = k_B T/q$ the thermal voltage ($V_T = 25.69$ mV at 25°C – 298.15 K).
For the simulation we chose to place the cathode at $x = 0$ and the anode at $x = L$ as a convention, $L$ being the total thickness of the device. If necessary, additional layers with different properties (mobility, doping, dielectric constant...) can be added to the simulation to reproduce, for example, a typical solar cell stack as shown in figure 1.5.d.
In order to numerically solve the system of equation presented above we need to specify the boundary conditions for the carrier densities:

$$\begin{aligned}n(0) &= N_c exp\left(-\frac{\phi_n}{V_T}\right) & n(L) &= N_c exp\left(-\frac{E_g - \phi_p}{V_T}\right) \\ p(0) &= N_v exp\left(-\frac{E_g - \phi_n}{V_T}\right) & p(L) &= N_v exp\left(-\frac{\phi_p}{V_T}\right)\end{aligned} \tag{1.10}$$

---

*Note that for notation convenience the $x$ dependence of the variables will be dropped in the remainder of this thesis. However, in a multilayer stack not only densities values are meant to vary with $x$ but also values such as mobilities and dielectric constant...

and the potential at the contacts:

$$q\left(V(L) - V(0) + V_{app}\right) = W_c - W_a \tag{1.11}$$

with $\phi_n$ and $\phi_p$ the electron and hole injection barrier at the cathode and anode, $V_{app}$ being the externally applied voltage and $W_a$ and $W_c$ the anode and cathode work functions respectively. The built-in potential is then given by $V_{bi} = (W_c - W_a)/q$. Note that the $E_g$ in equation 1.10 may not necessarily be the same if there are different layers in contact with the cathode and the anode.

The generation rate of charge $G$, in equation 1.7, is usually obtained by measuring the complex refractive index of all the layers and performing transfer matrix modeling.[160] As for the recombination rate $R$, it is typically expressed by adding the contribution from the band-to-band/bimolecular recombination and SRH recombination from equations 1.1 and 1.3. More details on the numerical methods used to solve this system of equations can be found in Ref. 106,159,161–163.

## REFERENCES

[1]  M. Nicholson, *The Power makers' challenge: And the need for fission energy*, Green Energy and Technology (Springer London, 2012).

[2]  I. Hore-Lacy, World Nuclear Association, and World Nuclear University, *Nuclear Energy in the 21st Century : World Nuclear University Press.* (Academic Press, 2006).

[3]  J. D. Sterman, L. Siegel, and J. N. Rooney-Varga, *Does replacing coal with wood lower CO2 emissions? Dynamic lifecycle analysis of wood bioenergy,* Environmental Research Letters **13**, 015007 (2018).

[4]  P. R. Shukla, J. Skea, E. Calvo Buendia, V. Masson-Delmotte, H.-O. Pörtner, D. C. Roberts, P. Zhai, R. Slade, S. Connors, R. van Diemen, M. Ferrat, E. Haughey, S. Luz, S. Neogi, M. Pathak, J. Petzold, J. Portugal Pereira, P. Vyas, E. Huntley, K. Kissick, M. Belkacemi, J. Malley, and (eds.), *Climate Change and Land: an IPCC special report on climate change, desertification, land degradation, sustainable land management, food security, and greenhouse gas fluxes in terrestrial ecosystems,* https://www.ipcc.ch/srccl/ (2019), accessed: 2020-01-15.

[5]  M. Collins, R. Knutti, J. Arblaster, J.-L. Dufresne, T. Fichefet, P. Friedlingstein, X. Gao, W. Gutowski, T. Johns, G. Krinner, M. Shongwe, C. Tebaldi, A. Weaver, and M. Wehner, *Long-term Climate Change: Projections, Commitments and Irreversibility. In: Climate Change 2013: The Physical Science Basis. Contribution of Working Group I to the Fifth Assessment Report of the Intergovernmental Panel on Climate Change,* https://www.ipcc.ch/site/assets/uploads/2018/02/WG1AR5_Chapter12_FINAL.pdf (2013), accessed: 2020-01-15.

[6]  *BP Statistical Review of World Energy 68$^{th}$ Edition,* https://www.bp.com/content/dam/bp/business-sites/en/global/corporate/pdfs/energy-economics/statistical-review/bp-stats-review-2019-full-report.pdf (2019), accessed: 2020-01-15.

**1**

[7] IEA report, *Renewables 2019,* `https://www.iea.org/reports/renewables-2019` (2019).

[8] Fraunhofer ISE report, `https://www.ise.fraunhofer.de/content/dam/ise/de/documents/publications/studies/Photovoltaics-Report.pdf` (2019).

[9] V. Sivaram, J. O. Dabiri, and D. M. Hart, *The Need for Continued Innovation in Solar, Wind, and Energy Storage,* Joule **2**, 1639 (2018).

[10] V. Sivaram and S. Kann, *Solar power needs a more ambitious cost target,* Nature Energy **1**, 16036 (2016).

[11] NREL, *Best research-cell efficiencies,* `https://www.nrel.gov/pv/assets/pdfs/best-research-cell-efficiencies.20191106.pdf` (2020), accessed: 2020-01-16.

[12] W. Shockley and H. J. Queisser, *Detailed balance limit of efficiency of p-n junction solar cells,* Journal of Applied Physics **32**, 510 (1961).

[13] K. Lee, N. Kim, K. Kim, H. D. Um, W. Jin, D. Choi, J. Park, K. J. Park, S. Lee, and K. Seo, *Neutral-Colored Transparent Crystalline Silicon Photovoltaics,* Joule **4**, 235 (2020).

[14] N. El-Atab, N. Qaiser, R. Bahabry, and M. M. Hussain, *Corrugation Enabled Asymmetrically Ultrastretchable (95%) Monocrystalline Silicon Solar Cells with High Efficiency (19%),* Advanced Energy Materials **9**, 1902883 (2019).

[15] R. Xia, C. J. Brabec, H.-L. Yip, and Y. Cao, *High-Throughput Optical Screening for Efficient Semitransparent Organic Solar Cells,* Joule (2019), 10.1016/J.JOULE.2019.06.016.

[16] Q. Xue, R. Xia, C. J. Brabec, and H. L. Yip, *Recent advances in semi-transparent polymer and perovskite solar cells for power generating window applications,* Energy and Environmental Science **11**, 1688 (2018).

[17] T. Yan, W. Song, J. Huang, R. Peng, L. Huang, and Z. Ge, *16.67% Rigid and 14.06% Flexible Organic Solar Cells Enabled by Ternary Heterojunction Strategy,* Advanced Materials **31** (2019), 10.1002/adma.201902210.

[18] D. Koo, S. Jung, J. Seo, G. Jeong, Y. Choi, J. Lee, S. M. Lee, Y. Cho, M. Jeong, J. Lee, J. Oh, C. Yang, and H. Park, *Flexible Organic Solar Cells Over 15% Efficiency with Polyimide-Integrated Graphene Electrodes,* Joule **4**, 1021 (2020).

[19] L. Yuan, Z. Wang, R. Duan, P. Huang, K. Zhang, Q. Chen, N. K. Allam, Y. Zhou, B. Song, and Y. Li, *Semi-transparent perovskite solar cells: Unveiling the trade-off between transparency and efficiency,* Journal of Materials Chemistry A **6**, 19696 (2018).

[20] C. Roldán-Carmona, O. Malinkiewicz, R. Betancur, G. Longo, C. Momblona, F. Jaramillo, L. Camacho, and H. J. Bolink, *High efficiency single-junction semi-transparent perovskite solar cells,* Energy and Environmental Science **7**, 2968 (2014).

[21] F. Fu, T. Feurer, T. Jäger, E. Avancini, B. Bissig, S. Yoon, S. Buecheler, and A. N. Tiwari, *Low-temperature-processed efficient semi-transparent planar perovskite solar cells for bifacial and tandem applications,* Nature Communications **6**, 1 (2015).

[22] X. Hu, X. Meng, L. Zhang, Y. Zhang, Z. Cai, Z. Huang, M. Su, Y. Wang, M. Li, F. Li, X. Yao, F. Wang, W. Ma, Y. Chen, and Y. Song, *A Mechanically Robust Conducting Polymer Network Electrode for Efficient Flexible Perovskite Solar Cells,* Joule **3**, 2205 (2019).

[23] D. Yang, R. Yang, S. Priya, and S. F. Liu, *Recent Advances in Flexible Perovskite Solar Cells: Fabrication and Applications,* Angewandte Chemie - International Edition **58**, 4466 (2019).

[24] P. Atkins and J. de Paula, *Physical Chemistry* (W. H. Freeman Company, New York, 2006).

[25] A. Köhler and H. Bässler, *Electronic Processes in Organic Semiconductors: An Introduction* (Wiley-VCH Verlag, Weinheim, Germany, 2015).

[26] O. V. Mikhnenko, P. W. Blom, and T. Q. Nguyen, *Exciton diffusion in organic semiconductors,* Energy and Environmental Science **8**, 1867 (2015).

[27] B. Schweitzer and H. Bässler, *Excitons in conjugated polymers,* Synthetic Metals **109**, 1 (2000).

[28] B. A. Gregg, *Excitonic solar cells,* Journal of Physical Chemistry B **107**, 4688 (2003).

[29] S. R. Forrest, *Excitons and the lifetime of organic semiconductor devices, Philosophical Transactions of the Royal Society A: Mathematical, Physical and Engineering Sciences,* **373** (2015), 10.1098/rsta.2014.0320.

[30] S. E. Shaheen, C. J. Brabec, N. S. Sariciftci, F. Padinger, T. Fromherz, and J. C. Hummelen, *2.5% efficient organic plastic solar cells,* Applied Physics Letters **78**, 841 (2001).

[31] M. A. Loi, S. Toffanin, M. Muccini, M. Forster, U. Scherf, and M. Scharber, *Charge Transfer Excitons in Bulk Heterojunctions of a Polyfluorene Copolymer and a Fullerene Derivative,* Advanced Functional Materials **17**, 2111 (2007).

[32] C. Deibel, T. Strobel, and V. Dyakonov, *Role of the Charge Transfer State in Organic Donor-Acceptor Solar Cells,* Advanced Materials **22**, 4097 (2010).

[33] K. Vandewal, J. Widmer, T. Heumueller, C. J. Brabec, M. D. McGehee, K. Leo, M. Riede, and A. Salleo, *Increased Open-Circuit Voltage of Organic Solar Cells by Reduced Donor-Acceptor Interface Area,* Advanced Materials **26**, 3839 (2014).

17

**1**

[34] K. Vandewal, S. Albrecht, E. T. Hoke, K. R. Graham, J. Widmer, J. D. Douglas, M. Schubert, W. R. Mateker, J. T. Bloking, G. F. Burkhard, A. Sellinger, J. M. Fréchet, A. Amassian, M. K. Riede, M. D. McGehee, D. Neher, and A. Salleo, *Efficient charge generation by relaxed charge-transfer states at organic interfaces,* Nature Materials **13**, 63 (2014).

[35] D. Qian, Z. Zheng, H. Yao, W. Tress, T. R. Hopper, S. Chen, S. Li, J. Liu, S. Chen, J. Zhang, X. K. Liu, B. Gao, L. Ouyang, Y. Jin, G. Pozina, I. A. Buyanova, W. M. Chen, O. Inganäs, V. Coropceanu, J. L. Bredas, H. Yan, J. Hou, F. Zhang, A. A. Bakulin, and F. Gao, *Design rules for minimizing voltage losses in high-efficiency organic solar cells,* Nature Materials **17**, 703 (2018).

[36] S. Li, L. Zhan, C. Sun, H. Zhu, G. Zhou, W. Yang, M. Shi, C.-Z. Li, J. Hou, Y. Li, and H. Chen, *Highly Efficient Fullerene-Free Organic Solar Cells Operate at Near Zero Highest Occupied Molecular Orbital Offsets,* Journal of the American Chemical Society **141**, 3073 (2019).

[37] L. Perdigón-Toro, H. Zhang, A. Markina, J. Yuan, S. M. Hosseini, C. M. Wolff, G. Zuo, M. Stolterfoht, Y. Zou, F. Gao, D. Andrienko, S. Shoaee, and D. Neher, *Barrierless Free Charge Generation in the High-Performance PM6:Y6 Bulk Heterojunction Non-Fullerene Solar Cell,* Advanced Materials **32**, 1906763 (2020).

[38] W. Chen, T. Xu, F. He, W. Wang, C. Wang, J. Strzalka, Y. Liu, J. Wen, D. J. Miller, J. Chen, K. Hong, L. Yu, and S. B. Darling, *Hierarchical nanomorphologies promote exciton dissociation in polymer/fullerene bulk heterojunction solar cells,* Nano Letters **11**, 3707 (2011).

[39] F. Paquin, G. Latini, M. Sakowicz, P. L. Karsenti, L. Wang, D. Beljonne, N. Stingelin, and C. Silva, *Charge separation in semicrystalline polymeric semiconductors by photoexcitation: Is the mechanism intrinsic or extrinsic?* Physical Review Letters **106**, 197401 (2011).

[40] T. M. Burke and M. D. McGehee, *How High Local Charge Carrier Mobility and an Energy Cascade in a Three-Phase Bulk Heterojunction Enable >90% Quantum Efficiency,* Advanced Materials **26**, 1923 (2014).

[41] S. Sweetnam, K. R. Graham, G. O. Ngongang Ndjawa, T. Heumüller, J. A. Bartelt, T. M. Burke, W. Li, W. You, A. Amassian, and M. D. McGehee, *Characterization of the polymer energy landscape in polymer:fullerene bulk heterojunctions with pure and mixed phases,* Journal of the American Chemical Society **136**, 14078 (2014).

[42] A. Miller and E. Abrahams, *Impurity conduction at low concentrations,* Physical Review **120**, 745 (1960).

[43] R. A. Marcus and N. Sutin, *Bba reviews on bioenergetics,* **811**, 265 (1985).

[44] H. Bässler, *Charge Transport in Disordered Organic Photoconductors a Monte Carlo Simulation Study,* physica status solidi (b) **175**, 15 (1993).

[45] C. W. Tang, *Two-layer organic photovoltaic cell,* Applied Physics Letters **48**, 183 (1986).

[46] G. Yu, J. Gao, J. C. Hummelen, F. Wudl, and A. J. Heeger, *Polymer photovoltaic cells: Enhanced efficiencies via a network of internal donor-acceptor heterojunctions,* Science **270**, 1789 (1995).

[47] Q. Liu, Y. Jiang, K. Jin, J. Qin, J. Xu, W. Li, J. Xiong, J. Liu, Z. Xiao, K. Sun, S. Yang, X. Zhang, and L. Ding, *18% Efficiency organic solar cells,* Science Bulletin (2020), 10.1016/j.scib.2020.01.001.

[48] Y. Firdaus, V. M. Le Corre, J. I. Khan, Z. Kan, F. Laquai, P. M. Beaujuge, and T. D. Anthopoulos, *Key Parameters Requirements for Non-Fullerene-Based Organic Solar Cells with Power Conversion Efficiency >20%,* Advanced Science **6**, 1802028 (2019).

[49] M. O. Reese, S. A. Gevorgyan, M. Jørgensen, E. Bundgaard, S. R. Kurtz, D. S. Ginley, D. C. Olson, M. T. Lloyd, P. Morvillo, E. A. Katz, A. Elschner, O. Haillant, T. R. Currier, V. Shrotriya, M. Hermenau, M. Riede, K. R. Kirov, G. Trimmel, T. Rath, O. Inganäs, F. Zhang, M. Andersson, K. Tvingstedt, M. Lira-Cantu, D. Laird, C. McGuiness, S. Gowrisanker, M. Pannone, M. Xiao, J. Hauch, R. Steim, D. M. Delongchamp, R. Rösch, H. Hoppe, N. Espinosa, A. Urbina, G. Yaman-Uzunoglu, J. B. Bonekamp, A. J. Van Breemen, C. Girotto, E. Voroshazi, and F. C. Krebs, *Consensus stability testing protocols for organic photovoltaic materials and devices,* Solar Energy Materials and Solar Cells **95**, 1253 (2011).

[50] A. Distler, T. Sauermann, H.-J. Egelhaaf, S. Rodman, D. Waller, K.-S. Cheon, M. Lee, and D. M. Guldi, *The Effect of PCBM Dimerization on the Performance of Bulk Heterojunction Solar Cells,* Advanced Energy Materials **4**, 1300693 (2014).

[51] W. R. Mateker and M. D. McGehee, *Progress in Understanding Degradation Mechanisms and Improving Stability in Organic Photovoltaics,* Advanced Materials **29**, 1603940 (2017).

[52] N. Y. Doumon, G. Wang, R. C. Chiechi, and L. J. A. Koster, *Relating polymer chemical structure to the stability of polymer:fullerene solar cells,* Journal of Materials Chemistry C **5**, 6611 (2017).

[53] N. Y. Doumon, M. V. Dryzhov, F. V. Houard, V. M. Le Corre, A. Rahimi Chatri, P. Christodoulis, and L. J. A. Koster, *Photostability of Fullerene and Non-Fullerene Polymer Solar Cells: The Role of the Acceptor,* ACS Applied Materials & Interfaces **11**, 8310 (2019).

[54] N. Y. Doumon, F. V. Houard, J. Dong, P. Christodoulis, M. V. Dryzhov, G. Portale, and L. J. A. Koster, *Improved photostability in ternary blend organic solar cells: The role of [70]PCBM,* Journal of Materials Chemistry C **7**, 5104 (2019).

[55] N. Y. Doumon, F. V. Houard, J. Dong, H. Yao, G. Portale, J. Hou, and L. J. A. Koster, *Energy level modulation of ITIC derivatives: Effects on the photodegradation of conventional and inverted organic solar cells,* Organic Electronics **69**, 255 (2019).

[56] N. Y. Doumon and L. J. A. Koster, *Effects of the Reduction and/or Fluorination of the TT-Units in BDT-TT Polymers on the Photostability of Polymer:Fullerene Solar Cells,* Solar RRL **3**, 1800301 (2019).

[57] N. Y. Doumon, G. Wang, X. Qiu, A. J. Minnaard, R. C. Chiechi, and L. J. A. Koster, *1,8-diiodooctane acts as a photo-acid in organic solar cells,* Scientific Reports **9**, 1 (2019).

[58] C. Zhang, T. Heumueller, S. Leon, W. Gruber, K. Burlafinger, X. Tang, J. D. Perea, I. Wabra, A. Hirsch, T. Unruh, N. Li, and C. J. Brabec, *A top-down strategy identifying molecular phase stabilizers to overcome microstructure instabilities in organic solar cells,* Energy and Environmental Science **12**, 1078 (2019).

[59] O. R. Yamilova, I. V. Martynov, A. S. Brandvold, I. V. Klimovich, A. H. Balzer, A. V. Akkuratov, I. E. Kusnetsov, N. Stingelin, and P. A. Troshin, *What is Killing Organic Photovoltaics: Light-Induced Crosslinking as a General Degradation Pathway of Organic Conjugated Molecules,* Advanced Energy Materials , 1903163 (2020).

[60] M. A. Green, E. D. Dunlop, J. Hohl-Ebinger, M. Yoshita, N. Kopidakis, and A. W. Ho-Baillie, *Solar cell efficiency tables (Version 28-55),* Progress in Photovoltaics: Research and Applications **28**, 3 (2020).

[61] L. Dou, J. You, J. Yang, C. C. Chen, Y. He, S. Murase, T. Moriarty, K. Emery, G. Li, and Y. Yang, *Tandem polymer solar cells featuring a spectrally matched low-bandgap polymer,* Nature Photonics **6**, 180 (2012).

[62] J. Zhao, Y. Li, G. Yang, K. Jiang, H. Lin, H. Ade, W. Ma, and H. Yan, *Efficient organic solar cells processed from hydrocarbon solvents,* Nature Energy **1**, 15027 (2016).

[63] Z. Xiao, X. Jia, and L. Ding, *Ternary organic solar cells offer 14% power conversion efficiency,* Science Bulletin **62**, 1562 (2017).

[64] W. Zhao, S. Li, H. Yao, S. Zhang, Y. Zhang, B. Yang, and J. Hou, *Molecular Optimization Enables over 13% Efficiency in Organic Solar Cells,* Journal of the American Chemical Society **139**, 7148 (2017).

[65] S. Zhang, Y. Qin, J. Zhu, and J. Hou, *Over 14% Efficiency in Polymer Solar Cells Enabled by a Chlorinated Polymer Donor,* Advanced Materials , 1800868 (2018).

[66] X. Che, Y. Li, Y. Qu, and S. R. Forrest, *High fabrication yield organic tandem photovoltaics combining vacuum- and solution-processed subcells with 15% efficiency,* Nature Energy **3**, 422 (2018).

[67] L. Meng, Y. Zhang, X. Wan, C. Li, X. Zhang, Y. Wang, X. Ke, Z. Xiao, L. Ding, R. Xia, H.-L. Yip, Y. Cao, and Y. Chen, *Organic and solution-processed tandem solar cells with 17.3% efficiency.* Science (New York, N.Y.) , eaat2612 (2018).

[68] J. Yuan, Y. Zhang, L. Zhou, G. Zhang, H. L. Yip, T. K. Lau, X. Lu, C. Zhu, H. Peng, P. A. Johnson, M. Leclerc, Y. Cao, J. Ulanski, Y. Li, and Y. Zou, *Single-Junction Organic Solar Cell with over 15% Efficiency Using Fused-Ring Acceptor with Electron-Deficient Core,* Joule **3**, 1140 (2019).

20

[69] Y. Cui, H. Yao, J. Zhang, T. Zhang, Y. Wang, L. Hong, K. Xian, B. Xu, S. Zhang, J. Peng, Z. Wei, F. Gao, and J. Hou, *Over 16% efficiency organic photovoltaic cells enabled by a chlorinated acceptor with increased open-circuit voltages,* Nature Communications **10**, 2515 (2019).

[70] Y. Lin, B. Adilbekova, Y. Firdaus, E. Yengel, H. Faber, M. Sajjad, X. Zheng, E. Yarali, A. Seitkhan, O. M. Bakr, A. El-Labban, U. Schwingenschlögl, V. Tung, I. McCulloch, F. Laquai, and T. D. Anthopoulos, *17% Efficient Organic Solar Cells Based on Liquid Exfoliated WS 2 as a Replacement for PEDOT:PSS,* Advanced Materials **31**, 1902965 (2019).

[71] *Asca by armor,* https://www.asca.com/, accessed: 12-02-2020.

[72] *Heliatek,* https://www.heliatek.com/, accessed: 12-02-2020.

[73] *Opvius,* http://www.opvius.com/, accessed: 12-02-2020.

[74] B. Fan, W. Zhong, L. Ying, D. Zhang, M. Li, Y. Lin, R. Xia, F. Liu, H. L. Yip, N. Li, Y. Ma, C. J. Brabec, F. Huang, and Y. Cao, *Surpassing the 10% efficiency milestone for 1-cm2 all-polymer solar cells,* Nature Communications **10**, 1 (2019).

[75] J. E. Carlé, M. Helgesen, O. Hagemann, M. Hö, I. M. Heckler, E. Bundgaard, S. A. Gevorgyan, R. R. Søndergaard, M. Jørgensen, R. García-Valverde, S. Chaouki-Almagro, J. A. Villarejo, and F. C. Krebs, *Overcoming the Scaling Lag for Polymer Solar Cells,* (2017), 10.1016/j.joule.2017.08.002.

[76] S. Dong, K. Zhang, B. Xie, J. Xiao, H.-L. Yip, H. Yan, F. Huang, and Y. Cao, *High-Performance Large-Area Organic Solar Cells Enabled by Sequential Bilayer Processing via Nonhalogenated Solvents,* Advanced Energy Materials **9**, 1802832 (2019).

[77] F. C. Krebs, T. Tromholt, and M. Jørgensen, *Upscaling of polymer solar cell fabrication using full roll-to-roll processing,* Nanoscale **2**, 873 (2010).

[78] *Roll-to-roll fabrication of polymer solar cells,* Materials Today **15**, 36 (2012).

[79] J. Yang, Y. Lin, W. Zheng, A. Liu, W. Cai, X. Yu, F. Zhang, Q. Liang, H. Wu, D. Qin, and L. Hou, *Roll-to-Roll Slot-Die-Printed Polymer Solar Cells by Self-Assembly,* ACS Applied Materials and Interfaces **10**, 22485 (2018).

[80] G. Wang, M. A. Adil, J. Zhang, and Z. Wei, *Large-Area Organic Solar Cells: Material Requirements, Modular Designs, and Printing Methods,* Advanced Materials **31**, 1805089 (2019).

[81] J. Lee, Y. Seo, S. Kwon, D. Kim, S. Jang, H. Jung, Y. Lee, H. Weerasinghe, T. Kim, J. Y. Kim, D. Vak, and S. Na, *Slot-Die and Roll-to-Roll Processed Single Junction Organic Photovoltaic Cells with the Highest Efficiency,* Advanced Energy Materials **9**, 1901805 (2019).

[82] D. Weber, $CH_3NH_3PbX_3$, *ein Pb(II)-System mit kubischer Perowskitstruktur,* Zeitschrift fur Naturforschung - Section B Journal of Chemical Sciences **33**, 1443 (1978).

21

[83] A. Kojima, K. Teshima, Y. Shirai, and T. Miyasaka, *Organometal Halide Perovskites as Visible-Light Sensitizers for Photovoltaic Cells,* Journal of the American Chemical Society **131**, 6050 (2009).

[84] M. M. Lee, J. Teuscher, T. Miyasaka, T. N. Murakami, and H. J. Snaith, *Efficient Hybrid Solar Cells Based on Meso-Superstructured Organometal Halide Perovskites,* Science **338**, 643 (2012).

[85] H.-S. Kim, C.-R. Lee, J.-H. Im, K.-B. Lee, T. Moehl, A. Marchioro, S.-J. Moon, R. Humphry-Baker, J.-H. Yum, J. E. Moser, M. Grätzel, and N.-G. Park, *Lead Iodide Perovskite Sensitized All-Solid-State Submicron Thin Film Mesoscopic Solar Cell with Efficiency Exceeding 9%,* Scientific Reports **2**, 591 (2012).

[86] E. T. Hoke, D. J. Slotcavage, E. R. Dohner, A. R. Bowring, H. I. Karunadasa, and M. D. McGehee, *Reversible photo-induced trap formation in mixed-halide hybrid perovskites for photovoltaics,* Chemical Science **6**, 613 (2015).

[87] F. Brivio, K. T. Butler, A. Walsh, and M. Van Schilfgaarde, *Relativistic quasiparticle self-consistent electronic structure of hybrid halide perovskite photovoltaic absorbers,* Physical Review B - Condensed Matter and Materials Physics **89**, 155204 (2014).

[88] C. Motta, F. El-Mellouhi, and S. Sanvito, *Charge carrier mobility in hybrid halide perovskites,* Scientific Reports **5**, 12746 (2015).

[89] T. Wang, B. Daiber, J. M. Frost, S. A. Mann, E. C. Garnett, A. Walsh, and B. Ehrler, *Indirect to direct bandgap transition in methylammonium lead halide perovskite,* Energy and Environmental Science **10**, 509 (2017).

[90] V. Sarritzu, N. Sestu, D. Marongiu, X. Chang, Q. Wang, S. Masi, S. Colella, A. Rizzo, A. Gocalinska, E. Pelucchi, M. L. Mercuri, F. Quochi, M. Saba, A. Mura, and G. Bongiovanni, *Direct or Indirect Bandgap in Hybrid Lead Halide Perovskites?* Advanced Optical Materials **6**, 1701254 (2018).

[91] L. M. Herz, *Charge-Carrier Mobilities in Metal Halide Perovskites: Fundamental Mechanisms and Limits,* ACS Energy Letters **2**, 1539 (2017).

[92] N. Onoda-Yamamuro, T. Matsuo, and H. Suga, *Dielectric study of $CH_3NH_3PbX_3$ (X = Cl, Br, I),* Journal of Physics and Chemistry of Solids **53**, 935 (1992).

[93] J. M. Frost, K. T. Butler, F. Brivio, C. H. Hendon, M. Van Schilfgaarde, and A. Walsh, *Atomistic origins of high-performance in hybrid halide perovskite solar cells,* Nano Letters **14**, 2584 (2014).

[94] L. M. Herz, *How Lattice Dynamics Moderate the Electronic Properties of Metal-Halide Perovskites,* Journal of Physical Chemistry Letters **9**, 6853 (2018).

[95] J. N. Wilson, J. M. Frost, S. K. Wallace, and A. Walsh, *Dielectric and ferroic properties of metal halide perovskites,* APL Materials **7**, 010901 (2019).

[96] M. Stolterfoht, C. M. Wolff, J. A. Márquez, S. Zhang, C. J. Hages, D. Rothhardt, S. Albrecht, P. L. Burn, P. Meredith, T. Unold, and D. Neher, *Visualization and suppression of interfacial recombination for high-efficiency large-area pin perovskite solar cells,* Nature Energy **3**, 847 (2018).

[97] M. Stolterfoht, P. Caprioglio, C. M. Wolff, J. A. Márquez, J. Nordmann, S. Zhang, D. Rothhardt, U. Hörmann, Y. Amir, A. Redinger, L. Kegelmann, F. Zu, S. Albrecht, N. Koch, T. Kirchartz, M. Saliba, T. Unold, and D. Neher, *The impact of energy alignment and interfacial recombination on the internal and external open-circuit voltage of perovskite solar cells,* Energy and Environmental Science **12**, 2778 (2019).

[98] V. M. Le Corre, M. Stolterfoht, L. Perdigón Toro, M. Feuerstein, C. Wolff, L. Gil-Escrig, H. J. Bolink, D. Neher, and L. J. A. Koster, *Charge Transport Layers Limiting the Efficiency of Perovskite Solar Cells: How To Optimize Conductivity, Doping, and Thickness,* ACS Applied Energy Materials **2**, 6280 (2019).

[99] H. J. Snaith, A. Abate, J. M. Ball, G. E. Eperon, T. Leijtens, N. K. Noel, S. D. Stranks, J. T. W. Wang, K. Wojciechowski, and W. Zhang, *Anomalous hysteresis in perovskite solar cells,* Journal of Physical Chemistry Letters **5**, 1511 (2014).

[100] E. L. Unger, E. T. Hoke, C. D. Bailie, W. H. Nguyen, A. R. Bowring, T. Heumüller, M. G. Christoforo, and M. D. McGehee, *Hysteresis and transient behavior in current–voltage measurements of hybrid-perovskite absorber solar cells,* Energy & Environmental Sciences **7**, 3690 (2014).

[101] W. Tress, N. Marinova, T. Moehl, S. M. Zakeeruddin, M. K. Nazeeruddin, and M. Grätzel, *Understanding the rate-dependent J–V hysteresis, slow time component, and aging in $CH_3NH_3PbI_3$ perovskite solar cells: the role of a compensated electric field,* Energy & Environmental Sciences **8**, 995 (2015).

[102] G. Richardson, S. E. O'Kane, R. G. Niemann, T. A. Peltola, J. M. Foster, P. J. Cameron, and A. B. Walker, *Can slow-moving ions explain hysteresis in the current–voltage curves of perovskite solar cells?* Energy & Environmental Sciences **9**, 1476 (2016).

[103] N. Tessler and Y. Vaynzof, *Preventing hysteresis in perovskite solar cells by undoped charge blocking layers,* ACS Applied Energy Materials **1**, 676 (2018).

[104] S. A. L. Weber, I. M. Hermes, S.-H. Turren-Cruz, C. Gort, V. W. Bergmann, L. Gilson, A. Hagfeldt, M. Graetzel, W. Tress, and R. Berger, *How the formation of interfacial charge causes hysteresis in perovskite solar cells,* Energy Environ. Sci. **11**, 2404 (2018).

[105] J. Mizusaki, K. Arai, and K. Fueki, *Ionic conduction of the perovskite-type halides,* Solid State Ionics **11**, 203 (1983).

[106] T. S. Sherkar, C. Momblona, L. Gil-Escrig, J. Ávila, M. Sessolo, H. J. Bolink, and L. J. A. Koster, *Recombination in perovskite solar cells: Significance of grain boundaries, interface traps and defect ions,* ACS Energy Letters **2**, 1214 (2017).

23

[107] C. Li, A. Guerrero, Y. Zhong, and S. Huettner, *Origins and mechanisms of hysteresis in organometal halide perovskites,* Journal of Physics: Condensed Matter **29**, 193001 (2017).

[108] M. H. Futscher, J. M. Lee, L. McGovern, L. A. Muscarella, T. Wang, M. I. Haider, A. Fakharuddin, L. Schmidt-Mende, and B. Ehrler, *Quantification of ion migration in $CH_3NH_3PbI_3$ perovskite solar cells by transient capacitance measurements,* Materials Horizons **6**, 1497 (2019).

[109] M. H. Futscher, M. K. Gangishetty, D. N. Congreve, and B. Ehrler, *Quantifying mobile ions and electronic defects in perovskite-based devices with temperature-dependent capacitance measurements: Frequency vs time domain,* Journal of Chemical Physics **152**, 044202 (2020).

[110] L. Bertoluzzi, C. C. Boyd, N. Rolston, J. Xu, R. Prasanna, B. C. O'Regan, and M. D. McGehee, *Mobile Ion Concentration Measurement and Open-Access Band Diagram Simulation Platform for Halide Perovskite Solar Cells,* Joule **4**, 109 (2020).

[111] J. M. Azpiroz, E. Mosconi, J. Bisquert, and F. De Angelis, *Defect migration in methylammonium lead iodide and its role in perovskite solar cell operation,* Energy & Environmental Science **8**, 2118 (2015).

[112] J. Haruyama, K. Sodeyama, L. Han, and Y. Tateyama, *First-principles study of ion diffusion in perovskite solar cell sensitizers,* Journal of the American Chemical Society **137**, 10048 (2015).

[113] P. Delugas, C. Caddeo, A. Filippetti, and A. Mattoni, *Thermally Activated Point Defect Diffusion in Methylammonium Lead Trihalide: Anisotropic and Ultrahigh Mobility of Iodine,* Journal of Physical Chemistry Letters **7**, 2356 (2016).

[114] C. Eames, J. M. Frost, P. R. Barnes, B. C. O'Regan, A. Walsh, and M. S. Islam, *Ionic transport in hybrid lead iodide perovskite solar cells,* Nature Communications **6**, 1 (2015).

[115] P. Calado, A. M. Telford, D. Bryant, X. Li, J. Nelson, B. C. O'Regan, and P. R. Barnes, *Evidence for ion migration in hybrid perovskite solar cells with minimal hysteresis,* Nature Communications **7**, 13831 (2016).

[116] M. T. Neukom, A. Schiller, S. Züfle, E. Knapp, J. Ávila, D. Pérez-del Rey, C. Dreessen, K. P. Zanoni, M. Sessolo, H. J. Bolink, and B. Ruhstaller, *Consistent Device Simulation Model Describing Perovskite Solar Cells in Steady-State, Transient, and Frequency Domain,* ACS Applied Materials & Interfaces **11**, 23320 (2019).

[117] M. T. Neukom, S. Züfle, E. Knapp, M. Makha, R. Hany, and B. Ruhstaller, *Why perovskite solar cells with high efficiency show small IV-curve hysteresis,* Solar Energy Materials and Solar Cells **169**, 159 (2017).

[118] M. V. Khenkin, E. A. Katz, A. Abate, G. Bardizza, J. J. Berry, C. Brabec, F. Brunetti, V. Bulović, Q. Burlingame, A. Di Carlo, R. Cheacharoen, Y. B. Cheng, A. Colsmann,

S. Cros, K. Domanski, M. Dusza, C. J. Fell, S. R. Forrest, Y. Galagan, D. Di Girolamo, M. Grätzel, A. Hagfeldt, E. von Hauff, H. Hoppe, J. Kettle, H. Köbler, M. S. Leite, S. F. Liu, Y. L. Loo, J. M. Luther, C. Q. Ma, M. Madsen, M. Manceau, M. Matheron, M. McGehee, R. Meitzner, M. K. Nazeeruddin, A. F. Nogueira, Ç. Odabaşı, A. Osherov, N. G. Park, M. O. Reese, F. De Rossi, M. Saliba, U. S. Schubert, H. J. Snaith, S. D. Stranks, W. Tress, P. A. Troshin, V. Turkovic, S. Veenstra, I. Visoly-Fisher, A. Walsh, T. Watson, H. Xie, R. Yıldırım, S. M. Zakeeruddin, K. Zhu, and M. Lira-Cantu, *Consensus statement for stability assessment and reporting for perovskite photovoltaics based on ISOS procedures,* Nature Energy **5**, 35 (2020).

[119] K. A. Bush, A. F. Palmstrom, Z. J. Yu, M. Boccard, R. Cheacharoen, J. P. Mailoa, D. P. McMeekin, R. L. Hoye, C. D. Bailie, T. Leijtens, I. M. Peters, M. C. Minichetti, N. Rolston, R. Prasanna, S. Sofia, D. Harwood, W. Ma, F. Moghadam, H. J. Snaith, T. Buonassisi, Z. C. Holman, S. F. Bent, and M. D. McGehee, *23.6%-efficient monolithic perovskite/silicon tandem solar cells with improved stability,* Nature Energy **2**, 1 (2017).

[120] F. Sahli, J. Werner, B. A. Kamino, M. Bräuninger, R. Monnard, B. Paviet-Salomon, L. Barraud, L. Ding, J. J. Diaz Leon, D. Sacchetto, G. Cattaneo, M. Despeisse, M. Boccard, S. Nicolay, Q. Jeangros, B. Niesen, and C. Ballif, *Fully textured monolithic perovskite/silicon tandem solar cells with 25.2% power conversion efficiency,* Nature Materials **17**, 820 (2018).

[121] *Oxford pv,* https://www.oxfordpv.com/, accessed: 26-02-2020.

[122] *Solliance,* https://www.solliance.eu/ (), accessed: 26-02-2020.

[123] *Wonder solar,* http://www.wondersolar.cn//, accessed: 26-02-2020.

[124] *Saule technologies,* https://sauletech.com/ (), accessed: 26-02-2020.

[125] Q. Jiang, Y. Zhao, X. Zhang, X. Yang, Y. Chen, Z. Chu, Q. Ye, X. Li, Z. Yin, and J. You, *Surface passivation of perovskite film for efficient solar cells,* Nature Photonics **13**, 460 (2019).

[126] P. Wang, R. Li, B. Chen, F. Hou, J. Zhang, Y. Zhao, and X. Zhang, *Gradient Energy Alignment Engineering for Planar Perovskite Solar Cells with Efficiency Over 23%,* Advanced Materials **32**, 1905766 (2020).

[127] J. Diekmann, P. Caprioglio, D. Rothhardt, M. Arvind, T. Unold, T. Kirchartz, D. Neher, and M. Stolterfoht, *Pathways towards 30% efficient perovskite solar cells,* (2019).

[128] L. M. Pazos-Outón, T. P. Xiao, and E. Yablonovitch, *Fundamental Efficiency Limit of Lead Iodide Perovskite Solar Cells,* Journal of Physical Chemistry Letters **9**, 1703 (2018).

[129] R. Lin, K. Xiao, Z. Qin, Q. Han, C. Zhang, M. Wei, M. I. Saidaminov, Y. Gao, J. Xu, M. Xiao, A. Li, J. Zhu, E. H. Sargent, and H. Tan, *Monolithic all-perovskite tandem*

*solar cells with 24.8% efficiency exploiting comproportionation to suppress Sn(ii) oxidation in precursor ink,* Nature Energy **4**, 864 (2019).

[130] A. Al-Ashouri, A. Magomedov, M. Roß, M. Jošt, M. Talaikis, G. Chistiakova, T. Bertram, J. A. Márquez, E. Köhnen, E. Kasparavičius, S. Levcenco, L. Gil-Escrig, C. J. Hages, R. Schlatmann, B. Rech, T. Malinauskas, T. Unold, C. A. Kaufmann, L. Korte, G. Niaura, V. Getautis, and S. Albrecht, *Conformal monolayer contacts with lossless interfaces for perovskite single junction and monolithic tandem solar cells,* Energy and Environmental Science **12**, 3356 (2019).

[131] *Solliance,* https://www.solliance.eu/2019/solliance-and-ecn-part-of-tno-exceed-the-performance-limit-of-standard-solar-cells/ (), accessed: 26-02-2020.

[132] W. Tress, K. Domanski, B. Carlsen, A. Agarwalla, E. A. Alharbi, M. Graetzel, and A. Hagfeldt, *Performance of perovskite solar cells under simulated temperature-illumination real-world operating conditions,* Nature Energy **4**, 568 (2019).

[133] J. Li, H. L. Cao, W. B. Jiao, Q. Wang, M. Wei, I. Cantone, J. Lü, and A. Abate, *Biological impact of lead from halide perovskites reveals the risk of introducing a safe threshold,* Nature Communications **11**, 1 (2020).

[134] *Rohs guide,* https://www.rohsguide.com/, accessed: 26-02-2020.

[135] *Saule technologies,* https://sauletech.com/rohs-compliance-tests-at-our-company/ (), accessed: 26-02-2020.

[136] X. Li, F. Zhang, H. He, J. J. Berry, K. Zhu, and T. Xu, *On-device lead sequestration for perovskite solar cells,* Nature **578**, 1 (2020).

[137] R. A. Street, M. Schoendorf, A. Roy, and J. H. Lee, *Interface state recombination in organic solar cells,* Physical Review B - Condensed Matter and Materials Physics **81**, 205307 (2010).

[138] W. Tress, *Perovskite solar cells on the way to their radiative efficiency limit–insights into a success story of high open-circuit voltage and low recombination,* Advanced Energy Materials , 1602358 (2017).

[139] Z. Wang, Q. Lin, B. Wenger, M. G. Christoforo, Y.-H. Lin, M. T. Klug, M. B. Johnston, L. M. Herz, and H. J. Snaith, *High irradiance performance of metal halide perovskites for concentrator photovoltaics,* Nature Energy **3**, 855 (2018).

[140] A. R. G. Lakhwani and R. H. Friend, *Bimolecular Recombination in Organic Photovoltaics,* Annual Review of Physical Chemistry **65**, 557 (2014).

[141] J. Benduhn, K. Tvingstedt, F. Piersimoni, S. Ullbrich, Y. Fan, M. Tropiano, K. A. McGarry, O. Zeika, M. K. Riede, C. J. Douglas, S. Barlow, S. R. Marder, D. Neher, D. Spoltore, and K. Vandewal, *Intrinsic non-radiative voltage losses in fullerene-based organic solar cells,* Nature Energy **2**, 1 (2017).

[142]  S. M. Menke, N. A. Ran, G. C. Bazan,  and R. H. Friend, *Understanding Energy Loss in Organic Solar Cells: Toward a New Efficiency Regime,* Joule **2**, 25 (2018).

[143]  P. Langevin, *Recombinaison et mobilités des ions dans les gaz,* Annales de Chimie et de Physique , 433 (1903).

[144]  D. Bartesaghi, I. d. C. Perez, J. Kniepert, S. Roland, M. Turbiez, D. Neher,  and L. J. A. Koster, *Competition between recombination and extraction of free charges determines the fill factor of organic solar cells,* Nature Communications **6:7083** (2015), 10.1038/ncomms8083.

[145]  A. Rahimi Chatri, S. Torabi, V. M. Le Corre,  and L. J. A. Koster, *Impact of Electrodes on Recombination in Bulk Heterojunction Organic Solar Cells,* ACS Applied Materials & Interfaces **10**, 12013 (2018).

[146]  C. L. Davies, M. R. Filip, J. B. Patel, T. W. Crothers, C. Verdi, A. D. Wright, R. L. Milot, F. Giustino, M. B. Johnston,  and L. M. Herz, *Bimolecular recombination in methylammonium lead triiodide perovskite is an inverse absorption process,* Nature Communications **9**, 293 (2018).

[147]  F. Ambrosio, J. Wiktor, F. De Angelis,  and A. Pasquarello, *Origin of low electron–hole recombination rate in metal halide perovskites,* Energy & Environmental Science **11**, 101 (2018).

[148]  C. Wolf, H. Cho, Y.-H. Kim,  and T.-W. Lee, *Polaronic Charge Carrier-Lattice Interactions in Lead Halide Perovskites,* ChemSusChem **10**, 3705 (2017).

[149]  X. Zhang, J.-X. Shen, W. Wang,  and C. G. Van de Walle, *First-Principles Analysis of Radiative Recombination in Lead-Halide Perovskites,* ACS Energy Letters **3**, 2329 (2018).

[150]  M. Stolterfoht, V. M. Le Corre, M. Feuerstein, P. Caprioglio, L. J. A. Koster,  and D. Neher, *Voltage-Dependent Photoluminescence and How It Correlates with the Fill Factor and Open-Circuit Voltage in Perovskite Solar Cells,* ACS Energy Letters , 2887 (2019).

[151]  W. Shockley and W. T. Read, *Statistics of the recombinations of holes and electrons,* Physical Review **87**, 835 (1952).

[152]  R. N. Hall, *Electron-hole recombination in germanium,* Physical Review **87**, 387 (1952).

[153]  G. Zuo, M. Linares, T. Upreti,  and M. Kemerink, *General rule for the energy of water-induced traps in organic semiconductors,* Nature Materials **18**, 588 (2019).

[154]  W. Brütting, *Physics of Organic Semiconductors*, edited by W. Brütting (Wiley, 2005) pp. 1–536.

[155]  A. Buin, R. Comin, J. Xu, A. H. Ip,  and E. H. Sargent, *Halide-Dependent Electronic Structure of Organolead Perovskite Materials,* Chemistry of Materials **27**, 4405 (2015).

**1**

[156] W. Zhang, V. M. Burlakov, D. J. Graham, T. Leijtens, A. Osherov, V. Bulović, H. J. Snaith, D. S. Ginger, and S. D. Stranks, *Photo-induced halide redistribution in organic-inorganic perovskite films,* Nature Communications **7**, 11683 (2016).

[157] C. G. Bischak, E. M. Sanehira, J. T. Precht, J. M. Luther, and N. S. Ginsberg, *Heterogeneous charge carrier dynamics in organic–inorganic hybrid materials: Nanoscale lateral and depth-dependent variation of recombination rates in methylammonium lead halide perovskite thin films,* Nano Letters **15**, 4799 (2015).

[158] Z. Liu, L. Krückemeier, B. Krogmeier, B. Klingebiel, J. A. Márquez, S. Levcenko, S. Öz, S. Mathur, U. Rau, T. Unold, and T. Kirchartz, *Open-Circuit Voltages Exceeding 1.26 v in Planar Methylammonium Lead Iodide Perovskite Solar Cells,* ACS Energy Letters **4**, 110 (2019).

[159] S. Selberherr, *Analysis and Simulation of Semiconductor Devices* (Springer-Verlag, Wien, Germany, 1984) p. 285.

[160] G. F. Burkhard, E. T. Hoke, and M. D. McGehee, *Accounting for Interference, Scattering, and Electrode Absorption to Make Accurate Internal Quantum Efficiency Measurements in Organic and Other Thin Solar Cells,* Advanced Materials **22**, 3293 (2010).

[161] L. J. A. Koster, E. C. P. Smits, V. D. Mihailetchi, and P. W. M. Blom, *Device model for the operation of polymer/fullerene bulk heterojunction solar cells,* Physical Review B **72**, 085205 (2005).

[162] T. S. Sherkar, C. Momblona, L. Gil-Escrig, H. J. Bolink, and L. J. A. Koster, *Improving the performance of perovskite solar cells: Insights from a validated device model,* Advanced Energy Materials , 1602432 (2017).

[163] T. S. Sherkar, V. M. Le Corre, M. Koopmans, F. Wobben, and L. J. A. Koster, *SIMsalabim GitHub repository,* (2020).

# 2

# LONG-RANGE EXCITON DIFFUSION IN MOLECULAR NON-FULLERENE ACCEPTORS

*The short exciton diffusion length associated with most classical organic semiconductors used in organic photovoltaics (5-20 nm) imposes severe limits on the maximum size of the donor and acceptor domains within the photoactive layer of the cell. Identifying materials that are able to transport excitons over longer distances can help advancing our understanding and lead to solar cells with higher efficiency. Here, we determine the exciton diffusion length in a wide range of non-fullerene acceptor (NFA) molecules using thickness-dependent external quantum efficiency measurements of bilayer solar cells. All NFAs exhibit surprisingly long exciton diffusion lengths in the range of 20 to 47 nm, which is consistent with ultrafast spectroscopy measurements. With the aid of quantum-chemical calculations, we are able to rationalize the exciton dynamics and draw basic design rules on the influence of the chemical structure and the importance of the end-group substituent on the crystal packing of NFAs.*

## **2.1.** Introduction

**2**

After a few years of stagnation in terms of efficiency, organic solar cells (OSCs) are back in the spotlight thanks to the advent of new non-fullerene acceptor (NFA) molecules.[1–3] NFAs have brought OSCs' power conversion efficiency (PCE) to new heights with records set between 16-18.2% for single-junction[4–10] and 15-17.3% for tandem cells.[11–14] While recent progress has been impressive, the aforementioned levels of performance are still below the predicted efficiency limit of 20% and 25% for single-junction and tandem cells, respectively.[15,16] Recent efforts towards increasing the PCE of OSCs have been motivated by research on new materials with improved charge carrier mobility and broader spectral absorption.[2,3,9] However, it is important that exciton formation, dissociation and subsequent charge collection efficiencies are all simultaneously maximized, yielding to the highest possible photocurrent.

In OSCs, successful absorption of a photon generates an exciton, a coulombically bound electron-hole pair.[17] Thermal dissociation of excitons within a low dielectric medium such as an organic semiconductor is highly improbable. To efficiently generate free charges, two semiconductors with suitable energetics, an electron donor and electron acceptor are intermixed, forming a so-called bulk-heterojunction (BHJ) cell. One of the prerequisites for efficient exciton harvesting is the fast exciton diffusion to the donor-acceptor interface, where it splits into free charges. The diffusion constant and the exciton lifetime set the optimal size of the donor and acceptor domains within the BHJ. Up until now, most of the work on exciton diffusion length ($L_D$) in OSCs has been focused on electron-donor (p-type) materials[18] with very few reports on molecular NFAs.[19,20] Recent work has shown that fused-ring acceptors such as indacenodithiophene end-capped with 1,1-dicyanomethylene-3-indanone (IDIC) exhibit long exciton diffusion length and diffusion constant of at least 0.02 cm$^2$ s$^{-1}$.[19] This is consistent with the large domain sizes of 20-50 nm often reported for high-efficiency NFA-based BHJ cells.[8,21–24] It is not yet fully understood why the exciton diffusion length in NFAs, such as IDIC, is significantly higher than in amorphous and other polycrystalline organic semiconductors (typically 5 to 20 nm).[18]

In this chapter, we present a study on the exciton diffusion length ($L_D$) in a wide range of NFAs[1–3,25–29] (chemical names of all materials can be found in the molecules, polymers and materials list) using thickness-dependent external quantum efficiency (EQE) measurements of bilayer solar cells and cross-checking the obtained values using transient absorption (TA) spectroscopy. We focused on best-in-class acceptor-donor-acceptor (A-D-A) NFAs comprising ITIC with different end-groups ranging from methyl (IT-M) to chlorine (IT-2Cl) and fluorine (IT-4F), including the current PCE world record holder Y6. The measured $L_D$ is found to vary amongst all NFAs studied, with IT-4F exhibiting the longest diffusion length of 45 nm. This value is >4 times higher than the ≈10 nm reported for the prototypical fullerene-based acceptor PC$_{71}$BM. To elucidate the origin of the long $L_D$, our collaborators combined crystallographic data with quantum-chemical calculations for each molecule. The simulations predict distinctly large excitonic couplings due to aligned transition dipole moments in the crystal, relatively small reorganization energies due to the stiff conjugated core, and quadrupolar symmetry of the excitation —i.e. small energetic disorder—the combination of which

leads to the large exciton diffusion lengths observed. Key relationships between $L_D$ and the chemical structure of the NFA are identified, leading to important design guidelines for future generation NFAs.

Chapter key findings:

- CuSCN acts as a good quenching interface to measure $L_D$ for NFAs.

- Bilayer EQE vs thickness and singlet-singlet annihilation give similar $L_D$ values.

- The exciton diffusion length in non-fullerene acceptors is strongly related to the stiffness of the conjugated core.

- New synthetic guidelines for longer exciton diffusion length.

## 2.2. NON-FULLERENE ACCEPTORS SERIES AND MATERIALS PROPERTIES
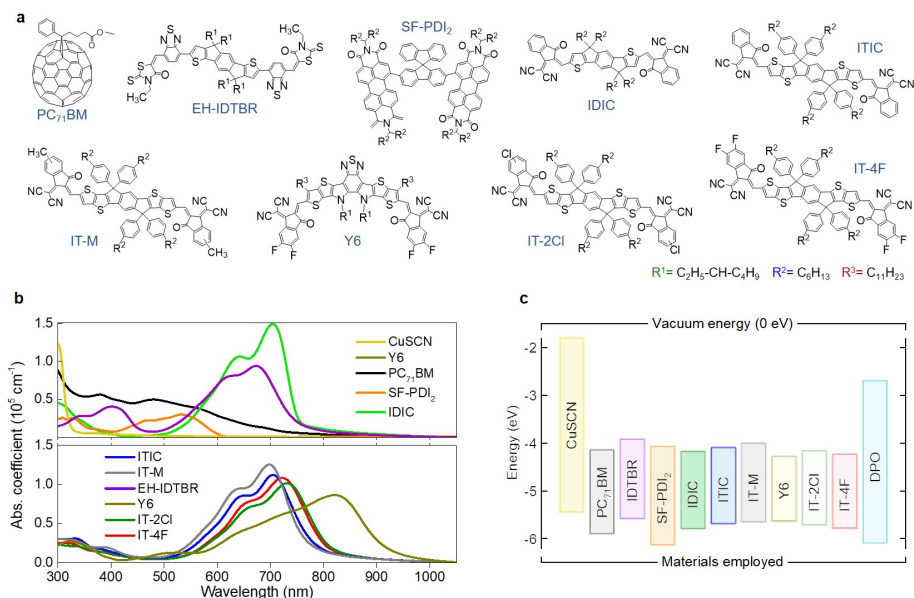


Figure 2.1: Materials, absorption, and energy levels of organic acceptors. (a) Chemical structure of the acceptors investigated in this study. Full names are provided in the materials list. (b) Absorption spectra and (c) HOMO/LUMO and optical gap (Eg) of the materials studied.

Figure 2.1.a illustrates the chemical structures of the acceptor materials studied,

while fig. 2.1.b shows their absorption spectra together with that of the hole-transport layer copper thiocyanate (CuSCN). The latter is a known wide bandgap (>3.4 eV) inorganic p-type semiconductor absorbing only in the ultraviolet (UV) region. [30,31] With the exception of SF-PDI$_2$, all NFAs absorb across the visible (Vis) all the way to the near-infrared, while exhibiting higher absorption coefficients than PC$_{71}$BM. Figure 2.1.c depicts the HOMO, LUMO and bandgap of the acceptors and the carrier-transport layers. [32]

## 2.3. EXCITON DIFFUSION LENGTH MEASUREMENTS USING PHOTOCURRENT TECHNIQUE.

Figure 2.2.a illustrates the structure of a planar CuSCN/acceptor heterojunction solar cell used to study the $L_D$. The use of CuSCN allows for efficient extraction of the photogenerated holes while simultaneously blocking electrons, effectively acting as exciton quencher for the organic absorber. Note that, efficient exciton quenchers for n-type organic semiconductor are scarce and CuSCN/n-type semiconductor platform for exciton diffusion studies has not been reported before. In the role of electron extracting layer, we employed the wide bandgap Phen-NaDPO (DPO) ((2-(1,10-phenanthrolin-3-yl)naphth-6-yl)diphenylphosphine oxide). [33] Adjusting the thickness of the organic semiconductor and measuring the OPV performance allows the study of $L_D$ within the organic layer, without the morphology-related complexities encountered in organic BHJs. [34] To estimate $L_D$ within the acceptor layer, we used a similar method to that described by Siegmund et al. [34] The EQE of the bilayer cells is measured as a function of acceptor thickness, and then the measured photocurrent is modelled using the exciton diffusion equation:

$$\frac{\partial n}{\partial t} = D\frac{\partial^2 n}{\partial^2 x} + G(x,t) - k_{PL}n - k_{FRET}n - \alpha n^2 \tag{2.1}$$

where, $n$ is the singlet exciton density at position $x$ in the absorber film, $D$ is the diffusion coefficient, $G(x,t)$ is the time-dependent exciton generation profile, $k_{PL}$ is the radiative decay rate in absence of quencher sites, $\alpha$ is an exciton-exciton annihilation rate constant, and $k_{FRET}$ denotes the rate of Förster resonance energy transfer (FRET) in the presence of a neighboring material.

To accurately measure $L_D$ of the NFAs with the bilayer cell, it is important to ensure that: (i) the exciton dissociation happens only at a well-defined quencher-acceptor interface; [35] (ii) the generation of exciton originates only from the acceptor; (iii) the photocurrent is not limited by the transport properties of the NFA layer. Figure 2.2.a shows the schematic of the device and a representative cross-sectional transmission electron microscopy (TEM) image of a CuSCN/NFA bilayer cell. Well-defined interfaces are visible across the device ensuring that requirement (i) is satisfied. Figure 2.2.b shows representative J-V curves for the bilayer CuSCN/NFA cells. Devices with IT-4F show a maximum power conversion efficiency (PCE) of 2.65% and $J_{SC}$ >5 mA cm$^{-2}$. The EQE spectra of the devices (figure 2.2.c) reveal that charge generation occurs across the entire acceptors' absorption spectra range while CuSCN does not contribute to the generation of
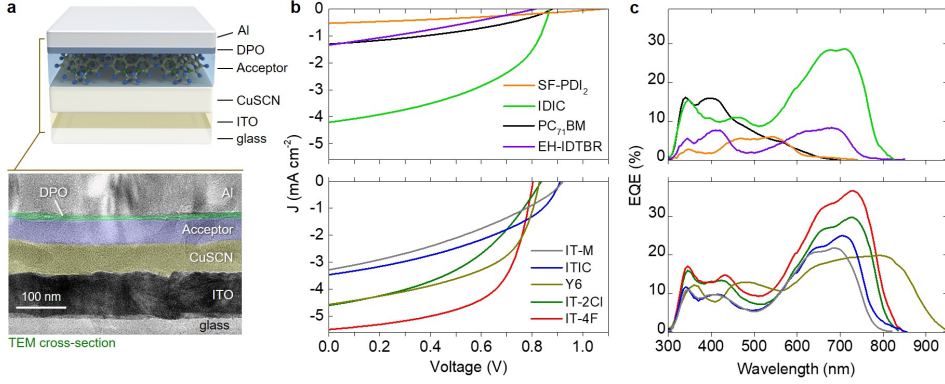
Figure 2.2: Device performance and EQE spectra of the bilayer CuSCN/acceptor devices. (a) Schematic of the device architecture and the cross-sectional transmission electron microscopy (TEM) image of a CuSCN/acceptor bilayer solar cell. (b) Current density-voltage (J-V) characteristics of OPV cells measured under simulated solar illumination. (c) Corresponding EQE spectra of the bilayer OPVs shown in b.

excitons (figure 2.1.b), hence satisfying requirement (ii). The requirement (iii) is also fulfilled as the performance of the bilayer solar cells is not limited by the charge transport of the acceptor materials as evident from the sufficiently high and ambipolar mobility values extracted using thin-film transistors (TFTs) and time-resolved microwave conductivity (TRMC) measurements see Ref. 32.

CuSCN is particularly suitable as an exciton quencher for this type of measurement since Förster resonant energy transfer (FRET) from CuSCN to the acceptor layer is negligible due to the very low fluorescence of CuSCN and the small overlap of its absorption with the acceptors' emission. [32] Exciton-exciton annihilation ($\alpha$) is also negligible at the considered intensities. As a result, the dominant exciton harvesting mechanism within the acceptor layer is exciton diffusion. Hence, equation 2.1 can be simplified under steady-state conditions with $k_{PL} = \frac{D}{L_D^2}$ such as:

$$\left( \frac{\partial^2}{\partial x^2} - \frac{1}{L_D^2} \right) n(x) = \frac{G(x)}{D} \tag{2.2}$$

which can be solved for any generation assuming that the excitons are fully quenched at the interface $n(interface) = 0$. The EQE can then be calculated considering that the photocurrent is only due to the exciton dissociation at the CuSCN/NFA interface:

$$EQE = \frac{J_{photo}}{J_{inc}} = \frac{q\eta_c D}{J_{inc}} \left. \frac{\partial n(x)}{\partial x} \right|_{interface} \tag{2.3}$$

where $J_{\text{photo}}$ and $J_{\text{inc}}$ are the generated photocurrent density and the incident light current density, $\eta_c$ the combination of the exciton splitting and extraction at the electrode efficiencies. [34] There are four main factors that influence the magnitudes of $J_{\text{photo}}$ and

33

EQE, namely the absorption coefficient, $\eta_c$, D and $L_D$ (appendix figure A.1.a & b). The contribution of the absorption is included in the generation profile $G(x, \lambda)$, evaluated using transfer-matrix modeling. [36] However, $\eta_c$ and D have no influence on the shape of the EQE vs thickness curve, only on its absolute value. As a result, we can only obtain the $D \times \eta_c$ product and, as such, we will not discuss those values at this point. Instead, we focus on fitting equations 2.2-2.3 to normalized EQE vs thickness data, as it is mostly influenced by $L_D$ hence allows reliable estimation of its magnitude. [34] The fits assumed that geminate and nongeminate recombination losses are independent of thickness which is valid in our case as confirmed by light-intensity and thickness dependent of the J-V characteristics of IT-4F devices (appendix figure A.1.c & d). We also coupled the results from solving Equation (2) with drift-diffusion simulation [37] (appendix figure A.1.e & f) to demonstrate that the photocurrent measurement is not limited by the mobility of the NFAs or the recombination. However, there could be cases (extremely thick layers or very low mobility, for example) where recombination losses do depend on thickness which can lead to incorrect values of the exciton diffusion length.

To estimate $L_D$, we measured the EQE spectra of the bilayer devices with different NFA layer thicknesses, whilst maintaining the thickness of the CuSCN layer to ≈60 nm. As shown in figure 2.3.a, the measured EQE (at $\lambda$ = 650 nm, see appendix figures A.2-A.10 for EQE at different $\lambda$) reaches a maximum value for acceptor thickness between 60 to 100 nm, which indicates long $L_D$ values. Analysis of the data yields an exciton diffusion length in IT-M and ITIC of $L_D$ = 25-30 nm. Incorporating electron-deficient elements like F or Cl into the end-capping groups, such as in the case of IT-2Cl and IT-4F acceptors, results in an increase of $L_D$ to 40-45 nm. For the rest of acceptors, $L_D$ are summarized in table 2.1. For the Y6 acceptor, with recently reported PCE values reaching in the range 15-18.2% when blended with best-in-class donor polymers, [3,5–7,9,10] we calculate an $L_D$ value of 35 nm. Additionally, we obtained $L_D \approx 10$ nm for $PC_{71}BM$, which is close to that of $C_{70}$ (7.4 nm) but significantly smaller than that of $C_{60}$ (18.5 nm) obtained using a photocurrent method. [35]

The fits reproduce well the experimental data (appendix figures A.2-A.10) and the values of $L_D$ are estimated based on the sensitivity of the fit over a range of thickness between 10-150 nm for at least four different excitation wavelengths. The accuracy of these fits depends on the experimental uncertainties of the EQE, the layer thicknesses, and the values of the complex refractive index. The variation in refractive index may explain the deviation from the fit for thin NFA layers. [34] We find that decent fits can be obtained, for most of the NFAs, when varying $L_D$ within a margin of ≈5-10 nm, see appendix figures A.2-A.10.

The photocurrent-based measurements of $L_D$ was independently validated using the singlet-singlet annihilation (SSA) method. [19] The details on the latter technique will not be discussed in this thesis. In a few words, it consists on using ultrafast transient absorption (TA) spectroscopy to measure exciton lifetimes as a function of excitation density. The measurement is carried out on neat films and does not require exciton quenching interfaces. When exciton annihilation occurs in the film, the exciton decay is accelerated with increasing excitation fluence. The exciton decay can be globally fit to a rate equation accounting for exciton annihilation and first order recombination of the excitons from which $L_D$ and D can be calculated. [19,32,38]
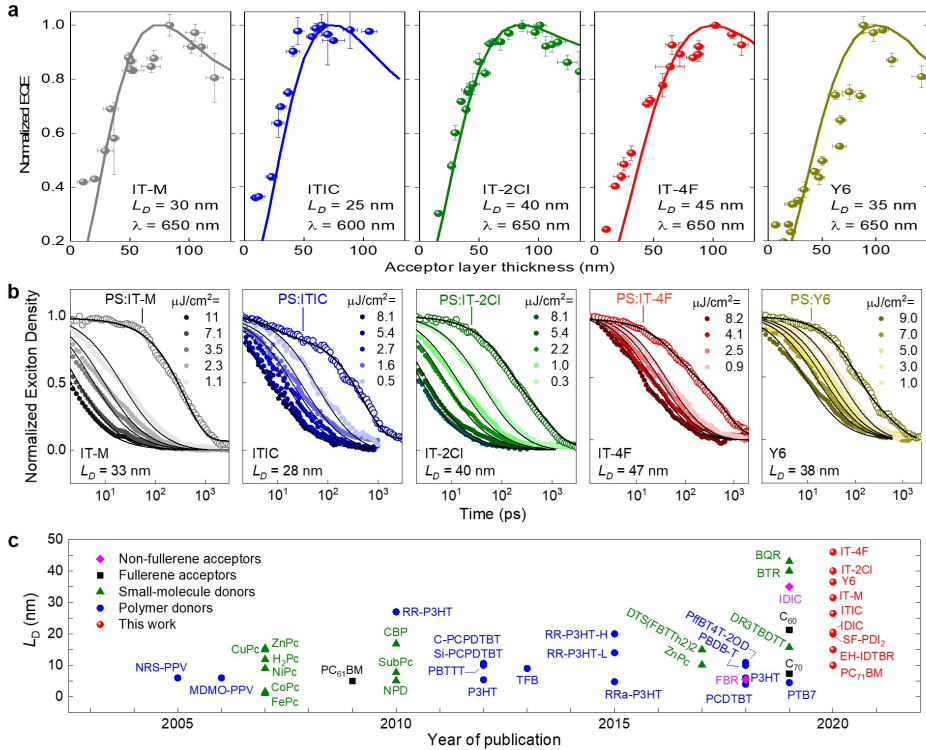
Figure 2.3: Exciton diffusion length estimated from the measurements of EQE spectra of CuSCN/NFA bilayer devices of different thicknesses (a) and SSA measurements (b). The EQE spectra of CuSCN/NFA bilayer devices measured using an excitation wavelength of $\lambda$ = 650 nm (600 nm for ITIC) and the singlet-singlet exciton annihilation decay in NFAs neat films with an excitation wavelength of 700 nm (750 nm for IT-4F). Fluence dependent singlet exciton decays of the neat films fitted to the exciton annihilation model, see Refs. 19,32 for more details. The exciton decays of the NFAs diluted in a polystyrene (PS) matrix are also superimposed in this figure. The experimental data (circles) are fitted (solid lines) for all NFA thicknesses. (c) Comparison of diffusion lengths reported from 2005 onwards for various types of donor and acceptor materials relevant to organic photovoltaics. Publication details can be found in Ref. 32.

A remarkable agreement between the $L_D$ values obtained from SSA analyses (figure 2.3.b) with those derived from the photocurrent measurements (Table 2.1), is evident. Notably, the $L_D$ value of 47 nm measured for IT-4F using SSA analyses is very close to $L_D$ = 45 nm inferred from the photocurrent method (figure 2.3). The SSA analyses also yield $D$ = 0.064 cm$^2$ s$^{-1}$ which is two times higher than IT-M and ITIC. The similarity in the exciton diffusion values measured between thin films and bilayer solar cells suggests that the values in table 2.1 represent the intrinsic $L_D$. In figure 2.3.c we compare the exciton diffusion values reported in the literature with those extracted here. Evidently, the NFAs studied here exhibit the highest $L_D$ amongst the OSCs materials. Longer $L_D$ have only been reported in conjugated polymer nanofiber (>200 nm),[39] small molecule J-aggregates (96 nm),[40] or organic single-crystals (> 1 $\mu$m).[41,42]

Table 2.1: Summary of diffusion length ($L_D$) values for all NFA materials studied.

| Acceptor | $L_{D,EQE}$ (nm) | $L_{D,TA}$ (nm) | $D$ (cm$^2$ s$^{-1}$) |
|---|---|---|---|
| PC$_{71}$BM | 10 | - | - |
| EH-IDTBR | 15 | - | - |
| SF-PDI$_2$ | 20 | - | - |
| IDIC | 24 | 17 | 0.011 |
| ITIC | 25 | 28 | 0.027 |
| IT-M | 30 | 33 | 0.03 |
| Y6 | 35 | 38 | 0.055 |
| IT-2Cl | 40 | 40 | 0.043 |
| IT-4F | 45 | 47 | 0.064 |

* $L_D$ obtained using photocurrent and transient absorption (TA) techniques. Diffusion constant ($D$) inferred from the TA measurements and was calculated by assuming the annihilation radius of singlet excitons to be 1 nm.

## 2.4. SYNTHETIC GUIDELINES TO INCREASE EXCITON DIFFUSION LENGTH FROM QUANTUM-CHEMICAL CALCULATIONS

Understanding the exciton dynamic is one of the key challenges in the pursuit of high-efficiency OSCs. While there have been numerous reports on small molecule and polymer donors as well as on fullerene derivatives (figure 2.3.c), there are few reports on NFAs and even no reports that correlate the main chemical structure and the end-group substituents with the exciton diffusion length and diffusion coefficient. Therefore, the link between the molecular structure and packing of the NFAs on the diffusion constant and the exciton diffusion length is investigated and some general synthetic design rules for future NFAs are drawn.

Our collaborators used quantum-chemical calculations to estimate the reorganization energy and the exciton transfer rate of NFAs depending on their structure and packing. The details on the quantum-chemical calculations are beyond the scope of this thesis and will not be discussed here, but can be found in Ref. 32. Here, the transfer rate ($v$) can be expressed depending on the molecular reorganization energy ($\lambda$) such as $v = \frac{V^2}{\hbar} \sqrt{\frac{\pi}{\lambda k_b T}} exp\left(\frac{-\lambda}{4 k_B T}\right)$ following the classical Marcus rate ($V$ is the electronic coupling element), despite all imperfections, this formula can be used for qualitative analysis of exciton transport. [43]

Substituting the obtained reorganization energies into the Marcus rate and assuming a constant electronic coupling element, we obtain a reasonable correlation between the reorganization energies and $L_D$ (figure 2.4.a). There are, however, a few outliers, in particular, the ITIC family has similar reorganization energies but different $L_D$. To explain this the excitonic coupling $V$ was calculated. Figure 2.4.c shows the calculated exciton transfer rates plotted versus the measured $L_D$ where a clear correlation can be seen.
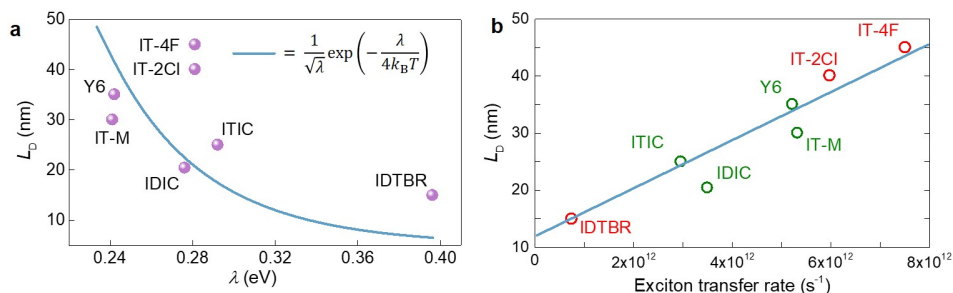
Figure 2.4: Quantum-chemical calculations of reorganization energy and the exciton transfer rate of NFAs. (a) The correlation of the measured diffusion length and the reorganization energy, with a fixed intramolecular excitonic coupling. The line corresponds to the Marcus rate. (b) Correlation between the measured exciton diffusion length and calculated exciton transfer rate. The line is the guide to the eye.

Therefore, the significant boost to the rate can be attributed to the stiffening of the conjugated core, from EH-IDTBR to ITIC to Y6, which reduces the activation barrier for the exciton transfer. For a given reorganization energy, the rate is then further enhanced by the crystalline packing, such as the one achieved in the crystal of IT-4F.

Another interesting observation is that a large coupling between the donor and acceptor blocks of the acceptor-donor-acceptor conjugated core leads to a quadrupolar-type excitation, with both acceptor blocks having an excess electron upon excitation. [44–46] The immediate implication is that the excited state does not have a dipole, but a quadrupole moment. Hence, the interaction of the excited molecule with the fluctuating fields created by the neighboring molecules in a film is of a quadrupole-quadrupole, not a dipole-quadrupole type. This reduces both energetic disorder (larger diffusing length) and external reorganization energy (larger exciton transfer rates), all thanks to the conjugated A-D-A molecular architecture. The quantum-chemical calculations combined with the measurements of $L_D$ on all the NFAs allows us to establish some general design rules that can help guide the synthesis of new NFAs with even longer exciton diffusion length:

1. Increased stiffness of the conjugated core of NFAs allows for low reorganization energies which allow for better exciton transfer.

2. Control of the end group substituent to improve the molecular packing allows for dramatic improvement of $L_D$. Adding halogenated end-groups appears to be the most promising approach.

3. Large coupling of the donor and acceptor blocks in A-D-A NFAs is necessary to ensure quadrupole-quadrupole interaction between excited and the neighboring molecules which reduces the energetic disorder and ultimately also benefits the exciton transfer.

## 2.5. CONCLUSIONS

The limited exciton diffusion length remains a bottleneck for high-efficiency organic photovoltaics as it limits the domain size in the donor-acceptor blend. Thus, understanding the structure-property relationship(s) may lead to design rules that can aid the synthesis of improved materials, ultimately leading to OPVs with improved performance. By measuring the exciton diffusion length in a wide range of best-in-class non-fullerene acceptor molecules in combination with quantum-chemical simulations, we were able to identify key properties on a molecular level that explain the long diffusion length (up to 47 nm) measured. This long-range exciton transport appears to underpin the tremendous success of this new generation of NFAs in carrier photogeneration and extraction leading to the record efficiencies reported recently.[6,9,10] Overall, our findings can be rationalized to three design rules that can aid the synthesis of new materials with long exciton diffusion lengths: (i) increase the stiffness of the conjugated core; (ii) engineer the end-group substituents for favorable crystal packing; (iii) increase the coupling between donor and acceptor blocks.

## REFERENCES

[1] Y. Lin, J. Wang, Z.-G. Zhang, H. Bai, Y. Li, D. Zhu, and X. Zhan, *An electron acceptor challenging fullerenes for efficient polymer solar cells,* Advanced Materials **27**, 1170 (2015).

[2] W. Zhao, S. Li, H. Yao, S. Zhang, Y. Zhang, B. Yang, and J. Hou, *Molecular optimization enables over 13% efficiency in organic solar cells,* Journal of the American Chemical Society **139**, 7148 (2017).

[3] J. Yuan, Y. Zhang, L. Zhou, G. Zhang, H.-L. Yip, T.-K. Lau, X. Lu, C. Zhu, H. Peng, P. A. Johnson, M. Leclerc, Y. Cao, J. Ulanski, Y. Li, and Y. Zou, *Single-junction organic solar cell with over 15% efficiency using fused-ring acceptor with electron-deficient core,* Joule **3**, 1140 (2019).

[4] Y. Cui, H. Yao, J. Zhang, T. Zhang, Y. Wang, L. Hong, K. Xian, B. Xu, S. Zhang, J. Peng, Z. Wei, F. Gao, and J. Hou, *Over 16% efficiency organic photovoltaic cells enabled by a chlorinated acceptor with increased open-circuit voltages,* Nature Communications **10**, 1 (2019).

[5] X. Xu, K. Feng, Z. Bi, W. Ma, G. Zhang, and Q. Peng, *Single-Junction Polymer Solar Cells with 16.35% Efficiency Enabled by a Platinum(II) Complexation Strategy,* Advanced Materials **31**, 1901872 (2019).

[6] Y. Lin, B. Adilbekova, Y. Firdaus, E. Yengel, H. Faber, M. Sajjad, X. Zheng, E. Yarali, A. Seitkhan, O. M. Bakr, A. El-Labban, U. Schwingenschlögl, V. Tung, I. McCulloch, F. Laquai, and T. D. Anthopoulos, *17% Efficient Organic Solar Cells Based on Liquid Exfoliated WS$_2$ as a Replacement for PEDOT:PSS,* Advanced Materials **31**, 1902965 (2019).

[7] T. Yan, W. Song, J. Huang, R. Peng, L. Huang, and Z. Ge, *16.67% Rigid and 14.06% Flexible Organic Solar Cells Enabled by Ternary Heterojunction Strategy,* Advanced Materials **31**, 1902210 (2019).

[8] M. A. Pan, T. K. Lau, Y. Tang, Y. C. Wu, T. Liu, K. Li, M. C. Chen, X. Lu, W. Ma, and C. Zhan, *16.7%-efficiency ternary blended organic photovoltaic cells with PCBM as the acceptor additive to increase the open-circuit voltage and phase purity,* Journal of Materials Chemistry A **7**, 20713 (2019).

[9] Q. Liu, Y. Jiang, K. Jin, J. Qin, J. Xu, W. Li, J. Xiong, J. Liu, Z. Xiao, K. Sun, S. Yang, X. Zhang, and L. Ding, *18% Efficiency organic solar cells,* Science Bulletin **65**, 272 (2020).

[10] Y. Lin, Y. Firdaus, M. I. Nugraha, F. Liu, S. Karuthedath, A. Emwas, W. Zhang, A. Seitkhan, M. Neophytou, H. Faber, E. Yengel, I. McCulloch, L. Tsetseris, F. Laquai, and T. D. Anthopoulos, *17.1% Efficient Single-Junction Organic Solar Cells Enabled by n-Type Doping of the Bulk-Heterojunction,* Advanced Science , 1903419 (2020).

[11] X. Che, Y. Li, Y. Qu, and S. R. Forrest, *High fabrication yield organic tandem photovoltaics combining vacuum- and solution-processed subcells with 15% efficiency,* Nature Energy **3**, 422 (2018).

[12] G. Liu, J. Jia, K. Zhang, X. Jia, Q. Yin, W. Zhong, L. Li, F. Huang, and Y. Cao, *15% Efficiency Tandem Organic Solar Cell Based on a Novel Highly Efficient Wide-Bandgap Nonfullerene Acceptor with Low Energy Loss,* Advanced Energy Materials **9**, 1803657 (2019).

[13] Y. Firdaus, Q. He, Y. Lin, F. A. A. Nugroho, V. M. Le Corre, E. Yengel, A. H. Balawi, A. Seitkhan, F. Laquai, C. Langhammer, F. Liu, M. Heeney, and T. D. Anthopoulos, *Novel wide-bandgap non-fullerene acceptors for efficient tandem organic solar cells,* Journal of Materials Chemistry A **8**, 1164 (2020).

[14] L. Meng, Y. Zhang, X. Wan, C. Li, X. Zhang, Y. Wang, X. Ke, Z. Xiao, L. Ding, R. Xia, H. L. Yip, Y. Cao, and Y. Chen, *Organic and solution-processed tandem solar cells with 17.3% efficiency,* Science **361**, 1094 (2018).

[15] Y. Firdaus, V. M. Le Corre, J. I. Khan, Z. Kan, F. Laquai, P. M. Beaujuge, and T. D. Anthopoulos, *Key Parameters Requirements for Non-Fullerene-Based Organic Solar Cells with Power Conversion Efficiency >20%,* Advanced Science **6**, 1802028 (2019).

[16] M. Azzouzi, J. Yan, T. Kirchartz, K. Liu, J. Wang, H. Wu, and J. Nelson, *Nonradiative Energy Losses in Bulk-Heterojunction Organic Photovoltaics,* Physical Review X **8**, 031055 (2018).

[17] B. Schweitzer and H. Bässler, *Excitons in conjugated polymers,* Synthetic Metals **109**, 1 (2000).

[18] O. V. Mikhnenko, P. W. Blom, and T. Q. Nguyen, *Exciton diffusion in organic semiconductors,* Energy and Environmental Science **8**, 1867 (2015).

[19] S. Chandrabose, K. Chen, A. J. Barker, J. J. Sutton, S. K. Prasad, J. Zhu, J. Zhou, K. C. Gordon, Z. Xie, X. Zhan, and J. M. Hodgkiss, *High Exciton Diffusion Coefficients in Fused Ring Electron Acceptor Films,* Journal of the American Chemical Society **141**, 6922 (2019).

[20] H. Cha, S. Wheeler, S. Holliday, S. D. Dimitrov, A. Wadsworth, H. H. Lee, D. Baran, I. McCulloch, and J. R. Durrant, *Influence of Blend Morphology and Energetics on Charge Separation and Recombination Dynamics in Organic Solar Cells Incorporating a Nonfullerene Acceptor,* Advanced Functional Materials **28**, 1704389 (2018).

[21] N. Bauer, Q. Zhang, J. J. Rech, S. Dai, Z. Peng, H. Ade, J. Wang, X. Zhan, and W. You, *The impact of fluorination on both donor polymer and non-fullerene acceptor: The more fluorine, the merrier,* Nano Research **12**, 2400 (2019).

[22] Y. Lin, F. Zhao, S. K. K. Prasad, J.-D. Chen, W. Cai, Q. Zhang, K. Chen, Y. Wu, W. Ma, F. Gao, J.-X. Tang, C. Wang, W. You, J. M. Hodgkiss, and X. Zhan, *Balanced Partnership between Donor and Acceptor Components in Nonfullerene Organic Solar Cells with >12% Efficiency,* Advanced Materials **30**, 1706363 (2018).

[23] Q. Fan, W. Su, Y. Wang, B. Guo, Y. Jiang, X. Guo, F. Liu, T. P. Russell, M. Zhang, and Y. Li, *Synergistic effect of fluorination on both donor and acceptor materials for high performance non-fullerene polymer solar cells with 13.5% efficiency,* Science China Chemistry **61**, 531 (2018).

[24] L. Zhang, H. Zhao, B. Lin, J. Yuan, X. Xu, J. Wu, K. Zhou, X. Guo, M. Zhang, and W. Ma, *A blade-coated highly efficient thick active layer for non-fullerene organic solar cells,* Journal of Materials Chemistry A **7**, 22265 (2019).

[25] S. Holliday, R. S. Ashraf, A. Wadsworth, D. Baran, S. A. Yousaf, C. B. Nielsen, C. H. Tan, S. D. Dimitrov, Z. Shang, N. Gasparini, M. Alamoudi, F. Laquai, C. J. Brabec, A. Salleo, J. R. Durrant, and I. McCulloch, *High-efficiency and air-stable P3HT-based polymer solar cells with a new non-fullerene acceptor,* Nature Communications **7**, 1 (2016).

[26] Q. Yan, Y. Zhou, Y. Q. Zheng, J. Pei, and D. Zhao, *Towards rational design of organic electron acceptors for photovoltaics: A study based on perylenediimide derivatives,* Chemical Science **4**, 4389 (2013).

[27] Y. Lin, Q. He, F. Zhao, L. Huo, J. Mai, X. Lu, C. J. Su, T. Li, J. Wang, J. Zhu, Y. Sun, C. Wang, and X. Zhan, *A Facile Planar Fused-Ring Electron Acceptor for As-Cast Polymer Solar Cells with 8.71% Efficiency,* Journal of the American Chemical Society **138**, 2973 (2016).

[28] S. Li, L. Ye, W. Zhao, S. Zhang, S. Mukherjee, H. Ade, and J. Hou, *Energy-Level Modulation of Small-Molecule Electron Acceptors to Achieve over 12% Efficiency in Polymer Solar Cells,* Advanced Materials **28**, 9423 (2016).

[29] H. Zhang, H. Yao, J. Hou, J. Zhu, J. Zhang, W. Li, R. Yu, B. Gao, S. Zhang, and J. Hou, *Over 14% Efficiency in Organic Solar Cells Enabled by Chlorinated Nonfullerene Small-Molecule Acceptors,* Advanced Materials **30**, 1800613 (2018).

[30] Y. Firdaus, A. Seitkhan, F. Eisner, W.-Y. Sit, Z. Kan, N. Wehbe, A. H. Balawi, E. Yengel, S. Karuthedath, F. Laquai, and T. D. Anthopoulos, *Charge Photogeneration and Recombination in Mesostructured CuSCN-Nanowire/PC$_{70}$BM Solar Cells,* Solar RRL **2**, 1800095 (2018).

[31] W.-Y. Sit, F. D. Eisner, Y.-H. Lin, Y. Firdaus, A. Seitkhan, A. H. Balawi, F. Laquai, C. H. Burgess, M. A. McLachlan, G. Volonakis, F. Giustino, and T. D. Anthopoulos, *High-Efficiency Fullerene Solar Cells Enabled by a Spontaneously Formed Mesostructured CuSCN-Nanowire Heterointerface,* Advanced Science **5**, 1700980 (2018).

[32] Y. Firdaus, V. M. Le Corre, S. Karuthedath, W. Liu, A. Markina, W. Huang, S. Chattopadhyay, M. M. Nahid, M. I. Nugraha, Y. Lin, A. Seitkhan, A. Basu, W. Zhang, I. McCulloch, H. Ade, J. Labram, F. Laquai, D. Adrienko, L. J. A. Koster, and T. D. Anthopoulos, *Long-range exciton diffusion in molecular non-fullerene acceptors,* Submitted (2020).

[33] W.-Y. Tan, R. Wang, M. Li, G. Liu, P. Chen, X.-C. Li, S.-M. Lu, H. L. Zhu, Q.-M. Peng, X.-H. Zhu, W. Chen, W. C. H. Choy, F. Li, J. Peng, and Y. Cao, *Lending Triarylphosphine Oxide to Phenanthroline: a Facile Approach to High-Performance Organic Small-Molecule Cathode Interfacial Material for Organic Photovoltaics utilizing Air-Stable Cathodes,* Advanced Functional Materials **24**, 6540 (2014).

[34] B. Siegmund, M. T. Sajjad, J. Widmer, D. Ray, C. Koerner, M. Riede, K. Leo, I. D. W. Samuel, and K. Vandewal, *Exciton Diffusion Length and Charge Extraction Yield in Organic Bilayer Solar Cells,* Advanced Materials **29**, 1604424 (2017).

[35] T. Zhang, D. B. Dement, V. E. Ferry, and R. J. Holmes, *Intrinsic measurements of exciton transport in photovoltaic cells,* Nature Communications **10**, 1 (2019).

[36] G. F. Burkhard, E. T. Hoke, and M. D. McGehee, *Accounting for Interference, Scattering, and Electrode Absorption to Make Accurate Internal Quantum Efficiency Measurements in Organic and Other Thin Solar Cells,* Advanced Materials **22**, 3293 (2010).

[37] L. J. A. Koster, O. Stenzel, S. D. Oosterhout, M. M. Wienk, V. Schmidt, and R. A. J. Janssen, *Morphology and Efficiency: The Case of Polymer/ZnO Solar Cells,* Advanced Energy Materials **3**, 615 (2013).

[38] S. Cook, H. Liyuan, A. Furube, and R. Katoh, *Singlet annihilation in films of regioregular poly(3-hexylthiophene): Estimates for singlet diffusion lengths and the correlation between singlet annihilation rates and spectral relaxation,* Journal of Physical Chemistry C **114**, 10962 (2010).

[39] X. H. Jin, M. B. Price, J. R. Finnegan, C. E. Boott, J. M. Richter, A. Rao, S. Matthew Menke, R. H. Friend, G. R. Whittell, and I. Manners, *Long-range exciton transport in conjugated polymer nanofibers prepared by seeded growth,* Science **360**, 897 (2018).

[40] H. Marciniak, X. Q. Li, F. Würthner, and S. Lochbrunner, *One-dimensional exciton diffusion in perylene bisimide aggregates,* Journal of Physical Chemistry A **115**, 648 (2011).

2

[41] B. A. Gregg, J. Sprague, and M. W. Peterson, *Long-range singlet energy transfer in perylene bis(phenethylimide) films,* Journal of Physical Chemistry B **101**, 5362 (1997).

[42] H. Najafov, B. Lee, Q. Zhou, L. C. Feldman, and V. Podzorov, *Observation of long-range exciton diffusion in highly ordered organic semiconductors,* Nature Materials **9**, 938 (2010).

[43] V. Stehr, R. F. Fink, B. Engels, J. Pflaum, and C. Deibel, *Singlet exciton diffusion in organic crystals based on marcus transfer rates,* Journal of Chemical Theory and Computation **10**, 1242 (2014).

[44] A. H. Balawi, S. Stappert, J. Gorenflot, C. Li, K. Müllen, D. Andrienko, and F. Laquai, *Direct and Energy-Transfer-Mediated Charge-Transfer State Formation and Recombination in Triangulene-Spacer-Perylenediimide Multichromophores: Lessons for Photovoltaic Applications,* Journal of Physical Chemistry C **123**, 16602 (2019).

[45] A. I. Ivanov, B. Dereka, and E. Vauthey, *A simple model of solvent-induced symmetry-breaking charge transfer in excited quadrupolar molecules,* Journal of Chemical Physics **146**, 164306 (2017).

[46] B. Dereka, A. Rosspeintner, Z. Li, R. Liska, and E. Vauthey, *Direct Visualization of Excited-State Symmetry Breaking Using Ultrafast Time-Resolved Infrared Spectroscopy,* Journal of the American Chemical Society **138**, 4643 (2016).

# 3

## CHARGE CARRIER EXTRACTION IN ORGANIC SOLAR CELLS GOVERNED BY STEADY-STATE MOBILITIES

*Charge transport in OPV devices is often characterized by steady-state mobilities. However, the suitability of steady-state mobilities to describe charge transport has recently been called into question, and it has been argued that dispersion plays a significant role. In this chapter, the importance of the dispersion of charge carrier motion on the performance of organic photovoltaic devices is investigated. An experiment to measure the charge extraction time under realistic operating conditions is set up. This experiment is applied to different blends and shows that extraction time is directly related to the geometrical average of the steady-state mobilities. This demonstrates that under realistic operating conditions the steady-state mobilities govern the charge extraction of OPV and gives a valuable insight in device performance.*

## **3.1.** Introduction

In the early 1990s, Sariciftci et al. described the first polymer:fullerene bulk heterojunction (BHJ) solar cell. [1] Since then organic photovoltaic (OPV) devices have attracted a lot of attention in the scientific community. The ability of organic semiconductors to be used in large-scale production and their high efficiency upon low light intensity make them promising materials for harvesting solar energy. State-of-the-art OPV devices now reach efficiencies up to 16-18.2% for single-junction [2–8] and 15-17.3% for tandem cells. However, despite being studied for decades, the underlying physics of OPVs is not yet fully understood and is still subject to debate.

In highly disordered materials, such as organic semiconductors, charge motion is based on thermally activated hopping. [9,10] This charge transport mechanism is characterized by lower electron and hole mobility values compared to inorganic semiconductors where band-like transport takes place. The transport in OPV is often described by the steady-state mobilities that can be obtained by a steady-state measurement, such as the space-charge limited current (SCLC) technique. [11–13]

However, time-of-flight (TOF) experiments and Monte Carlo (MC) simulations have shown that if the degree of both energetic and positional disorder is high enough, the fluctuations of the intersite distances create fast diffusion routes. [14,15] These routes increase the mobility of carriers located in high energetic states leading to their extraction before they have the time to thermalize, thus creating dispersion in current extraction on a short time scale. [14,15] Although the relative importance of the dispersive effect on OPV devices performance is conflicting in the literature, [16–18] reports have suggested that it is necessary to consider the influence of the dispersion effect in current extraction and that steady-state mobilities are not relevant to describe the transport in OPV devices. [17,18] In their study, they set up a MC simulation and an optoelectrical measurement based on a laser light pulse from which they measured the charge carrier mobility on a time scale of 100 fs after the exciton generation. [17,18] In the first nanoseconds, they observed a charge carrier mobility orders of magnitude higher than the one measured by steady-state measurements. This high mobility is due to the carriers being excited on the upper part of the density of states (DoS) that are extracted before losing their energy through thermalization. [17,18] The authors conclude that the steady-state mobilities are not pertinent to make relevant statements on OPV performance and that the thermalization loss plays a key role in the extraction.

On the other hand, van der Kaap and Koster used MC simulations to show that in organic diodes the thermalization has a limited impact on the performance. [16] In addition, other reports have also demonstrated that SCLC analysis can be successfully applied to organic solar cells and gives valuable insight into materials transport properties. [13,19–22] In fact, many studies have shown that the power conversion efficiency (PCE) [13] and fill factor (FF) [19–22] depend on the steady-state mobilities. Furthermore, it has also been shown that drift-diffusion simulations, which assume a near-equilibrium state and use steady-state mobilities as an input, successfully describe the characteristics of organic transistors, light-emitting diodes, and solar cells. [19,20,23–25] Transient signals of OPV devices have also been well reproduced by drift-diffusion simulation. For example, Albrecht et al. have been able to fit the time-delayed collection field (TDCF) signal using

drift-diffusion simulations. Even though they also see that during the first 50 ns after the charge generation a small effect of mobility relaxation has to be taken into account in order to reproduce the transient signal, it still shows that those simulations are suitable to describe the transient behavior of organic solar cells.[26] These studies raise the question of what is the influence of the current dispersion in OPV devices and whether steady-state mobilities can be used or not to characterize the transport and extraction in organic semiconductor devices.

In this chapter, we demonstrate that there is no need to consider the effect of dispersion and that steady-state mobilities are a suitable way to study the transport and extraction in OPV devices under realistic operating conditions: real OPV device configuration, the use of a multiple wavelength illumination light, and an intensity close to 1 sun. To that purpose, we carried out a combination of transient experiments and simulations to study the extraction in OPV devices. Several donor:acceptor blends have been tested, scanning a wide range of polymers backbones, values and ratio of the mobilities and efficiencies. This allows us to give a picture as broad as possible of what happens in OPV devices, and it shows what happens with some of the best materials at the time this study was performed.* Furthermore, these results are supported by transient drift-diffusion simulations performed for a wide range of parameters.

---

Chapter key findings:

- While dispersion is a known phenomenon in disordered semiconductors, it seems to play a limited role on the extraction in OPV devices under operating conditions.

- The characterization of the mobility using steady-state techniques is sufficient to discuss the transport and extraction in organic solar cells under operating conditions.

---

## 3.2. DESCRIPTION OF THE EXPERIMENT AND MODEL

First, a transient experiment was set up to study the extraction of charges. The dynamics of the charge carriers is studied by measuring the decay of the current density over time between two light intensities for different applied voltages. For t < 0, the device is kept under steady-state conditions at the higher light intensity, then at time zero the intensity is slightly reduced. One should note that the bias voltage is kept constant during the reduction of the light. This will result in the extraction of the extra carriers $\Delta q$ thus leading to a decay in current to reach the steady-state conditions at the lower light intensity; see figure 3.1. After the reduction of the light intensity, the charge carrier density will decay to match the steady-state conditions at the lower light intensity. The excess charge carriers will move by drift and diffusion toward the electrodes to be extracted, leading to a

---

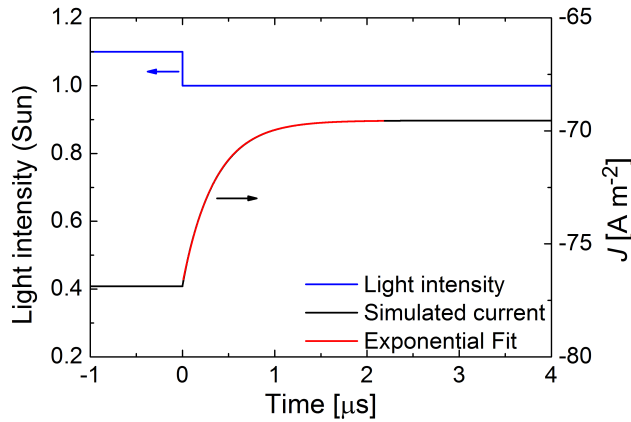*Note that this study was performed in 2016-2017 when the OPV best performing single junction PCE was ≈11%

Figure 3.1: Drift-diffusion simulation results for balanced mobilities, $\mu_n = \mu_p = 1 \times 10^{-3}$ cm$^2$ V$^{-1}$ s$^{-1}$. The decrease of the generation rate, blue line, which is directly proportional to the reduction of the light intensity, creates a decay of the current.

decay in current density. This decay of the extra charge carriers $\Delta q$ can be represented by the following equation:

$$\frac{\partial \Delta q}{\partial t} = -f \Delta q, \tag{3.1}$$

where the charge carrier extraction rate $f$ can be written as the sum of the drift and diffusion rates, $f^{\text{Drift}}$ and $f^{\text{Diffusion}}$ respectively, such as: [27]

$$f = f^{\text{Diffusion}} + f^{\text{Drift}}. \tag{3.2}$$

Considering that the charge carriers travel on average half of the active layer thickness ($L$) to be extracted at the electrode and neglecting space-charge effects so that the electrical field can be written as $V_{\text{eff}}/L$ with $V_{\text{eff}}$ the effective voltage drop across the device, the drift term can be expressed as the inverse of the transit time: [27]

$$f^{\text{Drift}} = 2\frac{\mu F}{L} = 2\frac{\mu V_{\text{eff}}}{L^2}, \tag{3.3}$$

where $\mu$ is the charge carrier mobility. In the same way, the diffusion contribution can be estimated using the Einstein relation: [27]

$$f^{\text{Diffusion}} = 2\frac{D}{(L/2)^2} = 8\frac{\mu k_b T}{q L^2}, \tag{3.4}$$

where $k_b$ is the Boltzmann constant, $T$ the temperature and $q$ the elementary charge. [27] Thus, according to equation 3.3, when the applied voltage ($V_a$) cancels the built-in electric field the effective voltage ($V_{\text{eff}}$) and so the drift rate are zero. In this condition, the extraction rate is minimum and only due to the diffusion rate, which does not depend

46

on the applied voltage, see equation 3.4. Therefore the mobility can be easily calculated by measuring the minimum of the extraction rate. In a first approximation, the decay in current ($J_{\text{decay}}$) can be considered as proportional to the decay of $\Delta q$. Thus solving equation 3.1 gives:

$$J_{decay} \propto J_0 \exp(-ft). \tag{3.5}$$

The expression of the current decay, described above, shows that with a simple exponential fit of the current decay the extraction rate can be calculated. Hence, by finding the voltage where the extraction rate is minimum, the mobility value can be determined. The effect of the recombination is neglected in the expression of the current in equation 3.5 because the recombination has a limited effect on the calculated mobility for reasonable mobilities and recombination rate constant values. In fact, as shown in appendix figure B.1, for very typical value of the bimolecular recombination rate constant, see equations 1.1-1.2, the calculated mobility only vary by a factor $\approx 2$, which is also similar to the experimental error when using the SCLC technique. The change of any injection barriers also has a negligible effect on the calculated mobility as shown in appendix figure B.2.

The advantage of this technique is that the device is maintained under conditions close to realistic operating conditions with an illumination intensity always close to 1 sun and under constant bias, as opposed to other transient techniques, such as TOF,[14] time-resolved electric-field-induced second harmonic generation (TREFISH)/TOF,[17,18] and transient photocurrent (TPC),[28] which are based on pulsed light. Keeping the device under illumination and bias close to the maximum power point ensures that the charge carrier densities[29,30] and the electrical field,[30] which can influence the charge carrier motion, will be similar to those observed in a working solar cell leading to a characterization of the transport properties closer to what happens under steady-state conditions.

## 3.3. DRIFT-DIFFUSION SIMULATION

Secondly, to validate the assumptions made above a transient 1D drift-diffusion simulation was set up. In this simulation, the active layer of the BHJ solar cell is modeled using an effective medium approximation that considers the BHJ as a one-phase semiconductor. The highest occupied molecular orbital (HOMO) of the effective semiconductor is taken as the HOMO value of the donor, and the lowest unoccupied molecular orbital (LUMO) of the effective semiconductor is taken as the LUMO value of the acceptor. The model describes the movement of the charges by drift due to the electric field and diffusion due to the gradient of charge carrier concentration, more details can be found in ref.[31,32]. The simulations also account for bimolecular recombination within the active layer, calculated using reduced Langevin law,[33] as it is commonly seen as the main recombination pathway limiting the performance of high-efficiency OPV devices.[34–36] One should also note that the drift-diffusion equations use the steady-state mobilities as an input and do not include any effects of charge carrier dispersion. So the dispersion in photocurrent observed in other reports[17,18] cannot be reproduced by the drift-diffusion simulation. However, these simulations are suitable in our case as this study
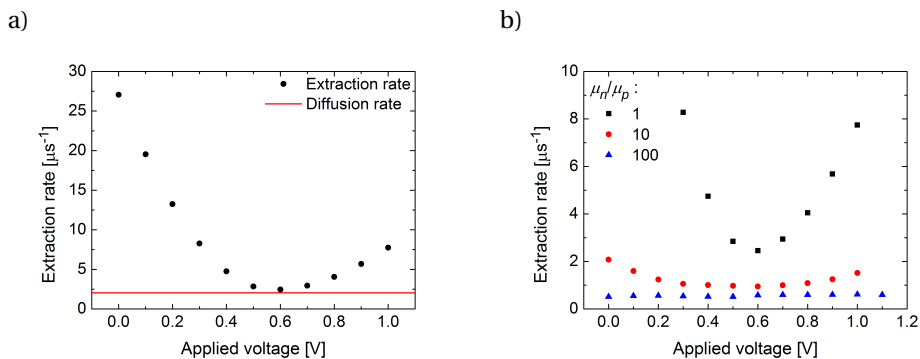
a)

b)



Figure 3.2: a)Simulated voltage dependence of the extraction rate for balanced mobilities, $\mu_n = \mu_p = 1 \times 10^{-3}$ cm$^2$ V$^{-1}$ s$^{-1}$, symbols, and minimum diffusion rate, red line, calculated with equation 3.4. b) Extraction rate for different mobility ratios.

aims to show that steady-state mobilities are the relevant parameters for OPV devices. In addition, if the drift-diffusion simulation can reproduce the experimental data, then dispersion does not play a significant role.

The simulation was first performed considering balanced mobilities. As shown in figure 3.1, the exponential fit accurately reproduces the current decay. The fitting is performed for different applied voltage and the extraction rate is calculated using Equation 3.5, see figure 3.2.a. The clear dependence of the extraction rate on applied voltage, as expected from Equations 3.2-3.4, is in fact observed. A minimum in extraction rate can be noticed at a voltage $V_{\min}$ when the extraction is only due to diffusion, $f = f^{\text{Diffusion}}$, at this point equation 3.4 can be used to calculate the value of the mobility. In the case of $\mu_n = \mu_p = 1 \times 10^{-7}$ m$^2$ V$^{-1}$ s$^{-1}$, the calculated mobility is equal to $1.2 \times 10^{-7}$ m$^2$ V$^{-1}$ s$^{-1}$, thus the values obtained by the fit are close to the input steady-state mobilities.

The same simulation was done for several ratios of the mobilities, and as the ratio increases the effect of the drift becomes less dominant and diffusion starts to play a more important role, figure 3.2.b. This observation is in agreement with the space charge effect observed in OPV devices with unbalanced mobilities, as the space charge creates an electrical field that shields the built-in field. [12,19] As in classic TPC, it is not possible with this experiment to dissociate the effect of the two carrier species. [28] However, as shown in table 3.1, the mobilities calculated using equation 3.4 are close to the geometrical average of the electron and hole mobilities. To conclude these simulations show that the simple model proposed previously is valid when there is no dispersion and that the mobility can be calculated using this simple experiment. In the following, the geometrical average of the steady-state mobilities will be used as a reference.

## 3.4. Experimental validation

Finally, to validate the hypothesis that the steady-state mobilities govern the extraction in OPV devices, the experiment presented previously was conducted for several donor:acceptor blends. If the mobilities obtained by the experiment are the same

Table 3.1: Calculated average mobility for different mobility ratios.

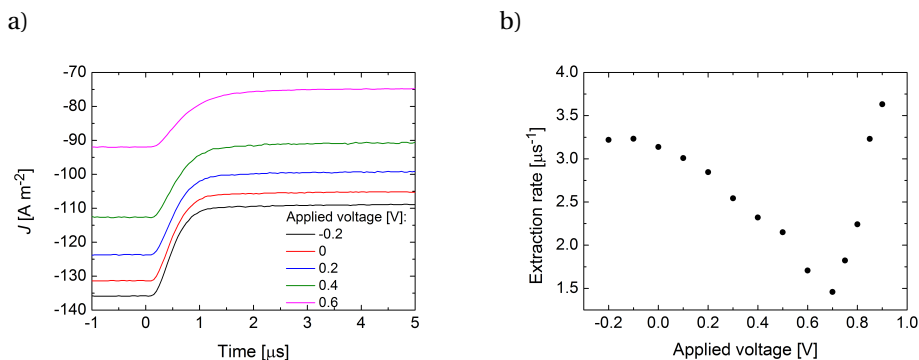| $\mu_n$ [cm$^2$ V$^{-1}$ s$^{-1}$] | $\mu_p$ [cm$^2$ V$^{-1}$ s$^{-1}$] | Ratio | Average $\mu^{\text{a)}}$ [cm$^2$ V$^{-1}$ s$^{-1}$] | Average $\mu^{\text{b)}}$ [cm$^2$ V$^{-1}$ s$^{-1}$] |
|---|---|---|---|---|
| $1\times10^{-3}$ | $1\times10^{-3}$ | 1 | $1\times10^{-3}$ | $1.2\times10^{-3}$ |
| $1\times10^{-3}$ | $1\times10^{-4}$ | 10 | $3.2\times10^{-4}$ | $4.7\times10^{-4}$ |
| $1\times10^{-3}$ | $1\times10^{-5}$ | 100 | $1\times10^{-4}$ | $2.6\times10^{-4}$ |

a) Geometrical average: $\mu = \sqrt{\mu_n \mu_p}$ ; b) Using equation 3.4

a)

b)



Figure 3.3: Extraction experiment results for a PTB7:PC$_{71}$BM solar cell showing a) the current decay for different applied voltage and b) the extraction rate, calculated with equation 3.5. These two results show the same trend that the results obtained with the drift-diffusion simulation in figures 3.1-3.2

as the one obtained with the SCLC technique, it would mean that the steady-state mobilities are in fact relevant to characterize the extraction and transport in the case of OPV devices. Solar cells, made of polythieno[3,4-b]-thiophene-co-benzodithiophene (PTB7) mixed with [6,6]-phenyl-C71-butyric acid methyl ester (PC$_{71}$BM), successfully illustrate the behavior presented previously, see figure 3.3. In fact, a clear minimum of the extraction rate at $V_a$ = 0.7 V and a well-defined effect of the drift are observed, as expected from equation 3.3. The decay of the current (see figure 3.3.b) also fits well with the model described above, showing an exponential decay. The measured mobility, $\mu$ = $4 \times 10^{-4}$ cm$^2$ V$^{-1}$ s$^{-1}$, is coherent with the geometrical average of the mobilities obtained from the SCLC measurement, $\mu = 3.2 \times 10^{-4}$ cm$^2$ V$^{-1}$ s$^{-1}$.[20] As the aim of this study is to show that these results can be broadened to other organic materials this experiment has been conducted on other blends. PC$_{71}$BM and PC$_{61}$BM have been used as acceptor blended with different donor polymers: MEH-PPV, P3HT, PTB7, PDPP5T, PBDTT-FTTE, PBDTTT-C, see full names in the materials list. These polymers have been chosen so that the resulting blends cover a wide range of mobility values from $10^{-5}$ to $10^{-3}$ cm$^2$ V$^{-1}$ s$^{-1}$, mobility ratio from 1 to 100, and efficiency from 2 to 3% in the case of P3HT:PC$_{61}$BM to 8-9% for PBDTT-FTTE:PC$_{71}$BM cell, see table 3.2 and appendix figure B.3-B.4. The tested blends give similar results as shown previously for PTB7:PC$_{71}$BM blends, see appendix figure B.5. The extracted mobility is in fact always close to the geometrical average of the measured SCLC mobilities, see table 3.2 and appendix figure B.3. One can also note that the obtained values are the same if a larger reduction of the light intensity

is performed. In fact, even when studying the most extreme case, which is light to dark transition, the lifetime obtained are the same, see appendix figure B.6. It also means that the extracted mobility reflects the behavior of all the charge carriers.

To gauge whether our experimental data are influenced by RC-time issues, the experiment was repeated (by Dr. Martin Stolterfoht at University of Potsdam) with different load resistors for measuring the current, a much smaller device area (1 mm²), and a faster time constant of the LED switching ($\approx$50 ns).[37] In other words, a faster setup was used. The resulting extraction rates at $V_{min}$ are very similar to the rates obtained in our lab: a load resistor of 50 $\Omega$ (as used in our lab) or 100 $\Omega$ give very similar mobilities $5 - 5.9 \times 10^{-4}$ cm² V⁻¹ s⁻¹ (expected $\approx 3 \times 10^{-4}$ cm² V⁻¹ s⁻¹). We even performed an extra experiment at short-circuit for the PTB7:P$_{71}$BM device (see appendix figure B.7.a) at the short-circuit condition, where the RC-time should have the biggest impact as the extraction is faster. We find that there is very little difference in the extraction rate depending on the load resistance when it is smaller than 200 $\Omega$. We also performed additional drift-diffusion simulations which include the load resistor and different device areas characteristic for typical measurement conditions, see appendix figure B.7.b. The parameters were chosen such that they are representative for PTB7:PC$_{71}$BM solar cells (see appendix table B.1 for details). These simulations reveal a negligible effect of the RC time on the extraction rate at $V_{min}$, meaning that measurements at $V_{min}$ provide accurate values of the charge carrier mobility.

Table 3.2: Extraction rate for different donor:acceptor blends

| Blend | $\mu_n$ [cm² V⁻¹ s⁻¹] | $\mu_p$ [cm² V⁻¹ s⁻¹] | Average $\mu$[a] [cm² V⁻¹ s⁻¹] | Extracted $\mu$[b] [cm² V⁻¹ s⁻¹] | Half-life time [$\mu$s] |
|---|---|---|---|---|---|
| MEH-PPV:PC$_{61}$BM | $1\times10^{-5}$[c] | $2.5\times10^{-5}$[c] | $1.6\times10^{-5}$ | $1.9\times10^{-5}$ | 2.8 |
| P3HT:PC$_{61}$BM | $1.9\times10^{-3}$[27] | $3.7\times10^{-5}$[27] | $2.7\times10^{-4}$ | $3.4\times10^{-4}$ | 1.0 |
| PTB7:PC$_{71}$BM | $3.5\times10^{-4}$[20] | $3\times10^{-4}$[20] | $3.2\times10^{-4}$ | $4.0\times10^{-4}$ | 0.48 |
| PDPP5T:PC$_{71}$BM | $3.1\times10^{-3}$[20] | $2.9\times10^{-3}$[20] | $3.0\times10^{-3}$ | $1.3\times10^{-3}$ | 0.58 |
| PBDTT-FTTE:PC$_{71}$BM | $1.3\times10^{-3}$[c] | $3.3\times10^{-4}$[c] | $6.5\times10^{-4}$ | $8.8\times10^{-4}$ | 0.45 |
| PBDTTT-C:PC$_{71}$BM | $2.1\times10^{-4}$[c] | $8\times10^{-5}$[c] | $1.3\times10^{-4}$ | $6.0\times10^{-4}$ | 0.97 |

a) Geometrical average: $\mu = \sqrt{\mu_n \mu_p}$; b) Using equation 3.4; c) appendix figure B.3.

In addition, the integration of the current decay makes it possible to measure the half-life time that shows that $\approx$1 $\mu$s is needed to extract 50% of the carriers; see Table 3.2. The microsecond time scale is far from the nanosecond time scale that has been reported by other groups in the case of extraction dominated by dispersion.[17,18] These two findings confirm that charge carrier thermalization has a limited effect on the device extraction when the devices are tested under realistic operating conditions. It is also in agreement with the conclusion of van der Kaap and Koster on organic diodes, where they have demonstrated that the steady-state mobility is only slightly enhanced, when the relaxation of high energetic charge carriers is taken into account, compared to the value in thermal equilibrium.[16]
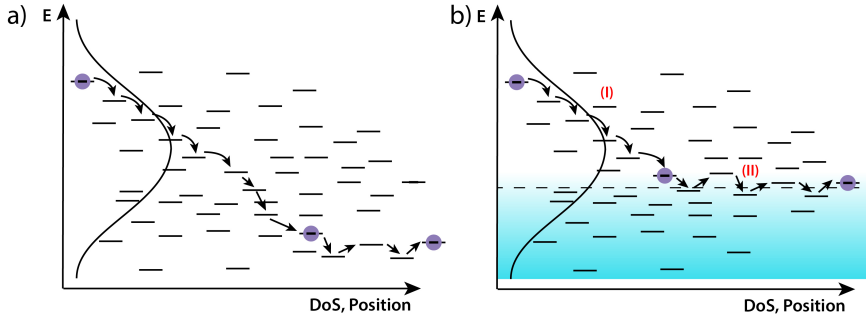
Figure 3.4: Different dynamics of charge carrier extraction depending on the illumination: a) fast transport of carriers generated in an empty DoS (by a light pulse in the dark) as they have more states availables at low energies since the DoS is empty; b) fast relaxation of the charge carrier (I) followed by a transport by hopping when reaching the bottom of the DoS which is filled (blue area) due to the constant illumination (II).

## 3.5. DISCUSSION

One could ask why the results obtained here differ from the conclusions obtained in other papers and why here the thermal relaxation of the "hot" carriers appears to make a limited contribution to the extraction. It can be explained by the fact that the testing conditions greatly influence the results and that care should be taken when choosing the conditions under which the transport will be characterized. For example the temperature, the fact to be under constant illumination and the background charge carrier densities have an influence on the relative importance of the "hot" carrier relaxation. [14–18] In preceding experiments and simulations, [17,18] the characterization of the transport is based on pulsed light on a device otherwise in the dark, that is, in the situation where the DoS is empty, see figure 3.4.a. Thus, the charge carriers generated by the light pulse never have the chance to reach a steady-state-like condition as they can go through the DoS without reaching a point where they will have to move through hopping close to the equilibrium level, see figure 3.4.b (2). [38] This can explain the high charge carrier mobilities and strong dispersion effect observed by these reports. However, as shown in figure 3.4.b, when the device is under steady-state condition the bottom of the DoS is filled hence the relaxation time of the charge carrier is much faster, as shown by van der Kaap and Koster in Ref. 16. After they relax the charge carriers have to move by hopping around the equilibrium level [38] leading to the mobility commonly observed in steady-state measurement. The case described in figure 3.4.b is more likely to describe what we observed in our experiment. One should note that the drawing depicted in figure 3.4 is not intended to represent a specific shape of the DoS. In a disordered system, the DoS will be smeared out (e.g., exponential, Gaussian) which will induce some form of dispersion as hot carriers can relax in the DoS. In both the exponential DoS and the Gaussian case, the mobility depends on the filling of the DoS. [29,30] However, the typical density of carriers in a solar cell under illumination is low (as compared to field-effect transistors, for example) typically between $10^{15}$ and $10^{16}$ cm$^{-3}$, [31] which means that the effect of illumination on mobility is not strong. However, charges that are photogenerated high up in the DoS will still thermalize and cause dispersion. In the present chapter, we show that

this thermalization is so rapid that it does not affect the extraction from an organic solar cell. To summarize, if one wants to make any statements on the transport and extraction in OPV devices, one must take care to choose operating conditions such that they reflect the real states of a working solar cell. Moreover, Blakesley and Neher have shown that a high amount of disorder is detrimental to the open-circuit voltage and would limit the efficiency. [39] So designing highly disordered materials, that would benefit from the effect of the dispersion for faster extraction, is not the best road to achieve high efficiency as it would lead to devices with a low open-circuit voltage.

## **3.6.** CONCLUSION

In conclusion, we have shown that the dispersion of the current plays a limited role in the charge carrier extraction in OPV devices. This result is supported by experimental data, for several donor:acceptor blends, which constantly show mobilities and half-life time on the same order of magnitude as those expected for the mobilities measured using the classic SCLC technique. In addition, the good agreement between drift-diffusion simulation and experimental results also shows that steady-state mobilities are sufficient to characterize the transport and extraction in OPV devices. Thus, steady-state mobilities that are found by SCLC technique give a valuable insight into the performance of OPV materials.

## REFERENCES

[1] N. S. Sariciftci, D. Braun, C. Zhang, V. I. Srdanov, A. J. Heeger, G. Stucky, and F. Wudl, *Semiconducting polymer-buckminsterfullerene heterojunctions: Diodes, photodiodes, and photovoltaic cells,* Applied Physics Letters **62**, 585 (1993).

[2] Y. Cui, H. Yao, J. Zhang, T. Zhang, Y. Wang, L. Hong, K. Xian, B. Xu, S. Zhang, J. Peng, Z. Wei, F. Gao, and J. Hou, *Over 16% efficiency organic photovoltaic cells enabled by a chlorinated acceptor with increased open-circuit voltages,* Nature Communications **10**, 1 (2019).

[3] X. Xu, K. Feng, Z. Bi, W. Ma, G. Zhang, and Q. Peng, *Single-Junction Polymer Solar Cells with 16.35% Efficiency Enabled by a Platinum(II) Complexation Strategy,* Advanced Materials **31**, 1901872 (2019).

[4] Y. Lin, B. Adilbekova, Y. Firdaus, E. Yengel, H. Faber, M. Sajjad, X. Zheng, E. Yarali, A. Seitkhan, O. M. Bakr, A. El-Labban, U. Schwingenschlögl, V. Tung, I. McCulloch, F. Laquai, and T. D. Anthopoulos, *17% Efficient Organic Solar Cells Based on Liquid Exfoliated WS$_2$ as a Replacement for PEDOT:PSS,* Advanced Materials **31**, 1902965 (2019).

[5] T. Yan, W. Song, J. Huang, R. Peng, L. Huang, and Z. Ge, *16.67% Rigid and 14.06% Flexible Organic Solar Cells Enabled by Ternary Heterojunction Strategy,* Advanced Materials **31**, 1902210 (2019).

[6] M. A. Pan, T. K. Lau, Y. Tang, Y. C. Wu, T. Liu, K. Li, M. C. Chen, X. Lu, W. Ma, and C. Zhan, *16.7%-efficiency ternary blended organic photovoltaic cells with PCBM as the acceptor additive to increase the open-circuit voltage and phase purity,* Journal of Materials Chemistry A **7**, 20713 (2019).

[7] Q. Liu, Y. Jiang, K. Jin, J. Qin, J. Xu, W. Li, J. Xiong, J. Liu, Z. Xiao, K. Sun, S. Yang, X. Zhang, and L. Ding, *18% Efficiency organic solar cells,* Science Bulletin **65**, 272 (2020).

[8] Y. Lin, Y. Firdaus, M. I. Nugraha, F. Liu, S. Karuthedath, A. Emwas, W. Zhang, A. Seitkhan, M. Neophytou, H. Faber, E. Yengel, I. McCulloch, L. Tsetseris, F. Laquai, and T. D. Anthopoulos, *17.1% Efficient Single-Junction Organic Solar Cells Enabled by n-Type Doping of the Bulk-Heterojunction,* Advanced Science , 1903419 (2020).

[9] J.-L. Bredas, J. P. Calbert, D. A. da Silva Filho, and J. Cornil, *Organic semiconductors: a theoretical characterization of the basic parameters governing charge transport,* Proc Natl Acad Sci U S A **99**, 5804 (2002).

[10] V. Coropceanu, J. Cornil, D. A. da Silva Filho, Y. Olivier, R. Silbey, and J.-L. Bredas, *Charge transport in organic semiconductors,* Chemical Reviews **107**, 926 (2007).

[11] J. C. Blakesley, F. A. Castro, W. Kylberg, G. F. A. Dibb, C. Arantes, R. Valaski, M. Cremona, J. S. Kim, and J.-S. Kim, *Towards reliable charge-mobility benchmark measurements for organic semiconductors,* Organic Electronics **15**, 1263 (2014).

[12] V. D. Mihailetchi, J. Wildeman, and P. W. M. Blom, *Space-charge limited photocurrent,* Physical Review Letters **94**, 126602 (2005).

[13] V. D. Mihailetchi, H. X. Xie, B. de Boer, L. J. A. Koster, and P. W. M. Blom, *Charge transport and photocurrent generation in poly(3-hexylthiophene): Methanofullerene bulk-heterojunction solar cells,* Advanced Functional Materials **16**, 699 (2006).

[14] L. Pautmeier, R. Richert, and H. Bässler, *Poole-frenkel behavior of charge transport in organic solids with off-diagonal disorder studied by monte carlo simulation,* Synthetic Metals **37**, 271 (1990).

[15] P. M. Borsenberger, E. H. Magin, M. D. Van Auweraer, and F. C. De Schryver, *The role of disorder on charge transport in molecularly doped polymers and related materials,* physica status solidi (a) **140**, 9 (1993).

[16] N. J. van der Kaap and L. J. A. Koster, *Charge carrier thermalization in organic diodes,* Scientific Reports **6**, 19794 (2016).

[17] A. Melianas, V. Pranculis, A. Devizis, V. Gulbinas, O. Inganäs, and M. Kemerink, *Dispersion-dominated photocurrent in polymer:fullerene solar cells,* Advanced Functional Materials **24**, 4507 (2014).

[18] A. Melianas, F. Etzold, T. J. Savenije, F. Laquai, O. Inganäs,  and M. Kemerink, *Photo-generated carriers lose energy during extraction from polymer-fullerene solar cells,* Nature Communications **6**, 8778 (2015).

[19] J. A. Bartelt, D. Lam, T. M. Burke, S. M. Sweetnam,  and M. D. McGehee, *Charge-carrier mobility requirements for bulk heterojunction solar cells with high fill factor and external quantum efficiency >90%,* Advanced Energy Materials **5**, 1500577 (2015).

[20] D. Bartesaghi, I. d. C. Perez, J. Kniepert, S. Roland, M. Turbiez, D. Neher,  and L. J. A. Koster, *Competition between recombination and extraction of free charges determines the fill factor of organic solar cells,* Nature Communications **6**, 7083 (2015).

[21] C. M. Proctor, J. A. Love,  and T.-Q. Nguyen, *Mobility guidelines for high fill factor solution-processed small molecule solar cells,* Advanced Materials **26**, 5957 (2014).

[22] D. Neher, J. Kniepert, A. Elimelech,  and L. J. A. Koster, *A new figure of merit for organic solar cells with transport-limited photocurrents,* Scientific Reports **6**, 24861 (2016).

[23] D. Rezzonico, B. Perucco, E. Knapp, R. Häusermann, N. A. Reinke, F. Müller,  and B. Ruhstaller, *Numerical analysis of exciton dynamics in organic light-emitting devices and solar cells,* Journal of Photonics for Energy **1**, 011005 (2011).

[24] J. J. Brondijk, F. Torricelli, E. C. P. Smits, P. W. M. Blom,  and D. M. de Leeuw, *Gate-bias assisted charge injection in organic field-effect transistors,* Organic Electronics **13**, 1526 (2012).

[25] R. Häusermann, E. Knapp, M. Moos, N. A. Reinke, T. Flatz,  and B. Ruhstaller, *Coupled optoelectronic simulation of organic bulk-heterojunction solar cells: Parameter extraction and sensitivity analysis,* Journal of Applied Physics **106**, 104507 (2009).

[26] S. Albrecht, W. Schindler, J. Kurpiers, J. Kniepert, J. C. Blakesley, I. Dumsch, S. Allard, K. Fostiropoulos, U. Scherf,  and D. Neher, *On the field dependence of free charge carrier generation and recombination in blends of pcpdtbt/pc70bm: Influence of solvent additives,* The Journal of Physical Chemistry Letters **3**, 640 (2012).

[27] L. J. A. Koster, M. Kemerink, M. M. Wienk, K. Maturová,  and R. A. J. Janssen, *Quantifying bimolecular recombination losses in organic bulk heterojunction solar cells,* Advanced Materials **23**, 1670 (2011).

[28] J. Seifter, Y. Sun,  and A. J. Heeger, *Transient photocurrent response of small-molecule bulk heterojunction solar cells,* Advanced Materials **26**, 2486 (2014).

[29] C. Tanase, E. J. Meijer, P. W. M. Blom,  and D. M. de Leeuw, *Unification of the hole transport in polymeric field-effect transistors and light-emitting diodes,* Physical Review Letters **91**, 216601 (2003).

[30] W. F. Pasveer, J. Cottaar, C. Tanase, R. Coehoorn, P. A. Bobbert, P. W. M. Blom, D. M. de Leeuw, and M. A. J. Michels, *Unified description of charge-carrier mobilities in disordered semiconducting polymers,* Physical Review Letters **94**, 206601 (2005).

[31] L. J. A. Koster, E. C. P. Smits, V. D. Mihailetchi, and P. W. M. Blom, *Device model for the operation of polymer/fullerene bulk heterojunction solar cells,* Physical Review B **72**, 085205 (2005).

[32] S. Selberherr, *Analysis and Simulation of Semiconductor Devices* (Springer-Verlag, Wien, Germany, 1984) p. 285.

[33] P. Langevin, *Recombinaison et mobilités des ions dans les gaz,* Annales de Chimie et de Physique , 433 (1903).

[34] G. Lakhwani, A. Rao, and R. H. Friend, *Bimolecular recombination in organic photovoltaics,* Annual Review of Physical Chemistry **65**, 557 (2014).

[35] A. Foertig, J. Kniepert, M. Gluecker, T. Brenner, V. Dyakonov, D. Neher, and C. Deibel, *Nongeminate and geminate recombination in ptb7:pcbm solar cells,* Advanced Functional Materials **24**, 1306 (2014).

[36] J. Kniepert, I. Lange, N. J. van der Kaap, L. J. A. Koster, and D. Neher, *A conclusive view on charge generation, recombination, and extraction in as-prepared and annealed p3ht:pcbm blends: Combined experimental and simulation work,* Advanced Energy Materials **4**, 1301401 (2014).

[37] V. M. Le Corre, A. Rahimi Chatri, N. Y. Doumon, and L. J. A. Koster, *Response to comment on "charge carrier extraction in organic solar cells governed by steady-state mobilities",* Advanced Energy Materials **8**, 1803125 (2018).

[38] J. J. M. van der Holst, F. W. A. van Oost, R. Coehoorn, and P. A. Bobbert, *Monte carlo study of charge transport in organic sandwich-type single-carrier devices: Effects of coulomb interactions,* Physical Review B **83**, 085206 (2011).

[39] J. C. Blakesley and D. Neher, *Relationship between energetic disorder and open-circuit voltage in bulk heterojunction organic solar cells,* Physical Review B **84**, 075210 (2011), pRB.

**3**

# 4

# PITFALLS OF SPACE-CHARGE-LIMITED CURRENT TECHNIQUE FOR PEROVSKITES

*Space-charge-limited current (SCLC) measurements have been widely used to study the charge carrier mobility and trap density in semiconductors. While such measurements have proven to be valuable to investigate the properties of amorphous silicon and organic semiconductors, their applicability to metal halide perovskites is not straightforward, due to the mixed ionic and electronic nature of these materials.*

*Here, we present a description of the pitfalls of SCLC measurements for perovskite semiconductors, with a main focus on the effect which mobile ions have upon this electrical characterization technique. We show, using drift-diffusion simulations, that the presence of ions strongly affects the measurement and that the usual analysis and interpretation of the values extracted from SCLC needs to be refined. In particular, we highlight that the trap density and mobility cannot be directly quantified using classical methods. We also discuss the advantages of pulsed-SCLC measurements to obtain reliable data with minimized influence of the ionic motion and the degradation of the perovskite under voltage stress. We then show that fitting the pulsed-SCLC measurement using drift-diffusion modeling is a reliable method to extract mobility, trap and ion densities simultaneously. As a proof of concept we obtain a trap density of $1.3 \times 10^{13}$ $cm^{-3}$, ion density of $1.1 \times 10^{13}$ $cm^{-3}$ and a mobility of 13 $cm^2 V^{-1} s^{-1}$ for MAPbBr$_3$ single-crystal.*

## 4.1. Introduction

O NE of the most common techniques to investigate the intrinsic transport properties as well as the trap density of a semiconductor is the so-called space-charge-limited current (SCLC) measurement. Due to the apparent simplicity of the measurement, it has been used extensively in the literature to study organic semiconductors, inorganic and hybrid organic-inorganic metal halide perovskites. [1–13] In fact, the measurement "only" consists of measuring a dark current-voltage (JV) characteristic of a single-carrier device, i.e. a device where the contacts on both sides of a semiconductor are aligned to the conduction (valence) band in such a way that only electrons (holes) are injected. One of the main advantages of this technique above other techniques such as charge carrier extraction by linearly increasing voltage, optical-pump-THz-probe photocon- ductivity and microwave conductivity, lies in the fact the electron and hole mobility and trap density can be probed independently. [14,15] In addition, the device configuration is similar to the one used in solar cells and other "sandwich structure" optoelectronic devices, where the vertical transport is probed, as opposed to the lateral transport that can be measured using field-effect transistors measurements. [15]

The widespread use of SCLC measurements in the field of organic semiconductors likely contributed to its rapid adoption by the perovskite community. As a result, a large num- ber of very influential publications have used this technique to quantify the transport and trapping properties in both single crystals and thin films. [4–13] However, the analysis of SCLC measurement data is sometimes oversimplified since the assumptions required to extract reliable values are often overlooked and not fully met, which leads to an over- or underestimation of the extracted values.

In this chapter, we investigate the applicability of SCLC measurement for perovskites using drift-diffusion (DD) modeling, and we show how we can correctly extract impor- tant parameters from the simulations. To the best of our knowledge, this is the first report on extracting both ion and trap density from SCLC measurements, in addition to accurately determining the charge carrier mobility.

Chapter key findings:

- Classical SCLC analysis of perovskite single-carrier devices need to be adapted to account for mobile ions.

- The point assigned to the trap-filled limit voltage in perovskite device is ac- tually related to the space-charge in the device and not just the trap density as shown in many papers.

- Pulsed-SCLC provides a more reliable measurement to control the influ- ence of the ions on the JV-curve.

- Fitting pulsed-SCLC with a drift-diffusion simulation enables to quantify not only the net charge but also the mobility, trap- and ion densities.

## 4.2. Typical pitfalls of the SCLC analysis

Ideally, SCLC measurements consist of a dark JV-curve measurement of a single-carrier device with symmetric ohmic contacts on either side of a semiconductor, as depicted in figure 4.1 (a). When the JV-curve is plotted on a log-log scale, several regimes can be identified; firstly a low voltage regime with a slope $\left(\frac{d\log(J)}{d\log(V)}\right)$ of 1, followed by a regime with a high slope (> 2) due to trap filling (if any), and finally, at high voltage, the so-called SCLC regime with a slope of 2. These three regimes are shown in figure 4.1 (b & c). Note that space charge effect also influences the trap-filled-limited (TFL) regime. Already several pitfalls of SCLC measurements arise from the simple characterization of these regimes, which have been reported in the literature: (i) the use of non-ohmic and/or asymmetric contacts can lead to slope > 2 regimes and needs to be accounted for while performing the SCLC analysis [1,16], (ii) the interpretation of the low voltage regime vary depending on several factors such as diffusion and, intrinsic-, trap- or dopant densities [17–20], (iii) the fitting and accuracy of the Mott-Gurney equation [21,22] for the quadratic regime at high voltages and (iv) the fitting Mark-Helfrich equation for the interpretation of the TFL regime. [17,23–25] Besides these pitfalls, perovskite materials—good electronic and ionic conductors—bring some new challenges of their own as the contributions of electronic and ionic species influence the current.

 Before discussing the influence of ions on SCLC measurements, we first discuss the ideal case where no ions are present as it is not always clear in the literature what values can be extracted and how.

SCLC measurements are one of the most common approaches to extract the mobility and trap density values of semiconductors and have been widely used in the perovskite literature. [6–11,26] As discussed in numerous papers [17,21,22] the mobility value can be extracted from the quadratic regime of the JV-curve by fitting the Mott-Gurney equation:

$$J = \frac{9}{8}\epsilon\mu\frac{(V - V_{BI})^2}{L^3},\tag{4.1}$$

where $J$ is the current density, $V$ and $V_{BI}$ the applied and built-in voltage, $\epsilon$ the dielectric constant, $L$ the thickness, $\mu$ the mobility. While some slightly different formulas were proposed to account for the presence of trapping, [17] equation (4.1) remains the most commonly used formula in the literature.

As previously mentioned, the trap density can be extracted from the plot of the JV-curve on a log-log scale. The most common approach is to calculate the trap density from the so-called trap-filled-limit voltage [17]:

$$V_{tfl} = \frac{qn_tL^2}{2\epsilon},\tag{4.2}$$

with $q$ the elementary charge. Even though this formula can be easily derived under the assumption that the amount of traps is larger than the number of free charges, it is not yet clarified which point of the JV-curve should be chosen as $V_{tfl}$. Most reports choose the voltage of the crossing point between the low voltage tangent with a slope of 1 and the trap-filled-limited regime tangent with a slope larger than 2, as shown in figure 4.1
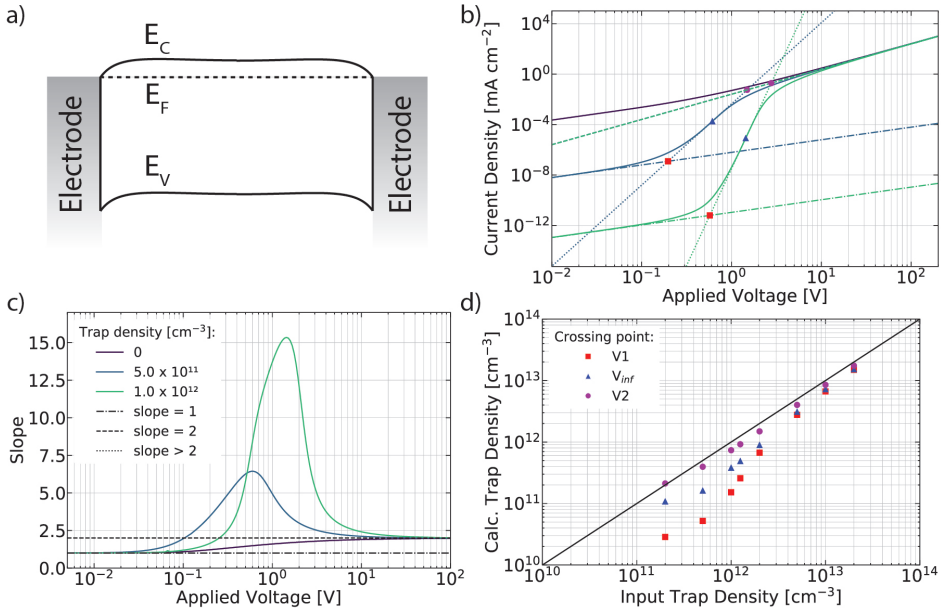
**4**



Figure 4.1: (a) Ideal device structure for SCLC measurement with symmetric ohmic contact and no injection barrier. (b) Simulated JV-curve of an electron-only device with a 100 μm thick perovskite between two perfect electrodes as in (a) varying the trap density. The dashed lines correspond to the different tangents with a slope of 1, 2 and >2, the color points in red, blue and magenta correspond to construction of $V1$, $V_{inf}$ and $V2$. (c) Evolution of the slopes of the JV-curves with voltage. (d) Evaluation of the accuracy of the trap density estimation depending on the voltage point taken as $V_{tfl}$. The parameters used in the simulations can be found in table C.1.

(b), which we call $V1$. However, others use the crossing point between the tangent space-charge-limited regime at high voltages and the trap-filled-limited regime, which we call $V2$.[27] Lastly, one may consider the inflection point ($V_{inf}$) as a viable option for the $V_{tfl}$ value.

In order to assess which voltage ($V1$, $V2$, or $V_{inf}$) yields the most accurate estimate of the trap density, we simulated JV-curves by varying the trap densities for a fixed thickness of 100 μm and extracted the values of $V1$, $V_{inf}$ and $V2$ and calculated the corresponding trap densities using equation 4.2. Figure 4.1 (d) shows that using $V1$ to calculate $V_{tfl}$ gives the worst estimation of trap density and can lead to errors of almost one order of magnitude in the estimated trap density. The error is largest when the trap density is low and the transition between the two regimes is shallow, i.e. when the slope of the TFL regime is low. As shown, $V2$ gives the most accurate value for the trap density and should be used instead. This is not so surprising as the transition from the TFL to the SCLC regime happens when all traps are filled and the free charge carrier density becomes larger than the number of traps, see figure C.1–C.3.

We also note that, for a given thickness, trap densities can only be resolved by SCLC measurements if the density of traps exceeds a certain threshold. In fact, the TFL regime

only appears if $n_t > n$ at low voltage. Hence, the minimum trap density leading to a TFL regime is given by the charge density $n_{diff}$ at low voltage (where the current is dominated by diffusion) in the absence of traps and dopants.[19,20] The minimum density of traps that is noticeable is thus given by

$$n_{t,min} = n_{diff} = 4\pi^2 \frac{kT}{q^2} \frac{\epsilon}{L^2}. \tag{4.3}$$

Assuming that the relative dielectric constant of perovskites is typically 25 and that the experiment is performed at 295 K, equation 4.3 implies that to resolve a trap density of $10^{11}$ cm$^{-3}$ the thickness of the perovskite layer needs to be at least 100 $\mu$m thick. For a trap density of $10^{16}$ cm$^{-3}$, 400 nm is sufficient to resolve the TFL regime. Thus, to observe a TFL regime, high-quality perovskites require a very thick film in the SCLC experiment. However, since $V_{tfl}$ is inversely proportional to $L^2$, it is possible to encounter difficulties as we have to measure at high voltages to reach the quadratic SCLC regime if the perovskite thickness is increased.

These important findings question the way SCLC measurements are reported in the literature. In the absence of a TFL regime, we note that the trap density is lower than $n_{t,min}$, depending on the thickness of the measured sample, rather than claiming the absence of traps.

## 4.3. INFLUENCE OF IONS ON SCLC MEASUREMENTS

One of the peculiar properties inherent to perovskite materials is the fact that they are both electronic and ionic conductors. As widely reported in the perovskite solar cells literature the movement of ions can have a dramatic impact on the JV-curves of perovskite solar cells and cause hysteresis.[28–31] Surprisingly, the influence of ions on the JV-curves of SCLC measurements has been largely overlooked and there are, to the best of our knowledge, few reports of the difference between forward (FW) and backward (BW) scan for SCLC measurement. FW(BW) scan is the measurement of a JV-curve from low (high) to high (low) voltages. A recent exception is the paper by Duijnstee et al.[32] The JV-curve from the SCLC measurement of a MAPbBr$_3$ single-crystal—taken from Ref. 32—is shown in figure 4.2 (a) and shows large hysteresis between FW and BW scan. This indicates that the movement of the ions has a large effect on the current and, hence, needs to be considered in the SCLC analysis when studying perovskites.

To gain more insight into how the ions affect the current we simulated a 100 $\mu$m thick perovskite single-crystal including trapping and mobile ions, as shown in figure 4.2 (b) and table C.1. First, we simulated a steady-state (or stabilized) scan where ions have time to redistribute at every voltage step followed by a simulation of the extreme cases of an infinitely fast FW and BW scan pre-biased at 0 and 200 V, respectively. For these scans, the ion distributions throughout the device are calculated at the prebias (here the first applied voltage) and kept fixed for all the other voltage steps. While there is no significant difference between the FW and steady-state scans, there is a dramatic hysteresis feature between the FW and BW sweep. The fact that the steady-state and FW scan are similar is not so surprising as the cations mostly stay in the bulk at low voltages because the perovskite layer is so thick. Therefore, the current at low voltage is hardly affected,
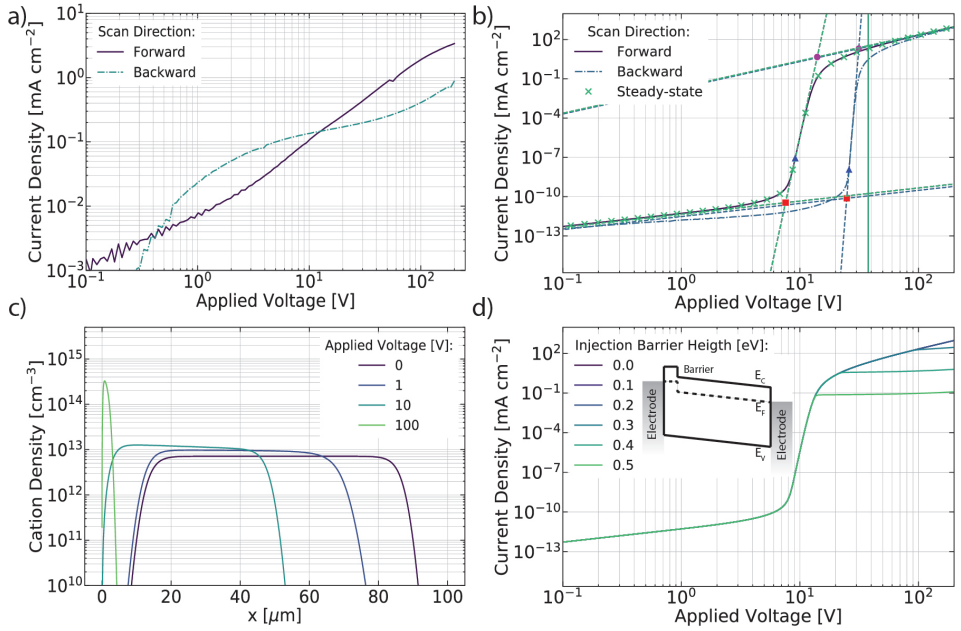
Figure 4.2: (a) Forward and backward JV-scan of a MAPbBr$_3$ perovskite single-crystal taken from Ref. 32 showing strong hysteresis. (b) Simulated JV-curves for forward, backward and steady-state scans to demonstrate the influence of ion migration on the JV-curve. The vertical line indicates the $V_{tfl}$ as calculated from equation 4.2. (c) Cation density distribution calculated for steady-state conditions at different bias voltages where it can be seen that the cations slowly migrate toward the electrode, the anion distribution can be found in figures C.1–C.3. (d) Effect of injection barrier next to the injecting electrode that saturates the current at high voltages. The parameters used in the simulation can be found in table C.1.

as depicted figure 4.2 (b). Even though the cations will accumulate at the electrode at high voltages, it still has a negligible effect as the electric field is high enough not to be affected. During the BW scan, the current is mostly affected at intermediate voltages as the ions are confined near the electrode effectively dedoping the bulk of the perovskite. The vertical line in figure 4.2 (b) indicates the $V_{tfl}$ as calculated from equation 4.2. We can note that $V2$ of the BW scan is a lot closer to $V_{tfl}$ than the one from the FW or steady-state scan. This tends to indicate that using a BW scan leads to a better estimate of the trap density. However, for this to be true the scan rate should be sufficiently high to ensure than ions do not have time to move throughout the JV measurement, which is difficult when scanning over a large voltage range. Additionally, we will show later that other effects may influence the BW scan making its use more difficult experimentally.

In summary, the ions have a large influence on the SCLC JV-curves but even more importantly the values of trap density extracted from this measurement are also largely dependent on the ions making it impossible to extract reliable values of the trap density using $V_{tfl}$.

While there is a clear effect of the ionic distribution on the simulated JV-curves we do not see such a drastic decrease and saturation in the current density in the BW scan com-
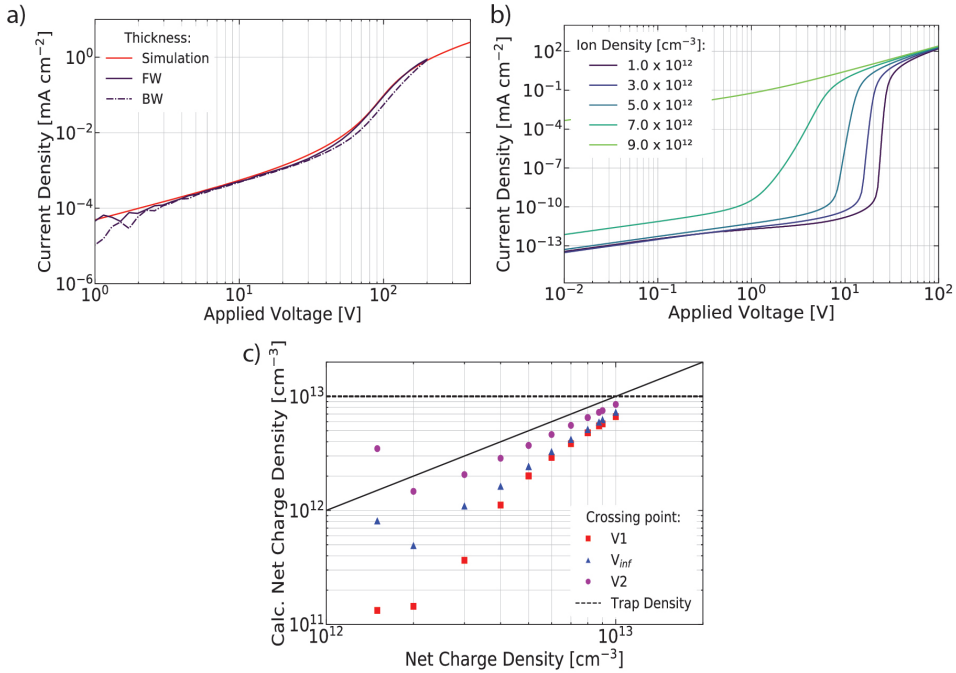
Figure 4.3: (a) Pulsed-SCLC measurement JV-curves with small hysteresis for a 160 $\mu$m thick MAPbBr$_3$ perovskite single crystal and the corresponding drift-diffusion fit. (b) Evolution of the pulsed SCLC JV-curves depending on the ion density for a fixed trap density at $1 \times 10^{13}$ cm$^{-3}$. The black solid line is a guide to the eye corresponding to the input net-charge, the dashed line corresponds to the input trap density. (c) Input vs calculated net-charge density using equation 4.4. The parameters used in the simulation can be found in table C.1 & C.2.

pared to the FW scan as in the experiment in figure 4.2 (a). This effect could be explained by the creation of an injection barrier next to the electrode when the applied bias is too strong. This barrier could originate from the degradation of the perovskite materials next to the electrode. Too many ions at the interface can result in the formation of a thin layer with a different bandgap. The simulation with a small injection ($\approx$0.2-0.3 eV) barrier in the layer next to the injecting electrode indeed shows a saturation of the current at high voltages, and therefore makes this a probable scenario to explain the shape of the hysteresis in the experimental JV curve. In addition, it has been shown in the literature that the reaction of the perovskite with the electrode or the ionic migration could create different phases like PbI$_2$ for example. [33] Unfortunately, such a degradation complicates the use of the BW scan to get a better estimate of the trap density.

To tackle the problem of hysteresis and fixing the position of the ions within the perovskite Duijnstee et al. proposed a pulsed SCLC method to obtain reliable JV-curves with suppressed the hysteresis. [32] This method consists of a short voltage pulse from 0 V to the wanted applied voltage and measuring the current before the ions have the time to move significantly. This method presents several advantages, on the one hand, it allows

the measurement of hysteresis free curves where the ions are effectively fixed to their position at 0 V and do not move throughout the JV-sweep and on the other hand, it avoids unwanted degradation and phase changes next to the electrodes that saturate the current at high voltages.

In the remainder of this chapter, we will discuss the pulsed-SCLC as this measurement is more reliable. [32] To simulate the pulsed-SCLC we first calculate the ion distribution at 0 V and then keep it fixed for the voltage sweep, making it equivalent to the infinitely fast scan described previously. Similar to the fast FW scan, the pulsed-SCLC and the steady-state scan give similar JV-curves, as shown in figure 4.2 (b). This similarity arises from the fact that the injected electron density and the filling of the traps are not as much affected by the movement ions, and especially cations. Figures C.1 & C.2 show that the cations mostly remain within the bulk of the perovskite and that the electron injection is not different for the 3 methods, which lead to completely filled traps at the same voltage. However, the situation is different for a fast BW scan prebiased at 200 V. Figure C.3 shows that in this case, the cations accumulate at the injecting electrode, which slows down the injection of electrons, and thereby the filling of the traps. Hence, $V_{tfl}$ shifts to higher voltages. Figure 4.3 (a) shows the measured pulsed-SCLC JV-curves for a 160 $\mu$m thick MAPbBr$_3$ single crystals. More details on the measurement can be found in Ref. 32. Figure C.4 shows the measurement performed on 3 different crystals with different thicknesses. The absence of hysteresis for all three crystals implies that the ions are indeed fixed around their 0 V positions. Additionally, there is no sign of degradation in the BW scan, which confirms the hypothesis that the accumulation of ions at high voltages creates a barrier for the injection that limits the current.

On top of the hysteresis, the ions significantly influence the actual shape of the JV-curve. We show in figure 4.3 (b) that as the ion density approaches the trap density, here at $1 \times 10^{13}$ cm$^{-3}$, the TFL regime disappears. In addition, $V1$, $V_{inf}$ and $V2$ are all affected by the ion density. This is due to the fact that ions are shielding the charge from the traps, and thereby reducing the net charge. If the ion and trap densities are within the same order of magnitude, equation 4.2 does not apply and needs to be rewritten in terms of net charges in the bulk such as:

$$V_{net} = \frac{q n_{net} L^2}{2\epsilon} = \frac{q(n_t - n_{ion})L^2}{2\epsilon} \tag{4.4}$$

Similarly, equation 4.3 can be expressed in terms of net charge in the bulk. Equivalently, this equation still holds when other types of charges, such as dopants, are added, as shown in figure C.5.

This is a crucial point for the interpretation of SCLC measurement for perovskites as it shows that we measure $V_{net}$ and the net charge in the bulk of the perovskite, rather than the $V_{tfl}$ and the trap density. This is well illustrated by figure 4.3 (c) where we show that as the ion density increases, i.e. the net charge decreases, the measured density deviates more from the actual trap density. This figure also shows that $V1$, which the most commonly used point for $V_{tfl}$ can not only be one order of magnitude off on predicting the net charge but also underestimates the trap density by almost 2 orders of magnitudes. Hence, previously reported trap density values from SCLC measurement showing a small slope for the TFL regime—probably indicating an ion density close to

the trap density—cannot be trusted.

Given the potential pitfalls of SCLC measurements when applying simplified equations such as the Mott-Gurney law or the expression for $V_{tfl}$, it appears more reasonable to fit drift-diffusion simulations to the measurement data. By doing so we can relax a few assumptions and obtain values for trap and ion densities as instead of the net charge when using equation 4.4. If necessary, the built-in voltage can also be accounted for by fitting both positive and negative voltage JVs, when different electrodes are used (which is not the case here). For this purpose, we use $SIMsalabim$, an open-source drift-diffusion simulation program, in the hope that it will enable researchers to fit their SCLC measurement to get more reliable values. More details about the simulation can be found in Refs. 31,34,35 and the code is available on GitHub. [36]

If we extract values from the 160 $\mu$m single-crystal JV-curve using the "classical" method—i.e. taking the $V_{tfl}$ as $V1$—from the FW scan in figure 4.2 (a) or even from the pulsed measurement in figure 4.3 (b) we get a trap density of $\approx 2 \times 10^{11}$ and $\approx 4.5 \times 10^{12}$ cm$^{-3}$ respectively. However, when the pulsed JV-curve is fitted using the drift-diffusion simulation, as shown in figure 4.3 (a) and table C.2, the simulation shows that trap- and ion densities are indeed very similar, approximately $1.3 \times 10^{13}$ and $1.1 \times 10^{13}$ cm$^{-3}$ respectively, giving a net charge in the bulk of $2 \times 10^{12}$ cm$^{-3}$. The trap density was underestimated by one to two orders of magnitude when using the "classical" method.

Even the values extracted by using the crossing points of the tangents from the pulsed measurement do not yield the correct values of neither the net-charge nor the trap density: $V1$, $V_{inf}$ and $V2$ give $4.5 \times 10^{12}$, $9.4 \times 10^{12}$ and $1.2 \times 10^{13}$ cm$^{-3}$, respectively. The TFL regime is not very pronounced so the net charge is overestimated, as in figure 4.3 (c) when $V_{net}$ is small. Clearly, under such conditions, fitting a drift-diffusion simulation becomes necessary to extract a value for the trap density. It also allows for an estimation of the mobility value, which would not have been accessible using the "classical" method and fitting Mott-Gurney law since the SCLC regime is not reached even at 200 V. Here, we find a mobility of approximately 13 cm$^2$ V$^{-1}$ s$^{-1}$.

## 4.4. CONCLUSIONS

We show that SCLC measurements have to be treated carefully when performed upon mixed ionic and electronic conductors, such as metal halide perovskites. We present some of the common pitfalls for SCLC analysis, and we show that to obtain a reasonable estimate of the $V_{tfl}$ and trap density, one needs to consider $V2$ rather than $V1$.

We then present a detailed analysis of the effect of mobile ions on the interpretation of SCLC measurement. Both simulation and experiments suggest that performing pulsed-SCLC measurement is necessary to minimize ion migration during the measurement. In this way, we obtain reliable and reproducible JV-curves and we avoid any degradation of the perovskite under large applied voltages. We show that even though we can extract the net charge in the perovskite bulk from the SCLC measurement, we can not directly extract trap density. This puts into question previous reports in the literature that may have underestimated the trap density by several orders of magnitude.

Finally, we show how we can accurately reproduce pulsed-SCLC experiments using drift-

diffusion modeling which enables us to quantify not only the net charge but also the mobility, trap- and ion densities. We propose a wider use of drift-diffusion simulations to fit pulsed-SCLC to extract meaningful values for the trap- and ion densities, and mobility in the case of perovskites and we provide an open-source solution to fit these measurements. We strongly encourage others to follow this approach and no longer perform analytical fits to JV data.

## References

[1] J. C. Blakesley, F. A. Castro, W. Kylberg, G. F. Dibb, C. Arantes, R. Valaski, M. Cremona, J. S. Kim, and J. S. Kim, *Towards reliable charge-mobility benchmark measurements for organic semiconductors,* Organic Electronics **15**, 1263 (2014).

[2] G. Zuo, M. Linares, T. Upreti, and M. Kemerink, *General rule for the energy of water-induced traps in organic semiconductors,* Nature Materials **18**, 588 (2019).

[3] V. M. V. V. M. Le Corre, A. A. R. Chatri, N. Y. N. Doumon, and L. J. A. Koster, *Charge Carrier Extraction in Organic Solar Cells Governed by Steady-State Mobilities,* Advanced Energy Materials **7**, 1701138 (2017).

[4] D. Shi, V. Adinolfi, R. Comin, M. Yuan, E. Alarousu, A. Buin, Y. Chen, S. Hoogland, A. Rothenberger, K. Katsiev, Y. Losovyj, X. Zhang, P. A. Dowben, O. F. Mohammed, E. H. Sargent, and O. M. Bakr, *Low trap-state density and long carrier diffusion in organolead trihalide perovskite single crystals,* Science **347**, 519 (2015).

[5] M. I. Saidaminov, A. L. Abdelhady, B. Murali, E. Alarousu, V. M. Burlakov, W. Peng, I. Dursun, L. Wang, Y. He, G. Maculan, A. Goriely, T. Wu, O. F. Mohammed, and O. M. Bakr, *High-quality bulk hybrid perovskite single crystals within minutes by inverse temperature crystallization,* Nature Communications **6**, 7586 (2015).

[6] Y. Liu, J. Sun, Z. Yang, D. Yang, X. Ren, H. Xu, Z. Yang, and S. F. Liu, *20-mm-Large Single-Crystalline Formamidinium-Perovskite Wafer for Mass Production of Integrated Photodetectors,* Advanced Optical Materials **4**, 1829 (2016).

[7] A. A. Zhumekenov, M. I. Saidaminov, M. A. Haque, E. Alarousu, S. P. Sarmah, B. Murali, I. Dursun, X.-H. Miao, A. L. Abdelhady, T. Wu, O. F. Mohammed, and O. M. Bakr, *Formamidinium Lead Halide Perovskite Crystals with Unprecedented Long Carrier Dynamics and Diffusion Length,* ACS Energy Letters **1**, 23 (2016).

[8] Q. Han, S.-H. Bae, P. Sun, Y.-T. Hsieh, Y. M. Yang, Y. S. Rim, H. Zhao, Q. Chen, W. Shi, G. Li, and Y. Yang, *Single Crystal Formamidinium Lead Iodide (FAPbI$_3$): Insight into the Structural, Optical, and Electrical Properties,* Advanced Materials **28**, 2253 (2016).

[9] F. Zhang, B. Yang, X. Mao, R. Yang, L. Jiang, Y. Li, J. Xiong, Y. Yang, R. He, W. Deng, and K. Han, *Perovskite CH$_3$NH$_3$PbI$_{3-x}$Br$_x$ Single Crystals with Charge-Carrier Lifetimes Exceeding 260 μs,* ACS Applied Materials & Interfaces **9**, 14827 (2017).

[10] B. Murali, E. Yengel, C. Yang, W. Peng, E. Alarousu, O. M. Bakr, and O. F. Mohammed, *The Surface of Hybrid Perovskite Crystals: A Boon or Bane,* ACS Energy Letters **2**, 846 (2017).

[11] Z. Gu, Z. Huang, C. Li, M. Li, and Y. Song, *A general printing approach for scalable growth of perovskite single-crystal films,* Science Advances **4**, 2390 (2018).

[12] D. Ju, Y. Dang, Z. Zhu, H. Liu, C. C. Chueh, X. Li, L. Wang, X. Hu, A. K. Jen, and X. Tao, *Tunable Band Gap and Long Carrier Recombination Lifetime of Stable Mixed $CH_3NH_3Pb_xSn_{1-x}Br_3$ Single Crystals,* Chemistry of Materials **30**, 1556 (2018).

[13] Z. Chen, Q. Dong, Y. Liu, C. Bao, Y. Fang, Y. Lin, S. Tang, Q. Wang, X. Xiao, Y. Bai, Y. Deng, and J. Huang, *Thin single crystal perovskite solar cells to harvest below-bandgap light absorption,* Nature Communications **8**, 1 (2017).

[14] L. M. Herz, *Charge-Carrier Mobilities in Metal Halide Perovskites: Fundamental Mechanisms and Limits,* ACS Energy Letters **2**, 1539 (2017).

[15] J. Peng, Y. Chen, K. Zheng, T. Pullerits, and Z. Liang, *Insights into charge carrier dynamics in organo-metal halide perovskites: From neat films to solar cells,* Chemical Society Reviews **46**, 5714 (2017).

[16] J. A. Röhr, *Direct Determination of Built-in Voltages in Asymmetric Single-Carrier Devices,* Physical Review Applied **11**, 054079 (2019).

[17] M. A. Lampert and P. Mark, *Current injection in solids ,* ((Academic Press, New York, 1970)).

[18] T. Kirchartz, *Influence of diffusion on space-charge-limited current measurements in organic semiconductors,* Beilstein Journal of Nanotechnology **4**, 180 (2013).

[19] G. A. H. Wetzelaer and P. W. M. Blom, *Ohmic current in organic metal-insulator-metal diodes revisited,* Physical Review B **89**, 241201 (2014).

[20] J. A. Röhr, T. Kirchartz, and J. Nelson, *On the correct interpretation of the low voltage regime in intrinsic single-carrier devices,* Journal of Physics Condensed Matter **29**, 205901 (2017).

[21] N. F. Mott and R. W. Gurney, *Electronic Processes in Ionic Crystals,* ((Oxford University Press, 1940)).

[22] J. A. Röhr, D. Moia, S. A. Haque, T. Kirchartz, and J. Nelson, *Exploring the validity and limitations of the Mott-Gurney law for charge-carrier mobility determination of semiconducting thin-films,* Journal of Physics Condensed Matter **30**, 105901 (2018).

[23] P. Mark and W. Helfrich, *Space-charge-limited currents in organic crystals,* Journal of Applied Physics **33**, 205 (1962).

[24] J. Fischer, W. Tress, H. Kleemann, J. Widmer, K. Leo, and M. Riede, *Exploiting diffusion currents at Ohmic contacts for trap characterization in organic semiconductors,* Organic Electronics **15**, 2428 (2014).

**4**

[25] J. A. Röhr, X. Shi, S. A. Haque, T. Kirchartz, and J. Nelson, *Charge Transport in Spiro-OMeTAD Investigated through Space-Charge-Limited Current Measurements,* Physical Review Applied **9**, 044017 (2018).

[26] Y.-X. Chen, Q.-Q. Ge, Y. Shi, J. Liu, D.-J. Xue, J.-Y. Ma, J. Ding, H.-J. Yan, J.-S. Hu, and L.-J. Wan, *General Space-Confined On-Substrate Fabrication of Thickness-Adjustable Hybrid Perovskite Single-Crystalline Thin Films,* Journal of the American Chemical Society **138**, 16196 (2016).

[27] F. Cai, L. Yang, Y. Yan, J. Zhang, F. Qin, D. Liu, Y.-B. Cheng, Y. Zhou, and T. Wang, *Eliminated hysteresis and stabilized power output over 20% in planar heterojunction perovskite solar cells by compositional and surface modifications to the low-temperature-processed TiO$_2$ layer,* Journal of Materials Chemistry A **5**, 9402 (2017).

[28] H. J. Snaith, A. Abate, J. M. Ball, G. E. Eperon, T. Leijtens, N. K. Noel, S. D. Stranks, J. T. W. Wang, K. Wojciechowski, and W. Zhang, *Anomalous hysteresis in perovskite solar cells,* Journal of Physical Chemistry Letters **5**, 1511 (2014).

[29] S. A. Weber, I. M. Hermes, S. H. Turren-Cruz, C. Gort, V. W. Bergmann, L. Gilson, A. Hagfeldt, M. Graetzel, W. Tress, and R. Berger, *How the formation of interfacial charge causes hysteresis in perovskite solar cells,* Energy and Environmental Science **11**, 2404 (2018).

[30] S. Van Reenen, M. Kemerink, and H. J. Snaith, *Modeling Anomalous Hysteresis in Perovskite Solar Cells,* Journal of Physical Chemistry Letters **6**, 3808 (2015).

[31] T. S. Sherkar, C. Momblona, L. Gil-Escrig, J. Ávila, M. Sessolo, H. J. Bolink, and L. J. A. Koster, *Recombination in Perovskite Solar Cells: Significance of Grain Boundaries, Interface Traps, and Defect Ions,* ACS Energy Letters **2**, 1214 (2017).

[32] E. A. Duijnstee, J. M. Ball, V. M. Le Corre, L. J. A. Koster, H. J. Snaith, and J. Lim, *Toward Understanding Space-Charge Limited Current Measurements on Metal Halide Perovskites,* ACS Energy Letters , 376 (2020).

[33] R. A. Kerner, P. Schulz, J. A. Christians, S. P. Dunfield, B. Dou, L. Zhao, G. Teeter, J. J. Berry, and B. P. Rand, *Reactions at noble metal contacts with methylammonium lead triiodide perovskites: Role of underpotential deposition and electrochemistry,* **7**, 41103 (2019).

[34] L. J. A. Koster, E. C. P. Smits, V. D. Mihailetchi, and P. W. M. Blom, *Device model for the operation of polymer/fullerene bulk heterojunction solar cells,* Physical Review B **72**, 85205 (2005).

[35] T. S. Sherkar, C. Momblona, L. Gil-Escrig, H. J. Bolink, and L. J. A. Koster, *Improving Perovskite Solar Cells: Insights From a Validated Device Model,* Advanced Energy Materials **7**, 1602432 (2017).

[36] T. S. Sherkar, V. M. Le Corre, M. Koopmans, F. Wobben, and L. J. A. Koster, *SIMsalabim GitHub repository,* (2020).

# 5

# Charge Transport Layers Limiting the Efficiency of Perovskite Solar Cells: How To Optimize Conductivity, Doping, and Thickness

*Perovskite solar cells (PSCs) are one of the main research topics of the photovoltaic community; with efficiencies now reaching up to 25% PSCs are on the way of catching up with classical inorganic solar cells. However, PSCs have not yet reached their full potential. In fact, their efficiency is still limited by non-radiative recombination, mainly via trap-states and by losses due to the poor transport properties of the commonly used transport layers (TLs). Indeed, state-of-the-art TLs (especially if organic) suffer from rather low mobilities, typically within $10^{-5} - 10^{-2}$ cm$^2$ V$^{-1}$ s$^{-1}$, when compared to the high mobilities, $1 - 10$ cm$^2$ V$^{-1}$ s$^{-1}$, measured for perovskites. This work presents a comprehensive analysis of the effect of the mobility, thickness and doping density of the transport layers based on combined experimental and modeling results of two sets of devices made of a solution processed high performing triple-cation (PCE≈ 20% ). The results are also crossed checked on vacuum processed MAPbI$_3$ devices. From this analysis, general guidelines on how to optimize a TL are introduced and especially a new and simple formula to easily calculate the amount of doping necessary to counterbalance the low mobility of the TLs.*

## 5.1. Introduction

Perovskite solar cells (PSCs) have attracted more and more attention in the pho-
tovoltaic research community. The number of published articles on PSCs keeps
increasing whereas the yearly number of publications even tripled between 2015 and
2017. Following the trend of the number of published papers the efficiency of perovskite
solar cells also skyrocketed within less than 10 years from 3.8%[1] to nearly 25.2%.[2]
The first jump in efficiency was linked to the establishment of solid-state perovskite
solar cells,[3,4] as opposed to the dye-sensitized structure previously used.[1] From this
point, the incredibly fast development of PSCs is due to optimization efforts on several
levels: (1) the deposition techniques highly improved leading to better film quality,
i.e. less rough, more compact with bigger grains.[5–7] (2) The chemical engineering
of the perovskite by using mixed-compound (cations, metal and/or halide) allowing
bandgap tunability and improving the stability.[8–11] (3) The optimization of the solar
cell stack by choosing more suitable charge selective transport layers (TL).[11–23]
As the perovskite layer quality improved the focus shifted to the optimization of the TLs.
Classical PSCs consist of a simple *n-i-p* or *p-i-n* structure, where the perovskite layer is
stacked between two TLs and electrodes. In principle, an efficient TL must fulfill several
aspects which include: (a) Favorable energy level alignment, for a good transfer of one
type of charge carrier while effectively blocking the other.[24–26] (b) Good chemical and
physical properties, to avoid detrimental reactions with the surrounding layers and the
environment, and also suitable surface properties[27] as this two points could otherwise
result in either a significant amount of traps at the interface and/or a poor perovskite
layer quality (rough or too many grain boundaries) when grown on top of the TL.[28] (c)
High transparency of the TLs to maximize the absorption in the perovskite layer[28] and
finally (d) Good transport properties to ensure a fast transport of the charge carriers
towards the extracting electrode.[28,29]
This study will focus on the last point (d) as most of the state-of-the-art TLs suffer
from a rather low mobility compared to the perovskite. Theoretical calculations on
perovskite structure give mobilities values ranging from several hundred to thousands
$cm^2$ $V^{-1}$ $s^{-1}$.[30] However, usual electrical techniques, such as field-effect transistors
measurement or space-charge-limited-current, report mobilities which are orders of
magnitudes lower on the range of 1 to several tens of $cm^2$ $V^{-1}$ $s^{-1}$.[15,17,30,31] In any
case the perovskite mobility is higher than that of most TLs and can therefore limit the
efficiency.
The aim of this chapter is to introduce easy-to-use guidelines for the optimization of
the TLs in terms of thickness, mobility and doping. In fact, one of the most common
strategies to tackle the problem of the TLs low mobilities is to use chemical doping.
While it had been experimentally shown[12,13,16,19,28] that doping the TLs is an efficient
way of improving the performance of PSCs, there are still remaining questions about
the efficacy of this strategy. For instance, what is the best approach to improve the TL:
increasing the TL mobility, reducing the thickness or doping? Moreover, the general
conditions to sufficiently dope a TL in order to achieve maximum photovoltaic perfor-
mance depending on the layer thickness and mobility remains an important question
today.

To this end, the role of TL mobility, thickness and doping have been examined through extensive drift-diffusion (DD) simulations that are based on a validated device model.[32] The simulation results are corroborated by transient extraction experiments which were conducted on two device structures consisting of the same highly efficient triple-cation perovskite layer but with different TL and device polarity (n-i-p and p-i-n). Notably, the current-voltage characteristics of our p-i-n devices could be well reproduced with the numerical simulations. Both simulations and experiments show that doping clearly improves the efficiency of PSCs but also that increasing the mobility of the TL is a more efficient approach to maximize the collection efficiency with the additional benefit of avoiding a potential additional degradation pathway due to the chemical dopant. Finally, we introduce a figure of merit solely based on the conductivity and thickness of the TLs so transport losses can be minimized.

---

Chapter key findings:

- The charge transport layers in perovskite solar cells need to be optimized carefully as they can strongly limit the fill factor.

- Two new and simple criteria are introduced to help tuning the transport layer thickness and/or conductivity to avoid transport losses in the TL.

---

**5**

## 5.2. New figures of merit for the optimization of the transport layers

Typical TL used in PSCs such as 2,2',7,7'tetrakis[N,N-di(4-methoxyphenyl)amino]9,9'-spirobifluorene (spiro-OMeTAD), poly(3hexylthiophene-2,5-diyl) (P3HT), poly [bis(4phenyl)(2,4,6-trimethylphenyl)amine] (PTAA), [6,6]-Phenyl-C71-butyric acid methyl ester (PCBM), to name just a few, have mobilities which are generally more than 3 orders of magnitude lower than the perovskite and are usually 10 to over 150 nm thick.[15,33,34] The mobility and thickness of the TL strongly impact the charge transport/extraction in PSCs and ends up drastically reducing the fill-factor (FF).[15,28] In this study, two sets of devices were investigated both based on the same active layer made of a highly efficient triple-cation perovskite[26,29] in p-i-n or n-i-p layout, as shown in figure 5.1.a & d. Both devices consist of a $C_{60}$ layer as electron transport layer (ETL). For the p-i-n structure the hole transport layer (HTL) thickness, made of PTAA, was varied and/or also doped using a small molecule (2,3,5,6-tetrafluoro-2,5cyclohexadiene-1,4-diylidene)dimalononitrile (F4TCNQ). Similarly, the HTL thickness of the n-i-p devices made of P3HT was also varied and doped using F4TCNQ. The 10 nm thick PTAA device demonstrated the highest performance reaching 20% . The current-density versus voltage (JV) curves (figure 5.1.b & e) show that the open-circuit voltage ($V_{OC}$) and the short-circuit current ($J_{SC}$) are not affected by the change in thickness or by the doping of the TL, the small loss in $J_{SC}$ is due to optical losses. However, the FF is strongly affected by both thickness and doping of the TL, the FF linearly decreases with the increase of the TL thickness and increase upon doping, see figure 5.1.

To gain some insight in the effect of TL properties on the FF a home-built device model
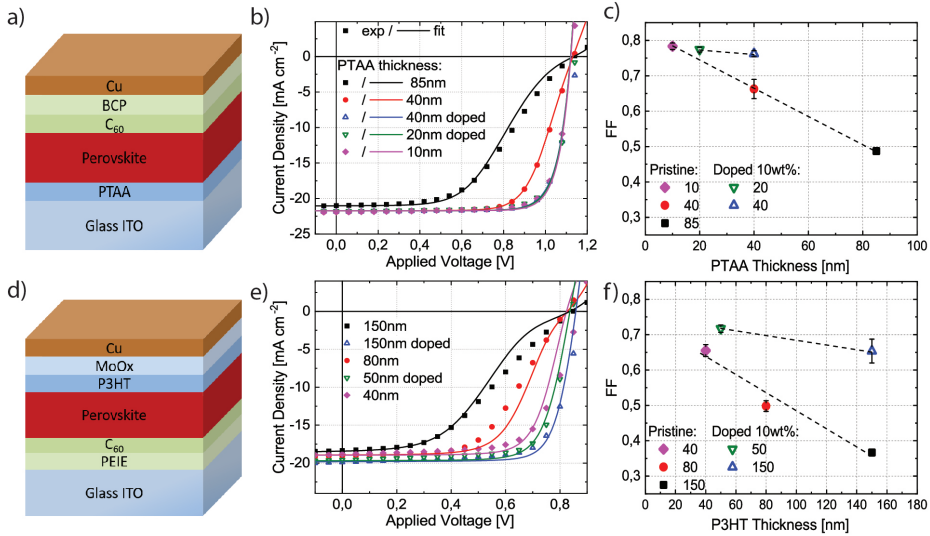


Figure 5.1: Schematic of the device structures investigated (a)& (d). Current-density versus voltage characteristics of the solar cells (b)& (e) for different HTL thickness and doping, the dots correspond to the experiment and the line to the numerical fit, the fitting parameters can be found in appendix D. The FF (c)& (f) of the two devices linearly depends on the HTL thickness but is also strongly enhanced by doping, filled dots corresponds to pristine TL whereas empty dots stand for a F4TCNQ 10wt% doped TL.

based on 1-dimensional DD equations is used.[32,35,36] Employing steady-state DD simulations permits the calculation of current-voltage characteristics, by solving the Poisson and continuity equations, see chapter 2. The simulations allow to disentangle the influence of a single parameter from others—which is difficult to realize in the experiment—and gives us a better understanding of the effect of a certain parameter on the solar cell performance. Our device model has already been validated[32,35] and reproduces accurately PSCs with different composition and structure. The accuracy of the device model is demonstrated here once again as it perfectly reproduces the behavior of the PTAA devices as seen in figure 5.1.b. The DD fit also shows that trap-assisted recombination at the interface between the perovskite and the TLs is the dominant recombination loss (see table S2). This is in agreement with previous reports on the losses in PSCs with various device architectures, processing methods, and perovskite compositions.[26,32,35,37] It thus appears that the dominance of interfacial recombination is a general rule in highly efficient PSCs stressing the importance of improved TLs. The simulation results in figure 5.2.a are obtained by varying only the mobility and/or the thickness of a pristine (i.e. not doped) TL. The linear dependence of the FF with the TL thickness is observed, see figure D.1.a, which goes hand in hand with the experimental results. Figure 5.1.a shows that for mobilities on the order of $10^{-4}$ to $10^{-3}$ cm$^2$ V$^{-1}$ s$^{-1}$ and thickness of 10-150 nm—which are typical for most TL and especially the organic ones—only $\approx$ 50-75% of the FF is retained, meaning that about 25-50%

of the FF is lost just because of the poor transport in the TLs. Note that the retained FF in figure 5.2 stands for the ratio between the actual FF and the maximum FF for high mobility TL. This effect, of course, gets less critical, when very thin TLs are used, however, experimentally the use of such thin layer ($< 10 - 20$ nm) is challenging and can result in less efficient or stable devices because of the formation of pinhole or bad surface properties. To summarize, reducing the mobility and increasing the thickness of the TL is highly detrimental to the FF. Grill et al. [15] also showed that the transit time ($t_{tr}$) of PSC is strongly affected by the $t_{tr}$ of the TL whereas ideally, the $t_{tr}$ should only depend on the active material. As a first estimate, the charge transport quality of a pristine TL (i.e. not doped) can be defined as the ratio between the transit time in the TL over the perovskite. The transit time can be written as:

$$t_{tr} = \frac{l}{\mu \times F},$$ 
(5.1)

with $l$ the thickness, $\mu$ the mobility and $F$ the electrical field, the electrical field can also be approximated to $V/l$ with $V$ being the voltage drop. The simulation shows that the FF loss is acceptable when:

$$\frac{t_{tr}^{TL}}{t_{tr}^{pero}} \propto \frac{l_{TL}^2 \times \mu_{pero}}{L_{pero}^2 \times \mu_{TL}} \lesssim 1,$$ 
(5.2)

as shown in figure 5.2.a. Indeed, when equation 5.2 is satisfied the transport losses due to the TL become negligible. A wide range of simulations with randomly picked parameters within a reasonable range describing the PSCs behavior, see SI, also shows that when equation 5.2 holds the FF is not affected by the TL. However, when equation 5.2 is not satisfied the FF is reduced.

If we consider a TL of 40 nm and a perovskite layer 300nm with a mobility of 1 cm$^2$ V$^{-1}$ s$^{-1}$, which is typical for PSCs, the required TL mobility to avoid FF losses is 0.01 cm$^2$ V$^{-1}$ s$^{-1}$, which is the same number than found by Tessler and Vaynzof in Ref. 38.

Consequently, the use of high mobility and/or very thin TLs seems to be required to guarantee high efficiency. Equation 5.2 also gives us a good criterion to optimize the TL thickness and gives a threshold to judge whether doping the TL is required.

 As mentioned above, one other way to tackle the issue of the TL low mobility is to use of doped TLs which help to maintain high performance. In fact, chemical doping of organic TLs [12,16,39] and atomic doping of oxides [19,40] has proven to be a successful strategy to counterbalance the poor transport properties of many TLs. While knowing that doping is, in general, a good strategy to improve the efficiency, the question of how much the TL needs to be doped to reach the best performance still remains. One of the main resulting effects of doping the TL is to increase its conductivity. Note that increasing the mobility as discussed previously also increases the conductivity. Ohm's law can be rewritten in term of conductivity such as the voltage drop within the TL can be quantified as:

$$V = R \times I = \frac{l \times J}{\sigma},$$ 
(5.3)

with $V$ the voltage drop, R the resistance, $I$ ($J$) the current (density), $l$ the thickness and $\sigma$ the conductivity. We assume that the TLs will have a negligible influence if the voltage
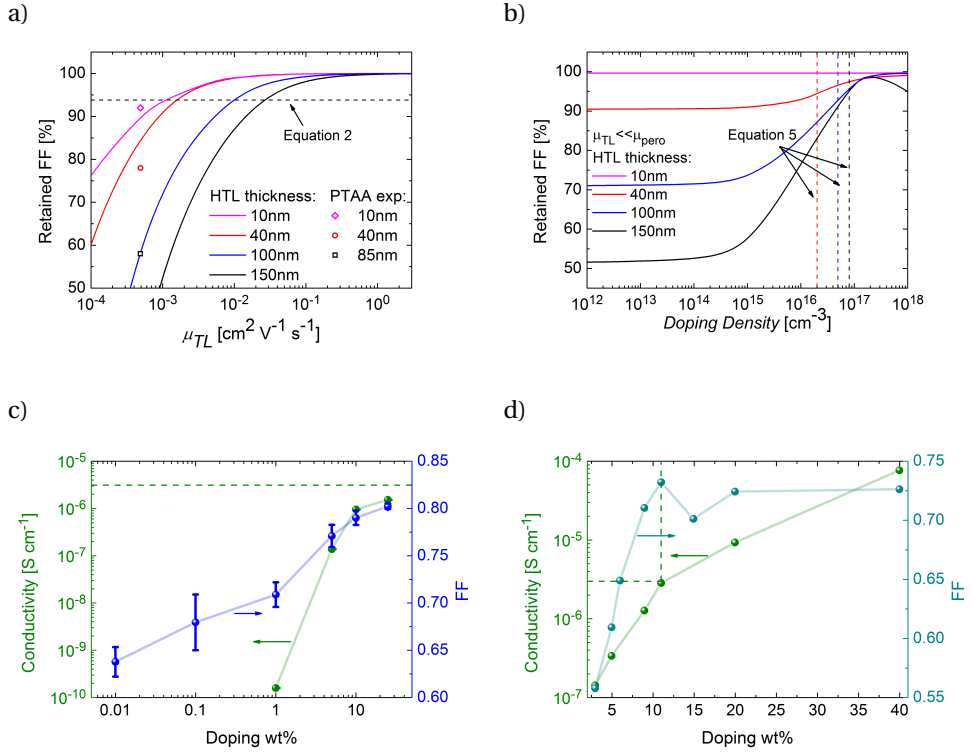
Figure 5.2: Simulations (a) show that reducing the mobility of the TLs drastically reduces the FF, however, simulations (b) and the experimental results on our PTAA devices (c) and devices from the literature (d, taken from Ref. 12) also show that this effect can be almost balanced by significant TL doping. The retained FF stands for the ratio between the considered FF over the FF when using a pristine high mobility TL. The dashed line in (a) is a guide to the eye to judge which points satisfy equation 5.2. The dashed lines in (b) correspond to the values calculated with equation 5.5. The simulations parameters can be found in the simulation section in appendix D.

drop across a TL is equal or less than the thermal voltage $V_T$, which is a reasonable assumption as carriers ought to be able to overcome a potential drop equivalent to $kT$ in energy. Below this assumption is confirmed by both simulations and experiments. The largest current that a solar cell supplies is equal to the short-circuit current density $J_{SC}$, so we require that:

$$\sigma = q\mu_{TL}N_D \geq \frac{l_{TL} \times J_{SC}}{V_T}. \tag{5.4}$$

Equation 5.4 gives us a new and easily accessible criterion on the required conductivity for an efficient TL, it also makes it easier to select and optimize a TL even before making the PSCs full stack. For example, if we consider a 40 nm thick TL and a $J_{SC}$ of 20 mA cm$^{-2}$, which are typical for perovskite solar cells, then we need a TL conductivity of at least $3 \times 10^{-6}$ S cm$^{-1}$.

Equation 5.4 can also be rewritten in term of doping density such as:

$$N_D = \frac{l_{TL} \times J_{SC}}{qV_T\mu_{TL}}.$$

(5.5)

Following this idea, the simulations were performed again including some doping of the TL to determine if the efficiency can be fully recovered and how much the TL needs to be doped. Two cases were studied with one thin (40 nm) and one thick HTL (150 nm)—similar results would be obtained if the ETL was studied—and the doping density within the TL was increased until the best performance is reached. In both cases, more than 95% of the FF is retained when using equation 5.5 and is very close to the maximum FF that can be reached by doping, see figure 5.2. In addition, a large-scale simulation of perovskite solar cells, see figure D.1.c, more than 10000 different solar cells were simulated to evaluate the accuracy of equation 5.4-5.5. In this simulation, the different relevant parameters of a PSCs were varied such as device thickness, mobilities and trapping densities, see table S2. Note that, to disentangle the effect of doping one TL only one of the two TL was set as "defective" in the simulations (i.e. with a low mobility) whereas, the other one was considered as "perfect" (i.e. with high mobility) and only the defective TL was then doped. In this simulation both the hole and electron TLs were alternatively considered as the defective one showing that this approach is relevant for both electron and hole TLs. In more than 90% of cases doping the TL helps to recover the FF loss due to the low TL mobility, therefore, equation 5.4–5.5 indeed gives an accurate description of the optimal doping.

The effect of doping the TL was studied in the case of the PTAA devices, where the concentration of the F4TCNQ dopant in a 40 nm thick PTAA layer was varied between 0.01 to 25wt%, see figure 5.2.c. The conductivity of the doped PTAA was also measured for the different doping concentration, however, it is important to note that the conductivity of the TL within the solar cell stack matters in equation 5.4, and therefore one has to be careful on how to measure this experimentally. In fact, as the perovskite layer is spin cast on top of the PTAA layer the solvent (DMF:DMSO) might wash some of the F4TCNQ-anions or PTAA away hence reducing the conductivity or thickness. To mimic this " washing-effect" the conductivities were measured as-cast and after spin coating a solution of DMF:DMSO following the same procedure as if it was the perovskite solution. On the one hand, the layer thickness was measured for both as-cast and washed films to see if there was PTAA washing as well, but the effect was negligible indicating that the PTAA is not washed away. On the other hand, a drop in conductivity by more than two orders of magnitude for washed films is measured, see D.2, which makes it evident that F4TCNQ-anions are not present in the films at the initial desired concentration, lowering the doping efficiency and inevitably the free charge carrier density.

The measured conductivity after washing is reported in figure 5.2.c. The increase of the conductivity correlates very well with the increase in FF in a similar fashion than what is seen in the simulation. Unfortunately, the conductivity does not reach the required value from equation 5.4 of $3 \times 10^{-6}$ S cm$^{-1}$ (green dotted line in figure 5.2 (c)) which is coherent with the fact that the maximum FF does not seem to be achieved yet in this device. Above 10wt% further increasing the dopant concentration only slightly increases the conductivity and, therefore, only a modest increase in the FF is observed, this is due

to a bad mixing of the dopant with the PTAA which degrades the morphology. In the future, replacing F4TCNQ by another dopant or changing the solvent would be a good strategy to reach higher doping efficiencies and $FFs$.

The P3HT cells were also doped with F4TCNQ 10wt% and show a significant improvement of the FF upon doping especially the 150 nm thick devices that show an improvement of 175% and helps to reach FF similar to much thinner P3HT thickness devices, see figure 5.1.e& f. However, for those devices, the limitation in $V_{OC}$ probably due to strong interfacial recombination seems to be limiting the performance more than the transport losses within the TL. [41]

A similar analysis was applied to fully vacuum deposited devices based on methylammonium lead iodide (MAPbI$_3$) stacked between a N1,N4-bis(tri-p-tolylphosphoranylidene) benzene-1,4-diamine (PhIm) doped fullerene C$_{60}$ ETL and a 2,2'-(perfluoronaphthalene 2,6- diylidene) dimalononitrile (F6-TCNNQ) doped N4,N4,N4'' ,N4'' -tetra([1,1'-biphenyl]4-yl)-[1,1':4',1'' -terphenyl]-4,4'' -diamine (TaTm) HTL, see Ref. 12 for full devices structure. Ref. 12 concluded that the ETL was not limiting the FF which is coherent with equation 5.4 giving $3 \times 10^{-6}$ S cm$^{-1}$ (for a 40 nm TL) which is lower than the measured conductivity of the ETL above $2 \times 10^{-4}$S cm$^{-1}$, showing again that equation 5.4 can also be applied for ETL. The HTL, however, has a rather low conductivity $\approx 1 \times 10^{-7}$ S cm$^{-1}$ and needs to be significantly doped to recover a high performance. The maximum efficiency, see figure 5.2.d, is reached for a 11wt% F6-TCNNQ doping and a conductivity of $3 \times 10^{-6}$ S cm$^{-1}$ which coincides perfectly with the value expected from equation 5.4. As the layers were all vacuum process there is no need to consider any washing effect. At higher doping concentration, even though the conductivity still significantly increases, the FF is not so much affected just as shown by the simulation meaning that the TL is now fully optimized in terms of transport and that the conductivity criterion presented here is accurate. However, the FF is still not ideal but this can probably be explained by significant the amount of recombination which tends to limit the FF in this system as shown in Ref. 35..

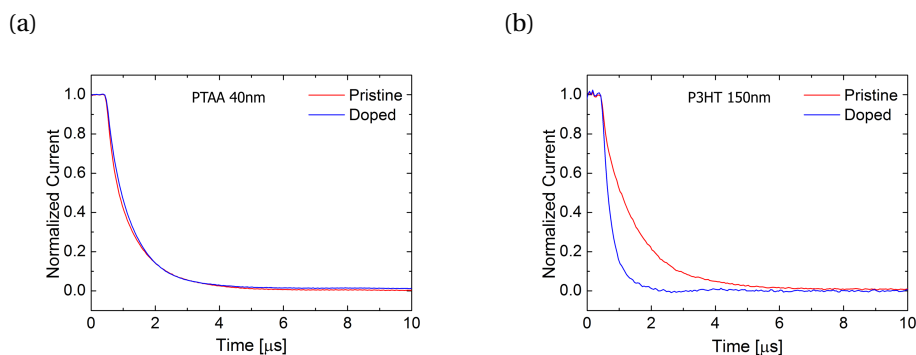(a)                                                    (b)



Figure 5.3: In the photocurrent decay experiment, the extraction is not really affected by the doping for a thin 40 nm PTAA HTL (a). However, for a thicker TL—here 150 nm thick P3HT HTL (c)—the extraction is enhanced upon TL doping leading to a faster decay of the current density. The experiment is shown at short-circuit conditions.

## 5.3. EFFECT OF THE TRANSPORT LAYERS ON TRANSIENT PHOTOCURRENT EXTRACTION MEASUREMENTS

An increase in FF can be related to two processes: a more efficient extraction or a reduced number of recombination pathways. [42] To further understand the effect of TL thickness and doping on the extraction dynamics of PSCs, a photocurrent decay experiment, similar to the one described in Ref. 43, was set up. The device is kept under 1 sun illumination, using white light, to establish steady state operating conditions. At time zero the light intensity is slightly reduced and the current decay is monitored over time giving the extraction rate by fitting a monoexponential decay. [43] The higher the decay rate $k$, i.e. shorter lifetime, the better the extraction. This experiment can be done at different applied voltage that is kept constant during the light reduction. The behavior of two devices was studied, one PTAA cell with a thin HTL of 40 nm and one P3HT cell with a thick HTL of 150 nm. The HTL of the two devices were then doped with 10wt% F4TCNQ. In the case of a thin 40 nm PTAA TL, see figure 5.3.a, the experiment shows that the extraction is not significantly affected by the doping of the TL. However, the experiment on a thick 150 nm P3HT device (b) show that doping plays a major role in the extraction. The decay of the current being much faster for a doped TL than for its pristine counterpart, see figure 5.3.b. Transient simulations were also performed (see figure D.3) for both thin and thick TL, with a TL mobility of $10^{-3}$ cm$^2$ V$^{-1}$ s$^{-1}$, they also show that doping has little effect on the extraction time for thin TL but leads to a significant improvement of the extraction of thick TLs. In addition, the simulations using high mobility TL show that it always leads to the fastest extraction which is coherent with the higher FF reported in figure 5.2 when using higher mobility TL.

 While it is straightforward that the extraction gets more efficient when the TL mobility
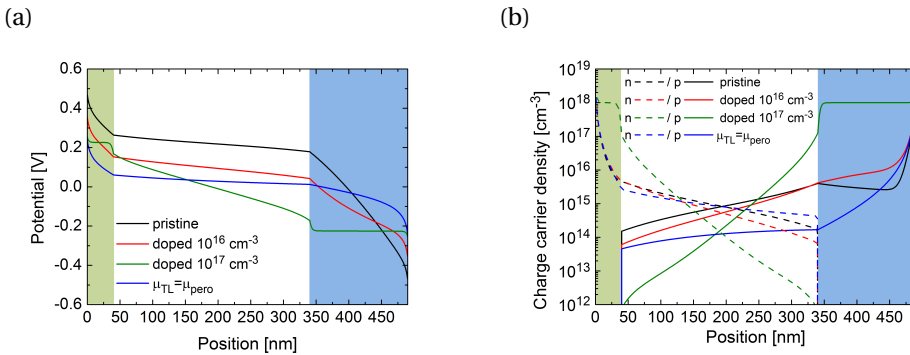
(a)                         (b)



Figure 5.4: Figure (a) shows the beneficial influence of TL doping that reduces the potential drop within the TL. Figure (b) shows that upon doping there is less accumulation of charge carriers in the perovskite and more in the TL. Therefore, the extraction is enhanced when doping a low mobility TL because there are more charge carriers that can get extracted next to the electrode which counterbalances the fact that they are slower. This explains why upon sufficient doping the extraction gets almost as good as when using high mobility TL. The potential and charge carrier density profiles are here shown at MPP. The simulations parameters can be found in appendix D.

is increased, charge carriers just move faster, it is not so clear how doping helps in case of low mobility. The simulations in figure 5.4.a & b highlight the two concomitant benefits of doping a low mobility TL: on the one hand it decreases the potential drop in the TL—as referred to in the derivation of equation 5.4 & 5.5—which results in a bigger potential drop within the perovskite layer and so to a higher electrical field, corresponding energy diagrams are available in appendix figure D.4. Note, that the data in figure 5.4 correspond to the maximum power point values (MPP) as this is the meaningful operating point for a solar cells, this explain the fact that the overall potential drop varies from one simulation to the next as $V_{MPP}$ is different. On the other hand, the charge carrier density within the perovskite is greatly reduced while the concentration in the TL increases tremendously. These two synergic effects explain why the current decays faster in the transient photocurrent experiment when a low mobility TL is doped. Under steady-state illumination, most charge carriers are close to their extracting electrode, see figure 5.4.b, so when the light is slightly reduced the carriers that were already there do not have to travel far to be extracted.

Another side effect of doping is that the lower carrier concentration within the perovskite also reduces the total amount of recombination, see figure D.5, for both thin and thick TL. It could explain why for a thin TL even though the extraction is not so much affected the FF still increases by 10% for the 40 nm PTAA device, see figure 5.1.c. For the 150 nm P3HT device the FF show a huge increase of 175% because it benefits from the two effects, enhanced extraction and lower recombination. It is worth noting that the thick pristine P3HT TL devices, see figure D.6, show a very strong voltage dependence of the extraction rate and also of the ratio of initial and final currents, see figure D.6.d, which is a sign of a substantial effect of recombination. The decay rate of the doped system tends to be way less affected by the applied voltage, hence, is less dominated by recombination which goes hand to end with the previous conclusion.

Finally, all the above-mentioned points demonstrate that the approach presented earlier of reducing the voltage drop within the TL is indeed crucial and that the criterion presented here is a key parameter to achieve high efficiency.

So far we only talked about organic TLs, however, all the reasoning described above is applicable for inorganic TLs, however, in most cases the inorganic TLs such as $TiO_2$ [40,44–46] or $SnO_2$ [47] have conductivities close to our criterion or above hence leading to only modest improvement of the FF. The main reason for the performance improvement in those cases is likely due to either trap-passivation or better energy level alignment showing up in an improved open-circuit voltage.

To summarize, the experiments and simulations consistently show that the extraction and consequently the FF is limited by the TL in common PSCs using low mobility TL that are not appropriately doped. So if low mobility TLs have to be used because of a lack of good alternatives then they need to be doped following the conductivity criterion described by equation 5.4. Doping the TL remains a very efficient approach of reaching high efficiencies when using low mobility but the best case scenario is always the case thin TL with high mobility.

## 5.4. Conclusion

In conclusion, simulation and experimental results were combined to show that transport layers are a limiting factor in the efficiency of perovskite solar cells. The low mobility of commonly used transport layers limits not only the extraction but also increases recombination. To counterbalance this effect two strategies can be used: doping the transport layer or using different materials with higher mobility. These two options are both viable and lead to high efficiency but using doping might lead to other issues such as parasitic absorption from the dopant, dopant diffusion and additional degradation pathways. Hence, finding new materials with high mobility appears to be the best strategy.

Two new and simple criteria are introduced to help tuning the transport layer thickness and/or conductivity to reach high efficiency. The first criterion helps to optimize the thickness of the transport layer and judge whether doping is required. The second criterion ensures that the TL conductivity is sufficient to ensure good transport. These criteria can be used prior to the fabrication of the full solar cells and will help to save time, materials and money in future optimization work.

**5**

## References

[1] A. Kojima, K. Teshima, Y. Shirai, and T. Miyasaka, *Organometal halide perovskites as visible-light sensitizers for photovoltaic cells,* Journal of the American Chemical Society **131**, 6050 (2009).

[2] M. A. Green, E. D. Dunlop, J. Hohl-Ebinger, M. Yoshita, N. Kopidakis, and A. W. Ho-Baillie, *Solar cell efficiency tables (Version 28-55),* Progress in Photovoltaics: Research and Applications **28**, 3 (2020).

[3] H.-S. Kim, C.-R. Lee, J.-H. Im, K.-B. Lee, T. Moehl, A. Marchioro, S.-J. Moon, R. Humphry-Baker, J.-H. Yum, J. E. Moser, M. Grätzel, and N.-G. Park, *Lead Iodide Perovskite Sensitized All-Solid-State Submicron Thin Film Mesoscopic Solar Cell with Efficiency Exceeding 9%,* Scientific Reports **2**, 591 (2012).

[4] M. M. Lee, J. Teuscher, T. Miyasaka, T. N. Murakami, and H. J. Snaith, *Efficient Hybrid Solar Cells Based on Meso-Superstructured Organometal Halide Perovskites,* Science **338**, 643 LP (2012).

[5] D. Bi, S.-J. Moon, L. Häggman, G. Boschloo, L. Yang, E. M. J. Johansson, M. K. Nazeeruddin, M. Grätzel, and A. Hagfeldt, *Using a two-step deposition technique to prepare perovskite (CH$_3$NH$_3$PbI$_3$) for thin film solar cells based on ZrO$_2$ and TiO$_2$ mesostructures,* RSC Advances **3**, 18762 (2013).

[6] W. Nie, H. Tsai, R. Asadpour, J.-C. Blancon, A. J. Neukirch, G. Gupta, J. J. Crochet, M. Chhowalla, S. Tretiak, M. A. Alam, H.-L. Wang, and A. D. Mohite, *High-efficiency solution-processed perovskite solar cells with millimeter-scale grains,* Science **347**, 522 (2015).

[7] D. Pérez-del Rey, P. P. Boix, M. Sessolo, A. Hadipour, and H. J. Bolink, *Interfacial Modification for High-Efficiency Vapor-Phase-Deposited Perovskite Solar Cells Based on a Metal Oxide Buffer Layer,* The Journal of Physical Chemistry Letters **9**, 1041 (2018).

[8] N. J. Jeon, J. H. Noh, W. S. Yang, Y. C. Kim, S. Ryu, J. Seo, and S. I. Seok, *Compositional engineering of perovskite materials for high-performance solar cells,* Nature **517**, 476 (2015).

[9] M. Saliba, T. Matsui, J.-Y. Seo, K. Domanski, J.-P. Correa-Baena, M. K. Nazeeruddin, S. M. Zakeeruddin, W. Tress, A. Abate, A. Hagfeldt, and M. Grätzel, *Cesium-containing triple cation perovskite solar cells: improved stability, reproducibility and high efficiency,* Energy & Environmental Science **9**, 1989 (2016).

[10] R. Prasanna, A. Gold-Parker, T. Leijtens, B. Conings, A. Babayigit, H.-G. Boyen, M. F. Toney, and M. D. McGehee, *Band Gap Tuning via Lattice Contraction and Octahedral Tilting in Perovskite Materials for Photovoltaics,* Journal of the American Chemical Society **139**, 11117 (2017).

[11] Y. Deng, Q. Dong, C. Bi, Y. Yuan, and J. Huang, *Air-Stable, Efficient Mixed-Cation Perovskite Solar Cells with Cu Electrode by Scalable Fabrication of Active Layer,* Advanced Energy Materials **6**, 1600372 (2016).

[12] C. Momblona, L. Gil-Escrig, E. Bandiello, E. M. Hutter, M. Sessolo, K. Lederer, J. Blochwitz-Nimoth, and H. J. Bolink, *Efficient vacuum deposited p-i-n and n-i-p perovskite solar cells employing doped charge transport layers,* Energy Environ. Sci. **9**, 3456 (2016).

[13] W. Chen, F.-Z. Liu, X.-Y. Feng, A. B. Djurišić, W. K. Chan, and Z.-B. He, *Cesium Doped NiO$_x$ as an Efficient Hole Extraction Layer for Inverted Planar Perovskite Solar Cells,* Advanced Energy Materials **7**, 1700722 (2017).

[14] H. Chen, W. Fu, C. Huang, Z. Zhang, S. Li, F. Ding, M. Shi, C.-Z. Li, A. K.-Y. Jen, and H. Chen, *Molecular Engineered Hole-Extraction Materials to Enable Dopant-Free, Efficient p-i-n Perovskite Solar Cells,* Advanced Energy Materials **7**, 1700012 (2017).

[15] I. Grill, M. F. Aygüler, T. Bein, P. Docampo, N. F. Hartmann, M. Handloser, and A. Hartschuh, *Charge Transport Limitations in Perovskite Solar Cells: The Effect of Charge Extraction Layers,* ACS Appl Mater Interfaces **9**, 37655 (2017).

[16] Z. Wang, D. P. McMeekin, N. Sakai, S. van Reenen, K. Wojciechowski, J. B. Patel, M. B. Johnston, and H. J. Snaith, *Efficient and Air-Stable Mixed-Cation Lead Mixed-Halide Perovskite Solar Cells with n-Doped Organic Electron Extraction Layers,* Advanced Materials **29**, 1604186 (2017).

[17] W.-Q. Wu, D. Chen, R. A. Caruso, and Y.-B. Cheng, *Recent progress in hybrid perovskite solar cells based on n-type materials,* Journal of Materials Chemistry A **5**, 10092 (2017).

[18] R. Fang, S. Wu, W. Chen, Z. Liu, S. Zhang, R. Chen, Y. Yue, L. Deng, Y.-B. Cheng, L. Han, and W. Chen, *[6,6]-Phenyl-$C_{61}$-Butyric Acid Methyl Ester/Cerium Oxide Bilayer Structure as Efficient and Stable Electron Transport Layer for Inverted Perovskite Solar Cells,* ACS Nano **12**, 2403 (2018).

[19] S. Sidhik, A. Cerdan Pasarán, D. Esparza, T. López Luke, R. Carriles, and E. De la Rosa, *Improving the Optoelectronic Properties of Mesoporous $TiO_2$ by Cobalt Doping for High-Performance Hysteresis-free Perovskite Solar Cells,* ACS Appl Mater Interfaces **10**, 3571 (2018).

[20] X. Zhao, L. Tao, H. Li, W. Huang, P. Sun, J. Liu, S. Liu, Q. Sun, Z. Cui, L. Sun, Y. Shen, Y. Yang, and M. Wang, *Efficient Planar Perovskite Solar Cells with Improved Fill Factor via Interface Engineering with Graphene,* Nano Letters (2018), 10.1021/acs.nanolett.8b00025.

[21] D. Ouyang, J. Xiao, F. Ye, Z. Huang, H. Zhang, L. Zhu, J. Cheng, and W. C. H. Choy, *Strategic synthesis of ultrasmall nico2o4 nps as hole transport layer for highly efficient perovskite solar cells,* Advanced Energy Materials **8**, 1702722 (2018).

[22] H. D. Pham, T. T. Do, J. Kim, C. Charbonneau, S. Manzhos, K. Feron, W. C. Tsoi, J. R. Durrant, S. M. Jain, and P. Sonar, *Molecular Engineering Using an Anthanthrone Dye for Low-Cost Hole Transport Materials: A Strategy for Dopant-Free, High-Efficiency, and Stable Perovskite Solar Cells,* Advanced Energy Materials **8**, 1703007 (2018).

[23] G. Yang, C. Chen, F. Yao, Z. Chen, Q. Zhang, X. Zheng, J. Ma, H. Lei, P. Qin, L. Xiong, W. Ke, G. Li, Y. Yan, and G. Fang, *Effective Carrier-Concentration Tuning of $SnO_2$ Quantum Dot Electron-Selective Layers for High-Performance Planar Perovskite Solar Cells,* Advanced Materials **30**, 1706023 (2018).

[24] P. Schulz, E. Edri, S. Kirmayer, G. Hodes, D. Cahen, and A. Kahn, *Interface energetics in organo-metal halide perovskite-based photovoltaic cells,* Energy & Environmental Science **7**, 1377 (2014).

[25] L. E. Polander, P. Pahner, M. Schwarze, M. Saalfrank, C. Koerner, and K. Leo, *Hole-transport material variation in fully vacuum deposited perovskite solar cells,* APL Materials **2**, 081503 (2014).

[26] M. Stolterfoht, C. M. Wolff, J. A. Márquez, S. Zhang, C. J. Hages, D. Rothhardt, S. Albrecht, P. L. Burn, P. Meredith, T. Unold, and D. Neher, *Visualization and suppression of interfacial recombination for high-efficiency large-area pin perovskite solar cells,* Nature Energy **3**, 847 (2018).

[27] S. Zhang, M. Stolterfoht, A. Armin, Q. Lin, F. Zu, J. Sobus, H. Jin, N. Koch, P. Meredith, P. L. Burn, and D. Neher, *Interface Engineering of Solution-Processed Hybrid Organohalide Perovskite Solar Cells,* ACS Applied Materials & Interfaces **10**, 21681 (2018).

[28] N. Marinova, W. Tress, R. Humphry-Baker, M. I. Dar, V. Bojinov, S. M. Zakeeruddin, M. K. Nazeeruddin, and M. Grätzel, *Light Harvesting and Charge Recombination in*

**5**

*$CH_3NH_3PbI_3$ Perovskite Solar Cells Studied by Hole Transport Layer Thickness Variation,* ACS Nano **9**, 4200 (2015).

[29] M. Stolterfoht, C. M. Wolff, Y. Amir, A. Paulke, L. Perdigón-Toro, P. Caprioglio, and D. Neher, *Approaching the fill factor Shockley–Queisser limit in stable, dopant-free triple cation perovskite solar cells,* Energy & Environmental Science **10**, 1530 (2017).

[30] F. Maddalena, P. P. Boix, C. Xin Yu, N. Mathews, C. Soci, and S. Mhaisalkar, *Charge Transport in Organometal Halide Perovskites,* in *Organic-Inorganic Halide Perovskite Photovoltaics* (Springer International Publishing, 2016) pp. 201–222.

[31] L. M. Herz, *Charge-Carrier Mobilities in Metal Halide Perovskites: Fundamental Mechanisms and Limits,* ACS Energy Letters **2**, 1539 (2017).

[32] T. S. Sherkar, C. Momblona, L. Gil-Escrig, H. J. Bolink, and L. J. A. Koster, *Improving Perovskite Solar Cells: Insights From a Validated Device Model,* Advanced Energy Materials **7**, 1602432 (2017).

[33] P. Vivo, J. Salunke, A. Priimagi, P. Vivo, J. K. Salunke, and A. Priimagi, *Hole-Transporting Materials for Printable Perovskite Solar Cells,* Materials **10**, 1087 (2017).

[34] J. Jiménez-López, W. Cambarau, L. Cabau, and E. Palomares, *Charge Injection, Carriers Recombination and HOMO Energy Level Relationship in Perovskite Solar Cells,* Scientific Reports **7**, 6101 (2017).

[35] T. S. Sherkar, C. Momblona, L. Gil-Escrig, J. Ávila, M. Sessolo, H. J. Bolink, and L. J. A. Koster, *Recombination in Perovskite Solar Cells: Significance of Grain Boundaries, Interface Traps, and Defect Ions,* ACS Energy Letters **2**, 1214 (2017).

[36] T. S. Sherkar, V. M. Le Corre, M. Koopmans, F. Wobben, and L. J. A. Koster, *SIMsalabim GitHub repository,* (2020).

[37] M. Stolterfoht, P. Caprioglio, C. M. Wolff, J. A. Márquez, J. Nordmann, S. Zhang, D. Rothhardt, U. Hörmann, Y. Amir, A. Redinger, L. Kegelmann, F. Zu, S. Albrecht, N. Koch, T. Kirchartz, M. Saliba, T. Unold, and D. Neher, *The impact of energy alignment and interfacial recombination on the internal and external open-circuit voltage of perovskite solar cells,* Energy and Environmental Science **12**, 2778 (2019).

[38] N. Tessler and Y. Vaynzof, *Preventing hysteresis in perovskite solar cells by undoped charge blocking layers,* ACS Applied Energy Materials **1**, 676 (2018).

[39] D. Liu, Y. Li, J. Yuan, Q. Hong, G. Shi, D. Yuan, J. Wei, C. Huang, J. Tang, and M.-K. Fung, *Improved performance of inverted planar perovskite solar cells with F4-TCNQ doped PEDOT:PSS hole transport layers,* Journal of Materials Chemistry A **5**, 5701 (2017).

[40] G. Yin, J. Ma, H. Jiang, J. Li, D. Yang, F. Gao, J. Zeng, Z. Liu, and S. F. Liu, *Enhancing Efficiency and Stability of Perovskite Solar Cells through Nb-Doping of TiO 2 at Low Temperature,* ACS Applied Materials & Interfaces **9**, 10752 (2017).

[41] M. Stolterfoht, P. Caprioglio, C. M. Wolff, J. A. Márquez, J. Nordmann, S. Zhang, D. Rothhart, U. Hörmann, A. Redinger, L. Kegelmann, S. Albrecht, T. Kirchartz, M. Saliba, T. Unold, and D. Neher, *The perovskite/transport layer interfaces dominate non-radiative recombination in efficient perovskite solar cells,* (2018).

[42] D. Bartesaghi, I. d. C. Perez, J. Kniepert, S. Roland, M. Turbiez, D. Neher, and L. J. A. Koster, *Competition between recombination and extraction of free charges determines the fill factor of organic solar cells,* Nature Communications **6:7083** (2015), 10.1038/ncomms8083.

[43] V. Le Corre, A. Chatri, N. Doumon, and L. Koster, *Charge Carrier Extraction in Organic Solar Cells Governed by Steady-State Mobilities,* Advanced Energy Materials **7**, 1701138 (2017).

[44] J. Peng, T. Duong, X. Zhou, H. Shen, Y. Wu, H. K. Mulmudi, Y. Wan, D. Zhong, J. Li, T. Tsuzuki, K. J. Weber, K. R. Catchpole, and T. P. White, *Efficient Indium-Doped $TiO_2$ Electron Transport Layers for High-Performance Perovskite Solar Cells and Perovskite-Silicon Tandems,* Advanced Energy Materials **7**, 1601768 (2017).

[45] S. Wang, B. Liu, Y. Zhu, Z. Ma, B. Liu, X. Miao, R. Ma, and C. Wang, *Enhanced performance of $TiO_2$-based perovskite solar cells with Ru-doped $TiO_2$ electron transport layer,* Solar Energy **169**, 335 (2018).

[46] X. Gu, Y. Wang, T. Zhang, D. Liu, R. Zhang, P. Zhang, J. Wu, Z. D. Chen, and S. Li, *Enhanced electronic transport in $Fe^{3+}$-doped $TiO_2$ for high efficiency perovskite solar cells,* Journal of Materials Chemistry C **5**, 10754 (2017).

[47] N. Zhou, Q. Cheng, L. Li, and H. Zhou, *Doping effects in $SnO_2$ transport material for high performance planar perovskite solar cells,* Journal of Physics D: Applied Physics **51**, 394001 (2018).

**5**

# 6

# IDENTIFICATION OF THE DOMINANT RECOMBINATION PROCESS FOR PEROVSKITE SOLAR CELLS BASED ON MACHINE LEARNING

*Over the past decade, perovskite solar cells have become one of the major research interests of the photovoltaic community and are now on the brink of catching up with the classical inorganic solar cells with efficiency now reaching up to 25%. However, significant improvements are still achievable by reducing recombination losses. The aim of this work is to develop a fast and easy-to-use tool to pinpoint the main losses in perovskite solar cells. We use large-scale drift-diffusion simulations to get a better understanding of the light intensity dependence of the open-circuit voltage and how it correlates to the dominant recombination process. We introduce an automated identification tool using machine learning methods to pinpoint the dominant loss using the light intensity-dependent performances as an input. The machine learning was trained using over 150000 simulations and gives an accuracy of the prediction up to 80%.*

## 6.1. INTRODUCTION

B IG data science and machine learning (ML) have drawn a lot of attention not only from industries such as Google, Facebook, Amazon and co. but also in the scientific community. There has been a tremendous increase in the number of studies using these techniques and in very different fields going from medicine to chemistry and physics. [1–9] ML techniques have proved to be very effective at predicting the properties of materials [3,9,10] but also at speeding up the material discovery process by suggesting new promising structures. [4–8]

In an era where high-throughput experimentation is made possible thanks to the use of autonomous robots [4,11] and where a large amount of data can be processed easily with the new data science and artificial intelligence (AI) tools openly-accessible online, science should turn into a more systematic/standard experimentation, data collection and analysis. This would allow scientists to spend more time exploring the data or new ideas rather than going through tedious and sometimes poorly reproducible lab work. If this line of thinking is applied to photovoltaic research, the future workflow of material and device development for solar cells may look like figure 6.1. In recent years, there have been only few attempts to develop tools corresponding to one or more of the steps described in figure 6.1. These studies showed that AI methods helped experimental planning to predict the next promising material to use/synthesize or experiment to make. [3,5–7] The use robots for high-throughput experiments [7,12,13] and automated data analysis [3,7,11] provides several advantages in terms of speed of material development and size/reproducibility of the experimental output demonstrating the power of this approach.

In order to pursue this reasoning for the study of perovskite solar cells (PSCs) we need
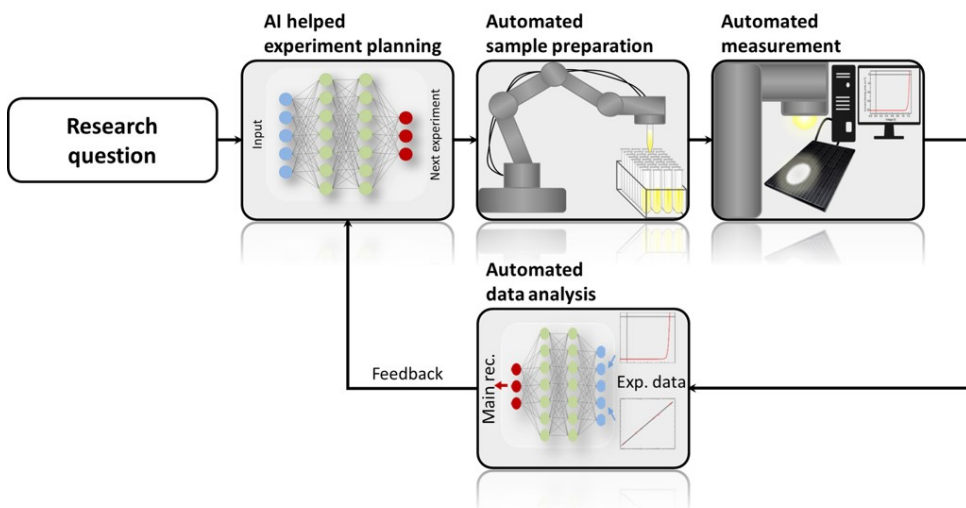


Figure 6.1: Potential closed-loop workflow for automated and high-throughput experimentation in photovoltaic research.

appropriate characterization tools that can accurately pinpoint whether the bulk or an interface limits the efficiency while being fast/easy and can also automatically analyze data. Here, we build a characterization tool to pinpoint bulk or interfaces recombination as the dominant loss based on light intensity-dependent current-voltage characteristics measurements.

Hybrid halide perovskites show desirable properties for use in thin-film solar cells, such as a large absorption coefficient, high charge carrier mobilities, and long diffusion lengths. [14–16] As a consequence, PSCs have attracted great interest, facilitating a remarkable rise in their efficiency over the past ten years. [14,17] This rise has been mainly driven by novel fabrication techniques which ensure very compact perovskite absorber films [18–21] with large grain sizes, [22] minimizing the non-radiative recombination losses through charge trapping at defects in the perovskite absorber bulk at the grain boundaries.

Now, efforts are being directed towards the tuning of electron and hole transport layers (ETL, HTL) [23–25] and interface engineering. [26–28] Nonetheless, in existing PSCs, Shockley-Read-Hall (SRH) trap-assisted recombination is still the dominant recombination loss whether it happens in the bulk via grain boundaries or at the interfaces (HTL/perovskite and perovskite/ETL). [29–37] There exist many reports on the recombination in perovskite solar cells, however, most of these experimental studies are performed on perovskite thin-films. [38–44]

Photoluminescence (PL) studies look at charge transfer rates at interfaces between perovskite thin-films and transport layers revealing the recombination kinetics. [24,43] Although these methods elucidate the fundamental optoelectronic properties and role of defect physics in recombination, they are often performed under non-operating solar cell conditions (i.e. non-solar fluences and/or not a full device configuration) and are often complex. [24,43] More recent reports also suggest that for high-efficiency perovskite the main recombination center is consistently located at the interface between the perovskite and the TLs. [33,34] It is therefore important to identify the dominant recombination losses, so that efforts can be directed towards improving the quality of the perovskite material or the interface in question. While the PL measurements have proven to be very effective at pinning out the dominant loss they require several sets of devices with different structures which make them very time-consuming.

Here, we present a more in-depth analysis on the light intensity measurement of PSCs and especially on the parameters influencing the slope ($\eta kT/q$ on a semi-log plot) of the open-circuit voltage ($V_{OC}$) versus light intensity curve, with $\eta$ the so-called ideality factor, $T$ the temperature, $k$ the Boltzmann constant and $q$ the elementary charge. The ideality factor is typically used to conclude on the dominant recombination process very simply by saying that an ideality factor close to one means that band-to-band recombination dominates [45] and an ideality factor close to two correspond to bulk SRH trap assisted recombination [46] while when it is in between this two values it is difficult to conclude.

However, here we show that this interpretation is not complete as other parameters influence the ideality factor and that the analysis of ideality factor needs to be coupled with other key figures such as the open-circuit voltage ($V_{OC}$), the short-circuit current ($J_{SC}$) and the fill factor ($FF$), doping and more. To remedy this issue we trained—using

6

large scale drift-diffusion (DD) simulations [31,32,47]—a ML algorithm based on decision trees to classify the light intensity measurement output to give the most likely dominant recombination. Our trained model was able to determine, within a matter of seconds, whether the dominant recombination process was band-to-band, interface or grain boundaries trap recombination with a 80% accuracy and this while only requiring the simple measurement of light intensity-dependent current-voltage characteristics (JVs). This represent, to the best of our knowledge, the first use of ML as identification tools of the dominant recombination process in PSCs over such a wide range of material properties. In a broader perspective, the ML approach could also be used for automated data analysis as in the workflow described in figure 6.1 as the experimental data used are simple, can be easily measured and that the ML algorithm provides a fast and easy way to analyze the data and provide feedback to choose the next relevant experiment.

Chapter key findings:

- The ideality facotr of perovskite solar cells does not only depend on the dominant recombination process making it a poor predictor of the main loss channel.

- Machine learning method trained using simulations can be used to predict the dominant recombination process in perovskite solar cells.

**6**

## 6.2. RELATIONSHIP BETWEEN IDEALITY FACTOR AND RECOMBINATION PROCESSES

The amount of charge recombination is directly related to the open-circuit voltage of a solar cell, whose light intensity dependence can reveal information about the dominant recombination mechanism under operating conditions. In the following section, we will describe the different possible scenarios that are relevant for PSCs: (i) band-to-band recombination (ii) SRH trap-assisted recombination and (iii) SRH trap-assisted recombination with one pinned charge carrier density. Since Auger recombination is negligible under non-concentrated illumination [48,49] it will be excluded from this analysis.
The $V_{OC}$ of a solar cell is the difference between the electron and hole quasi-fermi levels, and is approximated analytically by [45,50]

$$qV_{OC} = E_{gap} - kT\ln\left(\frac{N_{cv}^2}{np}\right) \tag{6.1}$$

where $E_{gap}$ is the band-gap of the photo-active material, $N_{cv}$ is the density of states in the conduction and valence bands, while $n$ and $p$ are electron and hole concentrations respectively. The ideality factor is given by how the $np$-product depends on the light intensity. This yields to different $\eta$ for different scenarios.
The total recombination rate in the solar cell is given by

$$R = R_b + R_{SRH}^{Bulk} + R_{SRH}^{Front\ int.} + R_{SRH}^{Back\ int.} \tag{6.2}$$

where $R_b$ is the band-to-band recombination rate and $R_{SRH}$ is the trap-assisted recombination rate described by the Shockley-Read-Hall (SRH) statistics in the bulk ($R_{SRH}^{Bulk}$) of the perovskite or at the interface with the front ($R_{SRH}^{Front\ int.}$) and back ($R_{SRH}^{Back\ int.}$) TLs. At $V_{OC}$, the total recombination rate ($R$) is equal to the charge generation rate ($G$) in the device. We used our DD simulations—available open-source on GitHub[47]—to study the different cases with dominant band-to-band recombination or SRH trap-assisted recombination with and without one pinned charge carrier density one at a time for a simple device structure, see parameters used in appendix E.
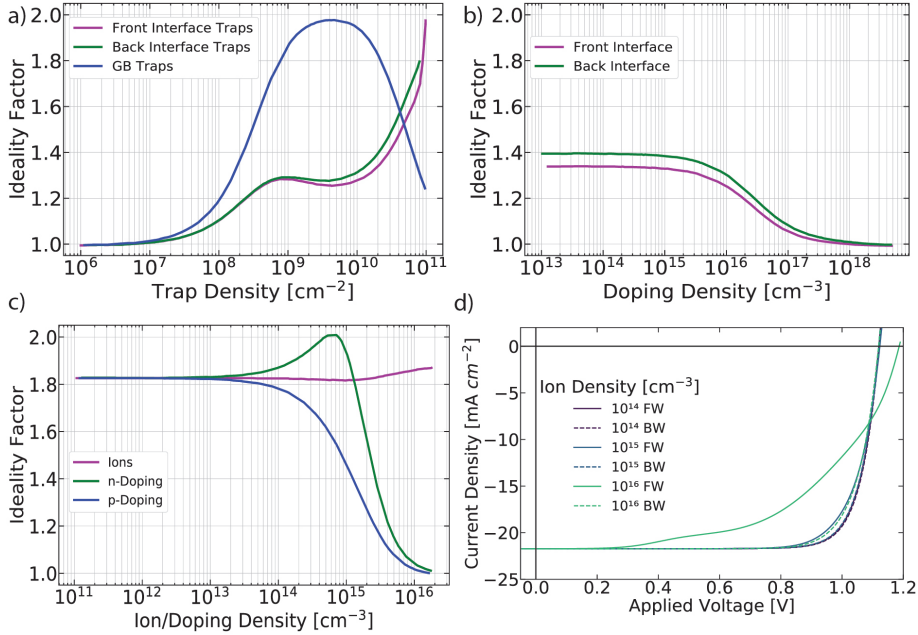


Figure 6.2: Simulated evolution of the ideality factor depending of the trap density (a), TL doping (b) and ion and doping density (c) in the perovskite layer, considering traps at the grain boundaries, front or back interfaces separately. Effect of the ions density on the degree of hysteresis (d). Parameters used in the simulation can be found in table E.1.

## CASE (I): DOMINANT BAND-TO-BAND RECOMBINATION

When band-to-band recombination is dominant ($R_b \gg R_{SRH}^{Bulk} + R_{SRH}^{Front\ int.} + R_{SRH}^{Back\ int.}$) in the device, at $V_{OC}$ the total recombination rate is

$$R \approx R_b = \gamma n p = G. \tag{6.3}$$

So

$$n = p = (G/\gamma)^{1/2}, \tag{6.4}$$

where $\gamma$ is the band-to-band recombination constant. Following Eq. (1), the $V_{OC}$ is now approximated by

$$qV_{OC} = E_{gap} - kT \ln\left(\gamma N_{cv}^2 \times \frac{1}{G}\right). \tag{6.5}$$

Since the charge generation rate ($G$) is proportional to the light intensity ($I$), the semi-log plot of $V_{OC}$ versus $I$ gives a slope of $kT/q$ or a ideality factor of $\eta = 1$. Therefore, $\eta = 1$ could indicate dominant band-to-band recombination in the device. [45] Note that for PSCs $\gamma$ has been found to be low [51–54] in the range of $10^{-9}$-$10^{-11}$ cm$^3$ s$^{-1}$. This could be explained by lattice distortion leading to a spatial separation of electrons and holes decreasing the probability of charge carriers to recombine. As a consequence, a hypothetical PSC where band-to-band recombination dominates must have a very high-quality perovskite and interfaces with very low defects density which would lead to high $V_{OC}$ as we will show later in this chapter.

## Case (ii): Dominant SRH recombination without pinning of one charge carrier density

If SRH recombination is dominant ($R_{SRH} \gg R_b$) in a device, at $V_{OC}$ the total recombination rate is

$$R \approx R_{SRH} = \frac{C_n C_p \Sigma_T}{C_n(n + n_1) + C_p(p + p_1)} \, np = G, \tag{6.6}$$

where $\Sigma_T$ is the electron trap density, $C_n$ and $C_p$ are the capture coefficients for electrons and holes respectively and, $n_1 = p_1 = N_{cv} \exp(-E_{trap}/kT)$. Typically $n \gg n_1$ and $p \gg p_1$ when traps act as recombination centers, [32,55] and so these constants can be neglected.

Now, if $n \approx p$ and assuming $C_n = C_p$ we get

$$R \approx R_{SRH} = C_p \Sigma_T p = G, \tag{6.7}$$

$$p = n = G/C_p \Sigma_T. \tag{6.8}$$

Following Eq. (1), the $V_{OC}$ is now approximated by

$$qV_{OC} = E_{gap} - kT \ln\left(C_p \Sigma_T N_{cv}^2 \times \frac{1}{G^2}\right). \tag{6.9}$$

In this case, the light intensity dependence of the $V_{OC}$ shows a slope of $2kT/q$ or a ideality factor of $\eta = 2$. And so, $\eta = 2$ represents dominant SRH recombination in the device, see figure 6.2.a.

Now, considering the special case of perovskite it is unlikely to have evenly distributed trap states throughout the material bulk. In fact, studies have shown that defects tend to migrate out of the bulk and toward the grain boundaries (GB) and interfaces leaving low trap densities within the bulk. [56,57] For this reason, we will only consider traps located at the GBs in this chapter.

In addition, as much as the previous derivation works well for traps evenly spread through the perovskite layer one must be more careful when considering spatially localized traps such as traps located at grain boundaries. In fact, upon high trap density at the GB a depletion region is created because of the charge of the traps hence it somewhat pins the opposite charge carrier density to compensate for the space-charge region leading to $\eta < 2$ see case (iii).

## CASE (III): DOMINANT SRH RECOMBINATION WITH ONE PINNED CHARGE CARRIER DENSITY

In this scenario trap assisted recombination is still dominant, however, one of the charge carriers is pinned to a finite value i.e. it stays roughly constant upon changing light intensity. This can happen in PSCs for several reasons:

- High trap density at the GB creating a depletion region (see above), see figure 6.2.a.

- Traps at the perovskite/TL interface with a doped TL where the charge carrier density is pinned to the doping level of the respective charge transport layer, see figure 6.2.b.

- Traps at the perovskite/TL interface thin undoped TL and an ohmic contact with the respective electrode. The ohmic contact pins the charge carrier density as the latter induces many charges in the charge transport layer, [58] see figure 6.2.a.

- Doping of the perovskite bulk.

If we take the example of a perovskite/ETL interface $n \gg p$ and $n \approx N_D^+$, where $N_D^+$ is the doping level in ETL. Therefore when SRH recombination is dominant at the perovskite/ETL interface, following Eq. (6) , at $V_{OC}$ the total recombination rate is

$$R \approx R_{SRH} = C_p \Sigma_T p = G, \tag{6.10}$$

$$p = G/C_p \Sigma_T \text{ and } n \approx N_D^+ \tag{6.11}$$

Now, following Eq. (1), the $V_{OC}$ when SRH recombination dominates at the perovskite/ETL interface, is approximated by

$$qV_{OC} = E_{gap} - kT \ln\left(\frac{C_p \Sigma_T N_{cv}^2}{N_D^+} \times \frac{1}{G}\right) \tag{6.12}$$

Similarly, when SRH recombination dominates at the HTL/perovskite interface, the $V_{OC}$ is approximated by

$$qV_{OC} = E_{gap} - kT \ln\left(\frac{C_n \Sigma_T N_{cv}^2}{N_A^-} \times \frac{1}{G}\right) \tag{6.13}$$

where $N_A^-$ is the doping level in the HTL. The light intensity dependence of the $V_{OC}$ now shows a slope of $kT/q$ or a ideality factor of $\eta = 1$. And so, just as in the case of dominant band-to-band recombination $\eta = 1$ which would make the prediction of the dominant recombination process only based on the ideality factor very inaccurate.

Figure 6.2.a shows the evolution of the ideality factor depending on the trap density either at the grain boundary or at one of the interfaces, see figure E.1 for more details. We can note that as expected from the derivation for very low trap densities $\eta \to 1$ as band-to-band recombination dominates. However, we can see that the evolution of the ideality factor respective to the trap density is not monotonously increasing and

depends on where the traps are located within the device, hence, the ideality factor can definitely not be used as a quantitative measure of the number of traps in the systems. We can also see the different scenarios leading to a reduced ideality factor because of the pinning of one charge carrier, whether it is related to a large number of traps at the GB (a, blue line), to a pinning because of thin TL and interfacial traps (a, magenta and green line) or because of the doping of the TL with interfacial traps (b), see figure E.1 & E.2.

Doping the perovskite bulk, whether it comes from the addition of a compound or because of oxidation of the metal, [59–61] also leads to a different ideality factor, as seen in figure 6.2.c. In fact upon sufficient doping one of the charge carrier density is pinned and again $\eta \rightarrow 1$. In the following of the chapter we will not consider doped perovskite.

Another important feature of PSCs is the presence of moving ions, we also simulated devices with different ion density, see figure 6.2.c and d, and realize that contrary to doping they do not affect the ideality factor significantly for stabilized JVs. In addition, we show that if a device shows little to no hysteresis for high voltage scan rate there is also no significant effect of ions on the stabilized performance and the ideality factor. This is well in line with the work by Tessler et al. [62] who showed that when a J-V characteristic does not show signs of hysteresis the device model can still reproduce the same material and device parameters without including ions. Hence, we will also not consider ions in the following simulations as they would also increase significantly the computational time.

To summarize here we showed that the analysis of the ideality factor is not as straightforward as expected and that other factors need to be taken into consideration. Hence despite giving valuable information the ideality factor cannot be used on its own to conclude anything about the dominant recombination process but have to be analyzed in correlation with other parameters.

## 6.3. Dataset for machine learning

Machine learning algorithms have proven to be very efficient classifier and here recognizing the dominant recombination process is nothing more than a classification problem. We are looking at three or four potential classes: (1) band-to-band recombination, (2) SRH recombination in the bulk and (3) interfacial SRH at the front (3a) or back (3b) interface. To accurately train a ML algorithm we need first a dataset on which the ML can be trained and tested on. To build a usable dataset we need to define enough descriptive features and, of course, have properly labeled data. In other words, we need a large amount of data on PSCs with light intensity-dependent performance and an already known dominant recombination process for each of the data points. This represents one of the big challenges in applying ML strategies to PSC research as there is no readily available dataset or database reporting performance values of PSCs with the corresponding limiting process. Despite the huge amount of data published every year on PSCs there is no real standard on what to characterize when a newly made device is reported aside from typical JV curve under 1 sun AM1.5 and even more problematic most of the time we focus on reporting on what has been improved compared to a

reference which is indeed important but it would also be insightful to investigate what is still limiting the device.

To overcome the issue of not having an experimental dataset to work with we decided to use DD simulations[31,32,47] to generate the needed data. DD simulations have already proven their ability to capture the physics of PSCs by reproducing a wide variety of devices with different perovskite composition and structure.[31,32,63–65] Hence, we are confident that it can give us meaningful and reliable data to work with. In order to get a representative dataset we randomly picked parameters within a reasonable range—see table E.2—based on commonly reported experimental values in the literature for the thickness and mobilities of all layers. For the recombination parameters that are more difficult to access with experiment we used previously published simulation work using either DD[31,32,63–65] or first-principle[51–54] simulation to set meaningful boundaries. We also chose to fix the bandgap of the perovskite to 1.6 eV (which corresponds to the bandgap of MAPbI$_3$) as we, for now, focus on a proof of concept but obviously the analysis presented below would also hold for a different bandgap by extending the simulation space for the said bandgap.

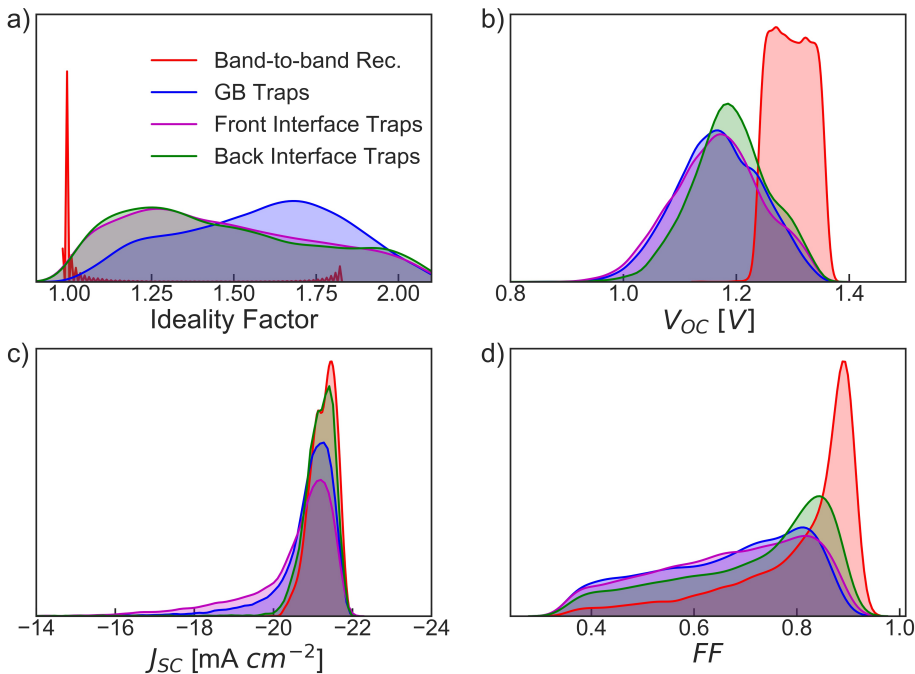Figure 6.3 presents the summary of the main performance parameters under 1 sun



Figure 6.3: Density for the different recombination types simulated of ideality factor (a), open-circuit voltage (b), short-circuit current (c) and fill factor (d) under 1 sun illumination. Parameters used in the simulation can be found in appendix E.

illumination and the ideality factor for over 150000 simulated solar cells. The ideality factor was fitted from simulated values from 5 different light intensities hence representing a total number of simulations of over 750000. One of the main advantages of using a dataset based on simulations is that each point can properly be labeled to their dominant recombination process (under 1 sun at maximum power point condition) as the contribution of each loss can be very easily disentangled from one another and the recombination fraction of each process can be calculated.

Without going further we can already draw some conclusions from the density plot presented in figure 6.3, the ideality factor not being sufficient to accurately distinguish the different recombination processes. In fact, as expected from the derivation made in the previous section $\eta \approx 1$ is not always a sign of dominant band-to-band recombination. However, if we consider ideality factor and $V_{OC}$ then we realize that $\eta \approx 1$ and $V_{OC} > 1.2$ $V$ is very likely to be band-to-band recombination. As mentioned in the previous section band-to-band limited devices exhibit impressively high $V_{OC}$ with a loss lower than 0.4V compared to the bandgap, this is due to the very low values of the band-to-band recombination constant in perovskite, however, to be band-to-band recombination limited the perovskite layer needs to be of very high quality with very low trap densities. This hints that by adding other features on top of the ideality factor we could improve the accuracy of the prediction of the dominant recombination process. Hence, moving to ML technique could help us predict the dominant recombination process by adding/tuning features that can preferably be easily measured.

## 6.4. Machine learning tree-based methods to iden-tify the dominant recombination process for perovskite solar cells

As mentioned earlier ML techniques are very effective for classification problems, here we chose to use two tree-based methods: single decision tree (ST) and random forest (RF). As they present the advantage of being more transparent than a typical neural network and that you can get more insight into what governs the decision by "drawing" the trained tree. All the ML training was made using the scikit-learn[66] toolbox. First, we start by defining three classes for the dominant recombination process: (1) band-to-band (2) GB traps (3) interfacial traps and train our ML to distinguish between the different scenarios. Note that to avoid any bias in our learning the dataset was balanced between the three classes and 1/4 of the dataset was used as a test set. The common approach used in the literature is to use only the ideality factor as a feature so we trained both ST and RF algorithm to using only $\eta$ giving an overall accuracy of $\approx$ 71% and $\approx$ 69% on the training and testing set respectively, see figure 6.4. The trust score, i.e. how much can you trust the prediction made by the ML, for each class can also be calculated, see figure E.3, giving 90% for band-to-band recombination dominant, 61% for the GB traps and 55% for interfacial traps. This means, for example, that if one inputs new numbers into the ML and the output is interfacial recombination then there is a 55% chance that this is indeed the dominant recombination process.
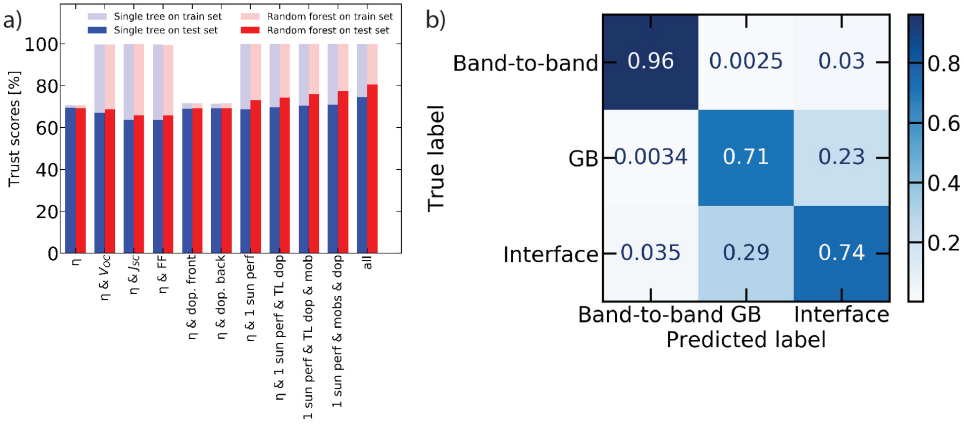
Figure 6.4: (a) Evolution of the trust score on training and test dataset depending on the features used to train single-tree or random-forest. The full dataset consists of over $10^5$ simulated devices, 1/4 of which was used as a test set. The best performance (80%) is obtained for RF using 5 different light intensity performances, doping and mobilities of all the layers as features. (b) Confusion matrix on the prediction for the best performing RF trained showing how often a prediction is correct (diagonal) depending on the dominant recombination process.

We can already note that the ideality factor alone gives a decent prediction as to whether the system is band-to-band or trap limited but is not enough to distinguish whether the traps are located at the interface or within the bulk at the GBs. Which is to be expected as it is difficult to distinguish between the two trap assisted recombination processes. However, figure 6.3.a shows that there is still a difference in the distribution for the 1 sun performance, hence, adding those features as descriptors should improve the prediction accuracy. We see that adding more features such as the 1 sun performance or the mobility and whether the TLs are doped or not help to improve the prediction of the ML algorithm. Note that in the simulation the TL is considered doped if it satisfies the doping criteria introduced in Ref. 63.

The best result—with an overall accuracy above 80%—was obtained with a random forest classifier when using the performance of all the simulated light intensities, the mobility of all layers and whether or not the TLs are doped. This improvement is due to a better differentiation between interfacial and GB traps recombination.

The normalized confusion matrix on the prediction, shown in figure 6.4.b, gives more insight in the accuracy of the prediction by showing the fraction of the predictions that are correct on the diagonal. The off-diagonal elements give the fraction of wrongly assigned predictions. In our best case, it shows that when the ML output is either band-to-band, GB or interfacial recombination the results can be trusted in 96%, 71% and 74% of the cases respectively. However, the accuracy of the prediction is not perfect which is mainly due to the fact that some interfacial dominant cases are mistaken as GB dominant and vice-versa; and also the presence of mixed cases where both GB and interface have a comparable contribution to the overall recombination.

To validate our analysis we chose experimental values from the literature that have the

appropriate bandgap, i.e. the right perovskite composition, where the dominant loss is known and where enough of the features are available. The first set of two devices is made of vacuum-processed $MAPbI_3$ in a nip or pin structure,[32] the main recombination process was determined by fitting DD simulations to light intensity dependent current-voltage characteristics. The second set of data is made of triple-cation perovskite $CsPbI_{0.05}[(FAPbI_3)_{0.89}(MAPbI_3)_{0.11}]_{0.95}$ in pin structure with changing interlayer or TLs, the dominant recombination process was accessed by performing PL measurement and also DD simulation for device 3-4.[33,63,67] For more details on the devices see table E.3.

Table 6.1: Parameters used as features for the random-forest algorithm to predict the dominant recombination of experimental perovskite solar cells. Find more information on the device structures in appendix E.

| Device number | Ref. | $V_{OC}$ [V] | $J_{SC}$ [mA cm$^{-2}$] | $FF$ | $\eta$ | Front TL doped | Back TL doped | Experimental dominant | ML prediction prediction recombination |
|---|---|---|---|---|---|---|---|---|---|
| 1 | 32 | 1.08 | -20.0 | 0.73 | 2 | yes | yes | mixed GB/interface | GB |
| 2 | 32 | 1.12 | -20.2 | 0.81 | 1.55 | yes | yes | mixed GB/interface | GB/interface |
| 3 | 33,63 | 1.09 | -21.65 | 0.779 | 1.42 | no | no | interface | interface |
| 4 | 33 | 1.17 | -21.7 | 0.786 | 1.42 | no | no | interface | interface |

We used the ideality factor, 1 sun illumination performance and doping of the TLs, see Table 6.1, as features for the random-forest. We find a good agreement between the prediction and the dominant recombination previously reported for these devices. Hence, despite the accuracy of the prediction not being perfect it still predicts quite well the dominant process for experimental devices proving that it could be used to analyze real experimental data for PSCs. To that aim all the data and the python code used in this study are available on GitHub[68] as well as the open-source DD simulation package SIMsalabim used to simulate PSCs.[31,32,47]

This result brings the hope that in the future we could use an even larger dataset with also experimental data to train ML methods and predict the dominant losses. This would be especially useful in the aim of more automated and high-throughput production of data where the analysis needs to be performed automatically and accurately or used as an online tool where the trained models would be available and could be used as a characterization tool for new studies. We could even think of adding all kinds of other experimental results as features to improve the accuracy of the ML even more. In addition, this line of thinking could also be easily adapted for other kinds of photovoltaic technology such as organic or quantum dots solar cells.

## 6.5. CONCLUSION

Despite being widely reported in the literature the analysis of the dominant recombination based on the ideality factor turns out to be less reliable than expected for perovskite solar cells as it is also strongly affected by other factors. In fact, by performing large scale simulation we have shown that the ideality factor does not only depends on the dominant recombination process but also on carrier pinning either because of the contacts or

doping. Hence, to draw any meaningful conclusion on the main loss process the analysis needs to be complemented by other features.

We show using machine learning procedures that the prediction of the dominant recombination process can be improved by adding the performances under different light intensities, doping and mobilities. A maximum prediction accuracy of 80% was obtained using random-forest algorithm which represents a 10% improvement compared to the use of the ideality factor only. The trained random-forest was also able to accurately predict the dominant recombination of experimental devices.

This study shows that performing large scale simulation and using machine learning tools could lead to a new type of automated data analysis that would be suitable for high-throughput experimentation.

## REFERENCES

[1] M. Haghighatlari, G. Vishwakarma, D. Altarawy, R. Subramanian, B. U. Kota, A. Sonpal, S. Setlur, and J. Hachmann, *ChemML: A Machine Learning and Informatics Program Package for the Analysis, Mining, and Modeling of Chemical and Materials Data,* (2019).

[2] J. Hachmann, M. A. F. Afzal, M. Haghighatlari, and Y. Pal, *Building and deploying a cyberinfrastructure for the data-driven design of chemical systems and the exploration of chemical space,* Molecular Simulation **44**, 921 (2018).

[3] B. Sanchez-Lengeling, L. M. Roch, J. D. Perea, S. Langner, C. J. Brabec, and A. Aspuru-Guzik, *A Bayesian Approach to Predict Solubility Parameters,* Advanced Theory and Simulations **2**, 1800069 (2019).

[4] D. P. Tabor, L. M. Roch, S. K. Saikin, C. Kreisbeck, D. Sheberla, J. H. Montoya, S. Dwaraknath, M. Aykol, C. Ortiz, H. Tribukait, C. Amador-Bedolla, C. J. Brabec, B. Maruyama, K. A. Persson, and A. Aspuru-Guzik, *Accelerating the discovery of materials for clean energy in the era of smart automation,* Nature Reviews Materials **3**, 5 (2018).

[5] S. Nagasawa, E. Al-Naamani, and A. Saeki, *Computer-Aided Screening of Conjugated Polymers for Organic Solar Cell: Classification by Random Forest,* The Journal of Physical Chemistry Letters **9**, 2639 (2018).

[6] B. Cao, L. A. Adutwum, A. O. Oliynyk, E. J. Luber, B. C. Olsen, A. Mar, and J. M. Buriak, *How To Optimize Materials and Devices via Design of Experiments and Machine Learning: Demonstration Using Organic Photovoltaics,* ACS Nano **12**, 7434 (2018).

[7] S. Sun, N. T. Hartono, Z. D. Ren, F. Oviedo, A. M. Buscemi, M. Layurova, D. X. Chen, T. Ogunfunmi, J. Thapa, S. Ramasamy, C. Settens, B. L. DeCost, A. G. Kusne, Z. Liu, S. I. Tian, I. M. Peters, J.-P. Correa-Baena, and T. Buonassisi, *Accelerated Development of Perovskite-Inspired Materials via High-Throughput Synthesis and Machine-Learning Diagnosis,* Joule **3**, 1437 (2019).

**6**

[8] F. Häse, L. M. Roch, and A. Aspuru-Guzik, *Next-Generation Experimentation with Self-Driving Laboratories,* Trends in Chemistry **1**, 282 (2019).

[9] A. Zakutayev, N. Wunder, M. Schwarting, J. D. Perkins, R. White, K. Munch, W. Tumas, and C. Phillips, *An open experimental database for exploring inorganic materials,* Scientific Data **5**, 180053 (2018).

[10] L. Wilbraham, R. S. Sprick, K. E. Jelfs, and M. A. Zwijnenburg, *Mapping binary copolymer property space with neural networks,* Chemical Science **10**, 4973 (2019).

[11] R. Xia, C. J. Brabec, H.-L. Yip, and Y. Cao, *High-Throughput Optical Screening for Efficient Semitransparent Organic Solar Cells,* Joule (2019), 10.1016/J.JOULE.2019.06.016.

[12] C. Xie, X. Tang, M. Berlinghof, S. Langner, S. Chen, A. Späth, N. Li, R. H. Fink, T. Unruh, and C. J. Brabec, *Robot-Based High-Throughput Engineering of Alcoholic Polymer: Fullerene Nanoparticle Inks for an Eco-Friendly Processing of Organic Solar Cells,* ACS Applied Materials & Interfaces **10**, 23225 (2018).

[13] S. Chen, Y. Hou, H. Chen, X. Tang, S. Langner, N. Li, T. Stubhan, I. Levchuk, E. Gu, A. Osvet, and C. J. Brabec, *Exploring the Stability of Novel Wide Bandgap Perovskites by a Robot Based High Throughput Approach,* Advanced Energy Materials **8**, 1701543 (2018).

[14] A. Kojima, K. Teshima, Y. Shirai, and T. Miyasaka, *Organometal halide perovskites as visible-light sensitizers for photovoltaic cells,* Journal of the American Chemical Society **131**, 6050 (2009).

[15] S. D. Stranks, G. E. Eperon, G. Grancini, C. Menelaou, M. J. Alcocer, T. Leijtens, L. M. Herz, A. Petrozza, and H. J. Snaith, *Electron-hole diffusion lengths exceeding 1 micrometer in an organometal trihalide perovskite absorber,* Science **342**, 341 (2013).

[16] E. Edri, S. Kirmayer, S. Mukhopadhyay, K. Gartsman, G. Hodes, and D. Cahen, *Elucidating the charge carrier separation and working mechanism of $CH_3NH_3PbI_3$-$xClx$ perovskite solar cells,* Nature Communications **5**, 3461 (2014).

[17] NREL, *Best research-cell efficiencies,* (07-2019).

[18] M. Liu, M. B. Johnston, and H. J. Snaith, *Efficient planar heterojunction perovskite solar cells by vapour deposition,* Nature **501**, 395 (2013).

[19] N. Ahn, D.-Y. Son, I.-H. Jang, S. M. Kang, M. Choi, and N.-G. Park, *Highly reproducible perovskite solar cells with average efficiency of 18.3% and best efficiency of 19.7% fabricated via lewis base adduct of lead (ii) iodide,* Journal of the American Chemical Society **137**, 8696 (2015).

[20] J.-P. Correa-Baena, M. Anaya, G. Lozano, W. Tress, K. Domanski, M. Saliba, T. Matsui, T. J. Jacobsson, M. E. Calvo, A. Abate, M. Graetzel, M. Hernan, and A. Hagfeldt, *Unbroken perovskite: Interplay of morphology, electro-optical properties, and ionic movement,* Advanced Materials **28**, 5031 (2016).

**6**

[21] M. Saliba, T. Matsui, J.-Y. Seo, K. Domanski, J.-P. Correa-Baena, M. K. Nazeeruddin, S. M. Zakeeruddin, W. Tress, A. Abate, A. Hagfeldt, and M. Graetzel, *Cesium-containing triple cation perovskite solar cells: improved stability, reproducibility and high efficiency,* Energy & Environmental Science **9**, 1989 (2016).

[22] W. Nie, H. Tsai, R. Asadpour, J.-C. Blancon, A. J. Neukirch, G. Gupta, J. J. Crochet, M. Chhowalla, S. Tretiak, M. A. Alam, H.-L. Wang, and A. D. Mohite, *High-efficiency solution-processed perovskite solar cells with millimeter-scale grains,* Science **347**, 522 (2015).

[23] C. Momblona, L. Gil-Escrig, E. Bandiello, E. M. Hutter, M. Sessolo, K. Lederer, J. Blochwitz-Nimoth, and H. J. Bolink, *Efficient vacuum deposited pin and nip perovskite solar cells employing doped charge transport layers,* Energy & Environmental Sciences **9**, 3456 (2016).

[24] S. Shao, M. Abdu-Aguye, L. Qiu, L.-H. Lai, J. Liu, S. Adjokatse, F. Jahani, M. E. Kamminga, H. Gert, T. T. Palstra, B. J. Kooi, J. C. Hummelen, and M. A. Loi, *Elimination of the light soaking effect and performance enhancement in perovskite solar cells using a fullerene derivative,* Energy & Environmental Science **9**, 2444 (2016).

[25] J. Choi, S. Song, M. T. Hörantner, H. J. Snaith, and T. Park, *Well-Defined Nanostructured, Single-Crystalline $TiO_2$ Electron Transport Layer for Efficient Planar Perovskite Solar Cells,* ACS nano **10**, 6029 (2016).

[26] H. Zhou, Q. Chen, G. Li, S. Luo, T.-b. Song, H.-S. Duan, Z. Hong, J. You, Y. Liu, and Y. Yang, *Interface engineering of highly efficient perovskite solar cells,* Science **345**, 542 (2014).

[27] J.-P. Correa-Baena, W. Tress, K. Domanski, E. H. Anaraki, S.-H. Turren-Cruz, B. Roose, P. P. Boix, M. Gratzel, M. Saliba, A. Abate, and A. Hagfeldt, *Identifying and suppressing interfacial recombination to achieve high open-circuit voltage in perovskite solar cells,* Energy & Environmental Science **10**, 1207 (2017).

[28] H. Tan, A. Jain, O. Voznyy, X. Lan, F. P. G. de Arquer, J. Z. Fan, R. Quintero-Bermudez, M. Yuan, B. Zhang, Y. Zhao, F. Fan, P. Li, L. N. Quan, Y. Zhao, Z.-H. Lu, Z. Yang, S. Hoogland, and E. H. Sargent, *Efficient and stable solution-processed planar perovskite solar cells via contact passivation,* Science **355**, 722 (2017).

[29] M. B. Johnston and L. M. Herz, *Hybrid perovskites for photovoltaics: Charge-carrier recombination, diffusion, and radiative efficiencies,* Accounts of Chemical Research **49**, 146 (2015).

[30] W. Tress, N. Marinova, O. Inganäs, M. K. Nazeeruddin, S. M. Zakeeruddin, and M. Graetzel, *Predicting the Open-Circuit Voltage of $CH_3NH_3PbI_3$ Perovskite Solar Cells Using Electroluminescence and Photovoltaic Quantum Efficiency Spectra: the Role of Radiative and Non-Radiative Recombination,* Advanced Energy Materials **5**, 1400812 (2015).

**6**

[31] T. S. Sherkar, C. Momblona, L. Gil-Escrig, H. J. Bolink, and L. J. A. Koster, *Improving the performance of perovskite solar cells: Insights from a validated device model,* Advanced Energy Materials , 1602432 (2017).

[32] T. S. Sherkar, C. Momblona, L. Gil-Escrig, J. Ávila, M. Sessolo, H. J. Bolink, and L. J. A. Koster, *Recombination in perovskite solar cells: Significance of grain boundaries, interface traps and defect ions,* ACS Energy Letters **2**, 1214 (2017).

[33] M. Stolterfoht, C. M. Wolff, J. A. Márquez, S. Zhang, C. J. Hages, D. Rothhardt, S. Albrecht, P. L. Burn, P. Meredith, T. Unold, and D. Neher, *Visualization and suppression of interfacial recombination for high-efficiency large-area pin perovskite solar cells,* Nature Energy **3**, 847 (2018).

[34] M. Stolterfoht, P. Caprioglio, C. M. Wolff, J. A. Márquez, J. Nordmann, S. Zhang, D. Rothhart, U. Hörmann, A. Redinger, L. Kegelmann, S. Albrecht, T. Kirchartz, M. Saliba, T. Unold, and D. Neher, *The perovskite/transport layer interfaces dominate non-radiative recombination in efficient perovskite solar cells,* (2018), arXiv:1810.01333 .

[35] R. Fang, S. Wu, W. Chen, Z. Liu, S. Zhang, R. Chen, Y. Yue, L. Deng, Y.-B. Cheng, L. Han, and W. Chen, *[6,6]-Phenyl-$C_{61}$-Butyric Acid Methyl Ester/Cerium Oxide Bilayer Structure as Efficient and Stable Electron Transport Layer for Inverted Perovskite Solar Cells,* ACS Nano **12**, 2403 (2018).

[36] S. Sidhik, A. Cerdan Pasarán, D. Esparza, T. López Luke, R. Carriles, and E. De la Rosa, *Improving the Optoelectronic Properties of Mesoporous $TiO_2$ by Cobalt Doping for High-Performance Hysteresis-free Perovskite Solar Cells,* ACS Appl Mater Interfaces **10**, 3571 (2018).

[37] G. Yang, C. Chen, F. Yao, Z. Chen, Q. Zhang, X. Zheng, J. Ma, H. Lei, P. Qin, L. Xiong, W. Ke, G. Li, Y. Yan, and G. Fang, *Effective Carrier-Concentration Tuning of $SnO_2$ Quantum Dot Electron-Selective Layers for High-Performance Planar Perovskite Solar Cells,* Advanced Materials **30**, 1706023 (2018).

[38] C. Wehrenfennig, G. E. Eperon, M. B. Johnston, H. J. Snaith, and L. M. Herz, *High charge carrier mobilities and lifetimes in organolead trihalide perovskites,* Advanced Materials **26**, 1584 (2014).

[39] H.-S. Duan, H. Zhou, Q. Chen, P. Sun, S. Luo, T.-B. Song, B. Bob, and Y. Yang, *The identification and characterization of defect states in hybrid organic–inorganic perovskite photovoltaics,* Physical Chemistry Chemical Physics **17**, 112 (2015).

[40] S. D. Stranks, V. M. Burlakov, T. Leijtens, J. M. Ball, A. Goriely, and H. J. Snaith, *Recombination kinetics in organic-inorganic perovskites: excitons, free charge, and subgap states,* Physical Review Applied **2**, 034007 (2014).

[41] Y. Yamada, T. Nakamura, M. Endo, A. Wakamiya, and Y. Kanemitsu, *Photocarrier recombination dynamics in perovskite $CH_3NH_3PbI_3$ for solar cell applications,* Journal of the American Chemical Society **136**, 11610 (2014).

**6**

[42] V. D'Innocenzo, A. R. Srimath Kandada, M. De Bastiani, M. Gandini, and A. Petrozza, *Tuning the light emission properties by band gap engineering in hybrid lead halide perovskite,* Journal of the American Chemical Society **136**, 17730 (2014).

[43] T. Leijtens, G. E. Eperon, A. J. Barker, G. Grancini, W. Zhang, J. M. Ball, A. R. S. Kandada, H. J. Snaith, and A. Petrozza, *Carrier trapping and recombination: the role of defect physics in enhancing the open circuit voltage of metal halide perovskite solar cells,* Energy & Environmental Sciences **9**, 3472 (2016).

[44] W. Zhang, V. M. Burlakov, D. J. Graham, T. Leijtens, A. Osherov, V. Bulović, H. J. Snaith, D. S. Ginger, and S. D. Stranks, *Photo-induced halide redistribution in organic-inorganic perovskite films,* Nature Communications **7**, 11683 (2016).

[45] L. J. A. Koster, V. D. Mihailetchi, R. Ramaker, and P. W. M. Blom, *Light intensity dependence of open-circuit voltage of polymer: fullerene solar cells,* Applied Physics Letters **86**, 123509 (2005).

[46] M. M. Mandoc, F. B. Kooistra, J. C. Hummelen, B. De Boer, and P. W. M. Blom, *Effect of traps on the performance of bulk heterojunction organic solar cells,* Applied Physics Letters **91**, 263505 (2007).

[47] T. S. Sherkar, V. M. Le Corre, M. Koopmans, F. Wobben, and L. J. A. Koster, *SIMsalabim GitHub repository,* (2020).

[48] W. Tress, *Perovskite solar cells on the way to their radiative efficiency limit–insights into a success story of high open-circuit voltage and low recombination,* Advanced Energy Materials , 1602358 (2017).

[49] Z. Wang, Q. Lin, B. Wenger, M. G. Christoforo, Y.-H. Lin, M. T. Klug, M. B. Johnston, L. M. Herz, and H. J. Snaith, *High irradiance performance of metal halide perovskites for concentrator photovoltaics,* Nature Energy **3**, 855 (2018).

[50] E. A. Schiff, *Low-mobility solar cells: a device physics primer with application to amorphous silicon,* Solar Energy Materials and Solar Cells **78**, 567 (2003).

[51] C. L. Davies, M. R. Filip, J. B. Patel, T. W. Crothers, C. Verdi, A. D. Wright, R. L. Milot, F. Giustino, M. B. Johnston, and L. M. Herz, *Bimolecular recombination in methylammonium lead triiodide perovskite is an inverse absorption process,* Nature Communications **9**, 293 (2018).

[52] F. Ambrosio, J. Wiktor, F. De Angelis, and A. Pasquarello, *Origin of low electron–hole recombination rate in metal halide perovskites,* Energy & Environmental Science **11**, 101 (2018).

[53] C. Wolf, H. Cho, Y.-H. Kim, and T.-W. Lee, *Polaronic Charge Carrier-Lattice Interactions in Lead Halide Perovskites,* ChemSusChem **10**, 3705 (2017).

[54] X. Zhang, J.-X. Shen, W. Wang, and C. G. Van de Walle, *First-Principles Analysis of Radiative Recombination in Lead-Halide Perovskites,* ACS Energy Letters **3**, 2329 (2018).

**6**

[55] J. Simmons and G. Taylor, *Nonequilibrium steady-state statistics and associated effects for insulators and semiconductors containing an arbitrary distribution of traps,* Physical Review B **4**, 502 (1971).

[56] J. M. Azpiroz, E. Mosconi, J. Bisquert, and F. De Angelis, *Defect migration in methylammonium lead iodide and its role in perovskite solar cell operation,* Energy & Environmental Science **8**, 2118 (2015).

[57] A. Buin, R. Comin, J. Xu, A. H. Ip, and E. H. Sargent, *Halide-Dependent Electronic Structure of Organolead Perovskite Materials,* Chemistry of Materials **27**, 4405 (2015).

[58] G. A. H. Wetzelaer and P. W. M. Blom, *Ohmic current in organic metal-insulator-metal diodes revisited,* Physical Review B **89**, 241201 (2014).

[59] Y. Zhou, J. Chen, O. M. Bakr, and H.-T. Sun, *Metal-Doped Lead Halide Perovskites: Synthesis, Properties, and Optoelectronic Applications,* Chemistry of Materials **30**, 6589 (2018).

[60] S. Shao, J. Liu, G. Portale, H.-H. Fang, G. R. Blake, G. H. ten Brink, L. J. A. Koster, and M. A. Loi, *Highly Reproducible Sn-Based Hybrid Perovskite Solar Cells with 9% Efficiency,* Advanced Energy Materials **8**, 1702019 (2018).

[61] S. Kahmann, S. Shao, and M. A. Loi, *Cooling, Scattering, and Recombination-The Role of the Material Quality for the Physics of Tin Halide Perovskites,* Advanced Functional Materials , 1902963 (2019).

[62] N. Tessler and Y. Vaynzof, *Insights from device modeling of perovskite solar cells,* ACS Energy Letters **5**, 1260 (2020).

[63] V. M. Le Corre, M. Stolterfoht, L. Perdigón Toro, M. Feuerstein, C. Wolff, L. Gil-Escrig, H. J. Bolink, D. Neher, and L. J. A. Koster, *Charge Transport Layers Limiting the Efficiency of Perovskite Solar Cells: How To Optimize Conductivity, Doping, and Thickness,* ACS Applied Energy Materials **2**, 6280 (2019).

[64] M. T. Neukom, A. Schiller, S. Züfle, E. Knapp, J. Ávila, D. Pérez-del Rey, C. Dreessen, K. P. Zanoni, M. Sessolo, H. J. Bolink, and B. Ruhstaller, *Consistent Device Simulation Model Describing Perovskite Solar Cells in Steady-State, Transient, and Frequency Domain,* ACS Applied Materials & Interfaces **11**, 23320 (2019).

[65] P. Calado, A. M. Telford, D. Bryant, X. Li, J. Nelson, B. C. O'Regan, and P. R. Barnes, *Evidence for ion migration in hybrid perovskite solar cells with minimal hysteresis,* Nature Communications **7**, 13831 (2016).

[66] F. Pedregosa, G. Varoquaux, A. Gramfort, V. Michel, B. Thirion, O. Grisel, M. Blondel, P. Prettenhofer, R. Weiss, V. Dubourg, J. Vanderplas, A. Passos, D. Cournapeau, M. Brucher, M. Perrot, and E. Duchesnay, *Scikit-learn: Machine learning in Python,* Journal of Machine Learning Research **12**, 2825 (2011).

[67] P. Caprioglio, M. Stolterfoht, C. M. Wolff, T. Unold, B. Rech, S. Albrecht, and D. Ne-her, *On the Relation between the Open-Circuit Voltage and Quasi-Fermi Level Split-ting in Efficient Perovskite Solar Cells,* Advanced Energy Materials **9**, 1901631 (2019).

[68] V. M. Le Corre, *Perovskite-Device-Doctor GitHub repository,* (2020).

**6**

# A

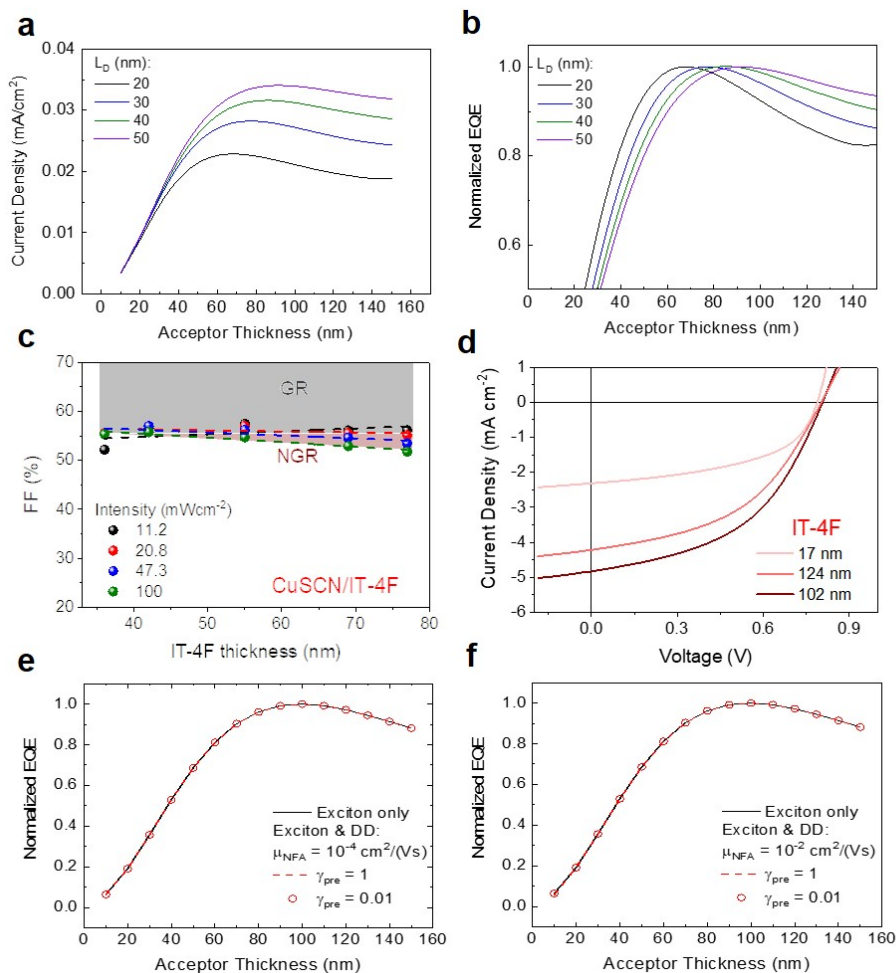# APPENDIX A: LONG-RANGE EXCITON DIFFUSION IN MOLECULAR NON-FULLERENE ACCEPTORS

Figure A.1: Simulated evolution of the photocurrent density. a, depending on $L_D$ shows that it influences the magnitude of the photocurrent. b, More importantly, it strongly influences the shape of the normalized EQE vs thickness by setting its maximum and the decay trend at high thicknesses. Hence fitting this curve is the right approach to get the best possible estimation of $L_D$.
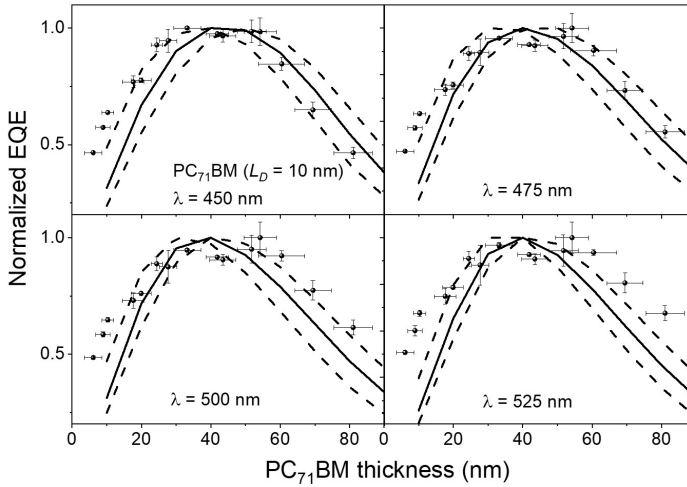
Figure A.2: EQE of CuSCN/PC$_{71}$BM bilayer devices under variation of the acceptor layer thickness for the excitation wavelength $\lambda$: a, 450 nm. b, 475 nm. c, 500 nm. d, 525 nm. The experimental data (circles) are fitted (solid lines) for all thickness. $L_D$ obtained from the fitting: 10 nm.
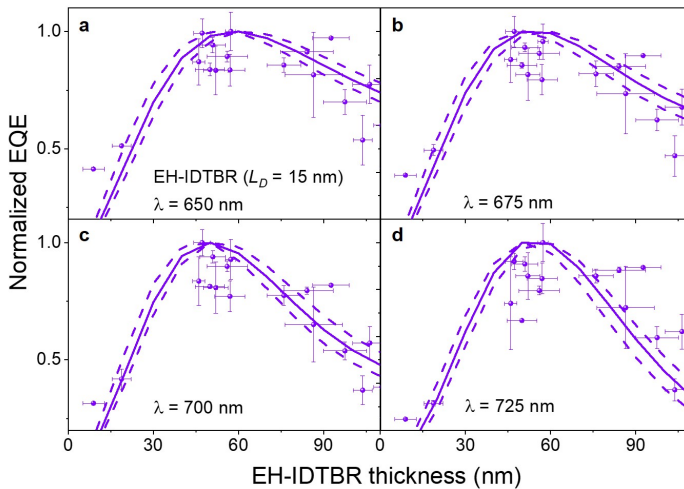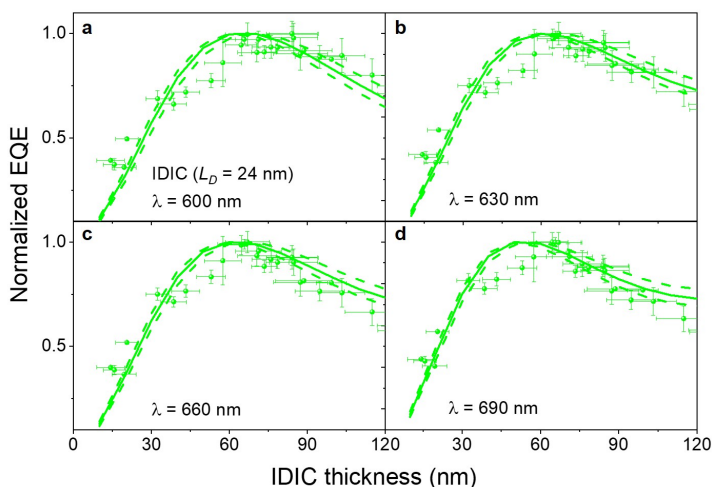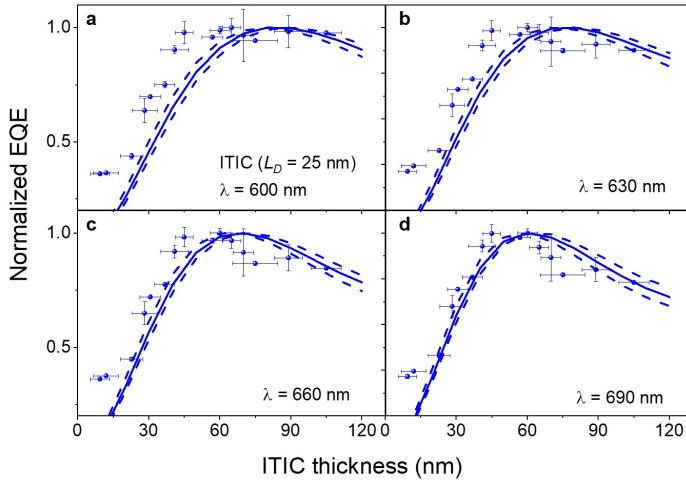


Figure A.3: EQE of CuSCN/EH-IDTBR bilayer devices under variation of the acceptor layer thickness for the excitation wavelength $\lambda$: a, 650 nm. b, 675 nm. c, 700 nm. d, 725 nm. The experimental data (circles) are fitted (solid lines) for all thickness. $L_D$ obtained from the fitting: 15 nm.
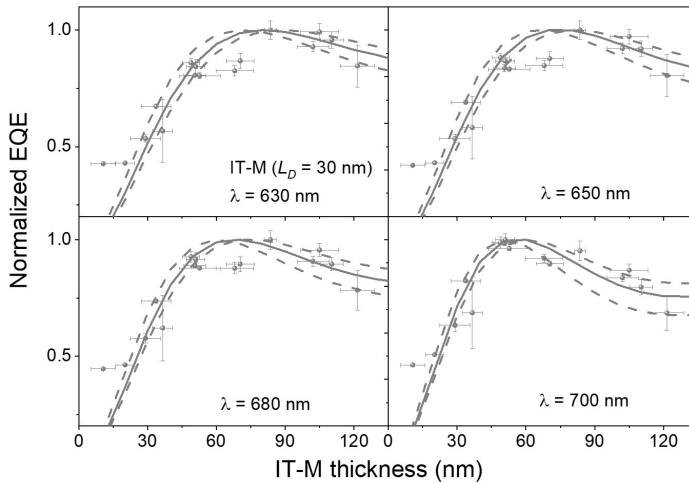
**A**
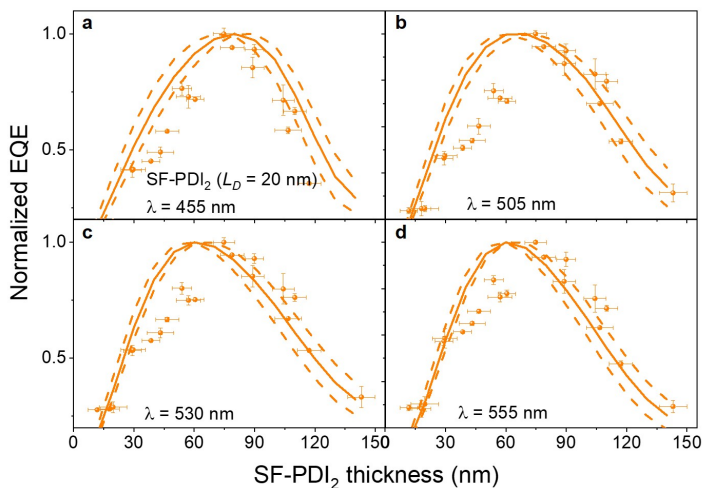


Figure A.4: EQE of CuSCN/SF-PDI2 bilayer devices under variation of the acceptor layer thickness for the excitation wavelength $\lambda$: a, 455 nm. b, 505 nm. c, 530 nm. d, 555 nm. The experimental data (circles) are fitted (solid lines) for all thickness. $L_D$ obtained from the fitting: 20 nm.



Figure A.5: EQE of CuSCN/IDIC bilayer devices under variation of the acceptor layer thickness for the excitation wavelength $\lambda$: a, 600 nm. b, 630 nm. c, 660 nm. d, 690 nm. The experimental data (circles) are fitted (solid lines) for all thickness. $L_D$ obtained from the fitting: 24 nm.
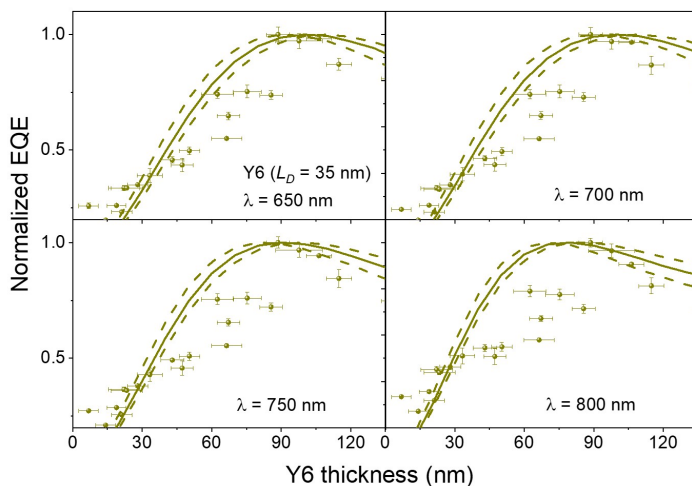
Figure A.6: EQE of CuSCN/ITIC bilayer devices under variation of the acceptor layer thickness for the excitation wavelength $\lambda$: a, 600 nm. b, 630 nm. c, 660 nm. d, 690 nm. The experimental data (circles) are fitted (solid lines) for all thickness. $L_D$ obtained from the fitting: 25 nm.



Figure A.7: EQE of CuSCN/IT-M bilayer devices under variation of the acceptor layer thickness for the excitation wavelength $\lambda$: a, 630 nm. b, 650 nm. c, 680 nm. d, 700 nm. The experimental data (circles) are fitted (solid lines) for all thickness. $L_D$ obtained from the fitting: 30 nm.
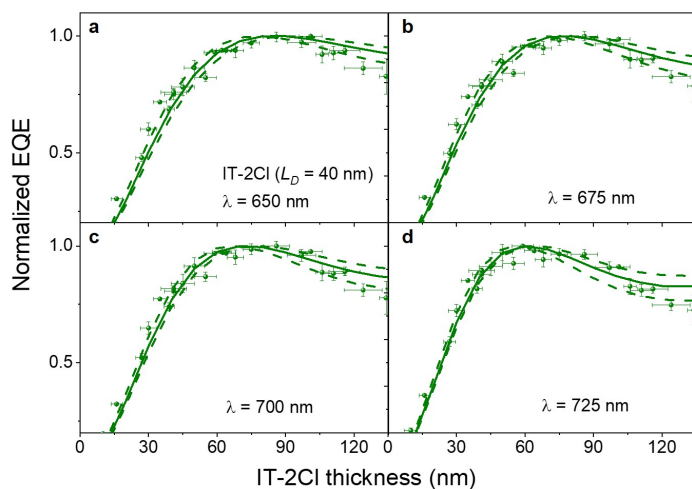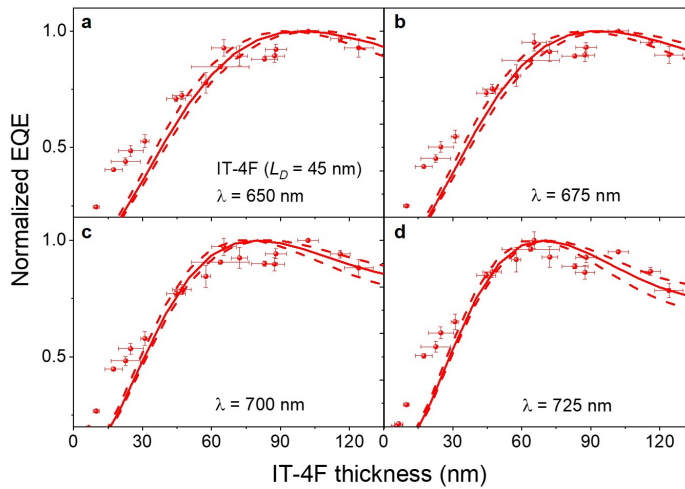
Figure A.8: EQE of CuSCN/Y6 bilayer devices under variation of the acceptor layer thickness for the excitation wavelength $\lambda$: a, 650 nm. b, 700 nm. c, 750 nm. d, 800 nm. The experimental data (circles) are fitted (solid lines) for all thickness. $L_D$ obtained from the fitting: 35 nm.



Figure A.9: EQE of CuSCN/IT-2Cl bilayer devices under variation of the acceptor layer thickness for the excitation wavelength $\lambda$: a, 650 nm. b, 675 nm c, 700 nm. d, 725 nm. The experimental data (circles) are fitted (solid lines) for all thickness. $L_D$ obtained from the fitting: 40 nm.

Figure A.10: EQE of CuSCN/IT-4F bilayer devices under variation of the acceptor layer thickness for the excitation wavelength $\lambda$: a, 650 nm. b, 675 nm. c, 700 nm. d, 725 nm. The experimental data (circles) are fitted (solid lines) for all thickness. $L_D$ obtained from the fitting: 45 nm.

# B

## APPENDIX B: CHARGE CARRIER EXTRACTION IN ORGANIC SOLAR CELLS GOVERNED BY STEADY-STATE MOBILITIES
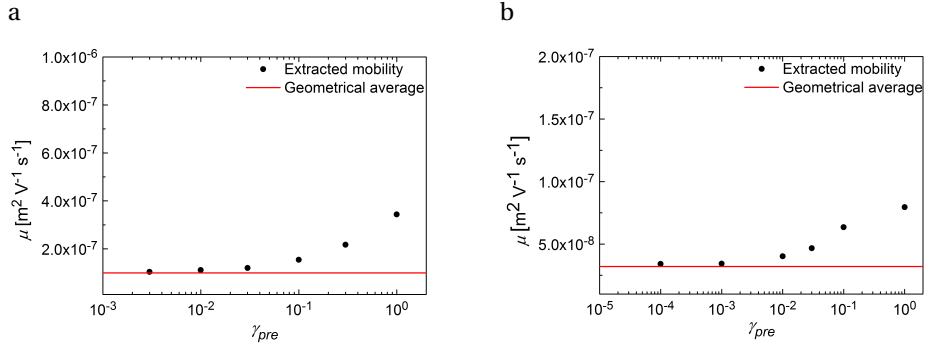
B

a

b



Figure B.1: Influence of bimolecular recombination on measured mobility for balanced (a) and unbalanced mobilities with $\mu_n / \mu_p = 10$ (b).
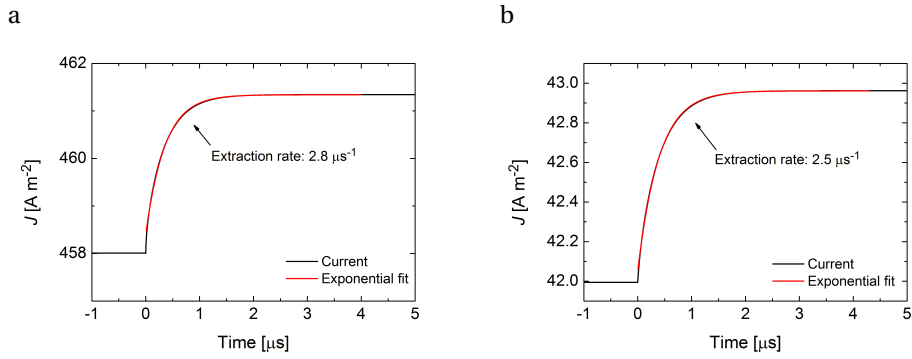
a

b



Figure B.2: Simulated current decay for different injection barriers on the extraction rate, (a) no barrier and (b) a barrier of 0.2 eV. One can note that the extracted lifetime is very similar in both cases leading to the same mobility. Thus, the extracted mobility does not depend strongly on the injection barrier.

Table B.1: Parameters used in the drift-diffusion for appendix figure B.7

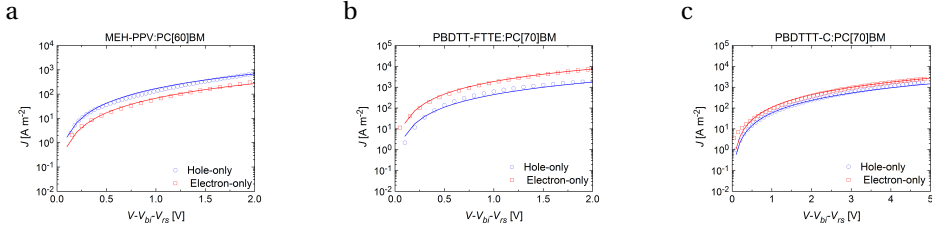| Parameter | Symbol | Value |
|---|---|---|
| Band gap | $E_{gap}$ | 1 eV |
| Effective density of states | $N_{cv}$ | $2.5 \times 10^{19}$ cm$^{-3}$ |
| Thickness | L | 100 $\mu m$ |
| Mobility | $\mu$ | $3 \times 10^{-4}$ cm$^{-2}$ V$^{-1}$ s$^{-1}$ |
| Relative dielectric constant | $\epsilon_r$ | 4 |
| Langevin recombination prefactor | $\gamma_{pre}$ | $3 \times 10^{-2}$ |
| Contact injection barrier | $\phi$ | 0.15 eV |

114

Figure B.3: Current-voltage curves of MEH-PPV:PC$_{61}$BM (a), PBDTT-FTTE:PC$_{71}$BM (b) and PBDTTT-C:PC$_{71}$BM (c) hole-only and electron-only devices. Symbols represent experimental data and the solid lines represent fit of the experimental data, performed for space charge limited current with thes Mott-Gurney law : $J = \frac{9}{8}\epsilon\mu\frac{V^2}{L^3}$ The mobilities of holes and electrons are thus extracted as fit parameters from the current-voltage curves.
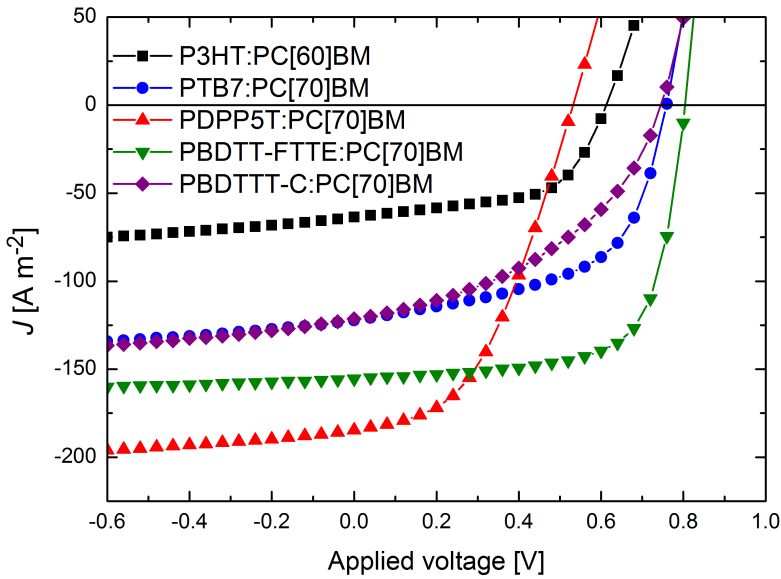


Figure B.4: Current-voltage curves of P3HT:PC$_{61}$BM, PTB7:PC$_{71}$BM, PDPP5T:PC$_{71}$BM, PBDTT-FTTE:PC$_{71}$BM and PBDTTT-C:PC$_{71}$BM solar cells. The measurements were done using a Steuernagel SolarConstant 1200 metal halide lamp; a silicon reference cell was employed to correct for spectral mismatch with AM1.5G spectrum and set the intensity of the lamp to 1 sun and recorded using a computer-controlled Keithley source meter in N2 atmosphere.
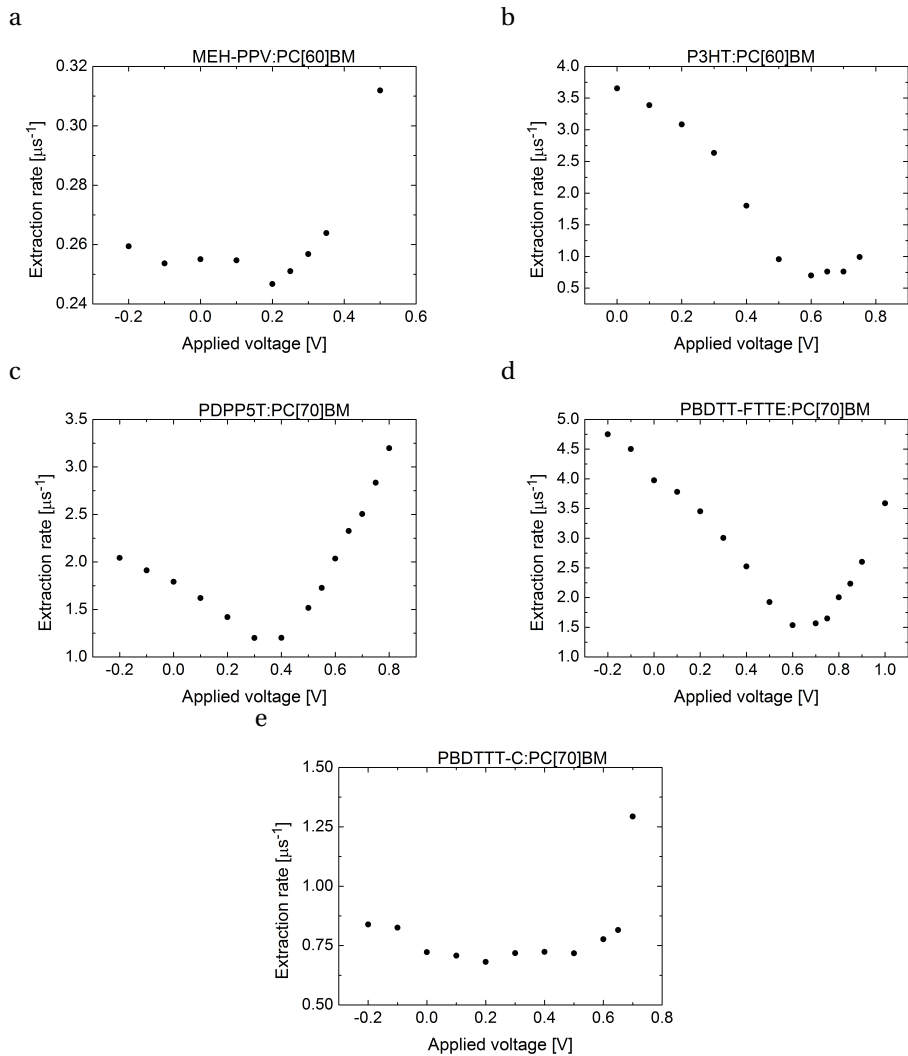
**B**

a



b



c



d



e



Figure B.5: Experimental results for different polymer:fullerene blends solar cell showing the extraction rate calculated with equation 3.5.

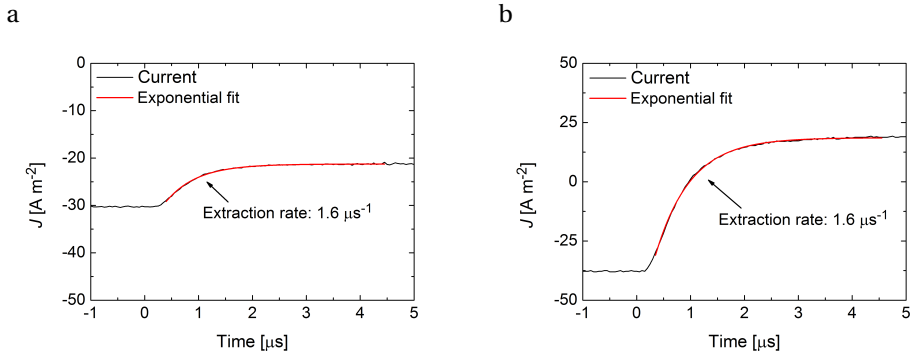a



b



Figure B.6: Current decay of PTB7:PC$_{71}$BM device for small reduction of the light intensity (a) and for light to dark perturbation (b). One can note that the same lifetime can be extracted leading to the same mobility in both experiments. Thus, it shows that the dynamics of all the extracted charge carriers can be related to the steady-state mobilities.
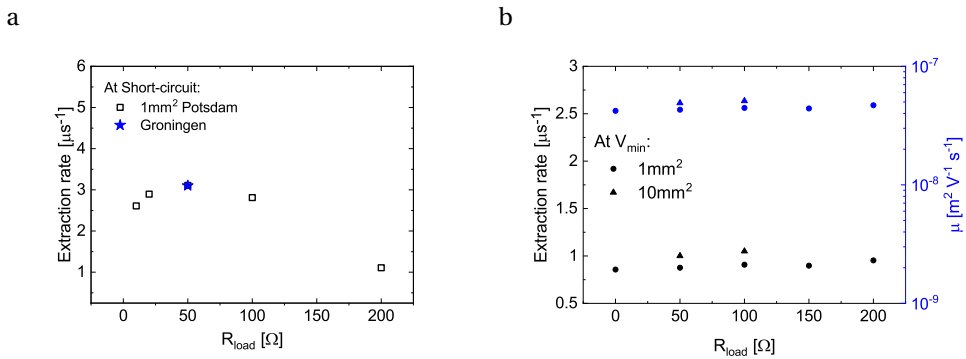
a



b



Figure B.7: a) Experimental extraction rate at short circuit condition of a PTB7:PC$_{71}$BM device (1 mm$^2$) with different load resistance also showing that RC-time does not affect the measurement when R < 200 $\Omega$. b) Extraction rates (black) and extracted mobilities (blue) from PTB7-like simulations including the influence of the load resistance of the measurement set-up and the capacitive effect of the device showing that the resistance and the area have a very small influence on our measurement at Vmin demonstrating the RC-effect does not strongly affect the extraction rate and the calculated mobility.

# C

## APPENDIX C: PITFALLS OF SPACE-CHARGE-LIMITED CURRENT TECHNIQUE FOR PEROVSKITES

Table C.1: Parameters used in the drift-diffusion for figure 1, figure 2 (b)-(c)

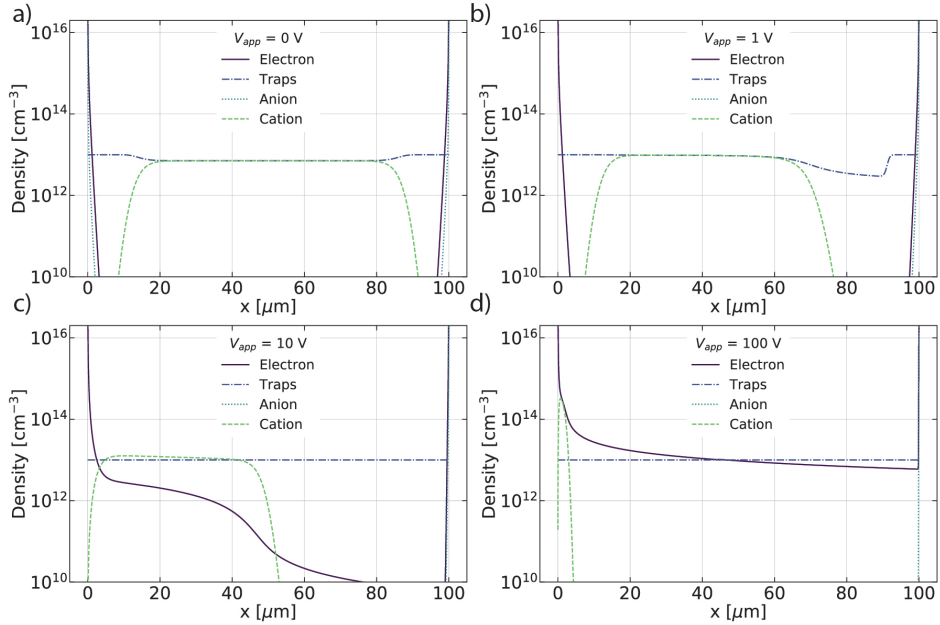| Parameter | Symbol | Value |
|---|---|---|
| **Perovskite Layer** | | |
| Conduction Band | $E_c$ | 3 eV |
| Valence Band | $E_v$ | 5 eV |
| Band gap | $E_{gap}$ | 2 eV |
| Effective density of states | $N_{cv}$ | $1 \times 10^{18}$ cm$^{-3}$ |
| Thickness | L | 100 $\mu$m |
| Mobility | $\mu$ | 10 cm$^{-2}$ V$^{-1}$ s$^{-1}$ |
| Relative dielectric constant | $\epsilon_r$ | 25.5 |
| Ion density | $n_{ion}$ | 0 or $10^{11} - 10^{14}$ cm$^{-3}$ |
| **Recombination** | | |
| Band-to-band recombination rate constant | $\gamma$ | $10^{-10}$ cm$^3$ s$^{-1}$ |
| Trap density | $n_t$ | 0 or $10^{11} - 10^{14}$ cm$^{-3}$ |
| Trapping level depth below $E_c$ | $E_{trap}$ | 1 eV |
| Electron (hole) capture coefficient | $C_n(p)$ | $10^{-7}$ cm$^3$ s$^{-1}$ |
| **Contact** | | |
| Contact work function | | 3.0 eV |

Figure C.1: (a-d) Density of electron, filled-traps, anion and cation for different applied voltage for a steady-state scan.

Table C.2: Parameters used in the drift-diffusion fit of the 160 $\mu$m thick single crystal MAPbBr$_3$ in figure 3 (a).

| Parameter | Symbol | Value |
|---|---|---|
| **Perovskite Layer** | | |
| Conduction Band | $E_c$ | 3.4 eV |
| Valence Band | $E_v$ | 5.6 eV |
| Band gap | $E_{gap}$ | 2.2 eV |
| Effective density of states | $N_{cv}$ | $1 \times 10^{18}$ cm$^{-3}$ |
| Thickness | L | 160 $\mu$m |
| Mobility | $\mu$ | 12.9 cm$^{-2}$ V$^{-1}$ s$^{-1}$ |
| Relative dielectric constant | $\epsilon_r$ | 25.5 |
| Ion density | $n_{ion}$ | $1.09 \times 10^{13}$ cm$^{-3}$ |
| **Recombination** | | |
| Band-to-band recombination rate constant | $\gamma$ | $10^{-10}$ cm$^3$ s$^{-1}$ |
| Trap density | $n_t$ | $1.32 \times 10^{13}$ cm$^{-3}$ |
| Trapping level depth below $E_c$ | $E_{trap}$ | 0.54 eV |
| Electron (hole) capture coefficient | $C_n(p)$ | $10^{-7}$ cm$^3$ s$^{-1}$ |
| **Contact** | | |
| Contact work function | | 3.82 eV |
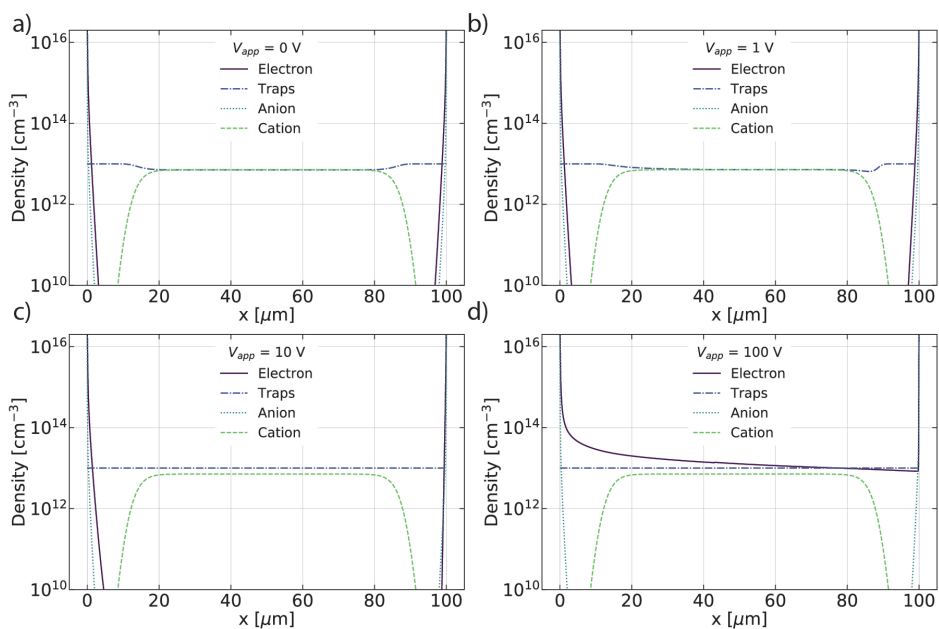
Figure C.2: (a-d) Density of electron, filled-traps, anion and cation for different applied voltage for a pulsed scan where the ion distribution is kept fixed at 0 V condition. We can note that the distribution of filled traps and electron is not too different between steady-state and pulsed scan which explain the very similar JV-curves in figure 2 (b).
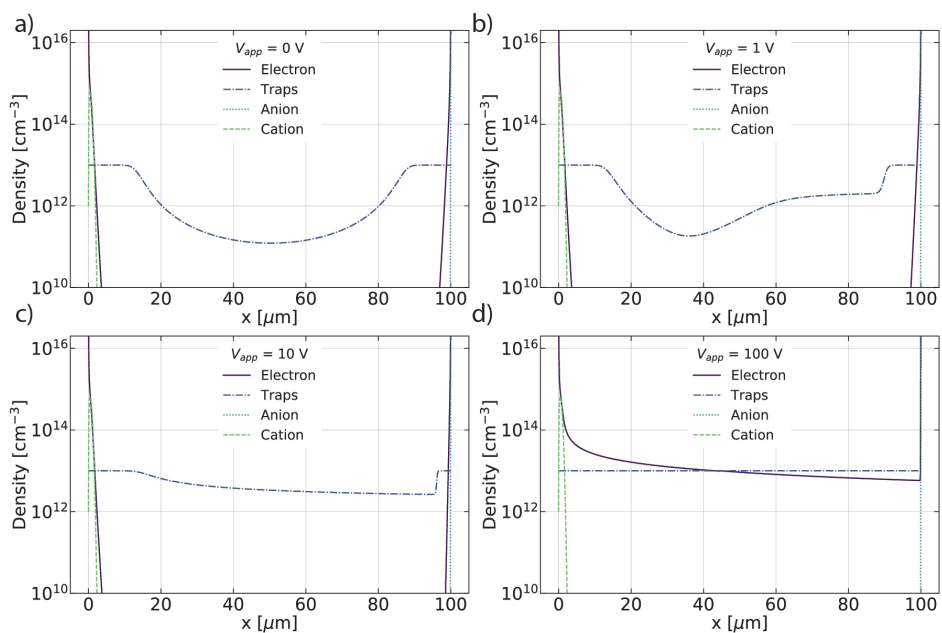
Figure C.3: (a-d) Density of electron, filled-traps, anion and cation for different applied voltage for a backward scan where the ion distribution is kept fixed at 200 V condition. We can note that the distribution of filled traps and electron is significantly affected by the accumulation of cation at the injecting electrode which explain the difference between JV-curves in figure 2 (b).
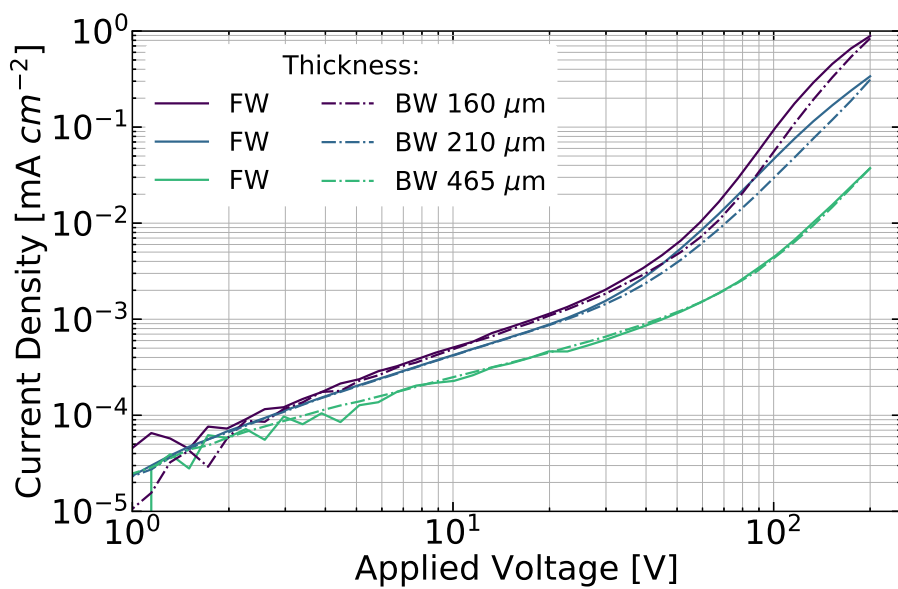
Figure C.4: Pulsed-SCLC JV-curves for 160, 210 and 465 $\mu$m thick MAPbI$_3$ single crystal.
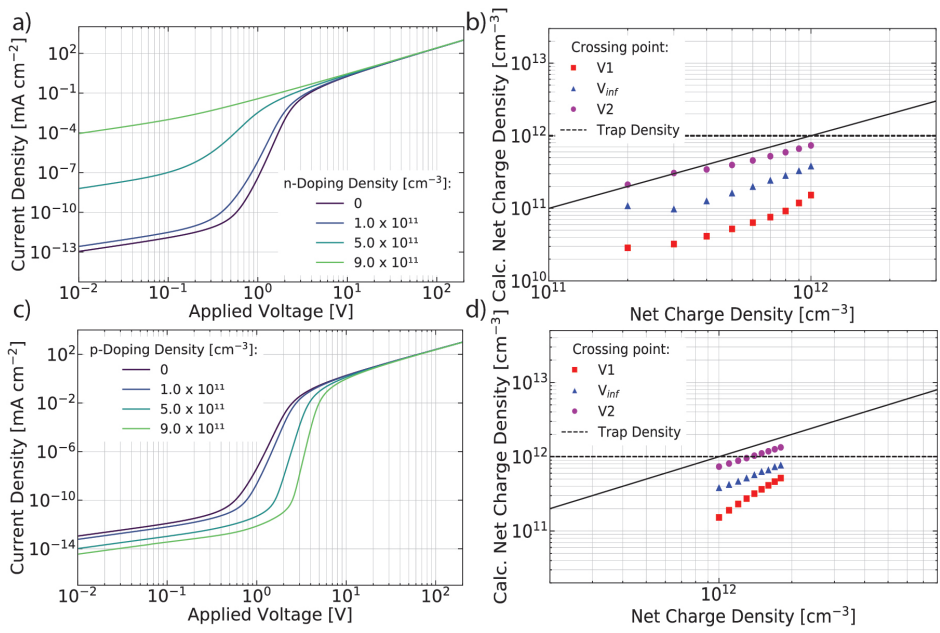
Figure C.5: Simulated pulsed-SCLC JV-curves for n-Doping (a) and p-Doping (c) of the perovskite bulk. (b & c) Extracted net-charge using equation 6. We note again that V2 is the best point to take as $V_{net}$ and that the SCLC really describe the net charge such as $n_{net} = n_t - n_{ion} + N_A - N_D$

# D

## APPENDIX D: CHARGE TRANSPORT LAYERS LIMITING THE EFFICIENCY OF PEROVSKITE SOLAR CELLS: HOW TO OPTIMIZE CONDUCTIVITY, DOPING, AND THICKNESS

**D**

Table D.1: Parameters used in the reference drift-diffusion simulation of the perovskite solar cells, both for the steady-state and transient simulation. Some of these values were chosen looking at reference [1]

| Parameter | Symbol | Value |
|---|---|---|
| **Perovskite Layer** | | |
| Band gap | $E_{gap}$ | 1.6 eV |
| Effective density of states | $N_{cv}$ | $3.1 \times 10^{18}$ cm$^{-3}$ |
| Relative dielectric constant | $\epsilon_r$ | 24.1 |
| Thickness | L | 300 nm |
| Electron mobility | $\mu_n$ | 1 cm$^{-2}$ V$^{-1}$ s$^{-1}$ |
| Hole mobility | $\mu_p$ | 1 cm$^{-2}$ V$^{-1}$ s$^{-1}$ |
| Bimolecular recombination rate constant | $\gamma$ | $1 \times 10^{-9}$ cm$^3$ s$^{-1}$ |
| **Electron transport layer (ETL)** | | |
| Relative dielectric constant | $\epsilon^{ETL}$ | 3.5 |
| Thickness | $L^{ETL}$ | 40 nm |
| Electron mobility | $\mu_n^{ETL}$ | $1 \times 10^{-3}$ cm$^{-2}$ V$^{-1}$ s$^{-1}$ |
| Hole mobility | $\mu_p^{ETL}$ | $1 \times 10^{-3}$ cm$^{-2}$ V$^{-1}$ s$^{-1}$ |
| Barrier for holes | | 0.5 eV |
| **Hole transport layer (HTL)** | | |
| Relative dielectric constant | $\epsilon^{HTL}$ | 3.5 |
| Thickness | $L^{HTL}$ | 40 nm |
| Electron mobility | $\mu_n^{HTL}$ | $1 \times 10^{-3}$ cm$^{-2}$ V$^{-1}$ s$^{-1}$ |
| Hole mobility | $\mu_p^{HTL}$ | $1 \times 10^{-3}$ cm$^{-2}$ V$^{-1}$ s$^{-1}$ |
| Barrier for electrons | | 0.5 eV |

Table D.2: Parameters used in the reference drift-diffusion simulation fit of the PTAA solar cells in figure 5.1.b

| Parameter | Symbol | Value |
|---|---|---|
| **Perovskite Layer** | | |
| Band gap | $E_{gap}$ | 1.6 eV |
| Effective density of states | $N_{cv}$ | $2.6 \times 10^{18}$ cm$^{-3}$ |
| Relative dielectric constant | $\epsilon_r$ | 24.1 |
| Thickness | L | 300 nm |
| Electron mobility | $\mu_n$ | 3.3 cm$^{-2}$ V$^{-1}$ s$^{-1}$ |
| Hole mobility | $\mu_p$ | 7.1 cm$^{-2}$ V$^{-1}$ s$^{-1}$ |
| Bimolecular recombination rate constant | $\gamma$ | $4.7 \times 10^{-9}$ cm$^3$ s$^{-1}$ |
| ETL/perovskite interface trap density | Tr$_{\text{ETL}}$ | $8.4 \times 10^{15}$ cm$^{-3}$ |
| HTL/perovskite interface trap density | Tr$_{\text{HTL}}$ | $1.5 \times 10^{12}$ cm$^{-3}$ |
| Electron(hole) capture coefficient | $C_n(p)$ | 1.1(5.6) $\times 10^{-9}$ cm$^3$ s$^{-1}$ |
| **Electron transport layer (ETL)** | | |
| Relative dielectric constant | $\epsilon^{ETL}$ | 3.5 |
| Thickness | $L^{ETL}$ | 40 nm |
| Electron mobility | $\mu_n^{ETL}$ | $3.4 \times 10^{-2}$ cm$^{-2}$ V$^{-1}$ s$^{-1}$ |
| Barrier for holes | | 0.3 eV |
| **Hole transport layer (HTL)** | | |
| Relative dielectric constant | $\epsilon^{HTL}$ | 3.5 |
| Thickness | $L^{HTL}$ | Vary |
| Hole mobility | $\mu_p^{HTL}$ | $4.9 \times 10^{-4}$ cm$^{-2}$ V$^{-1}$ s$^{-1}$ |
| Doping density | $N_D$ | 0 or $2.8 \times 10^{17}$ cm$^{-3}$ |
| Barrier for electrons | | 0.3 eV |
| **Electrode** | | |
| Anode/cathode injection barrier | | 0.08/0.07 |

Table D.3: Parameters used in the reference drift-diffusion simulation fit of the P3HT solar cells in figure 5.1.e

| Parameter | Symbol | Value |
|---|---|---|
| **Perovskite Layer** | | |
| Band gap | $E_{gap}$ | 1.6 eV |
| Effective density of states | $N_{cv}$ | $1 \times 10^{21}$ cm$^{-3}$ |
| Relative dielectric constant | $\epsilon_r$ | 24.1 |
| Thickness | L | 300 nm |
| Electron mobility | $\mu_n$ | 3.3 cm$^{-2}$ V$^{-1}$ s$^{-1}$ |
| Hole mobility | $\mu_p$ | 7.1 cm$^{-2}$ V$^{-1}$ s$^{-1}$ |
| Bimolecular recombination rate constant | $\gamma$ | $4.7 \times 10^{-9}$ cm$^3$ s$^{-1}$ |
| ETL/perovskite interface trap density | Tr$_{ETL}$ | $2.63 \times 10^{11}$ cm$^{-3}$ |
| HTL/perovskite interface trap density | Tr$_{HTL}$ | $3.0 \times 10^{14}$ cm$^{-3}$ |
| Electron(hole) capture coefficient | $C_n(p)$ | $7.2(1.6) \times 10^{-8}$ cm$^3$ s$^{-1}$ |
| **Electron transport layer (ETL)** | | |
| Relative dielectric constant | $\epsilon^{ETL}$ | 3.5 |
| Thickness | $L^{ETL}$ | 40 nm |
| Electron mobility | $\mu_n^{ETL}$ | $3.4 \times 10^{-2}$ cm$^{-2}$ V$^{-1}$ s$^{-1}$ |
| Barrier for holes | | 0.3 eV |
| **Hole transport layer (HTL)** | | |
| Relative dielectric constant | $\epsilon^{HTL}$ | 3.5 |
| Thickness | $L^{HTL}$ | Vary |
| Hole mobility | $\mu_p^{HTL}$ | $4.0 \times 10^{-3}$ cm$^{-2}$ V$^{-1}$ s$^{-1}$ |
| Doping density | $N_D$ | 0 or $1.5 \times 10^{16}$ cm$^{-3}$ |
| Barrier for electrons | | 0.3 eV |
| **Electrode** | | |
| Anode/cathode injection barrier | | 0.32/0.32 |

Table D.4: Parameters used in the reference drift-diffusion simulation of the perovskite solar cells, both for the steady-state. Some of these values were chosen looking at reference [1]

| Parameter | Symbol | Value |
|---|---|---|
| **Perovskite Layer** | | |
| Thickness | $L$ | 250 - 600 nm |
| Mobility | $\mu$ | $10^{-2}$ - 10 cm$^{-2}$ V$^{-1}$ s$^{-1}$ |
| Bimolecular recombination rate constant | $\gamma$ | $10^{-11} - 10^{-7}$ cm$^3$ s$^{-1}$ |
| Trap density | Tr | 0 or $10^{14} - 10^{17}$ cm$^{-3}$ |
| Capture coefficient | $C_n(p)$ | $10^{-11} - 10^{-5}$ cm$^3$ s$^{-1}$ |
| **Transport layer** | | |
| Thickness | $L^{TL}$ | 20 - 150 nm |
| Mobility | $\mu^{TL}$ | $10^{-4} - 1$ cm$^{-2}$ V$^{-1}$ s$^{-1}$ |

**D**

(a)                              (b)                              (c)
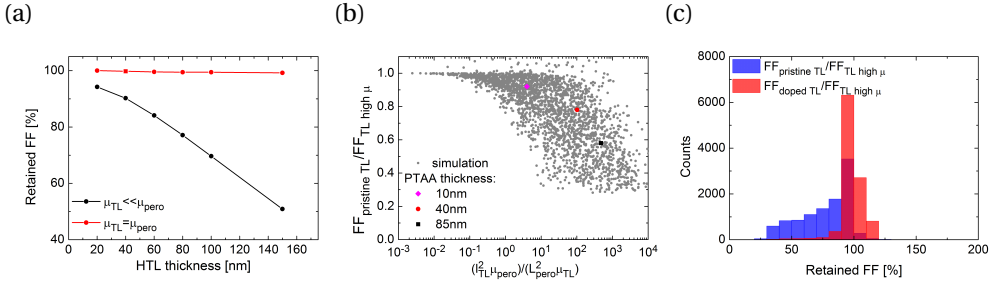


Figure D.1: Simulations (a) show the same linear dependence of the $FF$ with the TL thickness when $\mu_{TL} << \mu_{pero}$. A wide range simulation (b) was also performed to identify when the transport losses become significant, it shows that when $l_{TL} \times \mu_{pero} << L_{pero} \times \mu TL$ then the transport losses due to the TL are negligible however when $l_{TL} \times \mu_{pero} \gtrsim L_{pero} \times \mu_{TL}$ the $FF$ gets reduced and doping the TL becomes necessary. Figure (c) is the summary of the large-scale simulation performed to attest the validity of equation 5.4-5.5 in the paper. For this simulation the doping of the TL is calculated using equation 5.5.

Table D.5: Device performance averaged over a minimum of 5 devices. These devices have also been studied more extensively in ref. 2,3

| PTAA devices | | | | |
|---|---|---|---|---|
| PTAA thickness (nm) | Doping | $V_{OC}$ (V) | $J_{SC}$ (mA cm$^{-2}$) | FF |
| 85 | no | 1.13±0.01 | 19.48±0.27 | 0.49±0.01 |
| 40 | no | 1.14±0.004 | 20.34±0.32 | 0.66±0.03 |
| 40 | yes | 1.15±0.004 | 20.38±0.28 | 0.7623±0.01 |
| 20 | yes | 1.13±0.01 | 21.59±1.09 | 0.77±0.01 |
| 10 | no | 1.11±0.01 | 22.44±0.12 | 0.78±0.01 |
| P3HT devices | | | | |
| P3HT thickness (nm) | Doping | $V_{OC}$ (V) | $J_{SC}$ (mA cm$^{-2}$) | FF |
| 150 | no | 0.85±0.003 | 19.66±0.13 | 0.39±0.01 |
| 150 | yes | 0.88±0.01 | 19.28±0.36 | 0.65±0.03 |
| 80 | no | 0.81±0.02 | 18.46±0.18 | 0.50±0.02 |
| 50 | yes | 0.85±0.004 | 19.17±0.15 | 0.72±0.01 |
| 40 | no | 0.85±0.02 | 18.69±0.13 | 0.65±0.02 |
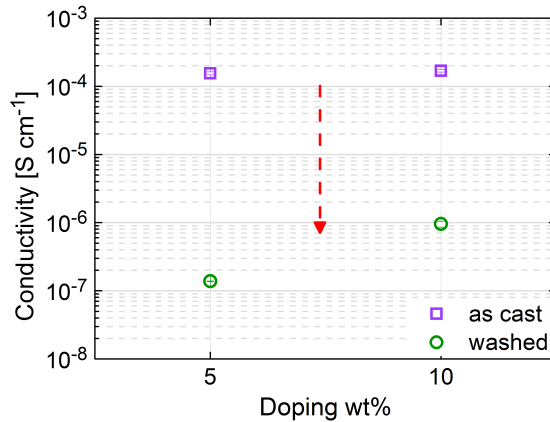


Figure D.2: Conductivity of F4TCNQ doped PTAA layers measured as-cast and after washing by a solution of DMF:DMSO showing a huge decrease upon washing indicating that F4TCNQ is washed away by the solvent.
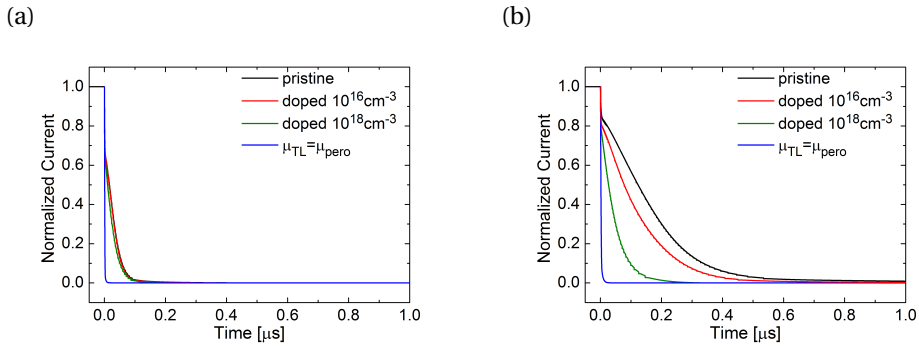
Figure D.3: The simulation results of the extraction experiment (see parameters in table S1) agrees with the experiment showing that, in general, for thin TLs (a) doping has a negligible effect on the extraction whereas for thick TLs (b) there is a significant improvement in the extraction. The blue trace in the simulations results also highlights that independently of the TL thickness using high mobility TL always leads to a faster extraction hence the better performance observed previously.
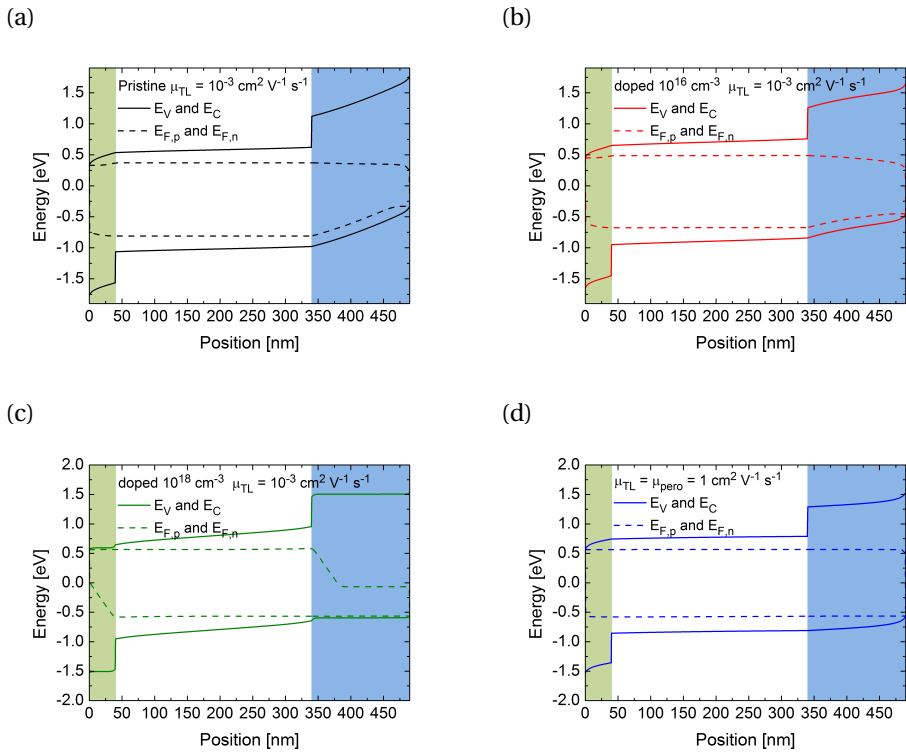


Figure D.4: Band diagram for 150nm thick HTL with different doping (a,b,c) and mobility (a,d) at MPP.

(a)

(b)
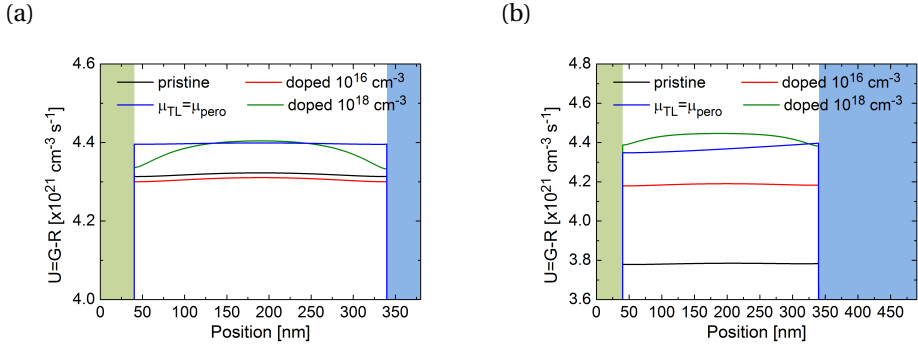


Figure D.5: Thanks to a faster extraction of the charge carriers from the perovskite layer, due to the doping of the TL, the recombination $R$ also decreases, while the homogeneous generation $G$ is kept constant, resulting into a higher net-generation $U$. Simulation results for a 40 nm (a) and 150 nm (b) thick TL with a mobility of $1 \times 10^{-3}$ cm$^2$ V$^{-1}$ s$^{-1}$.

(a)

(b)

(c)

(d)
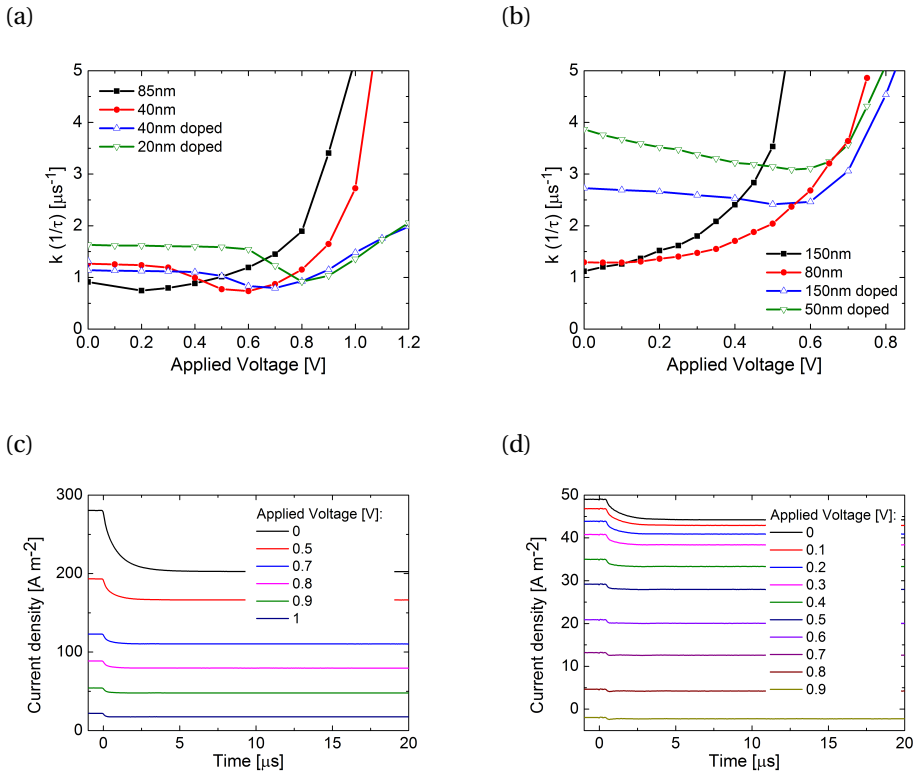


Figure D.6: Extraction rates and current drop of a 40 nm PTAA cell (a) & (c) and a 150 nm P3HT cell (b) & (d) for different applied voltages.

134
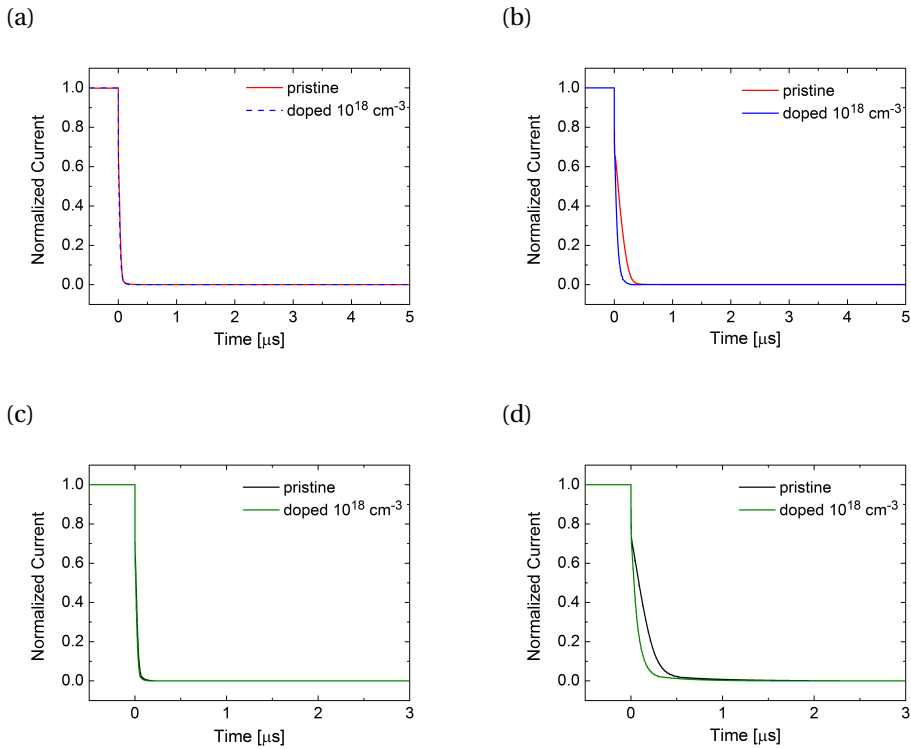
Figure D.7: Current decay including interface traps (a&b) or ions (c&d) with a thin and thick transport layer. Including traps and Shockley-Read-Hall recombination or ions in the simulation gives identical conclusions than when only bimolecular recombination is considered i.e. increasing the TL thickness increases the current decay time, doping of a thin TL does not change the extraction however it has a significant effect for a thick TL. Also the ions were fixed during the transient simulation as they are not expected to move in the microsecond timescale. [4,5]

**D**



Figure D.8: Effect of TL mobility on extraction time.

# REFERENCES

[1] T. S. Sherkar, C. Momblona, L. Gil-Escrig, J. Ávila, M. Sessolo, H. J. Bolink, and L. J. A. Koster, *Recombination in Perovskite Solar Cells: Significance of Grain Boundaries, Interface Traps, and Defect Ions,* ACS Energy Letters **2**, 1214 (2017).
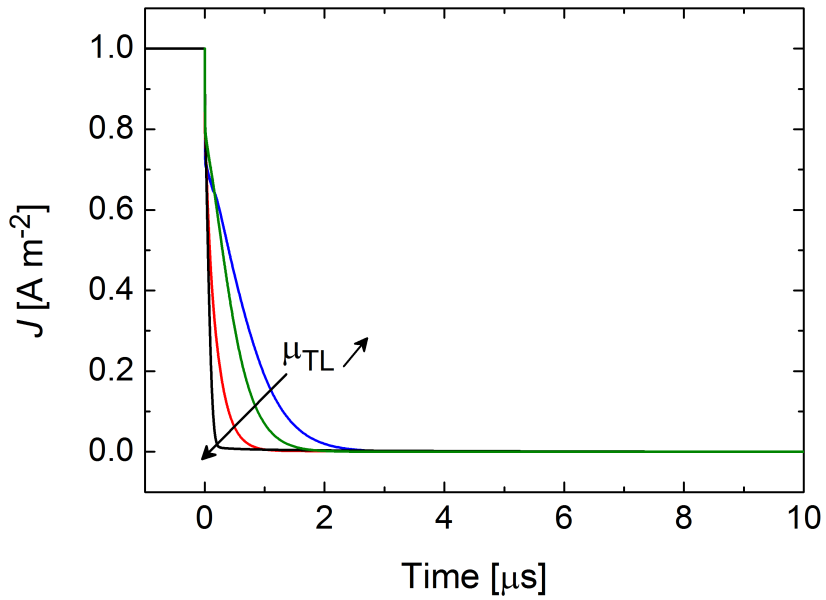
[2] S. Zhang, M. Stolterfoht, A. Armin, Q. Lin, F. Zu, J. Sobus, H. Jin, N. Koch, P. Meredith, P. L. Burn, and D. Neher, *Interface Engineering of Solution-Processed Hybrid Organohalide Perovskite Solar Cells,* ACS Applied Materials & Interfaces **10**, 21681 (2018).

[3] M. Stolterfoht, C. M. Wolff, J. A. Márquez, S. Zhang, C. J. Hages, D. Rothhardt, S. Albrecht, P. L. Burn, P. Meredith, T. Unold, and D. Neher, *Visualization and suppression of interfacial recombination for high-efficiency large-area pin perovskite solar cells,* Nature Energy **3**, 847 (2018).

[4] J. Shi, Y. Li, Y. Li, D. Li, Y. Luo, H. Wu, and Q. Meng, *From Ultrafast to Ultraslow: Charge-Carrier Dynamics of Perovskite Solar Cells,* Joule **2**, 879 (2018).

[5] S. A. Weber, I. M. Hermes, S. H. Turren-Cruz, C. Gort, V. W. Bergmann, L. Gilson, A. Hagfeldt, M. Graetzel, W. Tress, and R. Berger, *How the formation of interfacial charge causes hysteresis in perovskite solar cells,* Energy and Environmental Science **11**, 2404 (2018).

**D**

# E

# APPENDIX E: IDENTIFICATION OF THE DOMINANT RECOMBINATION PROCESS FOR PEROVSKITE SOLAR CELLS BASED ON MACHINE LEARNING

Table E.1: Parameters used in the drift-diffusion simulation for figure 2, S1, S2 and S3.

| Parameter | Symbol | Value |
|---|---|---|
| **Perovskite Layer** | | |
| Band gap | $E_{gap}$ | 1.6 eV |
| Effective density of states | $N_{cv}$ | $2 \times 10^{18}$ cm$^{-3}$ |
| Thickness | L | 300 nm |
| Mobility | $\mu$ | 1 cm$^{-2}$ V$^{-1}$ s$^{-1}$ |
| Relative dielectric constant | $\epsilon_r$ | 24.1 |
| **Transport layer** | | |
| Thickness | $L^{TL}$ | 40 nm |
| Mobility | $\mu^{TL}$ | $10^{-4}$ cm$^{-2}$ V$^{-1}$ s$^{-1}$ |
| Doping density | $N_D^+$ & $N_A^-$ | $10^{13} - 5 \times 10^{18}$ cm$^{-3}$ |
| Relative dielectric constant | $\epsilon_r$ | 3.5 |
| Barrier for the minority carrier | | 0.5 eV |
| **Recombination** | | |
| Bimolecular recombination rate constant | $\gamma$ | $10^{-10}$ cm$^3$ s$^{-1}$ |
| Number of grain boundary | | 0 - 1 |
| Grain boundary trap density | $\Sigma_{T,GB}$ | 0 or $10^6 - 1 \times 10^{11}$ cm$^{-2}$ |
| HTL/perovskite interface hole trap density | $\Sigma_{T,HTL}$ | 0 or $10^6 - 1 \times 10^{11}$ cm$^{-2}$ |
| ETL/perovskite interface electron trap density | $\Sigma_{T,ETL}$ | 0 or $10^6 - 1 \times 10^{11}$ cm$^{-2}$ |
| Electron (hole) capture coefficient | $C_n(p)$ | $10^{-7}$ cm$^3$ s$^{-1}$ |
| **Contact** | | |
| Anode/cathode injection barrier | | 0 eV |

**E**

Table E.2: Parameters used in the large scale drift-diffusion simulation of perovskite solar cells.

| Parameter | Symbol | Value |
|---|---|---|
| **Perovskite Layer** | | |
| Band gap | $E_{gap}$ | 1.6 eV |
| Effective density of states | $N_{cv}$ | $2 \times 10^{18}$ cm$^{-3}$ |
| Thickness | L | 300 - 700 nm |
| Mobility | $\mu$ | $5 \times 10^{-3}$ - 10 cm$^{-2}$ V$^{-1}$ s$^{-1}$ |
| Relative dielectric constant | $\epsilon_r$ | 24.1 |
| **Transport layer** | | |
| Thickness | $L^{TL}$ | 10 - 100 nm |
| Mobility | $\mu^{TL}$ | $10^{-4} - 1$ cm$^{-2}$ V$^{-1}$ s$^{-1}$ |
| Doping density | $N_D^+$ & $N_A^-$ | $10^{14} - 10^{18}$ cm$^{-3}$ |
| Relative dielectric constant | $\epsilon_r$ | 3.5 |
| Barrier for the minority carrier | | 0.5 eV |
| **Recombination** | | |
| Bimolecular recombination rate constant | $\gamma$ | $10^{-11} - 10^{-9}$ cm$^3$ s$^{-1}$ |
| Number of grain boundary | | 0 - 3 |
| Grain boundary trap density | $\Sigma_{T,GB}$ | 0 or $10^7 - 5 \times 10^{11}$ cm$^{-2}$ |
| HTL/perovskite interface hole trap density | $\Sigma_{T,HTL}$ | 0 or $10^7 - 5 \times 10^{11}$ cm$^{-2}$ |
| ETL/perovskite interface electron trap density | $\Sigma_{T,ETL}$ | 0 or $10^7 - 5 \times 10^{11}$ cm$^{-2}$ |
| Electron (hole) capture coefficient | $C_n(p)$ | $10^{-8} - 10^{-6}$ cm$^3$ s$^{-1}$ |
| **Contact** | | |
| Anode/cathode injection barrier | | 0 - 0.2 eV |

Table E.3: Details on the experimental devices.

| Device number | Device structure | Processing technique perovskite | Analysis method | Reference |
|---|---|---|---|---|
| 1 | ITO/TaTm:F$_6$-TCNNQ/TaTm/CH$_3$NH$_3$PbI$_3$/C60/C60:PhIm/Ag | vacuum | DD fitting | 1 |
| 2 | ITO/C60:PhIm/C60/CH$_3$NH$_3$PbI$_3$/TaTm/TaTm:F$_6$-TCNNQ/Ag | vacuum | DD fitting | 1 |
| 3 | ITO/PTAA/CsPbI$_{0.05}$[(FAPbI$_3$)$_{0.89}$(MAPbI$_3$)$_{0.11}$]$_{0.95}$/C60/BCP/Cu | spin-coating | PL & DD fitting | 2,3 |
| 4 | ITO/PFN/PTAA/CsPbI$_{0.05}$[(FAPbI$_3$)$_{0.89}$(MAPbI$_3$)$_{0.11}$]$_{0.95}$/LiF/C60/BCP/Cu | spin-coating | PL | 2 |

Figure E.1: Evolution of the ideality factor and recombination fraction depending of the trap density at the grain boundary (a), front (b) and back interface (c).



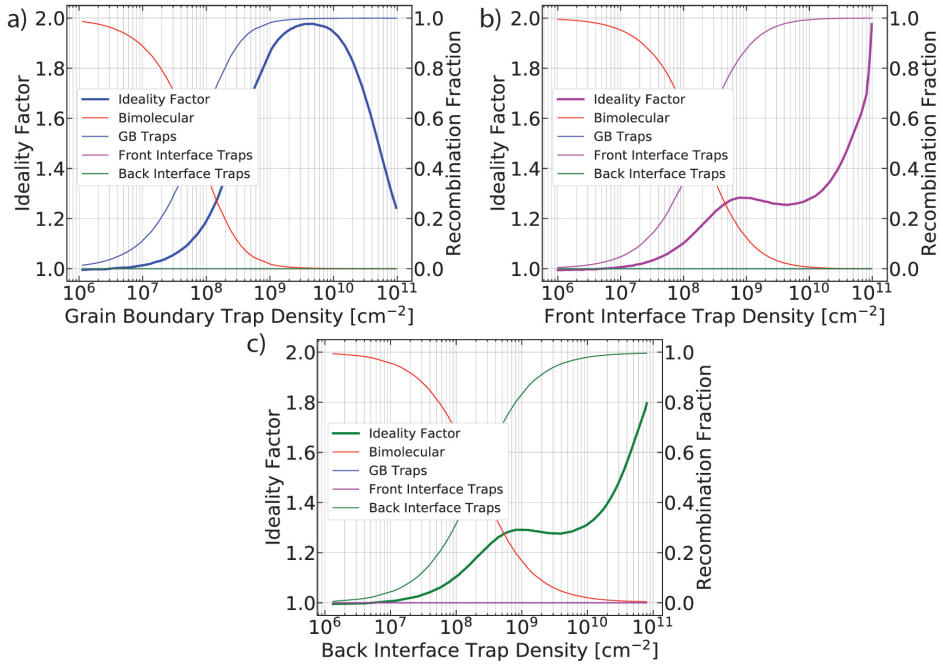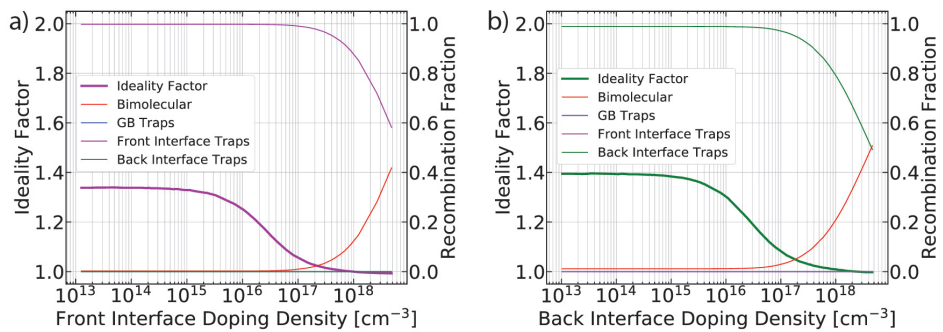Figure E.2: Evolution of the ideality factor and recombination fraction depending of the doping density of the front (a) and back transport layer (b).
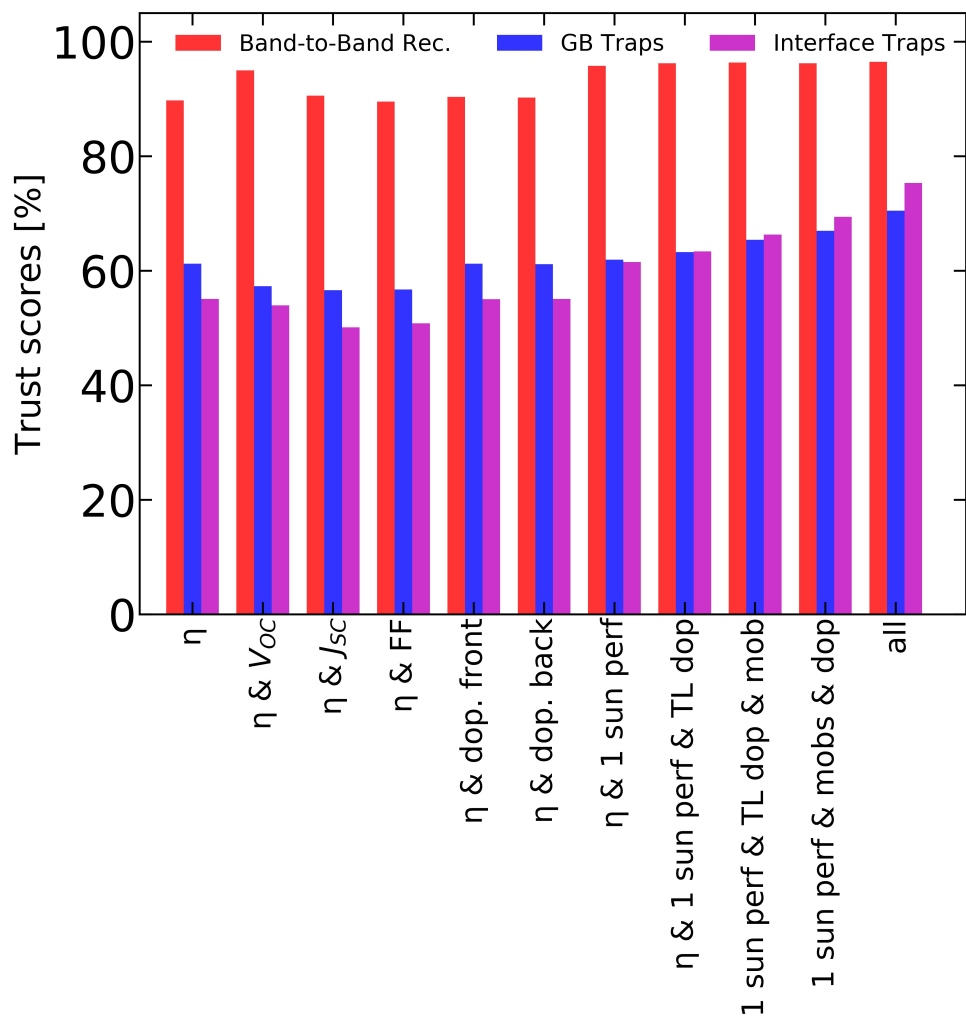
Figure E.3: Evolution of the trust score on the test dataset depending on the features used to train random-forest. We can note that adding more features largely helps improving the predictions of interfacial traps.

## References

[1] T. S. Sherkar, C. Momblona, L. Gil-Escrig, J. Ávila, M. Sessolo, H. J. Bolink, and L. J. A. Koster, *Recombination in perovskite solar cells: Significance of grain boundaries, interface traps and defect ions,* ACS Energy Letters **2**, 1214 (2017).

[2] M. Stolterfoht, C. M. Wolff, J. A. Márquez, S. Zhang, C. J. Hages, D. Rothhardt, S. Albrecht, P. L. Burn, P. Meredith, T. Unold, and D. Neher, *Visualization and suppression of interfacial recombination for high-efficiency large-area pin perovskite solar cells,* Nature Energy **3**, 847 (2018).

[3] V. M. Le Corre, M. Stolterfoht, L. Perdigón Toro, M. Feuerstein, C. Wolff, L. Gil-Escrig, H. J. Bolink, D. Neher, and L. J. A. Koster, *Charge Transport Layers Limiting the Efficiency of Perovskite Solar Cells: How To Optimize Conductivity, Doping, and Thickness,* ACS Applied Energy Materials **2**, 6280 (2019).

**E**

# SUMMARY

Our rising need for energy combined with the realization that we need to drastically reduce our consumption of fossil energy to mitigate climate change, forces us to find better and cleaner ways to produce energy. While the price of solar energy has significantly decreased over the past two decades there is still a long way to go for solar to be a truly important part of our energy production.

To increase the relative proportion of our energy produced with solar we not only need to make more efficient solar panels but also diversify the applications. Organic and perovskite solar cells present advantages for both objectives, they can be used in combination with classical technology in tandem or multi-junction structures to improve their efficiency. They can also be used in a broader range of applications as both technology can be solution-processed, made flexible, semi-transparent and perform well under low light intensity conditions. These characteristics open many doors for the future where solar energy production will not only be confined to roof-top and solar farms applications but also in a more building-integrated fashion such as semi-transparent solar windows or even used to power internet of things products.

While significant progress have been made on increasing the efficiency of both organic and perovskite solar cells, progress still need to be made in understanding the key loss processes and how to characterize and properly quantify the different losses.

The first part of this thesis focuses on one of the bottlenecks of organic solar cells: the exciton diffusion length. Having a long enough exciton diffusion length is crucial to ensure charge separation in low dielectric constant organic semiconductor blends. In **chapter 2**, we report the exciton diffusion length on 9 acceptors including some of the highest performing materials to date. This chapter also provides some insight on the influence of the chemical structure of the non-fullerene acceptors on the exciton diffusion length and especially the influence of end-groups.

As a natural next step after discussing the exciton dynamics we then focus on the extraction dynamics of the subsequently generated free charges. More specifically the influence of dispersion on the extraction time under operating conditions. In fact, the accuracy and relevance of the values obtained when characterizing the transport of organic semiconductors using classical methods were called into question as they usually underestimate the influence of non-thermalized charges. In **chapter 3**, we combine experiments and simulations to show that non-thermalized carriers only have a small influence on the extraction under operating conditions.

In the second part of this thesis, we study perovskite materials and their application to solar cells. We start by discussing the intrinsic properties of single-crystal perovskite using single-carrier devices and the so-called space-charge-limited measurements. In **chapter 4** we present a perspective on the pitfalls of using such a technique on perovskite materials and especially how the ionic movement can drastically influence the outputs and lead to ill-based conclusions on the defect density extracted from these

measurements. We also propose an alternative measurement procedure to get reliable current-voltage characteristics that are less affected by ionic motion. This measurement combined with drift-diffusion fitting of the current-voltage characteristics allows us to extract, simultaneously, values for the mobility, trap and ion densities.

In the last two chapters, extensive simulations are used to discuss the factors limiting the efficiency of perovskite solar cells. In **chapter 5** we show that the transport properties of the transport layers strongly influence the device performance. We introduce two new figures of merit to help to tune the thickness and/or conductivity of the transport layers to avoid transport losses. Both simulations results and experimental results on solution and vacuum processed PSCs show that when the requirement imposed by one or the other of the figure of merit is met transport losses due to the transport layers are negligible.

Finally, in **chapter 6** the use of simulation trained machine learning as a tool for the identification of the dominant recombination process in PSCs is presented. The machine learning toolbox provides a good platform to quickly identify the dominant loss without having to perform any kind of fitting procedure of the experimental data and could be used in combination with high-throughput experimentation. This chapter also provides an in-depth analysis of the light intensity dependence of the open-circuit voltage ($V_{OC}$) and how it relates to the dominant recombination process. It also shows that the analysis of such a measurement needs to be made with care as transport and doping properties of the different layers also influence the results.

# SAMENVATTING

Ons toenemende energiegebruik, in combinatie met het feit dat we het gebruik van fossiele brandstoffen moeten verminderen om klimaat verandering tegen te gaan, noodzaakt ons tot het vinden van betere en schonere manieren van energieproductie. Terwijl de prijs van zonne-energie enorm is gedaald in de afgelopen 20 jaar, is er nog steeds een lange weg te gaan totdat zonne-energie een belangrijk deel van de totale energieproductie inneemt. Om zonne-energie een belangrijkere rol te laten spelen zal de efficiëntie van zonnepanelen omhoog moeten, en zal er gekeken moeten worden naar het uitbreiden van de toepassingen van zonnecellen.

Organische zonnecellen en perovskiet zonnecellen hebben voordelen voor beide doelen. Zo kunnen ze beiden gebruikt worden in tandem and multi-junctie zonnecellen door ze bijvoorbeeld te combineren met bestaande technologieën om de efficiëntie te verbeteren. Vanwege de verwerkbaarheid vanuit oplossing, de mogelijkheid voor flexibele en gedeeltelijk transparante cellen, en de goede prestatie onder weinig licht, maakt het mogelijk om beiden materialen te gebruiken voor een breder scala aan toepassingen. Deze eigenschappen maken het mogelijk om zonnepanelen in de toekomst niet alleen op het dak of in zonneboerderijen te zien, maar ook in gebouw geïntegreerde installaties door middel van bijvoorbeeld gedeeltelijk transparante zonneramen, en als energie toevoer voor de Internet of Things. Tot dusver zijn er enorme vorderingen gemaakt wat betreft de efficiëntie van organische en perovskiet zonnecellen. Desondanks is er meer fundamenteel onderzoek nodig naar het begrijpen van de processen waarbij ladingsdragers verloren gaan.

Het eerste deel van dit proefschrift is gericht op één van de grootste knelpunten in organische zonnecellen, namelijk de korte excitondiffusielengte. Een lange excitondiffusielengte is van cruciaal belang voor ladingsscheiding in materialen met een lage diëlektrische constante, zoals organische halfgeleiders.

In hoofdstuk 2 wordt de excitondiffusielengte van 9 verschillende acceptanten, waarvan sommigen de best presterende materialen van dit moment zijn, berekend. Dit hoofdstuk geeft ook inzicht in de invloed van chemische structuren van fullereen-vrije acceptoren op excitondiffusielengte. Hierbij wordt de nadruk vooral gelegd op de eindgroepen van deze materialen.

De focus ligt daarna op de extractiedynamica van de gegenereerde vrije lading, en specifiek op de invloed van de spreiding van de extractietijd onder operationele omstandigheden. De nauwkeurigheid en relevantie van de gerapporteerde waardes van ladingstransport in organische halfgeleiders wordt door sommigen in twijfel getrokken omdat deze de invloed van niet gethermaliseerde lading zouden onderschatten. In hoofdstuk 3 combineren we daarom experimenten en simulaties om te laten zien dat niet gethermaliseerde ladingsdragers maar van kleine invloed zijn op de operationele condities.

In het tweede deel van dit proefschrift worden perovskiet materialen, en het gebruik daarvan in zonnecellen, behandeld. De nadruk ligt op perovskiet kristallen, om het mo-

147

gelijk te maken om de intrinsieke eigenschappen te bekijken. In de conventionele half-geleider natuurkunde worden halfgeleiders vaak gekarakteriseerd met behulp van metingen van ruimteladingsbegrensde stroom. Echter wordt in hoofdstuk 4 een perspectief gegeven op de valkuilen van dit soort metingen op perovskiet gebaseerde diodes, vanwege hun gemengde ionische en elektronische aard. De ionenmigratie in perovskiet materialen kan een dramatisch effect hebben op de elektronische geleiding, en kan daardoor leiden tot verkeerde conclusies, met name wat betreft de concentratie van defecten. Het hoofdstuk bespreekt een voorstel voor een alternatieve meetmethode waarbij de ionenmigratie minimaal is. Met behulp van deze methode, in combinatie met drift-diffusie simulaties is het mogelijk om de mobiliteit en en de concentratie van zowel ionen als defecten te achterhalen.

De laatste twee hoofdstukken van dit proefschrift onthullen uitgebreidere simulaties die gebruikt worden om een beter begrip te krijgen van de verschillende factoren die de efficiëntie van perovskietzonnecellen kunnen beperken. In hoofdstuk 5 wordt allereerst aangetoond dat de transporteigenschappen van de transportlagen de prestatie van de zonnecellen sterk kunnen beïnvloeden. Om transportverliezen in transportlagen te voorkomen worden er twee vereisten geïntroduceerd die kunnen helpen bij zowel het afstemmen van de dikte als het geleiden van lading. Via zowel simulaties als experimenten wordt aangetoond dat de transportverliezen in de transportlagen verwaarloosbaar zijn als tenminste een van de vereisten wordt behaald.

Tot slot wordt het gebruik van simulatie getrainde machine learning als hulpmiddel voor identificatie van dominante recombinatieprocessen in perovskiet zonnecellen besproken. Machine learning biedt een goed platform om de dominante verliezen snel te identificeren zonder dat enige vorm van aanpassing van de experimentele gegevens nodig is. Dit hoofdstuk geeft ook een diepgaande analyse van de lichtintensiteitsafhankelijkheid van de openklemspanning, en hoe deze zich verhoudt in relatie tot de dominante recombinatieprocessen. Tot slot laat het zien dat de analyse van dergelijke metingen met zorg moet gebeuren, aangezien transport- en doteringseigenschappen van de verschillende lagen de resultaten sterk kunnen beïnvloeden.

# Curriculum Vitæ

## Vincent M. Le Corre

| | |
|---|---|
| 13-10-1992 | Born in Villiers-le-bel, France. |

### Education

2015–2019      PhD. Physics
Groningen, Netherlands

| | |
|---|---|
| *Thesis:* | Lessons learned from device modeling of organic & perovskite solar cells |
| *Promotor:* | Prof. dr. L. J. A. Koster |

2014–2015      Research Master in Physical-Chemistry of Materials (Double degree)
University of Bordeaux
Bordeaux, France

2012–2015      Master in Chemistry and Physics
Graduate School of Chemistry, Biology and Physics of Bordeaux (ENSCBP)
Bordeaux, France

2010–2012      Classes Préparatoires aux Grandes Ecoles
Pothier Highschool
Orléans, France

# LIST OF PUBLICATIONS

23. Jonas Diekmann, Pietro Caprioglio, Moritz H. Futscher, **Vincent M. Le Corre**, Sebastian Reichert, Frank Jaiser, Malavika Arvind, Carsten Deibel, Bruno Ehrler, Thomas Unold, Thomas Kirchartz, Dieter Neher and Martin Stolterfoht, *Pathways towards 30% efficient single-junction perovskite solar cells*, Submitted.

22. **Vincent M. Le Corre**, Elisabeth A. Duijnstee, Omar El Tambouli, James M. Ball, Henry J. Snaith, Jongchul Lim and L. Jan Anton Koster, *Revealing Charge Carrier Mobility and Defect Densities in Metal Halide Perovskites via Space-Charge-Limited Current Measurements*, ACS Energy Letters, 2021, 6, 1087–1094.

21. **Vincent M. Le Corre**, Tejas S. Sherkar, Marten Koopmans and L. Jan Anton Koster, *Identification of the Dominant Recombination Process for Perovskite Solar Cells Based on Machine Learning*, Cell Reports Physical Science 2021, 2, 100346.

20. Elisabeth A. Duijnstee, **Vincent M. Le Corre**, Michael B. Johnston, L. Jan Anton Koster, Jongchul Lim and Henry J. Snaith, *Understanding Dark Current-Voltage Characteristics in Metal-Halide Perovskite Single Crystals*, Physical Review Applied 15, 014006.

19. **Vincent M. Le Corre**, Zishuai Wang, L. Jan Anton Koster and Wolfgang Tress, *Device Modeling of Perovskite Solar Cells: Insights and Outlooks*, in Soft-Matter Thin Film Solar Cells: Physical Processes and Device Simulation, edited by Jingzheng Ren and Zhipeng Kan (AIP Publishing, Melville, New York, 2020), Chapter 4, pp. 4-1–4-32.

18. Licheng Hou, Jie Lv, Friso Wobben, **Vincent M. Le Corre**, Hua Tang, Ranbir Singh, Min Kim, Fufang Wang, Haitao Sun, Wenjing Chen, Zhenguo Xiao, Manish Kumar, Tongle Xu, Weimin Zhang, Iain McCulloch, Tainan Duan, Huling Xie, L. Jan Anton Koster, Shirong Lu and Zhipeng Kan, *Effects of Fluorination on Fused Ring Electron Acceptor for Active Layer Morphology, Exciton Dissociation, and Charge Recombination in Organic Solar Cells*, ACS Applied Materials & Interfaces 2020, 12, 50, 56231–56239.

17. Yuliar Firdaus, Carr Hoi Yi Ho, Yuanbao Lin, Emre Yengel, **Vincent M. Le Corre**, Mohamad I. Nugraha, Emre Yarali, Franky So, and Thomas D. Anthopoulos, *Efficient Double- and Triple-Junction Nonfullerene Organic Photovoltaics and Design Guidelines for Optimal Cell Performance*, ACS Energy Letters, 2020, 5, 3692–3701.

16. Yuliar Firdaus*, **Vincent M. Le Corre***, Safakath Karuthedath, Wenlan Liu, Anastasia Markina, Wentao Huang, Shirsopratim Chattopadhyay, Masrur Morshed Nahid, Mohamad I. Nugraha, Yuanbao Lin, Akmaral Seitkhan, Aniruddha Basu, Weimin Zhang, Iain McCulloch, Harald Ade, John Labram, Frédéric Laquai, Denis Andrienko, L. Jan Anton Koster, Thomas D. Anthopoulos, *Long-range exciton diffusion in molecular non-fullerene acceptors*, Nature Communications, 2020, 11:5220 *equal contribution.

15. Elisabeth A. Duijnstee, James M. Ball, **Vincent M. Le Corre**, L. Jan Anton Koster, Henry J. Snaith and Jongchul Lim, *Towards Understanding Space-charge Limited Current Measurements on Metal Halide Perovskites*, ACS Energy Letters 2020, 5, 376-384.

14. Dingqin Hu, Qianguang Yang, Haiyan Chen, Friso Wobben, **Vincent M. Le Corre**, Ranbir Singh, Hua Tang, L. Jan Anton Koster, Tainan Duan, Zhipeng Kan, Zeyun Xiao, and Shirong Lu, *15.34% Efficiency All-Small-Molecule Organic Solar Cells with Improved Fill Factor Enabled by a Fullerene Additive*, Energy Environmental Science, 2020, 13, 2134-2141.

13. Yuliar Firdaus, Qiao He, Yuanbao Lin, Ferry Anggoro Ardy Nugroho, **Vincent M. Le Corre**, Emre Yengel, Ahmed H. Balawi, Akmaral Seitkhan, Frédéric Laquai, Christoph Langhammer, Feng Liu, Martin Heeney and Thomas D. Anthopoulos, *Novel Wide-Bandgap Non-fullerene Acceptors for Efficient Tandem Organic Solar Cells*, Journal of Materials Chemistry A, 2020, 9, 1164-1175.

12. Juliane Kniepert, Andreas Paulke, Lorena Perdigón-Toro, Jona Kurpiers, Huotian Zhang, Feng Gao, Jun Yuan, Yingping Zou, **Vincent M. Le Corre**, L. Jan Anton Koster, and Dieter Neher, *Reliability of charge carrier recombination data determined with charge extraction methods*, Journal of Applied Physics 2019, 126, 205501.

11. Martin Stolterfoht, **Vincent M. Le Corre**, Markus Feuerstein, Pietro Caprioglio, L. Jan Anton Koster and Dieter Neher, *Voltage dependent photoluminescence and how it correlates to the fill factor and open-circuit voltage in perovskite solar cells*, ACS Energy Letters 2019, 4, 2887-2892.

10. **Vincent M. Le Corre**, Martin Stolterfoht, Lorena Perdigón-Toro, Markus Feuerstein, Christian Wolff, Lidón Gil-Escrig, Henk J. Bolink, Dieter Neher and L. Jan Anton Koster, *Charge Transport Layers Limiting the Efficiency of Perovskite Solar Cells: How To Optimize Conductivity, Doping, and Thickness*, ACS Applied Energy Materials 2019, 2 (9), 6280-6287.

9. Yuliar Firdaus, **Vincent M. Le Corre**, Jafar I. Khan, Zhipeng Kan, Frédéric Laquai, Pierre M. Beaujuge and Thomas D. Anthopoulos, *Key Parameters Requirements for Non-Fullerene-Based Organic Solar Cells with Power Conversion Efficiency >20%*, Advanced Science 2019, 6, 1802028.

8. Nutifafa Y. Doumon, Mikhail V. Dryzhov, Félix V. Houard, **Vincent M. Le Corre**, Azadeh Rahimi Chatri, Panagiotis Christodoulis and L. Jan Anton Koster, *Photostability of Fullerene and Non-Fullerene Polymer Solar Cells: The Role of the Acceptor*, ACS Applied Materials & Interfaces 2019, 11, 8, 8310-8318.

7. **Vincent M. Le Corre**, Azadeh Rahimi Chatri, Nutifafa Y. Doumon and L. Jan Anton Koster, *Response to Comment on "Charge Carrier Extraction in Organic Solar Cells Governed by Steady-State Mobilities"*, Advanced Energy Materials 2018, 8, 1803125.

6. Fallon J. M. Colberts, Martijn M. Wienk, Ruurd Heuvel, Weiwei Li, **Vincent M. Le Corre**, L. Jan Anton Koster and René A. J. Janssen, *Bilayer-Ternary Polymer Solar Cells Fabricated Using Spontaneous Spreading on Water*, Advanced Energy Materials 2018, 8, 1802197.

5. Ru-Ze Liang, Maxime Babics, Victoria Savikhin, Weimin Zhang, **Vincent M. Le Corre**, Sergei Lopatin, Zhipeng Kan, Yuliar Firdaus, Shengjian Liu, Iain McCulloch, Michael F. Toney, Pierre M. Beaujuge, *Carrier Transport and Recombination in Efficient "All-Small-Molecule" Solar Cells with the Nonfullerene Acceptor IDTBR*, Advanced Energy Materials 2018, 8, 1800264.

4. Azadeh Rahimi Chatri, Solmaz Torabi, **Vincent M. Le Corre** and L. Jan Anton Koster, *Impact of Electrodes on Recombination in Bulk Heterojunction Organic Solar Cells*, ACS Applied Materials & Interfaces 2018, 10, 14, 12013-12020.

3. **Vincent M. Le Corre**, Azadeh Rahimi Chatri, Nutifafa Y. Doumon and L. Jan Anton Koster, *Charge Carrier Extraction in Organic Solar Cells Governed by Steady-State Mobilities*, Advanced Energy Materials 2017, 7, 1701138.

2. Solmaz Torabi, Megan Cherry, Elisabeth A. Duijnstee, **Vincent M. Le Corre**, Li Qiu, Jan C. Hummelen, George Palasantzas and L. Jan Anton Koster, *Rough electrode creates excess capacitance in thin-film capacitors*, ACS Applied Materials & Interfaces 2017, 9, 27290-27297.

1. Yangqin Gao, **Vincent M. Le Corre**, Alexandre Gaïtis, Marios Neophytou, Mahmoud Abdul Hamid, Kazuhiro Takanabe and Pierre M. Beaujuge, *Homo-Tandem Polymer Solar Cells with $V_{OC}$ > 1.8 V for Efficient PV-Driven Water Splitting*, Advanced Materials 2016, 28, 3366–3373.

# ACKNOWLEDGEMENTS

The end, it is a bittersweet moment as I am now feeling torn between the fact that I am happy to be done but also partly regret that it did not last longer. Finishing a PhD is not something that comes easy and I have to admit that it took more effort than I thought it would. However, I have no regret for my decision to pursue a PhD. It was hard, depressing at times, as most PhDs are I guess, but it was also great. What a pleasure to spend days after days, sometimes months, to solve a problem and finally getting it. That "Eureka" moment is well worth all the difficult times that lead to it. It is so very satisfying to understand something new and even better getting to discuss/debate about it with your peers.

One of the essential parts for a happy PhD is a good supervisor and I have to say that on that part I have been very lucky. *Jan Anton* thank you so much for everything! You have been great and working with you has been a pleasure and I hope we will continue to work together for the years to come. Your door was always open for a chat or to discuss work and that is rare and priceless. It makes all of us feel safe because we know that if we really need it you will be here to help. You have the extraordinary ability to adapt your type of supervision to the students in front of you by either giving them more guidelines and meeting often or by giving the freedom to explore their ideas and working on their projects. Through my PhD I was happy to be given that freedom as you probably came to realize that I am not a big fan to be told what to do and how to do it. I know I was not always easy and I had the bad tendency to cut you in the middle of your sentence (for that I am sorry) but for some reason, you always found to keep the discussion cordial and nice so thank you for that. Thank you also for letting me handle the collaboration we had, whether they originated from my contacts or yours, it is so valuable for me.

We went through some difficult times together on some of the works we did, most notably the comment on my first paper... This period was rather difficult for me, and I expect not so easy for you too. But you managed to get us back on track and give what I think is a proper answer. Then not so long after came the "Red, White and Blue" story, I remember a few weeks when every day we thought we finally got it all to realize again that we did not. I remember the frustration we both had at the time, it was on paper such a beautiful story and we tried so hard to make it work. Again you handled the situation in what I think is the best possible way. As we were both getting on each other's nerves you told me that we should both stop working on that project for a while and come back at it with fresh eyes in a couple of months. As it turned out this was indeed the best thing to do, as without even thinking about I did solve that problem a few months after. It was for sure not as nice as the initial story and not publishable but at least we understood what was happening. We even managed to turn that story into something positive which now constitutes chapter 6. Overall this was a good lesson, now I know that it is sometimes better to let a story rest for a while and come back to it fresh, I will remember that for the rest of my career.

Finally, just thank you for being so great, maybe you do not realize but all your students know how lucky they are to have you as a supervisor. The "Best PhD Supervisor" award you got was well deserved and I wish you could get even more recognition for the work you do. Some other professors would have a lot to learn from the way you lead your group and handle your students. If more of them were like you I am convinced that there would be fewer reports of depression among PhD students and academia would be a better place.

I would like to thank all the members of that joined our group over the years, in chronological order: *Davide, Niels, Solmaz, Jian, Tejas, Nutifafa, Azi, Marten*. It was nice sharing the office with you guys and I will miss sitting on the couch with my coffee and distract all of you! Thanks for all the interesting discussions we had over the whiteboard those were great and I will miss those exchange of ideas.

*Tejas*, thank you SO much for being one of the nicest guys I know and making my integration into the Groningen lifestyle so quick. I still remember my first week where you invited me to go for dinner to Wereldburgers and later we joined your friends to go out. You showed me Chupitos (that may have been a mistake) and a lot of other cool places. I do not remember everything from that first night but I know it was great and gave me a nice start in Groningen. I could go on and talk about all the nice trips and all the nice evenings and parties. My experience of Groningen would not have been the same without you.

*Nutifafa*, you have been a great office mate and conference travel buddy we had such a great time at our first conference in Poland with great food! Man, I still remember that plate from the first restaurant we went to where none of us could finish all the meat, and also that great Thai place where we went most of the nights after. It was always nice to see you put on your serious face to give your (always great) talks. I wish you and your wife all the best and hope to cross your path someday at another conference!

*Marten*, I was so happy when you joined the group, you have always been among those who actively participate in the good group atmosphere whether it is in the office or outside during a borrel or at a party. You have been the code master in the group for a while now and thanks a lot for that you made a lot of our lives easier. I wish you all the best for the end of your PhD and I will try my best to be there when you defend so we can celebrate properly. But most importantly, thank you for agreeing to be my paranymph!

Thanks also all the students that I had the pleasure to supervise and work with: *Sanne, Elisa, Elisabeth, Johann, Wouter, Tristan, Felix, Omar, Friso, Mare, Jelte*, all this work would not have been possible without you guys and I wish you all the best for your future studies and work.

The POE group members contributed to a very friendly and relaxed atmosphere at work. *Maria* thank you for always reminding us to "plug (y)our brains!" but also for making sure that we had social events during the year, those were great. I will remember the nice time we had during our Christmas dinners, group outings, the evenings of the FOM conference in Veldhoven and especially our after-lunch coffee breaks during which *Simon* and *Bart* always had such a nice time to joke around and make fun of the French people and their accent. By the way, *Bart*, I still have not seen "Au service de la France" maybe someday I will...

I would also like to thank all the great collaborators I had during those 4 years, *Yuliar*

(KAUST), *Zhipeng* (CIGIT), *Elisabeth* (Oxford), *Martin* (Postdam), *Jonathan* (Oxford), *Karen* (Erlangen-Nuremberg).

Special shoutout to *Elisabeth* for all the phone/skype calls on the SCLC projects trying to understand what was happening, working with you is always a pleasure. Waiting forward to read your thesis! Good luck for the end of your PhD I wish you all the best.

During my PhD I also got the chance to organize a lot of events, mostly vrijmibo and borrels with the GSSE PhD council and Gopher 2018, and let's be honest those were the evenings that made PhD life bearable. So I wanna thank the GSSE team: *Sabrina, Daniel, Olivier, Christian, Monique, Frita, Yvonne, Carmen, Renate, Saurabh.* And also my girls from Gopher : *Ioana, Steffie, Caroline, Alina, Xuelai* and *Shaomin.*

*Renate*, I will miss dearly our daily coffee breaks and our discussions. You are an awesome friend and a great person. Thank you for being patient enough to handle me, I am not sure I deserved that. I hope the rest of your PhD goes well and that we will meet again.

Now moving on to the nicest group of PhDs ever, my beloved "Team Groningen": *Désirée, Niek, Anne-Grete, Joana, Paolo, Sharon, Annique, Hannah, Adele, Filippo, Steven and Alberto.* Girls/Guys, I love you all and I miss you already. All the evenings at Blocks and Barrels enjoying some good steaks (thanks *Dave* too), going out to Warhol or Pakhuis, the unforgettable King's nights parties, the GoT nights... So many great memories!

Special thanks to *Sharon* that was awesome enough to endure me and my hangover "accidents" for almost two years. I wish you and *Patrick* a very happy life together you both deserve it.

My *Pepelepu* and *little Bacon* we had so much fun together so many parties and some unforgettable trips too. Our trip to Peru was without question one of the best trips I have ever made which is not surprising looking at the awesome company I had. And what a great way to start a new year!

*Rish* meeting you was such a pleasure and I have Alberto to thanks for that. The three of us had some amazing nights out we must have finished hundreds of tequila bottles and so many balloons together. The nights were crazy and the day after difficult but it was worth it. Little *Julius* is a lucky kid he has an awesome dad and mother, all the best to you and *Ena*.

*Marc*, it was great having you as a housemate we had a lot of fun together, I still remember the first time I brought you out. You can in a bit late and just order two beers and you directly chucked one and then started drinking the other one normally and when I asked you why you look at me and said "I needed to catch up!" at that moment I knew we would be good friends.

*Daniele*, it is sad that we only met at the end, but we had some good time together and I am happy we enjoyed every minute of it before it ended. I wish you all the best for the end of your PhD and the rest of your career, which I have no doubt will go very well.

Finally, I would like to thanks all the others I had the pleasure to meet in Groningen either at work or during parties. My time in Groningen was great thanks to you!

Bon maintenant passons aux Français!

Commençons par ceux qui me suivent depuis le plus longtemps plus de 10 ans main-

tenant: *Maxime, Ismaël, Virak, Alexandre, Julien* et tous les autres *alcooliques anonymes*. Tellement de souvenir tous ensemble depuis le collège pour certains et le lycée pour les autres. On a fait tellement de choses ensemble, on a tous grandi ensemble. Je sais maintenant que peu importe où je pars vivre et pendant combien de temps vous ferez toujours partie de ma vie. Je suis douloureusement conscient qu'en partant vivre à l'étranger j'ai raté énormément de choses, des anniversaires, des soirées, des vacances mais j'ai toujours essayé de faire de mon mieux pour être présent dans les moments qui comptent et je promets de continuer de mon mieux. J'espère tous vous voir le jour de ma défense de thèse histoire que l'on puisse fêter ça correctement.

Au passage, une petite note pour *Max* et *Isma* qui se sont toujours délectés de mon merveilleux accent anglais pendant nos années de lycée, qui l'eut cru que je serais celui d'entre nous qui écrirait une thèse en anglais, hein?!

Maintenant passons aux PDGs de l'amour, que dire de ces 3 années d'école si ce n'est qu'elles étaient géniales. Pour être honnête l'école me manque, en fait non, c'est pas vraiment l'école qui me manque c'est vous tous *NB, AG, CJ, RB, GG, CS, AL, TB, CG, MB, AP, ELC, CS, PC* 9A CP (BA) qui me manquez. Souvent j'aimerait pouvoir me refaire une dernière petite soirée tranquille au Foy' avec des bonnes bières et un petit BBQ comme en fin de 1A, c'était le bon temps. Retrouver la colopepito avec les best colocs ever *Nidou* et *Gait*. Refaire des parties de cap's au lever du jour après un tournois, des BP en apéros, des pérudos entre deux cours...

*Alex*, c'est probablement toi qui m'auras supporté le plus longtemps, entre les deux années de coloc et le stage en Arabie Saoudite mon pauvre tu en as bavé! Je me souviens de te voir craquer quand je te répondais pas (bien sur je ne faisais pas exprès) mais je me souviens aussi que tu étais là dans les moments difficiles aussi. On se rappellera d'une mise dans la baignoire après une soirée dont on ne parlera pas ou du petit cadeau bleuté laissé lâchement sur ta terrasse hahaha, bref tu en as vu de toutes les couleurs mais tu es toujours là donc merci frérot.

*Coco*, ça n'a pas toujours été facile mais sans toi j'en serais pas là aujourd'hui. C'est bon d'avoir quelqu'un avec qui l'on peut échanger des idées. Quelqu'un à qui on fait confiance et dont le jugement compte que ça soit sur les papiers ou présentations que l'on s'envoie régulièrement ou sur le reste. On sait l'un comme l'autre que peu importe le problème auquel on est confronté l'autre sera là à n'importe quelle heure du jour ou de la nuit pour donner conseil ou réconforter. Je sais que je ne me confis pas souvent mais le fait de savoir que je peux me suffit donc merci pour ça.

And last but not least my brother from another mother, mon petit *Nidou*. Toujours fidèle au poste dans les bons comme dans les mauvais moments et Dieu sait qu'on est passé par les deux ensembles. Je me souviendrais des appels où on avait juste à se dire: "mec faut que je bouge" et l'autre était là sans poser de questions. Des kebabs par centaines et des bières par milliers, des préchauffes à deux en 1A, des tournois de cap's de légende, des soirées complètement dingues à Groningen avec beaucoup trop de shot et de ballons mais surtout beaucoup trop de sous dépensés avec un petit record qui doit approcher les 300-350 à deux! Ce n'est pas bien on le sait mais qu'est-ce que c'était bien! QLF on le sait! Merci d'avoir accepter d'être mon paranymph je ne m'imagine pas défendre sans toi dans la salle et surtout à la soirée qui s'ensuivra.

Enfin, les plus importants, maman et papa, merci pour tout, je suis bien conscient des sacrifices que vous avez fait pour nous trois. Vous nous avez toujours mis au-dessus de vos propres besoins et on ne pourra jamais vous remercier suffisamment pour ça. Cette thèse n'est qu'un petit effort dans cette direction, même si je sais bien que rien de ce que l'on pourra accomplir ne sera à la hauteur de ce que vous mériteriez. Vous avez été plus que géniaux avec nous et je vous aime profondément.

Cari et Toto, je pense fort à vous aussi, j'espère que vous êtes un peu fière de votre « grand » frère. Et oui Carine j'ai dit " grand " !! On ne se le dit pas souvent mais je suis bien content de vous avoir tous les deux comme frère et sœur et je suis sûr que même dans le futur on arrivera à se retrouver en famille et avoir des bons moments. Et de toute façon on n'a pas le choix, on a fait un pacte, noël c'est en famille!

Petit mot de la fin, alors maman, tu vois qu'au final je l'ai réussi mon « année prochaine » ?!

Vincent